Design and Performance Evaluation of a Permanent Magnet Vernier Machine For Wind Turbine Generator Applications

by

Pushman Michael Tlali

Dissertation approved for the degree of Doctor of Philosophy in Electrical Engineering in the Faculty of Engineering at Stellenbosch University

Supervisor: Prof. R-J. Wang

December 2019

Declaration

By submitting this dissertation electronically, I declare that the entirety of the work contained therein is my own, original work, that I am the sole author thereof (save to the extent explicitly otherwise stated), that reproduction and publication thereof by Stellenbosch University will not infringe any third party rights and that I have not previously in its entirety or in part submitted it for obtaining any qualification.

Signature: .....
P. M. Tlali

Date: ..... December 2019 .....

Abstract

Design and Performance Evaluation of a Permanent Magnet Vernier Machine For Wind Turbine Generator Applications

P. M. Tlali

Department of Electrical and Electronic Engineering,
University of Stellenbosch,
Private Bag X1, Matieland 7602, South Africa.

Dissertation: PhD Eng (Electrical)

December 2019

Wind power conversion has emerged as one of the attractive and rapidly growing renewable energy resources. Research in this field has indicated a crucial need of developing new or improved electrical machine technologies, as they are essential components in this application. Currently, a cascaded arrangement of mechanical gearbox and a medium- or high-speed machine is the common configuration implemented in wind turbine systems. However, to avoid gearbox issues and to improve on the system reliability, there has been a paradigm shift towards the use of direct drive generators (DDGs) with full scale converters. Since the DDGs runs at the low turbine speed, they usually have heavy structure and bulky sizes due to high torque requirements.

The past decades have seen a renewed interest in permanent magnet vernier (PMV) machine, which originates from the integration of the magnetic gearing concept with the conventional permanent magnet synchronous machine (PMSM). The inherent magnetic gearing effect of this type of machine enables it to have high torque density, potential for lighter weight and more compactness than conventional PMSMs, while maintaining the similar structural simplicity. Consequently, it appears to be a suitable candidate for low-speed and/or high-torque applications such as wind turbine DDGs. Despite the above mentioned advantages, the PMV machines are notably characterized by lower power factor that may increase the converter rating requirement and subsequently the system cost.

The aim of this research is to develop and evaluate the PMV machine technology for use in the wind power conversion systems. The basic research methodology employed is to first derive fundamental analytical equations that describe the unique performance characteristics of PMV machines, and then to establish a dedicated finite element method based design optimization environment for the design and analysis of PMV machines. In order to show the merits and demerits of PMV machines, a detailed comparison between an optimally designed PMV machine and a conventional PMSM of the same power rating will also be conducted. To validate the performance and design methodology used, an optimally designed prototype PMV machine is constructed, experimentally tested and compared with an existing PMSM machine. In addition, the feasibility of using PMV machine technology for large wind power applications (3 MW) is also evaluated in terms of performance, costs, size and weight. The outcome from this work outlines the advantages and disadvantages of the PMV machine technology and provide insight on the potential of this technology for MW scale wind power applications.

Uittreksel

Ontwerp en Werkverrigting Evaluasie van 'n Permanente Magneet Vernier Masjien For Wind Turbine Generator Applications

P. M. Tlali

Departement Electriese en Electroniese Ingenieurswese,
Universiteit van Stellenbosch,
Privaatsak X1, Matieland 7602, Suid Afrika.

Proefskrif: PhD Ing (Electriese)

Desember 2019

Windkrag omskakeling het na vore gekom as een van die aanloklike en snelgroeiende hernubare energiebronne. Navorsing in hierdie veld het gedui op die noodsaaklikheid daarvan om verbeterde elektriese masjien tegnologieë te ontwikkel, aangesien dié komponente noodsaaklik is in windkrag toepassings. Die mees algemene konfigurasie wat tans in windturbine stelsels geïmplementeer word, is 'n opstelling met 'n meganiese ratkas en 'n medium- of hoë spoed masjien in kaskade gekoppel. Ten einde ratkas probleme op te los en om die betroubaarheid van die stelsels te verbeter het 'n paradigma skuif na die gebruik van direk aangedrewe generators (DDGs) met volskaalse omsetters plaasgevind. Aangesien direk aangedrewe generators teen die lae turbine spoed loop, is hulle struktuur gewoonlik groot en swaar, as gevolg van die hoë draaimoment vereistes.

In die afgelope dekades het 'n hernude belangstelling in permanente magneet vernier (PMV) masjiene ontstaan vanuit die integrasie van die magnetiese rat konsep met die konvensionele permanente magneet sinkroonmasjien (PMSM). Die inherente magnetiese rat effek van hierdie tipe masjien stel dit in staat om 'n hoë draaimomentdigtheid, die potensiaal vir 'n kleiner gewig en 'n meer kompakte vorm as konvensionele PMSMe te hê, terwyl dieselfde eenvoudige struktuur behou kan word. Daarom blyk dit om 'n gepaste kandidaat vir lae-spoed en/of hoë-draaimoment toepassings soos wind turbine DDGs te wees. Ondanks hierdie voordele, word PMV masjiene gekarakteriseer deur 'n laer arbeidsfaktor wat die vereiste omsetter grote en gevolglik die stelsel koste mag verhoog.

Die doel van hierdie navorsing is om die PMV masjien tegnologie te ontwikkel en te evalueer vir gebruik in windkrag stelsels. Die basiese navorsingsmetodologie wat gebruik is, is om eerstens fundamentele analitiese vergelykings af te lei wat die unieke werking van PMV masjiene beskryf, en om dan 'n toegewyde optimeringsomgewing vir die ontwerp en analise van PMV masjiene daar te stel, gebaseer op die eindige-element metode. Ten einde die voor- en nadele van PMV masjiene uit te lig, sal 'n gedetaileerde vergelyking tussen 'n optimaal geontwerpde prototipe PMV masjien en 'n konvensionele PMSM met dieselfde kendrywing gemaak word. Om die geldigheid van die ontwerpsmetodiek en die werkverrigting berekeninge te bevestig, is 'n optimaal geontwerpde prototipe PMV masjien gebou, eksperimenteel getoets en vergelyk met 'n bestaande PMSM masjien. Verder is die moontlikheid om PMV masjien tegnologie vir groot windkrag toepassings (3 MW) te gebruik ook geëvalueer in terme van werkverrigting, koste, grote en gewig. Die uitkomste van hierdie werk werp lig op die voor- en nadele van die PMV masjien tegnologie en verskaf insig in die potensiaal van hierdie tegnologie vir MW-skaal windkrag toepassings.

List of Publications

Journals

- Tlali, P., Gerber, S. and Wang, R.-J.: Optimal design of an outer-stator magnetically geared permanent magnet machine. *Magnetics, IEEE Transactions on*, vol. 52, no. 2, pp. 1-10, Feb 2016. ISSN 0018-9464.
- Wang, R., Matthee, A., Gerber, S. and Tlali, P.: Calculation of torque performance of a novel magnetic planetary gear. *IEEE Magnetics Letters*, vol. 7, pp. 1-5, 2016. ISSN 1949-307X.
- Wang, R.-J., Bronn, L., Gerber, S. and Tlali, P.: An axial flux magnetically geared permanent magnet wind generator. *IEEJ Transactions on Electrical and Electronic Engineering*, vol. 10, no. S1, pp. S123-S132, 2015.

International Conferences

- Tlali, P.M., Wang, R., and Gerber, S.: Comparison of PM vernier and conventional synchronous 15 kW wind generators. In: *2018 XIII International Conference on Electrical Machines (ICEM)*, pp. 2065-2071. Sep 2018, Alexandroupoli, Greece. ISSN 2381-4802.
- Tlali, P.M., Wang, R-J. and Gerber, S.: Magnetic gear technologies: A review. In: *Electrical Machines (ICEM), 2014 XXI International Conference on*, pp. 539-545, Sept 2014, Berlin, Germany.
- Wang, R-J., Bronn, L., Gerber, S. and Tlali, P.M.: Design and evaluation of a disc-type magnetically geared PM wind generator. In: *Power Engineering, Energy and Electrical Drives (POWERENG), 2013 Fourth International Conference on*, pp. 1259-1264. May 2013, Istanbul, Turkey.

National Conferences

- Tlali, P. and Wang, R.-J.: Mass and volume optimization of a permanent magnet vernier machine. In: *Southern African Universities Power Engineering Conference (SAUPEC)*, pp. 315-319. January 2017, Stellenbosch, South Africa.
- Tlali, P., van der Merwe, J., Wang, R.-J. and Gerber, S.: Design aspects of a magnetically geared permanent magnet machine with an outer stator. In: *Southern African Universities Power Engineering Conference (SAUPEC)*. January 2016, Vereeniging, South Africa.
- Tlali P.M., Gerber, S. and Wang, R-J.: Gear ratio selection of an outer-stator magnetically geared machine. In: *Southern African Universities Power Engineering Conference (SAUPEC)*, pp. 242-248, January 2014, Durban, South Africa.

Acknowledgements

I would like to express my sincere gratitude to the following people and organizations :

My promoter **Prof. Rong-Jie Wang** - for his outstanding supervision, insightful guidance, patience and unwavering support throughout the course of my research.

Special thanks to **ABB Corporate Research** (Sweden) for providing a financial support for this project.

Dr. Stiaan Gerber for his great help and wise advice on usage of FEA packages.

EMLab workshop staff: **Petro Petzer, André Swart, Howard Koopman and Murray Jumat** for their assistance on the prototype assembling and test bench set-up.

Akshay Rathilall and Charles Agenbach for their great input on the mechanical design and analysis of the machine.

Ts'epang Jebetle and Kenan Cloete for their assistance on the prototype mechanical design and their input on other production stages.

Christoph Botha for his help with the variable speed drive control.

EMLab colleagues for their friendship and scientific exchanges.

Many thanks to **my Family and Friends** for their persistent support and continued encouragement throughout my educational career.

Greatest gratitude to Almighty God for
daily life, endless love and blessings.

Dedications

To my beloved parents

'Mé 'Mahlakametsa A. Tlali and Ntate Nk'unyane S. Tlali

Contents

List of Figures

List of Tables

Nomenclature

Subscripts

$_n$	n^{th} specific harmonic component, with "n=1" being the fundamental
$_{PM}$	A quantity due to the effect of the Permanent Magnets alone

Accents or Overscores

$\hat{F}_{PM}$	Amplitude of PM MMF distribution
$\vec{M}$	PM's magnetization vector
$\vec{M}_r$	Radial component of PM's magnetization vector
$\vec{M}_\theta$	Tangential component of PM's magnetization vector
$\vec{r}$	Radial axis in cylindrical coordinates system
$\vec{\theta}$	Tangential axis in cylindrical coordinates system

Abbreviations

2D	Two-Dimensional
3D	Three-Dimensional
AC	Alternating Current
AGE	Air-Gap Element
CMG	Coaxial Magnetic Gear
DC	Direct Current
DD-PMG	Direct-Drive Permanent Magnet Generator
DDG	Direct-Drive Generator
DFDSR	Doubly-Fed Dual Stator Reluctance
DR-PMV	Dual-Rotor Permanent Magnet Vernier
DS-PMV	Dual-Stator Permanent Magnet Vernier
DSPM	Doubly-Salient Permanent Magnet
EMF	Electromotive Force
FEA	Finite Element Analysis
FEM	Finite Element Methods
FMMG	Flux Modulated Magnetically Geared
FMP	Flux Modulating Piece
FRPM	Flux Reversal Permanent Magnet
FSCW	Fractional Slot Concentrated Windings
FSPM	Flux Switching Permanent Magnet

GA	Genetic Algorithm
G-DFIG	Geared Doubly Fed Induction Generator
G-PMG	Geared Permanent Magnet Generator
GW	Giga-Watt
HTS	High Temperature Superconducting
kW	kilo-Watt
MB	Moving Band
MGIM	Magnetically Geared Induction Machine
MGPM	Magnetically Geared Permanent Magnet
MGPM-SM	Magnetically Geared PM Machine with Separate Modulator
MMF	Magneto-Motive Force
MMFD	Modified Method of Feasible Directions
MW	Mega-Watt
NSGA-II	Non-Dominated Sorting Genetic Algorithm-II
OW	Overlapping Winding
OW-PMV	Overlapping Winding Permanent Magnet Vernier
PDD	Pseudo Direct Drive
PEC	Power Electronic Converter
PF	Power Factor
PM	Permanent Magnet
PMSM	Permanent Magnet Synchronous Machine
PMV	Permanent Magnet Vernier
PS-PMV	Pole Split (or Split Tooth) Permanent Magnet Vernier
RES	Renewable Energy Sources
RPM	Revolutions Per Minute
SPM	Surface-mounted Permanent Magnet
TFPM	Transverse Flux Permanent Magnet
THD	Total Harmonic Distortion
VFRM	Variable Flux Reluctance Machine

Symbols

$\mathbf{A}$	Magnetic vector potential	[Wb/m]
A	Electric Loading	[kA/m]
A_{co}	Active conductor area in a slot	[m^2]
A_s	Active conductor area of slot	[m^2]
A_{slot}	Available slot area	[m^2]
$\mathbf{B}$	Magnetic flux density	[T]
B_g	Air-gap magnetic loading	[T]
B_g	Air-gap flux density due to PMs	[T]
B_{PM}	Open circuit flux density due to PMs	[T]
B_r	Remanent flux density	[T]

c_o	Ratio of slot opening to slot pitch	[−]
D	Electrical flux density	[C/m^2]
D	Total machine diameter	[mm]
D_g	Air-gap diameter	[mm]
D_{in}	Inner diameter of the machine	[mm]
D_{out}	Outer diameter	[mm]
dq0	Direct, quadrature and zero sequence axes reference frame	[−]
E	Electrical field strength	[V/m]
E_d	Direct axis component of induced voltage	[V]
e_m	Induced electromotive force	[V]
e_{ph}	Induced electromotive force	[V]
E_{ph}	Phase back-EMF magnitude	[V]
E_{ph-rms}	RMS magnitude of induced EMF	[V]
E_q	Quadrature axis component of induced voltage	[V]
F_c	Air-gap MMF due to armature currents	[A]
ff	Slot fill-factor	[−]
F_{PM}	Air-gap MMF due to the PM	[A]
g	Physical clearance between stator and rotor PMs	[mm]
$g^{'}$	Effective air-gap length	[mm]
G	Jacobian matrix of global nodal coordinates	[−]
G_r	Gear ratio	[−]
H	Magnetic field strength	[A/m]
h_m	Radial thickness of PM	[mm]
h_t	Radial height of the stator tooth	[mm]
I_d	Direct axis component of phase current	[A]
I	RMS amplitude of current	[A]
I_{ph}	Phase current	[A]
I_ϕ	Phase current	[A]
I_q	Quadrature axis component of phase current	[A]
I_s	RMS phase current	[A]
J	Current density	[A/mm^2]
J	Current density	[A/mm^2]
k	kth iteration number of optimization process	[−]
K_{add}	Vernier machine's additional constant	[−]
K_{conv}	Vernier machine's conventional constant	[−]
k_d	Stator winding distribution factor	[−]
K_{dq0}	Parks transformation or dq0 transformation matrix	[−]
k_p	Stator winding pitch factor	[−]
k_{PM}	Ratio of PM span relative to pitch angle	[−]
K_s	Linear current density	[kA/m]
K_{vern}	Vernier machine's constant	[−]

K_w	Stator winding factor	[−]
L	Machine stack length	[mm]
l_a	Machine electromagnetic active stack length	[mm]
L_d	Direct axis component of inductance	[H]
l_e	Coil's single side end-winding length	[m]
L_e	End-winding inductance	[H]
L_{gs}	Synchronous inductance	[H]
L_{le}	End-winding leakage inductance	[H]
L_m	Main inductance	[H]
L_q	Quadrature axis component of inductance	[H]
l_{st}	Stator tooth radial length	[mm]
L_{stk}	Machine active stack length	[m]
l_{st_a}	Stator tooth additional thickness	[mm]
l_{st_b}	Stator tooth base thickness	[mm]
m	Stator winding phase number	[−]
N	Number of coil turns	[−]
n_a	Number of coil parallel circuits	[−]
N_m	Modulating pole pieces number	[−]
N_{mb}	Number of moving band elements	[−]
N_{ph}	Number of turns per phase	[−]
n_s	Rotor speed in revolutions per minute	[r/min]
N_s	Modulating pole pieces number	[−]
P_c	Core loss	[W]
P_{core}	Core losses	[W]
P_{cu}	Copper loss power	[W]
P_{EM}	Air-gap electromagnetic power	[W]
p_{fm}	Pole-pieces number of flux-modulator	[−]
P_{fric}	Frictional loss power	[W]
p_h	Pole-pair number of lower pole-count PM rotor	[−]
P_{in}	Input power	[W]
p_l	Pole-pair number of higher pole-count PM rotor	[−]
P_{le}	End-winding leakage permeance	[Wb/A]
P_{mech}	Mechanical loss power	[W]
P_{PM}	Permanent magnet losses	[W]
P_{out}	Active output power	[W]
p_r	Rotor magnetic pole-pair number	[−]
p_{rh}	Rotor magnetic pole-pair number on high-speed rotor	[−]
p_{rl}	Rotor magnetic pole-pair number on low-speed rotor	[−]
p_s	Stator magnetic pole-pair number	[−]
$p_s^{'}$	The number of pole-pairs in a base section of machine	[−]
P_t	NSGA-II parent population	[−]

$P_{windage}$	Windage loss power	[W]
q	Number of slots per pole per phase	[−]
Q	Number of stator slots	[−]
Q_{out}	Reactive output power	[VAR]
q_{ph}	Number of slots per pole per phase in a base section of machine	[−]
Q_s	Stator slots number	[−]
$Q_s^{'}$	The number of slots in a base section of machine	[−]
Q_t	NSGA-II offspring population	[−]
r	Average air-gap radius	[mm]
R_{cm}	Shunt resistance	[Ω]
r_g	Air-gap radius	[mm]
R_m	Rotor PM inner radius	[mm]
R_{ph}	Phase resistance	[Ω]
R_r	Rotor yoke inner radius	[mm]
R_s	Stator outer radius	[mm]
R_ϕ	Phase resistance	[Ω]
R_t	A set combining parent and offspring populations in NSGA-II	[−]
S_{out}	Apparent output power	[VA]
t	Base sections of a machine	[−]
t	time instance	[sec]
T	Electrical period	[sec]
T	Electromagnetic torque	[Nm]
$T_{air-gap}$	Air-gap electromagnetic torque	[Nm]
T_{avg}	Average torque	[Nm]
T_c	Conductor temperature	[°C]
T_{cogg}	Cogging torque	[Nm]
T_{EM}	Average electromagnetic torque	[Nm]
T_g	Air-gap torque	[Nm]
t_{md}	Modulator radial thickness	[mm]
t_{mh}	Rotor PM radial thickness	[mm]
T_{rip}	Torque ripple	[Nm]
t_{ry}	Rotor yoke radial thickness	[mm]
t_{st}	Stator tooth thickness	[mm]
t_{sy}	Stator yoke radial thickness	[mm]
U_ϕ	Terminal voltage in ABC reference frame	[V]
V_d	Direct axis component of terminal voltage	[V]
V_g	Air-gap volume	[m^3]
V_q	Quadrature axis component of terminal voltage	[V]
V_s	RMS terminal voltage	[V]
$\mathbf{X}$	Vector of geometric variables in optimization	[−]
X_{sg}	Synchronous reactance	[Ω]

$\mathbf{Y}$	Vector of objective functions in optimization	[−]
y_q	Stator magnetic pole pitch in slot numbers	[−]
Y_T	Specific conductor material thermal coefficient	[K^{-1}]
z	Number of conductors per slot	[−]

Greek Symbols

α	Initial angular position of the alternating current	[rad.]
α_{ph}	Slot pitch in a base section of a machine	[−]
λ_{ph}	Flux linkage	[Wb.t]
Λ	Total permeance	[Wb/A]
Λ_o	Average permeance	[Wb/A]
Λ_v	Magnitude of specific v^{th} harmonic permeance	[Wb/A]
μ_r	Relative permeability of a specific material	[H/m]
Ω_e	Area of an individual element in a mesh	[m^2]
φ_v	Angle between the induced back-EMF and the terminal voltage	[rad.]
φ	Magnetic flux	[Wb]
σ_{mi}	Modulator piece inner angle to pitch ratio	[−]
σ_{mo}	Modulator piece outer angle to pitch ratio	[−]
σ_{pm}	PM span to pole-pitch ratio	[−]
σ_s	Stator slot angle to pitch ratio	[−]
σ_{so}	Stator slot open to pitch angle ratio	[−]
τ_s	Slot angle	[rad.]
τ_{so}	Slot opening angle	[rad.]
θ	Angular position along the air-gap	[rad.]
θ_i	Rotor initial angle	[rad.]
θ_{mi}	Modulator piece inner angle	[rad.]
θ_{mo}	Modulator piece outer angle	[rad.]
θ_{mp}	Modulator pitch angle	[rad.]
θ_{pm_p}	PM pitch angle	[rad.]
θ_{pm_s}	PM actual span angle	[rad.]
θ_r	Angular reference point	[rad.]
θ_s	Stator slot angle	[rad.]
θ_{so}	Slot opening pitch ratio	[−]
θ_{sp}	Stator slot pitch angle	[rad.]
ω_e	Electrical angular speed of the rotor	[rad/s]
ω_{fm}	Mechanical angular speed of the flux modulator	[rad/s]
ω_h	Mechanical angular speed of high-speed PM rotor	[rad/s]
ω_l	Mechanical angular speed of low-speed PM rotor	[rad/s]
ω_r	Mechanical angular speed of the rotor	[rad/s]
ω_{rh}	Mechanical angular speed of high-speed PM rotor	[rad/s]
ω_{rl}	Mechanical angular speed of low-speed PM rotor	[rad/s]

Chapter 1

Introduction

A steadily increasing global electrical energy demand in conjunction with environmental concerns on the heavy use of fossil fuels has led to the desirability and constant pursuit of renewable energies. Besides the fact that wind power is currently one of the most harnessed form of renewable energy, the interest in its harvesting has lately taken on a more accelerated pace, resulting into rapid growth of wind energy sector. This in turn, has equally led to a high demand and further development of electrical machines since they are essential components in wind-to-electrical energy conversion systems. Consequently, a tangible research effort has been applied to improve their efficiency and reliability, while also simultaneously striving for their cost effective manufacturing.

Furthermore, a light weight with compact structure and high torque handling capability at low operational speeds are some of the features sought on electrical machines used in wind power applications. Although the doubly-fed induction and conventional synchronous generators are currently the most popular concepts in this application, some emerging electrical machine technologies are receiving a lot of attention. Amongst others, the permanent magnet Vernier machine is considered as a promising alternative that can potentially offer better performance in many aspects. By virtue of their inherent magnetic gearing principle that renders them high torque densities, PMV machines have good capabilities to satisfy most of the machine requirements or characteristics needed in the drive-trains of wind turbine systems. Therefore, this research work is aimed at designing and assessing the viability of using PMV machines in this application.

1.1 Background

Fossil fuels have been the world-wide primary source of energy for electricity generation, while the renewable energies were mostly treated as their supplements. With the projected rapid increase of world's electrical energy demands in the future, the irreversible depletion of fossil fuel reserves is a great concern. In addition, the resultant emissions from the consumption of these fuels are strongly associated with the major environmental pollutants and a subsequent escalation of global warming, which adversely affect the earth's ecosystem. Hence, the reliability and sustainability of fossil fuels are no longer guaranteed, especially with the consideration of severe pollutant restrictions recently being put in place. On the other hand, renewable energy sources (RES) appear to be more attractive as they are generated from abundantly available natural resources. Besides, their extraction processes and usage involves less pollution. Therefore, increasing the

percentage contribution of renewable energy sources in the energy composition can boost not only the energy supply security, but also the environmental protection.

Of all the RESs, wind power has proved to have great potentials in electricity generation, and its exploitation has swiftly developed in the past decades. Its dramatic growth is evident from Fig. 1.1, whereby the cumulative installed worldwide wind energy capacity is estimated to have increased more than four-folds within a period of ten years to an approximate total of 539 GW by the end of 2017 [1; 2]. This is about 24 % contribution to global electricity generated from total major renewable energy sources (Hydro, Solar, Wind, Bio-power and Geo-thermal) by that time.

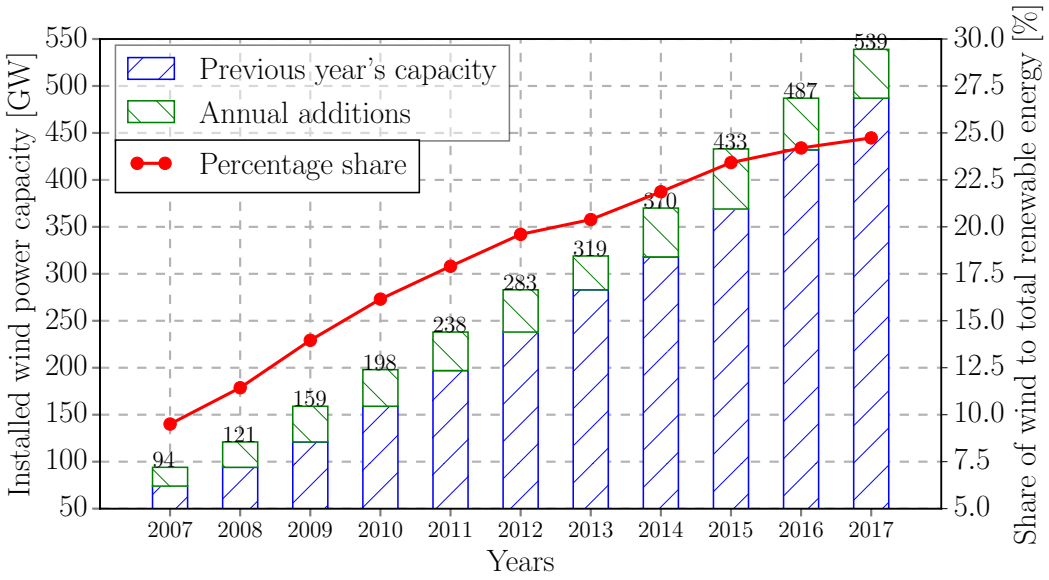

Figure 1.1: Approximation of cumulative installed and growth rate of wind energy in the past ten years up to 2017 [1–3].

Considering the indicated annual growth rate, it is anticipated that the net electricity generation from wind power will be approximately 1352 billion kWh by the end of 2020, which will make it the second largest renewable source of electricity production, after hydro-power (as indicated by Fig. 1.2) [4].

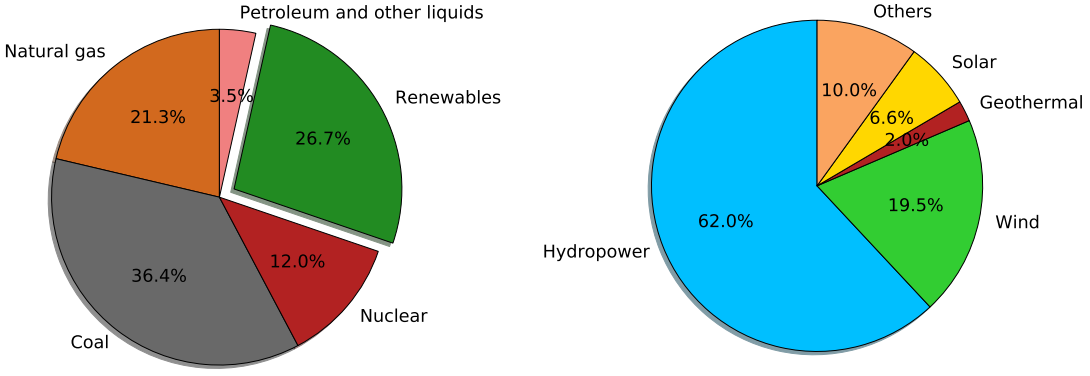

(a) (b)

Figure 1.2: Outlook of world net electricity generation by fuel type in 2020 [4]: (a) total sources (b) renewable sources.

Electrical machines are essential components in the wind power generation applications, since they perform a pivotal role of mechanical-to-electrical energy conversion within a wind turbine (i.e. when used in generator mode). Owing to the global fast growing interest in wind energy harvesting, high efficiency and reliable electrical generators are also in demand so that most of the power captured by the turbine blades can be successfully converted. Common wind turbine drive-train configurations, especially in variable-speed power electronic converter (PEC) grid connected types, employ directly-driven generator (DDG) system and the mechanically geared medium or high speed generator system (Fig. 1.3). These concepts can be further classified according to the absence or number of gearbox stages used in a configuration. As summarized in Table 1.1 for machines with output ratings of at least 1 MW, the number of gearbox stages incorporated in a drive-train also gives a general indication of operating speed margins for a generator. Thus, DDGs typically have lowest operating speeds because they are directly connected to the low-speed rotating turbine shaft with large torque. But in geared-drives, the mechanical gearbox with single or multiple stages is connected in cascaded arrangement to step up the input speed to the generator and simultaneously scale down the torque from the blades shaft. The utilization of gearbox enables the smaller and lighter machine design in comparison to the DDGs.

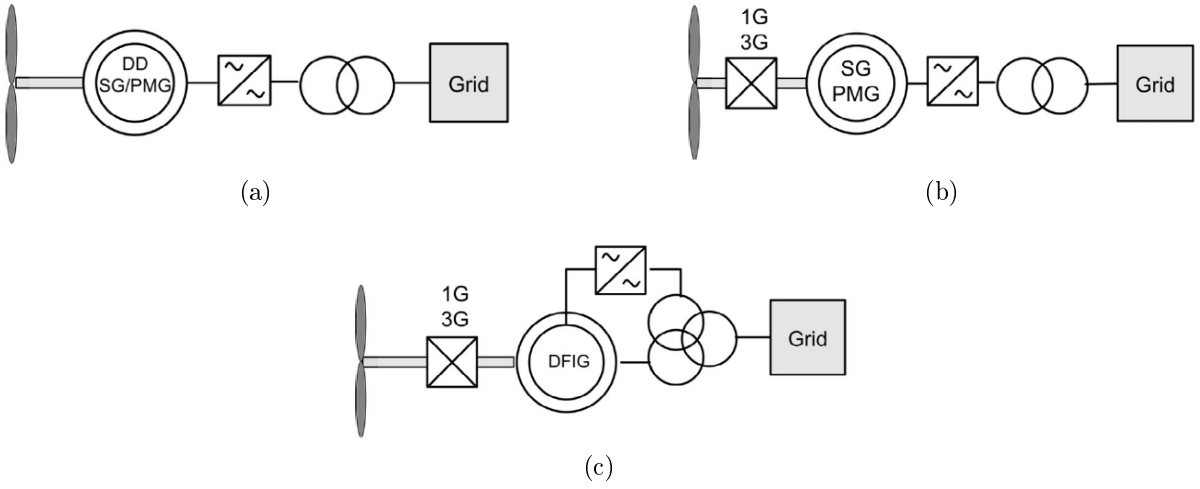

Figure 1.3: Common wind turbine drive-train layouts with PEC grid connected [5]: (a) direct-drive electrically excited or PM excited synchronous generators (b) geared electrically excited or PM excited synchronous generators (c) geared doubly-fed induction generator (G-DFIG).

Table 1.1: Classification of wind turbine drive-train configurations [74–77].

Concept	Definition	Gearbox	Speed*	Generator type
Direct-drive	Low-Speed	None	$\leq$ 50 rpm	PM synchronous
				Wound rotor synchronous
Geared-drive	Medium-speed	Single or Two-stage	100-500 rpm	PM synchronous
				Wound rotor type
	High-speed	Three-stage	$\geq$ 1000 rpm	PM synchronous
				G-DFIG

* The indicated speed ranges are for machines with output capacity of at least 1 MW.

Although the mechanically geared wind generator systems possess certain advantages [5; 74; 78], the general perception emanating from historic failures of wind turbine gearboxes is that they are exposed to reliability issues [76; 86–88]. That is, they are prone to frictional losses, teeth wearing, have high acoustic noise and are subjected to the risk of permanent damage under overload conditions. Consequently, condition monitoring and regular maintenance are necessary to mitigate the possible risk of gearbox failure, which may lead to turbine's long downtime or expensive replacements. On the other hand, the DDGs have low part count, simple mechanical structure and are more reliable [89]. In spite of that, the main concern on this configuration is the rapid increase of their size and weight at high power level and low speed applications. Hence, they may also not be the perfect solution in large-scale wind turbine systems.

The overall performance comparison at a Mega-Watt system output capacity for the DDGs and geared generator configurations, as discussed by numerous authors [5; 78–84], is summarized in Table 1.2, whereby the above mentioned points are further confirmed. As indicated in the table, the DFIG enjoys most of the merits, such as the lowest cost, weight and size. However, the higher efficiency and increased reliability of PM DDGs still justifies their suitability over DFIGs, particularly in offshore applications where the reliability of multi-stage gearbox in DFIGs is usually the major concern and drawback from logistics point of view. It is interesting to see the remarkable weight and size reduction brought in by the integration of the mechanical gear and PMG, relative to that of the PM DDG. But in the light of multi-stage gearbox troubles, some designers have currently opted for a combination of just one-stage gearbox and a PMG, named the multibrid system [70; 82]. This arrangement seems to be the good trade-off between a three-stage gearbox connected DFIGs and/or PMGs and DDGs. Its superiority is further illustrated by Li *et al* for different ranges (0.75-10 MW) of output capacity, whereby the multibrid system has smaller volume, lower cost per kilowatt and system cost in comparison to the PM DDG [70].

Although the multibrid concept's copper loss is appreciably lower than that of the DDGs, the total loss shows an opposite result, as the incorporation of the gearbox adds significantly to the total system losses. Additionally Li *et al* have shown that the single-stage gearbox's weight and cost immensely increases with the increasing gear ratio and power ratings [70]. Consequently, the indicated advantages are limited by certain boundaries of conditions. The above mentioned points clearly show that there is no universal preference between the two drive-train configurations popularly used in wind turbines. Hence, exploring other different arrangements may reveal some beneficial improvements.

Table 1.2: Common wind turbine drive-train comparison [5; 78–84].

	DD-PMG	G-PMG	G-DFIG
Gearbox	None	1-3 stage	1-3 stage
PEC rating	Full scale	Full scale	Partial scale
Cost	High	Medium	Low
Mass	High	Medium to low	Low
Volume	High	Medium to low	Low
Reliability	High	Medium	Medium
Efficiency	High	Medium	Medium

1.2 Magnetically Geared Machines

As an alternative to the stated common configurations currently implemented, magnetically geared permanent magnet (MGPM) machines have recently been proposed for use in wind power application [90–92]. The MGPM machines are essentially a combination of a flux-modulated coaxial magnetic gear (CMG) and a conventional medium to high speed permanent magnet synchronous machine (PMSM). Flux modulated CMGs consist of three main components, being a ferromagnetic flux modulating ring, a low and a high pole count PM rotors. The flux-modulating ring is situated in-between the two PM rotors since it is specifically intended to modulate the air-gap fields originating from either one of the rotors to have one of the major field harmonics with same number of poles as the PM rotor on the other side. In this way, the selected harmonic of the modulated air-gap fields from the first rotor will also have the same rotating speed as the second PM rotor and vice versa. The magnetic engagement between all the three components is thus enabled, and the steady torque transmission can be realized.

The basic structure of a flux modulated CMG is shown in Fig. 1.4. One component, either a PM rotor or a modulating ring, is usually fixed while the other two are left to freely rotate. A mathematical relationship between the number of flux modulating pole-pieces and the two rotor PM pole-pairs is expressed as [6; 7]:

$$N_m = p_h + p_l \tag{1.1}$$

where N_m, p_h and p_l represent the number of modulating pole-pieces, the pole-pair numbers on the lower pole-count PM rotor and higher pole-count PM rotor, respectively. It should be noted that the subscripts 'h' and 'l' give the indication of the relative speeds of the rotor in case they both rotating. That is, the lower pole-count PM rotor with p_h pole-pairs will always have higher rotational speed compared to the higher pole-count PM rotor with p_l pole-pairs. When the flux modulator is kept stationary, the gearing ratio is given by [6; 7; 93]:

$$G_r = -\frac{\omega_h}{\omega_l} = -\frac{p_l}{p_h} \quad \text{or} \quad G_r = -\left(\frac{N_m}{p_h} - 1\right) \tag{1.2}$$

where ω_h and ω_l are the angular speeds of the high-speed (p_h pole-pairs) and the low-speed (p_l pole-pairs) PM rotors, respectively. The negative sign indicates that the two rotors rotate in opposite directions. If one of the PM rotors is held still, the gear ratio

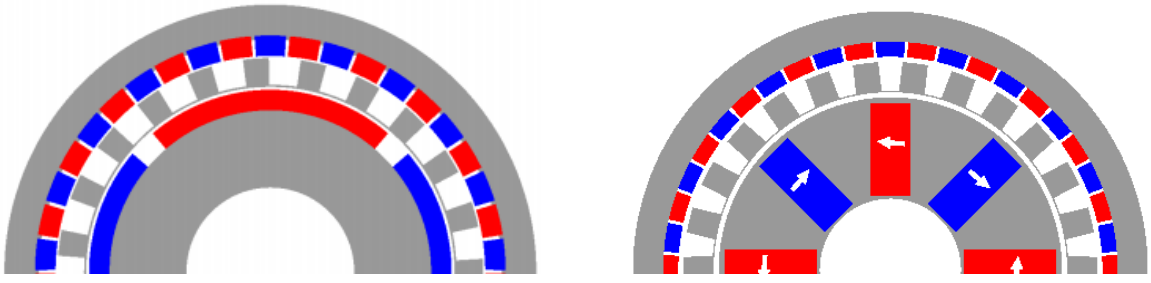

(a) (b)

Figure 1.4: Radial flux modulated coaxial magnetic gears [6; 7]: (a) surface mounted PMs on both rotors and (b) flux concentrating inner PM rotor.

between the rotating flux modulator and the other rotating PM rotor is given by [93]:

$$G_r = \frac{\omega_h}{\omega_m} = \frac{N_m}{p_h} \quad \text{or} \quad G_r = \frac{p_l}{p_h} + 1 \tag{1.3}$$

with ω_m being the flux modulator angular speed, and the G_r is positive since the PM rotor and the flux modulating ring will rotate in the same direction. The high pole-count PM rotor is normally the one that is kept static in this case. This is simply because there is small numeric difference between its PM pole-pair number (p_l) and the number of the ferromagnetic pole-pieces (N_m), which would result in a low G_r if these two were chosen to be the rotating components.

In an analogous manner to the mechanical gears, the G_r in flux modulated CMGs also amplifies the torque from the high speed rotating to the low speed rotating component. By considering the torque on the low-speed rotating component, this type of magnetic gears are reported to have the torque density in excess of $100\,\mathrm{kN/m^3}$, which is competitive to that of the mechanical gears [94–97]. The contact-less magnetic gearing effect in flux modulated CMGs is a direct result of the air-gap field modulation, which then offers the CMG several potential benefits over the mechanical counterparts, such as [10; 92; 98]:

- Contact-less power transfer and quiet operation
- Inherent overload protection
- Little maintenance, and
- Potential for high torque density and efficiency

The artful integration of the flux modulated CMGs with the conventional electrical machines enables a direct connection of the low-speed high-torque turbine shaft onto the machine without an additional external gearbox. Consequently, the whole system can potentially have light weight and small volume. Thus, the most attractive features of the CMGs are automatically utilized in the magnetically geared machines demonstrating certain unique advantages. There are several topological variations of magnetically geared machines which depend on the various integration methods between the CMG and the electric machine. With the notion that magnetically geared machines are derived from the CMGs, they can be generally classified into the two major groups, being the directly integrated- and the flux modulated geared machines. A further breakdown of these two categories is shown in Fig. 1.5.

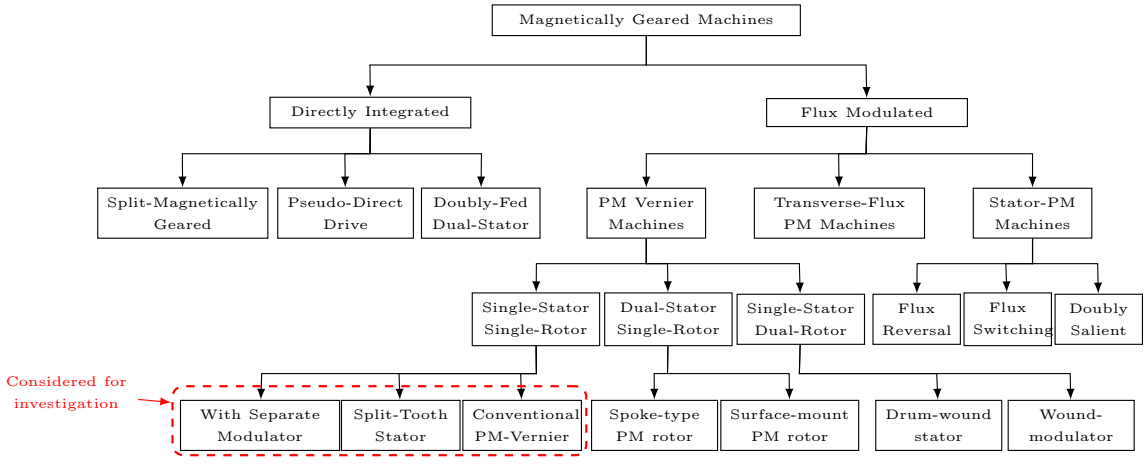

Figure 1.5: Overview of magnetically geared permanent magnet machines.

1.2.1 Directly integrated magnetically geared machines

Directly integrated magnetically geared machines are regarded as those with simple mechanical integration where the incorporated electrical machine and the flux modulated CMG share the common rotor. Since there is not much change on their respective original structures, the machine and the CMG can still be physically identified although they are mechanically integrated. Qu *et al* demonstrated the relationship between the CMGs and the two most prominent machines in this class, on both the operating principles and structure layout [99]. In addition, an illustration of how the CMGs can be converted to each of these two machines is also explained.

The conceptually simplest and perhaps the most obvious type of the directly integrated magnetically geared machines is *split-magnetically geared machines* [90; 98; 100–103]. Although the PM synchronous machine is the commonly used type of electrical machine for this combination, resulting in magnetically geared PM (MGPM) machines, the induction machine can also be used, which will then produce magnetically geared induction machine (MGIM) [104; 105]. The MGPM machines typically have three air-gaps and two rotating components. According to the relative positions of the two PM sets on either side of the shared rotor yoke, the split MGPM system can have the CMG and the PM machine with magnetically coupled or decoupled magnetic circuits, as illustrated in Fig. 1.6 [8; 62].

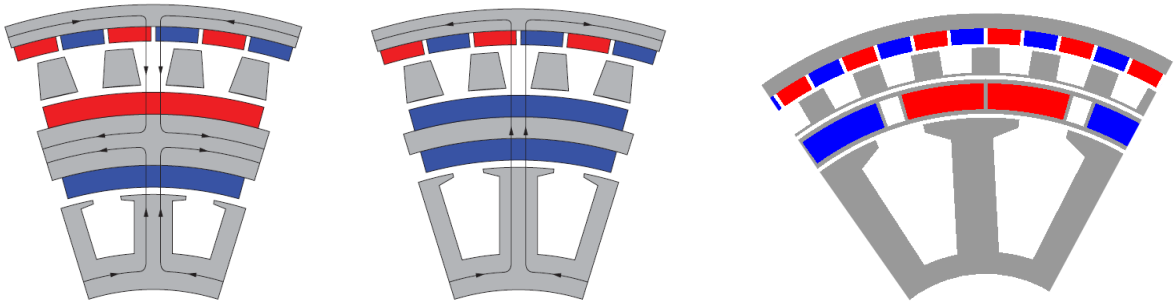

(a) (b) (c)

Figure 1.6: Split magnetically geared PM synchronous machine variations [8; 9]: (a) decoupled, (b) coupled with surface mounted common rotor and (c) coupled with common PMs inserted in laminated carrier.

The decoupled option is less favoured because the rotor yoke tends to be thicker in order to accommodate the magnetic flux from the gear and the machine. That is, since the shared yoke acts as a flux return path from the two magnetically separated devices, it usually gets thicker to avoid over saturation and use up the radial space that could otherwise be used to increase the air-gap radius of the inner subordinate component. For the coupled case, the minimum shared rotor yoke thickness will only be determined by mechanical constraints. Realizing that the yoke is of less significance to the magnetic circuit, Gerber and Wang proposed an alternative design of the common PM rotor in the form of a laminated magnetic carrier with slots available to just insert one set of PMs visible to both the gear and the machine, instead of the surface mounted rotor with two PM sets on both sides [8]. In addition to reducing the losses, the structure already shields the PMs from the centrifugal forces at higher rotating speeds, while an additional retaining can or other form of fixture would be necessary to protect the PM set on the outer side of the surface mounted rotor.

The second type of the directly integrated MGPM machines is widely known as the *pseudo-direct drive* (PDD), which was first described by Atallah *et al* in 2008 [10]. The analysis on it and proposal for different applications was later done by several authors where its attractive features were further confirmed [106–109]. This machine has a fixed slotted stator with coils wound around the teeth and the PMs mounted on the teeth surface adjacent to the air-gap. The other two components, i.e. the magnetic modulating ring and the PM rotor with lower pole count, then becomes the low-speed and high-speed mechanical terminals, respectively. The stator armature's fundamental rotating field has the same pole-pair number and angular speed as those of the inner PM rotor. In the same manner to the flux modulated CMG in Fig. 1.4 with the outer PM rotor held stationary and the gear ratio described by Eqn. 1.3, both the PM rotor and the modulating ring rotates in the same direction. Hence another way to think of this machine is that it can be derived from the CMG configuration in Fig. 1.4 by slotting the yoke of the PM rotor with high pole-pair number, and inserting the winding. The added stator winding must have the frequency and pole-pair number matching with that of the lower pole count PM rotor.

As shown by Fig. 1.7, the PDD has two air-gaps and two concentric mechanically rotating components. Although the structure layout is considered to be slightly simplified relative to that of the three air-gaps split-magnetically geared machines, the PDD is still complex due to multiple rotating components and strong magnetic forces acting between them. Besides the concern on thermal performance and the possible demagnetization of the PMs on the stator surface, there is a long magnetic path with relatively larger reluctance between the high speed rotor PMs and armature winding's matching field harmonics. This may encourage a heavy field leakage between the three system components and result in reduced machine performance.

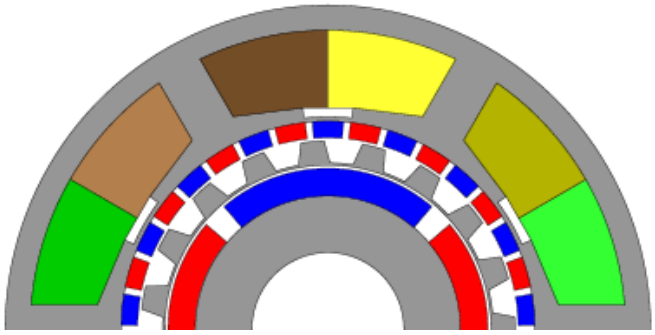

Figure 1.7: Outer stator pseudo direct drive [10]

The last machine type in this class is the *doubly-fed dual-stator reluctance* (DFDSR) machine which is formed by basically replacing the PM rotors with stators as shown in Fig. 1.8 [11; 110; 111]. The rotating field harmonics are generated by feeding the stators with 3-phase alternating current (AC) sources. Since the aim is to have different magnetic pole numbers with different angular speeds as in the PM excited CMGs, the stators are also likely to have various slots and winding arrangements with different excitation frequencies. The modulating ring is the only rotating component but there are still two air-gaps to allow relative movement between the three components. One advantage of this machine is that the problems associated with the PMs such as demagnetization or strong magnetic forces, are avoided. The downside of it is that both the power factor and the torque quality get relatively poor.

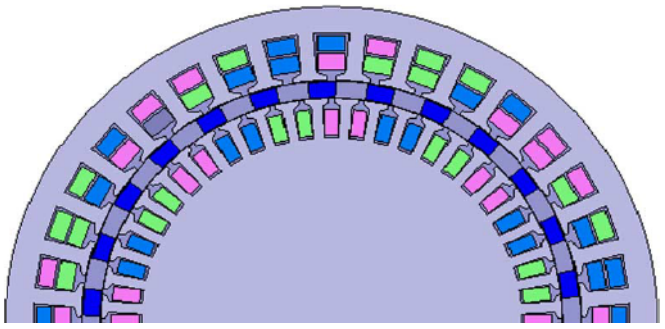

Figure 1.8: Doubly-fed dual-stator reluctance (DFDSR) machine [11].

The directly integrated class of magnetically geared machines discussed above, especially those based on PM excitation (MGPMs) have lighter weight, compact structure and boasts on exceptionally good torque densities which are in excess of 60 kNm/m^3 [112]. In addition, the high power factor of an incorporated PM machine is generally retained in integrated MGPM machines, except in the case of the MGIM where boosting windings have to be added for power factor improvement. Although the MGPM machines have relatively high PM material requirements, the high torque-per-PM-mass and torque density that is at least twice as that of conventional PM machines justifies it to be efficiently used. Apart from the radial flux MGPM machines discussed above, axial-flux MGPM machines have been analyzed and they have proved to have high torque densities [113]. Axial-flux MGPM machines have an added advantage that CMG and electrical machine components can be designed to have two separate shafts if necessary, which would allow them to be used in hermetically sealed applications.

Nevertheless, the major disadvantages of the MGPM machines are high PM material usage and mechanical structure complexity. The latter drawback is due to the fact that these machines have at least double air-gaps and two concentrically rotating components. Thus, their construction for larger power level applications also poses the manufacturing challenges and constraints. While it is perceptible that too much PM volume in these machines contributes to their high cost, they are also plagued by severe end-effects stimulated by the physical arrangement of two PM arrays acting opposite to each other. Gerber and Wang demonstrated that the axial flux leakage in radial flux CMGs and MGPM machines can have severe impact on the torque rating [114]. Logically, this calls for the use of non-magnetic but mechanically strong materials for the casing as additional losses can be induced in ferromagnetic casings.

1.2.2 Flux-modulated magnetically geared machines

In contrast to the directly integrated magnetically geared machines, the class of the flux modulated magnetically geared (FMMG) machines were derived from the development of an existing electrical machine concept. But, with the advent of the high energy density rare earth PM materials, which has replaced the DC coil excitations previously used in the primitive models, these machines can also be linked to the newly emerged flux modulated CMGs due to the observed similarities in their basic operation principles. That is, they work on the same concept of magnetic gearing through the modulation of the air-gap fields as in CMGs, hence they are logically regarded as *flux modulated magnetically geared machines*. Unlike in CMGs, it is not necessary to maintain two mechanical clearances

and/or two rotating components since the flux modulating ring can be combined with either the stator or the rotor core. There are three main types of machines in the class of FMMG machines, being:

- Permanent magnet vernier (PMV) machines
- Stator permanent magnet machines
- Transverse flux permanent magnet (TFPM) machines

The stator PM machines have evolved from the principle of DC field excited *variable flux reluctance machines* (VFRM), and they can be traced back to the early inventions such as the stator PM alternator by Rauch and Johnson proposed in the mid 1990s (Fig. 1.9) [12]. As their collective name suggests, the PMs are placed on the stator while the flux-modulating pieces become one component with the rotor yoke, creating a simple salient rotor structure. The location of the PMs on the stator leads to three different types of stator PM machines named as the *flux-switching PM* (FSPM), *flux-reversal PM* (FRPM) and the *doubly-salient PM* (DSPM) machines depicted in Fig. 1.10 [13; 15; 16].

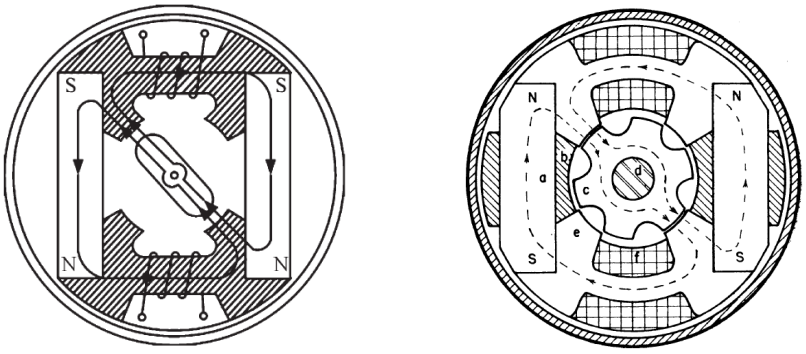

(a) (b)

Figure 1.9: Variable flux reluctance PM (VFRPM) machine [12] (a) 2-salient pole rotor and (b) 6-salient pole rotor.

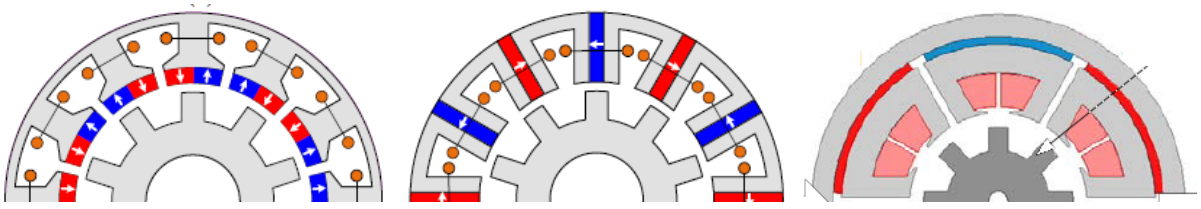

(a) (b) (c)

Figure 1.10: Stator PM flux-modulated magnetically geared machines [13–16]: (a) flux-reversal (FRPM), (b) flux-switching (FSPM) and (c) doubly-salient (DSPM).

In the FSPM, one PM pole is sandwiched in between each stator tooth, the FRPM has a pair of PM poles on the stator-teeth surface adjacent to the air-gap while the DSPM has the PM poles alternately inserted in the stator yoke. The non-overlapping concentrated winding is commonly employed in these machines even though it is possible to apply conventional distributed winding [115; 116]. Comparison between these stator PM machines reveals that FSPM machine has better performance characteristics than the other two [14; 15; 117]. One of the main drawbacks of the FRPM is a significant PM flux leakage

that negatively impacts its performance, while the DSPM is hampered by the low PM material utilization ratio leading to a poor torque per PM mass ratio.

The second group of FMMG machines is the PMV machines, which, unlike the stator PM machines, has the PMs mounted on the rotor. The modulating pieces are combined with the stator to be one component so as to add more compactness to their structure. PMV machine concepts were derived from the decades old principle of electrically excited vernier machines by incorporating a PM rotor. The early vernier machine designs, such as those proposed by Chubb [19], Dicke [20] and Lee [118], had obvious drawbacks of manufacturing difficulties and low efficiencies due to complex electrical excitation arrangement [119]. Although this idea remained dormant for several years after its earliest inventions, more interest and substantial studies on it resurfaced with the electromagnets being replaced by the PMs, leading to the the emergence of the PMV machine [46; 100; 120]. Their success to being torque dense competitive machines was further enhanced by the advancement in high energy product PM materials. The three basic structures of the PMV machines are shown by Fig. 1.11. The conventional PMV is usually designed with distributed overlapping windings, whereas the other two configurations employ the tooth concentrated non-overlapping winding.

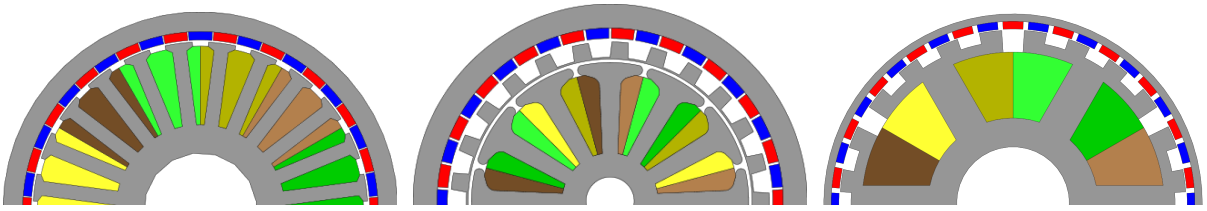

(a) (b) (c)

Figure 1.11: Basic permanent magnet vernier machines' structures: (a) conventional PMV, (b) with separate modulator and (c) split-teeth stator PMV.

Transverse flux PM machines consists of three identical single phase rings enclosed in a housing. Each ring is made up of the stator segments, the coils and the PM rotor assembly. Figure 1.12 illustrates the simplest configuration of the TFPM machines. The adjacent single phase stator cores are stacked at 120 electrical degrees shifts relative to each other in order to form a symmetrical 3-phase distribution [17; 18]. The fundamental design convention is that the rotor magnetic poles be more than those of the stator (usually by a factor of two), which implies they engage through the magnetic gearing [121]. However, one main distinction of the TFPM to conventional electrical machines is that its stator flux distributions are perpendicular to the rotor movement. In addition to having a simple structure configuration, the TFPM machines are more compact and have good power densities.

It is clear from their description that the topologies of the machines under the class of the FMMG can be derived from either the flux modulated CMG or from their basic primitive concepts by adding the PMs and applying some minimum structural changes. One of the common characteristic property that make them belong to one family is that they share the same torque production principle. That is, since the number of stator and rotor magnetic poles are always different, the torque in these machines is produced from the modulation of the air-gap field harmonics by stationary or rotating salient pole-pieces.

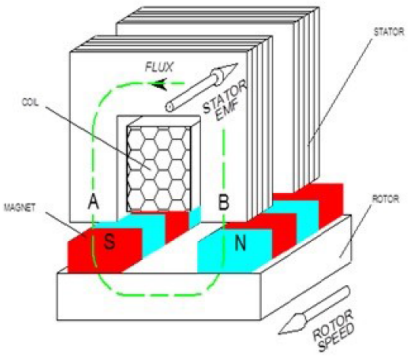

Figure 1.12: Transverse-flux PM (TFPM) machine structure [17; 18].

This inherent magnetic gearing effect closely relates them to the flux modulated CMGs.

In comparison to the traditional PMSM machines, the torque density capability in the FMMG machines comes as a result of their pole-ratio acting as a scaling factor to the basic torque equation parameters. In other words, the rotor-to-stator pole-ratio appears to be an indirect additional coefficient that boosts their torque performance even at relatively low electromagnetic loading, as shown below [14; 122]:

$$\begin{aligned}
\textbf{PMV machines:} \quad & T_{\text{air-gap}} \propto \frac{m}{2}\boxed{\frac{p_r}{p_s}}AB_gV_g \\
\textbf{TFPM machines:} \quad & T_{\text{air-gap}} \propto \frac{m}{2}\boxed{p_r}AB_gV_g \\
\textbf{Stator PM machines:} \quad & T_{\text{air-gap}} \propto \frac{m}{2}\boxed{\frac{N_s}{p_s}}AB_gV_g \qquad (1.4) \\
\Rightarrow \quad & A = \text{Electric loading} \\
& B_g = \text{Air-gap magnetic loading} \\
& V_g = \text{Air-gap volume}
\end{aligned}$$

The implications of the above equation (Eqn. 1.4) is that the higher pole-ratio will theoretically give a machine design with a higher torque density. Therefore, in order to utilize the magnetic gearing effect for torque improvement, the FMMG machines are normally designed with a large margin between the stator and rotor magnetic pole-pairs whenever possible.

With regard to their performance, both the TFPM and the stator-PM FMMG machines have a characteristically high cogging torque and flux leakage [123; 124]. In TFPM machines, these problems are addressed by gluing the laminated magnetic steel shunts between the stator poles to block the field leakage from the rotor PMs [125; 126]. Although it does help in leakage reduction, it is not a complete fix, since even in the presence of the magnetic shunts, the cogging and ripple torques remain significantly higher compared to other conventional PM machine types. The shunts also add more to the manufacturing complexity and costs. Moreover, the cost of the TFPM rapidly increases with an increase in power density, while the cogging torque also gets worsened, as reported by Dobzhanskyi [18]. On the other side, the fringing leakage flux in stator PM machines also deteriorates their torque density, which leads to them having low PM material utilization factor. That means, in addition to higher torque ripple, these machines have small torque output per-kilogram of PM material, and this may result in the increase for their cost.

They also seem to be performing better at medium to high speeds, hence they may not be favorable for low speed applications like wind turbine generators.

The PMV machine appears to be the best performers out of the three FMMG machines because it has higher torque density than any of them. Although they do have some leakage fields problem, their cogging and ripple torques are much smaller and they are even less than those of traditional PMSM machines if proper pole-slot combination is selected.

1.3 Literature Review on PM Vernier Machines

In 1933, Chubb patented a vernier motor for use as either a low-speed synchronous motor or a reduction gear in small applications such as clocks, phonographs or speedometers [19]. The machine was comprised of the stator and rotor components with uniformly spaced magnetizable teeth, and the AC excited stator winding inducing the rotating magnetic field. The stator and rotor were designed to have different numbers of teeth, with the said difference being equivalent to the order of rotating magnetic field. Consequently, the main fields coupling them could only be transferred through the coincident teeth at each time incident. This then resulted in the rotor having different rotational speed to that of the rotating magnetic field by a definite ratio, and the realized phenomenon was defined as the *vernier action*. In other words, a vernier action between the rotor and stator is realized as a result of the relatively large variation in the maximum magnetic permeance axes due to just a small rotor displacement. Coincidentally, about two years before Chubb's invention, Dicke had filed for the patent of the vernier motor which was published in 1937 [20]. His invention had the same operation principles to that of Chubb, with the target application being the clocks as well. The two vernier motors are shown in Fig. 1.13.

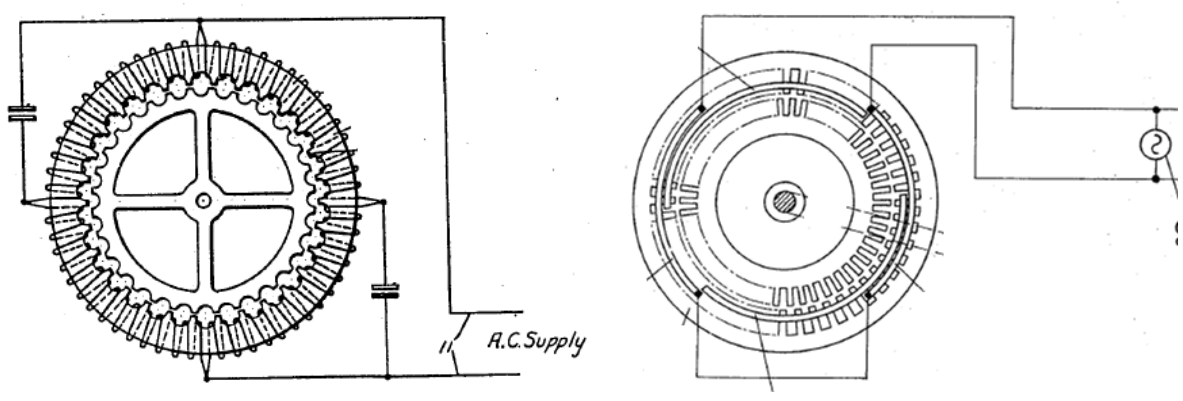

(a) (b)

Figure 1.13: Some of the earliest vernier motor inventions (a) by L.W. Chubb [19] and (b) by O.H. Dicke [20].

Lee went on to present a less cumbersome vernier motor design and provided a much clearer mathematical presentation of vernier motor operation principles in terms of permeance and magnetic flux harmonic equations [118]. His analysis expressed the gear ratio between the rotor and stator fields in terms of the number of rotor and stator teeth, and showed that they rotate in different directions. Furthermore, he was able to reveal that

the vernier machine's torque has two components resulting from the engagement of the fundamental and modulated harmonics of the permeance and flux waves. During this time, the vernier machines had less recognition compared to other machines since they had bulky sizes and low torque to mass ratio due to the usage of less efficient electromagnets as their excitation sources. Besides having poor power factors, their torque densities were estimated to be less than that of induction machines too.

Unsurprisingly, the idea of vernier motors only got revitalized in late 1900s after a number of publications introduced the high torque density Vernier machines by replacing an electromagnet with a PM (so-called PM Vernier machines). [46; 100; 120]. The two remarkable papers by Toba & Lipo and Ishizaki *et al*, provided a thorough understanding on the operation principles of PM vernier machines and mathematically revealed the reason why they may offer better torque densities than traditional synchronous PM machines at low speed applications. From the above discussion, it can be reasonably concluded that PMV machine concepts were derived from the incorporation of the decades old vernier machine principles with the PM machines. But, in the light of the currently popular flux-modulated CMGs, they may also be regarded as the simplified versions of MGPM machines due to their certain similarities. Figure 1.14 shows a simplified hierarchical trend that may have led to the origin of PMV machines, either from the MGPM machines or from the electromagnetic excited vernier machines.

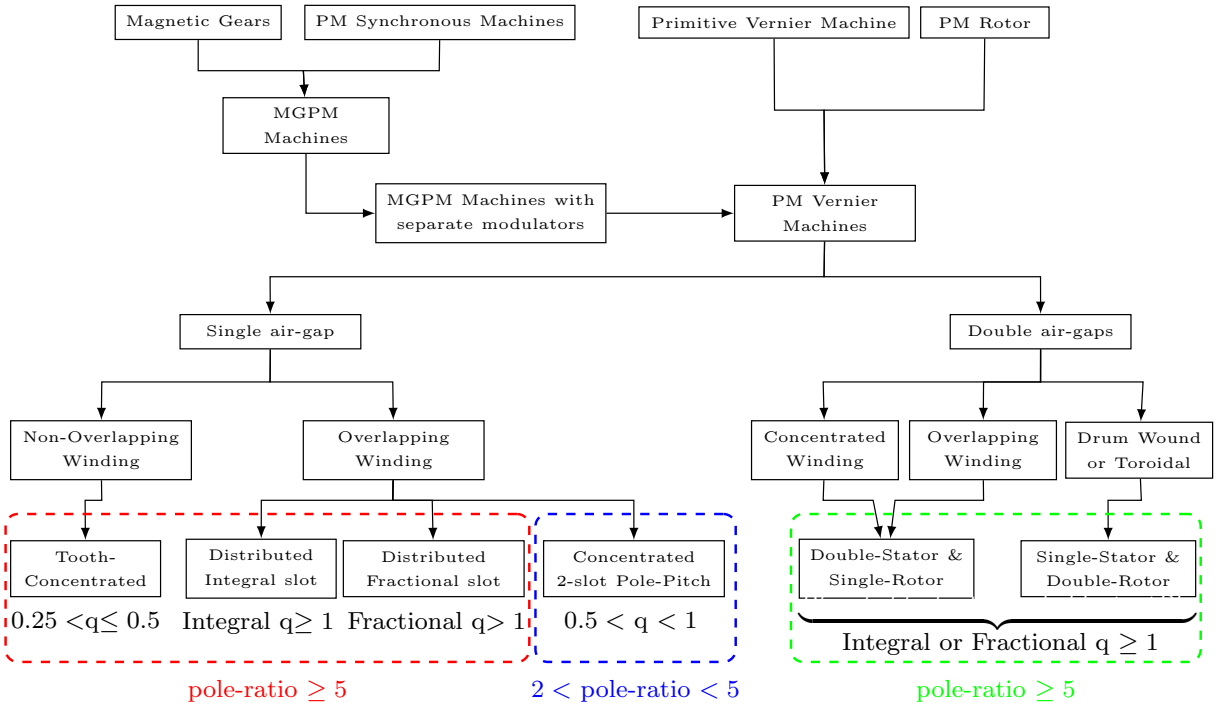

Figure 1.14: Hierarchical development of permanent magnet vernier machines

The interest on PMV machines has gained an increasing momentum in the last two decades. That is because the PMV machines have relatively simple and compact structure, and high torque density that is comparable to that of the MGPM machines. In addition, they generally have fairly small cogging torque and can easily realize minimum torque ripples if well designed. Hence, they are attractive machine types that utilize the magnetic gearing concept while avoiding complicated structure configurations. Subsequently,

these characteristic advantages make the PMV machines the potential alternatives to the conventional PM synchronous machines in wind energy conversion applications.

The cross-sectional view of a basic three-phase PMV machine is shown in Fig. 1.15. Both the rotor yoke and the stator core are constructed from the steel lamination. Moreover, the rotor has many surface-mounted PMs with alternating polarity, while the stator has a toothed-pole structure with either concentrated or distributed 3-phase winding. Although both the rotor and the stator look like those of the traditional PMSM, the distinctive difference in its operation is brought in by the ring of ferromagnetic pole-pieces located between the two components, named the flux-modulator. The primary duty of the flux modulator is to modulate the magnetic fields originating from one component to the other, so that the new field with harmonic order equivalent to the fundamental field of the second component are created. In an analogous manner to the flux-modulated CMGs, the following general rule (Eqn. 1.5) exists to govern the number of the flux modulating pieces (N_m), stator pole-pairs (p_s) and the rotor pole-pairs (p_r) for the unique vernier effect to take place. Common stator slots selection rules are applicable to determine the number of slots and type of winding required to achieve the stator magnetic poles:

$$N_m = p_r \pm p_s \tag{1.5}$$

As a consequence, the stator and rotor pole-pairs will always have different numbers, which is the unique distinction of this type of machine in comparison to the conventional PMSM. Then the field generated from stator winding has to be synchronized with the modulated rotor PM field harmonics for steady torque transmission. Thus, a small rotation of the PM rotor results into a large change on the armature flux angle, rendering the PMV machine suitability for high-torque and low-speed operations.

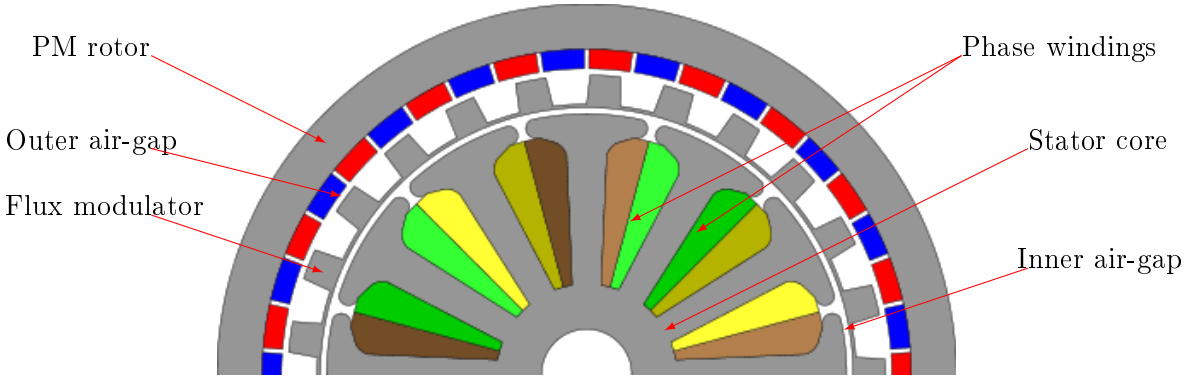

Figure 1.15: Basic structure of the PMV machine.

1.3.1 Topological variations in PMV machines

In an attempt to obtain a PMV machine with an improved performance, several different topologies have been proposed in the literature. These structural variants may also be viewed as different combinations of the basic PM rotor types with the common stator winding arrangements. But the flux modulating pieces' (FMPs) shape and position relative to the stator adds another important dimension that needs a critical consideration in the formation of the PMV machines. The FMPs enable the magnetic coupling between

the rotor and stator, so they are the key determinants in both the PMV machine's physical layout and electromagnetic circuit. Several prominent PMV machine topologies are given in this section with a brief discussion of their performance features.

1.3.1.1 Magnetically geared permanent magnet machines with separate modulators (MGPM-SM)

By omitting the inner PM rotor of the inner-stator type *split-magnetically geared machine* in Fig. 1.6, an MGPM-SM machine is formed, as previously shown in Fig. 1.15 [28; 42; 127; 128]. In this case, the high speed rotating field is generated by the stator winding instead of the PMs. Thus, the stationary armature substitutes the high speed PM rotor. This topology is considered to be one type of machine that represents the simplified PMV machine in terms of its constituent components' structure visualization. It has greater freedom of the stator configuration compared to other PMV machines to be discussed latter in this section. This is because the three components are kept mechanically separate from each other, which helps in understanding the machine's operation. Consequently the stator slot number and winding type are not directly related to the PM rotor's pole number and ferromagnetic pole-pieces. The stator design freedom was demonstrated in [42], in which both the distributed and tooth concentrated winding types with equal pole-pairs were evaluated. Although distributed windings are widely known for comparatively long end-windings, the induced voltage and output torque profiles possess certain advantages over that of the concentrated windings for this machine type.

The maximum torque magnitude is achieved when the span angle of the ferromagnetic pieces is almost or exactly equal to that of the air-spaces in between them [28; 129]. However, little to no impact was observed on peak torque as a result of relative position of the modulator to the stator [42]. While maintaining the stator and FMPs as two separate components, the air-gap between them may also be set to possible minimum practical length in the case where the PM rotor is the only rotating component. This would simplify the mechanical construction and also reduce the magnetic reluctance between these two components. According to Wang *et al* [42], the alternative mode, whereby the modulator acts as a low speed rotating component while the PM rotor is fixed stationary, has similar back EMF properties to that of rotating PM rotor mode. But, the non-linearity of the magnetic circuit becomes more apparent as a result of varying position of modulator relative to the stator, which then encourages the fringing effects and ultimately results in the larger torque ripples.

1.3.1.2 Split-tooth permanent magnet vernier machine

It can easily be realized that the second air-gap between the inner stator and the stationary flux modulating pieces (FMPs) in MGPM-SM machine (Fig. 1.15) may be completely eliminated as it contributes to unnecessary additional magnetic reluctance. That is, the FMPs and the stator teeth can be merged into a single component. Accordingly, an intriguing PMV topology was proposed in [23; 25; 37], which is called a *split-tooth PMV machine*. It can have either inner or outer stator with each tooth split into numerous FMPs (or auxiliary teeth) for field modulation purposes, as shown in Fig. 1.16. Apart from the advantage of simple structure that comes as a result of having only one air-gap, this machine is also easy to manufacture since it has a simpler winding layout and only two main components. Tooth concentrated windings are more suitable and normally used

in this machine type. Therefore, the compact armature winding structure and minimum end-winding effects (loss and inductance) form the additional merits over the conventional PMV machines as they normally use overlapping windings. As reported by Liu *et al*, the minor magnetic coupling between the phases enables this machine to be fault tolerant designed, enhancing its reliability and efficiency [37]. Prior studies have verified its performance and concluded that it can offer low-speed / high torque operation and high torque density because the space is better utilized [23; 48]. On the other hand, according to Toba and Lipo, the slots between the stator teeth manifests themselves as large *dead spaces* in the case of large machines, which may be one of the drawbacks [46].

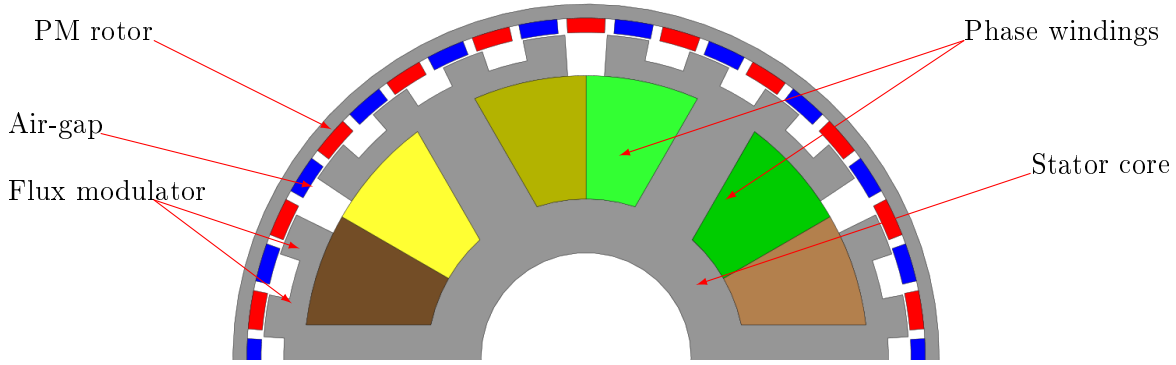

Figure 1.16: Split-tooth permanent magnet vernier machine.

In an attempt to further improve the performance of this type of machine, either the PMs or an additional windings are inserted in the gaps between the FMPs [50; 130–134]. Although the former technique does improve torque and induced voltage magnitudes, this all comes at an expense of more PM material used, and the voltage total harmonic distortion (THD) is worsened [130]. One possibility to avoid excessive PM material usage would be to adopt a consequent pole rotor structure. Although this may benefit from reluctance torque as the machine would now be doubly salient, it is also understood that it causes unbalanced flux flow as a result of missing PM polarity and have more axial leakage flux. With the latter method, it was claimed that the operating speed range is likely to be widened due to the improved flux weakening capability brought by the increased self inductance from FMP windings [50]. As it would be expected, the phase angle difference between the stator and FMP windings was also indicated to be a prevailing issue. At increased rotational speeds, frequency dependent core and PM losses become more significant as well, leading to both reduced efficiency and rise in temperature [135]. This may be attributed to the rich harmonic content of tooth concentrated windings employed in PS-PMV machines.

1.3.1.3 Conventional overlapping winding PM vernier machine

Another alternative way to develop a structurally simpler machine from that of MGPM-SM machine (Fig. 1.15) is by merging each modulating piece to a corresponding stator tooth (see Fig. 1.17). That means the number of flux modulating pieces and that of stator slots or teeth must strictly be the same. Although the stator structure may largely look like that of the normal PMSM, the difference is that the number of stator teeth has to be configured in such a way that they will also act to modulate the magnetic fields from the rotor PMs. This typically leads to stator with large number of slots yet smaller number of

poles in armature winding is required. Therefore, distributed overlapping winding (OW) arrangement is usually employed for this machine type. The distributed overlapping winding has a drawback of long overhang windings. Often, short-pitch windings are used to mitigate this effects and to suppress unwanted MMF harmonics. In order to realize the speed and/or torque gearing action as well as steady torque transmission, the number of stator slots (Q_s), rotor PM pole-pairs (p_r) and armature pole-pairs (p_s) are related by Eqn 1.6 with N_m in Eqn. 1.5 substituted by Q_s.

$$Q_s = p_r \pm p_s \tag{1.6}$$

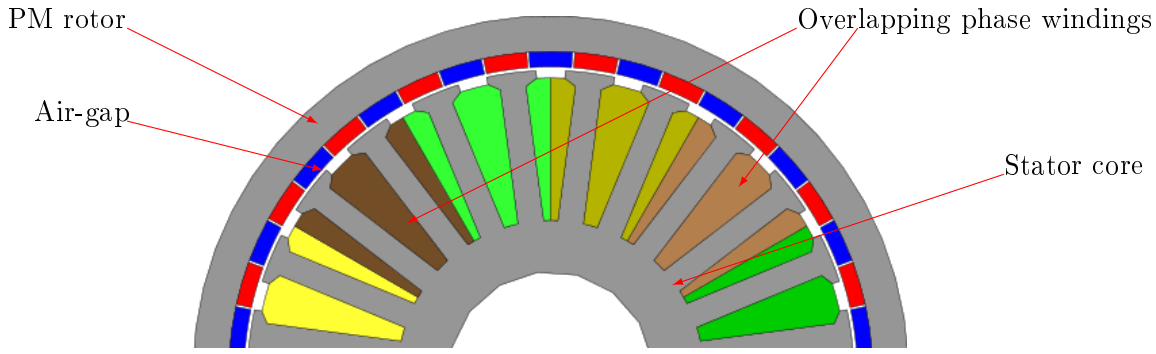

Figure 1.17: Conventional overlap winding vernier PM machine.

1.3.1.4 Dual-stator permanent magnet vernier (DS-PMV) machine

The idea of double-stator machines has been proposed and extensively explored in PMSM machine topologies. Even though their mechanical geometry gets a bit more complex, they proved to have impressive torque density capability and better performance compared to their single stator counterparts. Additionally, the two sets of armature windings offers not only the high power density but also more flexibility for winding connections. Hence, by artfully incorporating the concepts of PMV- and double-stator machines, exceptional torque densities can be obtained while the machine space is also effectively utilized.

Accordingly, the double-stator PMV (DS-PMV) machine topology illustrated in Fig. 1.18 has recently been introduced and analysed by several researchers [36; 45; 136]. It was claimed that the heavy magnet flux leakage and low PM utilization experienced in single-stator PMV machines can be greatly reduced in this configuration [43]. In actual fact, the most important strategy to reap these benefits was to have the inner- and outer-stator teeth shifted by half tooth pitch relative to each other [43; 136]. Consequently, the teeth compensates for each other against leakage flux and engage more PMs to simultaneously contribute to the air-gap flux density. Seemingly related, a combination of conventional inner-stator with vernier outer-stator structure produces a kind of semi-DS-PMV machine. In the outer air-gap, the working harmonic is that of the modulated space field whereas the fundamental harmonic in the inner air-gap between the PM rotor and inner stator is engaged. Hence the vernier effect is still achieved on the outer air-gap, albeit synchronous machine is realized on the inner air-gap, which then ameliorates the power factor.

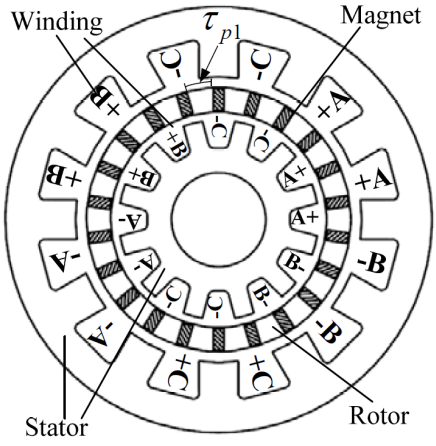

Figure 1.18: DS-PMV machine [21].

While the initial research focused mostly on the topology introduction and operating principle explanation of the DS-PMV machine, Li *et al* presented a detailed design procedure and efficient design methodology, which included analytical sizing equations and geometric relationship formulas [21]. Their effort was of more importance on the preliminary design stage to provide initial machine parameters and indicative performance without much dependence on the finite element analysis (FEA). On one hand, other variations such as interior spoke-type PMs and high temperature superconducting (HTS) modulator were proposed in a bid to further improve the DS-PMV machine performance [49; 136], whereby it was concluded that the power or torque density were increased at the expense of high cogging and ripple torque.

1.3.1.5 Dual-rotor permanent magnet vernier (DR-PMV) machine

Another new kind of PMV machine proposed in the literature is the dual-rotor permanent magnet vernier (DR-PMV) machine. Basically, there are two ways of developing such a fascinating structure:

- By integrating the vernier structure and two concentric PM rotors in one volume, with the stator having open-slot drum windings Fig. 1.19(a) [22], or
- By embedding the armature windings into the air-slots in between the modulating segments of coaxial flux modulated magnetic gear Fig. 1.19(b) [137; 138].

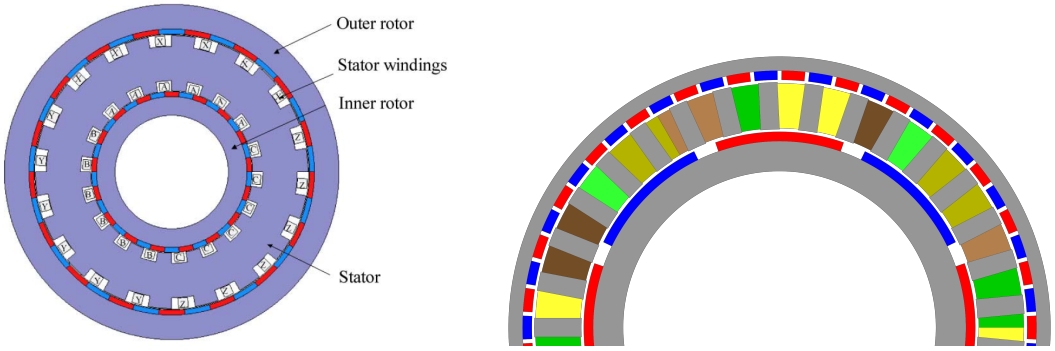

(a) (b)

Figure 1.19: Double-rotor PMV machines (a) drum winding structure [22] (b) wound modulator type.

Both topologies have one set of stator windings being shared by the inner- and outer-rotors. The former approach may benefit more from less copper loss due to the reduced stator end-winding length since the coils are wound around the stator core. In contrast, the latter configuration uses traditional overlapping windings with a yoke-less stator to reduce the flux leakage. Therefore, some strategies are required to strengthen the complex modulator-stator component to withstand strong PM forces and handle weight of the windings.

It was observed that the DR-PMV machine exhibits strong electromagnetic coupling with high power factor [139]. Again, the better performance comes as the result of utilizing the fundamental field harmonic in the inner air-gap since the inner rotor and stator normally have equal pole-pair number. Wang *et al* suggested and demonstrated the three operating modes of this machine type [139], i.e. coaxial magnetic gear, a generator or a multi-terminal motor. As it was established by other studies solely focused on CMGs [139], that increasing the modulator radial height results into more magnetic path reluctance and decreased torque magnitude in gear mode. On one side, if the DR-PMV machine is operated as a generator, the induced back-EMF and efficiency improves with an increase in stator teeth height since more windings area is needed. Similar effect on back-EMF and torque is seen with adjusting of modulator or stator tooth's arc length, which in turn increases or decrease the slot area. This means that a reasonable design compromise has to be made in order to achieve acceptable torque transmission and efficiency at the same time.

1.3.2 PMV machines main components design

Surface-mounted PM rotors have been widely used from the inception stages of the PMV machines due to their ease of construction. But the closer look at analytical equations revealed that the torque and back EMF magnitudes get maximized at relatively thinner PM thickness instead of thick PMs like in traditional PMSM. Thus, even though thicker PMs increases the air-gap flux density, they also compromise the flux modulation effect of first order permeance harmonics due to their increased reluctance. In addition, surface-mounted PM rotors tend to have more leakage flux and inductance that contributes to core losses and poor power factor. This prompted the introduction of flux focusing spoke-type PM rotor. The magnetic air-gap length of the spoke-type PM rotor is smaller than that of surface-mounted PM rotors, and it is independent to the PM thickness. Hence, there is potential for improved torque density and power factor. However, rotor pole saturation is one aspect to consider as that might also weaken the flux modulation effect due to increased magnetic reluctance and losses. Halbach PM arrangement, known for superior qualities due to its self-shielding effects and typically reduced rotor yokes was also investigated by Li *et al* [33]. In contrast to the expected benefits, the torque density was drastically reduced, with insignificant positive change of power factor.

Considering the expensive PM material costs, consequent-pole PM rotors were also proposed in a quest to reduce the PM material usage. But the advantage of cheaper machine and reduced leakage flux is obtained at the expense of slightly decreased torque density. The ring of flux modulating pieces is the key component that enables the vernier effect in PMV machines. That is, it determines both the magnitude and shape of the working air-gap magnetic flux harmonics. Therefore, the flux modulating pieces' shape and thickness has huge impact on obtaining the desired harmonic spectrum for improved per-

formance. Although they may not be the optimal shapes, the rectangular and trapezoidal ferromagnetic FMPs are usually employed in PMV machines. A design compromise seems always to be necessary between thicker and thinner FMPs as they represent the conflicting mechanical and magnetic performances. The use of HTS bulks for flux-modulation component generally improved most of the performance aspects in PMV machines [49; 140] from the simulation analysis. But the practical implementation of this material is still held back by the cooling set-up requirements needed to be incorporated within the machine.

In designing a stator armature windings, one of the objectives is to have shorter end-windings that will use less copper and have lower ohmic losses and smaller end-winding leakage inductance. To this aim, fractional-slot concentrated windings (FSCW) are commonly used whenever possible. But the challenge with FSCWs is that they are rich in harmonic content which adversely affects the vernier effect due to having smaller fundamental field harmonic magnitudes and FMP saturation caused by higher order field harmonics. The FSCW higher order harmonics also offset the torque ripple magnitudes in PMV machines. On one side, the distributed overlapping windings have good flux density distribution. Their main short-coming is the long end-windings that adds more to winding losses and leakage inductance, thereby reducing the PMV machine's performance.

1.3.3 General comparative studies of PMV machines

For a new or resurfacing machine technology to attract more attention from research institutions and establish its industrial market demand, it is always important to draw its similarities and differences, merits and demerits relative to the already existing technologies. To this aim, it is common to find the comparison of PM vernier machine with other machine designs such as magnetically geared PM machine [29; 34] and PM synchronous machines [29; 62]. In most of these comparative studies, torque handling capability and quality, weight and generated back-EMF properties are always on the forefront of the considered attributes.

On the other hand, a range of comparisons between either different PMV configurations or their excitation methods are also available. For instance, Niu *et al* made a quantitative study on single-rotor single-stator (conventional PMV), double-rotor single-stator (DR-PMV) and double-stator single-rotor (DS-PMV) drum-winding machines [22]. Because drum-windings' coils are normally wound around the stator yoke, it makes DR-PMV machines perform much better relative to other machines using the same winding type or conventional windings as it has a better winding utilization factor and greatly reduces end-winding length. In contrast, double or single stator drum-winding PMV machines have longest end-windings since only one side of the coils is exposed to the air-gap. Ho *et al* and Li *et al* looked into the benefits and drawbacks of rotor and stator mounted PMV machines [48; 141], while Li and his colleagues also assessed the use of Halbach arranged PMs [33].

Although stator-mounted PMV machines have lower PM material volume requirement, the torque density gets decreased and torque ripple gets worse in comparison to rotor-mounted PMV machines, which have larger and more sinusoidal back-EMF. The torque ripple in stator mounted PMV machines comes as a result of high harmonic content in

air-gap flux density, which also contributes largely to the core losses. It is also important to note that majority of these mentioned studies relied only on the electromagnetic FEA, which may subject to necessary practical validation, especially when it comes to the losses.

The superiority of the PMV over the conventional PMSM machine in terms of torque density was pinpointed in two separate studies by Fu [29] and Gerber [62], whereby they also proved that the cogging/ripple torque percentage is relatively low in PMV machines. Both authors also reach a common conclusion that, in spite of the low power factor, PMV machine could still out-perform the conventional PMSM in regard to the operating efficiency at certain speed ranges. Again, it was found that the back-EMF properties of the PMV machine has good quality. Therefore, it is a promising substitute for the traditional PMSM machines.

Yet again, Liu *et al* [34] and Fu [29] presented comparative studies of PMV and MGPM machines. Even though both machines work on the same principle of magnetic gearing, MGPM machines have remarkably high torque handling capability. Moreover, the PMV machine posses an inferior power factor to its counterpart, which would then give an impression that MGPM machine will always out-class the PMV considering the output power and efficiency. However, the MGPM machine has at-least two air-gaps and two rotating parts, making a very complicated structure from the mechanical design perspective. It is also characterized by excessive PM material usage, which means the cost is another inherent main drawback in it.

The single-stator single-rotor vernier machines, whether pole-splitting or conventional, are believed to be at the same level of structure simplicity and reliability with the traditional PMSM machines. Owing to their low power factor, double-rotor or stator PMV machines have recently emerged as new design alternatives that have improved power factor while maintaining their advantages of high torque density. In addition, the dual-stator or rotor PMV machines also achieves a good space utilization. But, this obviously compromise their simplicity or reliability since a third component and two air-gaps are now involved. Consequently, it can only be fair to compare these technologies with the dual-stator or rotor PMSM machines.

Table 1.3 gives a summary of the pros and cons for PMSM, MGPM and different PMV machines as extracted from the literature.

1.3.4 Literature review summary

There is always an on-going debates about which drive-train technology is better than the other between directly driven synchronous PM and mechanically geared machines in wind turbine applications. Both configurations have their own inherent strengths and weaknesses that makes it tricky to decide on which one could be more suitable than the other.

On a different note, since the magnetic gearing concept became prevalent in research institutions, MGPM machine was also introduced as the alternative to the two existing technologies. Although its superiority is mostly proven by simulation based comparisons, it shows promising advantages that makes it an all-in-one machine type. However, its reception into the industry such as in wind power applications, is still suspended by the

Table 1.3: Traditional PMSM, PMV and MGPM machine comparison.

	Traditional PMSM	Conventional PMV	DS-PMV	DR-PMV	MGPM
Torque/power density	Low	Moderately high	High	High	Higher
Efficiency	High	High	Higher	High	High
PM material requirement	Low - one PM rotor	Low - one PM rotor	Moderate	High	Higher
Power factor	Very good	Poor	Good	Good	Very good
Mechanical structure	Simple	Simple	Moderately complex	Moderately complex	More complex
Practical feasibility for MW scale	Already in use	High - more prototype testing required	Fair - complex structure & heavy	Fair - complex structure & heavy	Reasonable - complex structure & expensive

foreseeable manufacturing complications, which makes it arguable on whether it has any practical economic benefits, especially in large power applications.

In the same manner as in MGPM machines, PM vernier machines work on the principle of magnetic gearing, but have a very simple structure while retaining most of the outstanding properties. The low power factor is identified as their notable drawback that remains deterrent for their general performance. Consequently, several new PMV topologies and winding configurations have been proposed in a bid to upgrade it. Even though they do have significant improvement, some of the proposed modifications compromise the known strengths such as light weight and mechanical simplicity. Several papers that focus on the design of PMV machines have been reviewed in order to observe the current status of the research related to this type of machines. The information summarized from these publications does not necessarily present an absolute truth about all research activities taking place in this field as the literature survey may not be exhaustive. But it rather provides a general trend on the research interests and achievement so far.

When considering the physical sizes of the PMV machines as shown by Fig. 1.20, it can be seen that most researchers are currently focusing on small machines which are used for analysis in FEM or principle demonstration prototypes. The number of prototyped designs relative to those machines only analysed on FEM further prove the point that they are not yet been produced for commercial or industrial applications. There is also a good agreement with the output power ratings of these machines as provided by Fig. 1.21, where majority of them deliver only less than 10 kW. Moreover, most machines presented in the literature are not designed according to any specific application requirements (labelled as unclassified in Fig. 1.21) as they are meant to either illustrate a novel topology or just show performance characteristics.

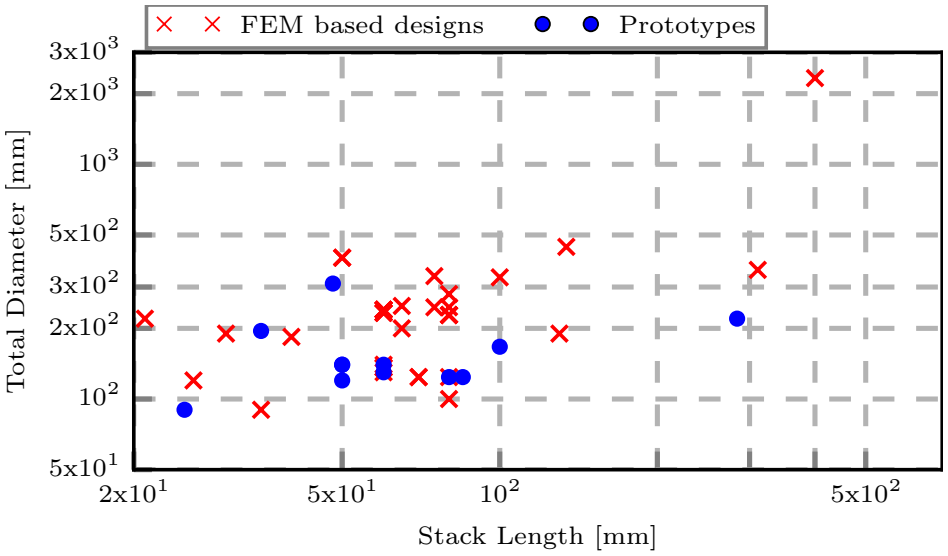

Figure 1.20: Distribution of PMV machines sizes from the literature, [21–62].

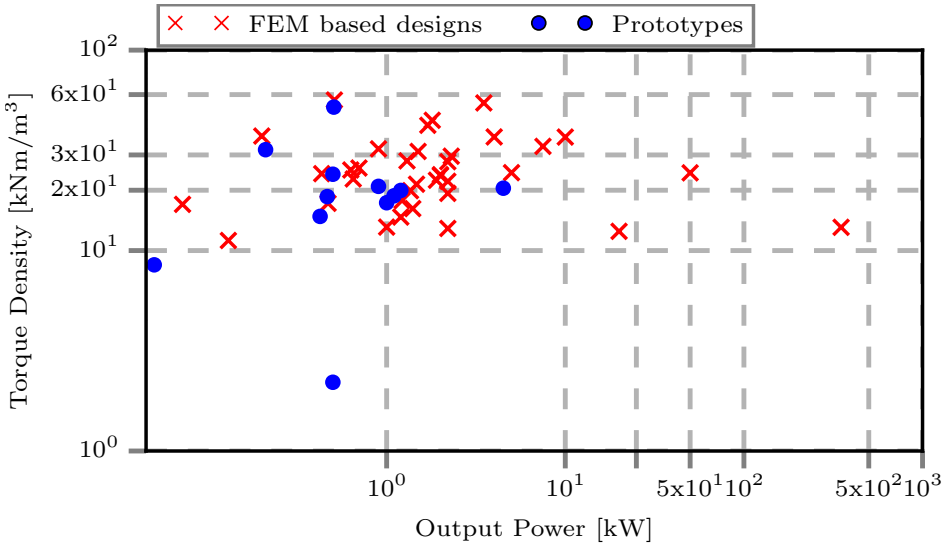

Figure 1.21: Distribution of PMV machines torque densities and rated powers based on some literature publications [21–62].

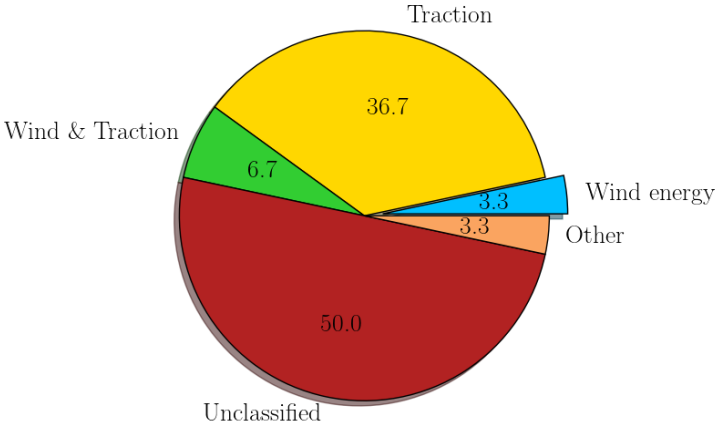

Figure 1.22: Some published papers on PMV machine design sorted according to their target applications [21–50].

1.4 Problem Statement

The principle of magnetic gearing has led to the development of a new class of electrical machines, known as *magnetically geared machines*. Significant research has been done on various types of these machines, which revealed their distinct advantages over other traditional machine types. Amongst the prominent magnetically geared machine technologies presented and analyzed in the literature, the PMV machine was identified as most promising due to its convincing practical implementation feasibility (easy to manufacture), low PM usage and high torque density.

Previous studies on PMV machines focused mainly on the principle demonstration, torque density and power factor improvement by either using different materials or by introducing more novel topological modifications. However, the suitable design optimization strategy and the in-depth investigation of its performance characteristics are still inadequate in literature. The reason why PMV machines have not yet penetrated the mass-production or commercial market is likely because the feasibility of implementing these machines for practical applications is not fully justified. While the target application seems to be largely towards the electric vehicle drives, it is also appealing to investigate them in wind power applications especially the utility-scale designs. Therefore, the current study seeks to cover these lacking points in an attempt to gain deep insight into the performance limitations and further improvements on the capability of this type machine. From the manufacturability perspective, single-stator and single-rotor PMV is still the most attractive Vernier machine topology. A techno-economic evaluation for the PMV machine technology specifically for wind power application can provide valuable information to wind power industry.

It is also important to note that this research study on PMV machine technology is motivated by the findings from the recently completed research projects in our research group [8; 62; 109]. These studies developed and evaluated three prominent MGPM machine technologies (including PMV machine technology), but at a small power level as is the case with most published studies in literature. It is thus necessary to investigate the performance capability of PMV machine technology for high power applications.

For this study, the important research questions are listed as follows:

- What is the most advantageous configuration of conventional (single-stator and singe-rotor) PMV machine in terms of performance characteristics?
- What are the appropriate analytical equations to describe the operation and performance properties of PMV machines? and what modifications are required in order to adopt the established classical PMSM machine theory?
- What are the suitable design strategy and design procedure for the PMV machine?
- What are the key design parameters and performance indexes that can be used in a design optimization process of the machine?
- How does a PMV machine compare with a conventional direct-drive (DD) PMSM in wind power application in terms of performances, costs and size?

- Is it practically feasible and economically viable to develop MW output level PMV generator for wind power application?

1.5 Objectives

In this research, the main aim is to develop and evaluate the permanent magnet vernier machine technology for use in the wind power generation applications, which can be further broken down into the following objectives.

- Derive fundamental analytical equations that describe the performance characteristics of a PMV machine based on classical PMSM machine theory. The analytical equations can help gain the insights of working principle and provide quick preliminary design variables for FEA based design process.
- Establish a dedicated FEA based design optimization environment, where design strategies, performance calculation and optimization can be implemented.
- Analyse the generation and interaction of different field harmonics in PMV machines so that the steady-state torque transmission mechanism and the influences of high orders modulated space harmonics to the stator teeth saturation, core loss and PM demagnetization risk can be clearly explained.
- Optimize and compare PMV machines with other traditional machines such as DD-PMSM in terms of cost, volume and weight, and mechanical structure complexity at both small and large output power levels. This comparison will illustrate if the PMV machine is a feasible substitute of DD-PMSM machines in wind generator applications.
- To validate the performance and the design methodology of PMV machines. An optimally designed PMV prototype will be manufactured for practical testing and comparison with the existing DD-PMSM machine in the lab.

1.6 Layout of The Dissertation

The basic layout of the remainder of the dissertation is arranged as follows:

Chapter 2 : The theory of the basic operating principles of the PM vernier machine is described with initial reference to the flux modulated CMGs. Important characteristics of this machine are explained in terms of simplified analytical equations which give an insight to its operation and performance parameters. These provide a clear direction into the proper design of PMV machines.

Chapter 3 : The computation of the electrical design variables based on the equivalent circuit equations and FEM modeling is presented in this chapter. The formulated field-circuit model is employed to do the steady-state design and performance analysis of the PMV machine throughout the study.

Chapter 4 : The establishment of FEM based electromagnetic design approach and optimization environment establishment are described in this chapter. A brief explanation of

the used FEM modelling tools and optimization strategies are provided. The developed modelling and optimization process is implemented to investigate various PMV machines at different output levels.

Chapter 5 : This chapter is dedicated to the discussion of the mechanical design, construction and assembling of the 15 kW prototype PMV machine. The manufactured prototype's practical evaluation process and results analysis are also provided.

Chapter 6 : This chapter focuses on the design study of a conventional PMV machine for utility-scale wind turbine applications. A comparison of this machine type with traditional PMSM machine is made at a 3 MW output power range in order to evaluate its potentials in this application.

Chapter 7 : In this chapter, the general conclusions drawn and original contributions achieved in this study are documented. Furthermore, the recommendations are provided for future research topics related to this study.

Chapter 2

Principle of Permanent Magnet Vernier Machines

In an electric machine's characteristic evaluation, vital information is normally deduced from the magnitude and harmonic composition of the air-gap magnetic flux density. For a PM machine, both the magnet flux and armature reaction field contribute to the total air-gap MMF, and its waveform shape depends on the air-gap permeance and PMs' magnetization pattern. Unlike conventional PM machines, the operating principle of the PMV machines is principally based on the intelligent utilization of the selective air-gap magnetic flux density harmonics. Therefore, it is a logical procedure to begin by providing the origin of the above important constituents in order to explain the PMV machine's operation.

2.1 Flux Distribution in an Uniform Air-Gap Adjacent to PM Rotor

Multi-pole PM rotors can be configured into various topologies and different excitation orientations [142]. By considering the position of the PM relative to the rotor yoke, the most used rotor topologies include surface-mounted PM (SPM), inset and interior PM rotors. The SPM is widely used due to the simplicity to construct such a PM rotor as the PMs are stuck on the surface of the yoke. However, SPM rotors can have some issues in high speed machines since the PM eddy current losses will rapidly increase, and the retaining sleeves may be needed for the inner rotor SPM machines to protect the PMs against the centrifugal forces. The following description of the PM MMF waveform will be mainly based on the SPM rotor machine. The PM rotor's MMF distribution is directly dependent on the topology and PM's magnetization direction. By assuming that the PMs are uniformly magnetized throughout their cross-section, and using the polar coordinates system, the PMs' magnetization vector $\vec{M}$ consists of radial and tangential components, given by:

$$\vec{M} = \vec{M}_r\vec{r} + \vec{M}_\theta\vec{\theta} \tag{2.1}$$

For radially magnetized surface-mounted PMs with linear second quadrant demagnetization curve characteristics, the vector $\vec{M}$ is perpendicular to the magnet's curved surface. This means that the tangential vector of the magnetization is insignificant, and normally taken as zero for analysis simplification purposes. Therefore, with the remanent flux

density of the PM denoted as B_r, $\vec{M}$ components become:

$$\begin{aligned} \vec{M}_{r,n} &= \frac{4}{n\pi}\frac{B_r}{\mu_o}\sin\left(k_{PM}\frac{n\pi}{2}\right) \\ \vec{M}_{\theta,n} &= 0 \qquad\qquad \text{with } n = 1,3,5,...\infty \end{aligned} \tag{2.2}$$

where k_{PM} is the ratio of the actual PM span relative to available PM pitch angle and μ_o is the vacuum permeability. Based on the above assumptions, and with the PM rotor on a static condition, a developed air-gap MMF distribution can generally be expressed as:

$$F_{PM}(\theta,\theta_r) \cong \sum_{n=1,3,5,...}^{\infty} \vec{M}_{r,n}\frac{h_m}{\mu_r}\cos\{np_r(\theta-\theta_r)-\theta_i\} \tag{2.3}$$

where θ, θ_r, θ_i and p_r are the angular position along the air-gap, rotor reference angle, rotor initial angle and number of rotor PM pole-pairs, μ_r and h_m are the PM's relative permeability and radial thickness, respectively.

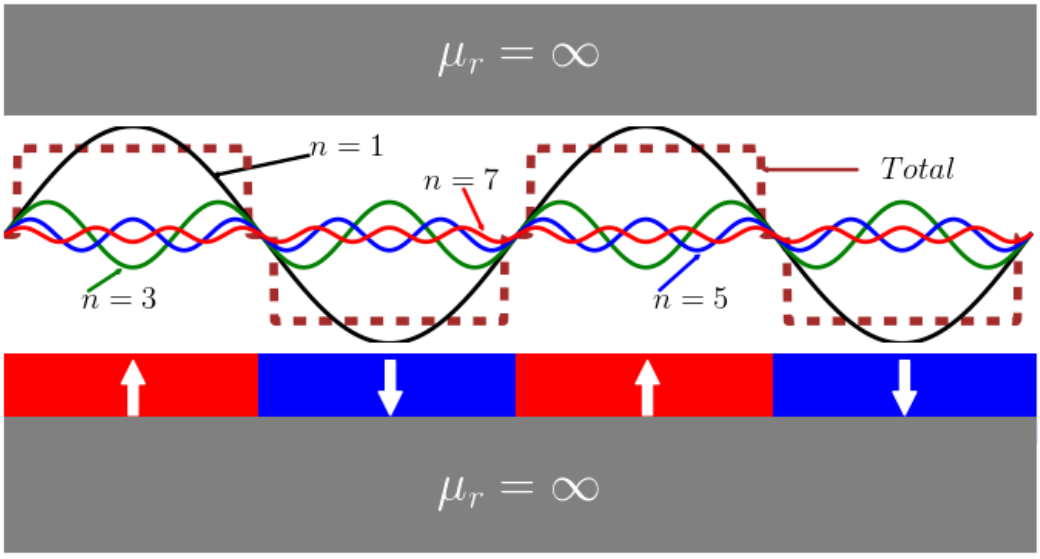

Figure 2.1: Approximation of MMF harmonic waveforms in an uniform air-gap for radially magnetized PMs.

From Eqn. 2.3 and Fig. 2.1, it can be seen that the amplitude of the quasi-square MMF distribution due to radially magnetized surface-mounted PM rotor, can be approximated by using only the dominant fundamental component of F_{PM} by employing the following equation.

$$\hat{F}_{PM} \cong F_{PM1} \cong \frac{4}{\pi}\frac{B_r h_m}{\mu_o\mu_r}\sin\left(k_{PM}\frac{\pi}{2}\right) \tag{2.4}$$

The term $\sin(k_{PM}\frac{n\pi}{2})$ in Eqns 2.2 and 2.4 reflects the n^{th} order PM pitch factor. The influence of varying PM pole-span on MMF harmonics is illustrated on Fig. 2.2 for two PM pole-pairs. Depending on the value of k_{PM}, the higher order harmonics can be either positive or negative, but there are also some specific k_{PM} values where certain harmonics have zero magnitudes. It can be seen that the third and fifth harmonics have zero magnitude when k_{PM} is around 0.67 and 0.80 respectively, while the seventh harmonic is zero at both k_{PM} equals to 0.57 and 0.86. The fundamental harmonic's magnitude shows a small increment from k_{PM} of 0.8 and above, whereas the fifth and

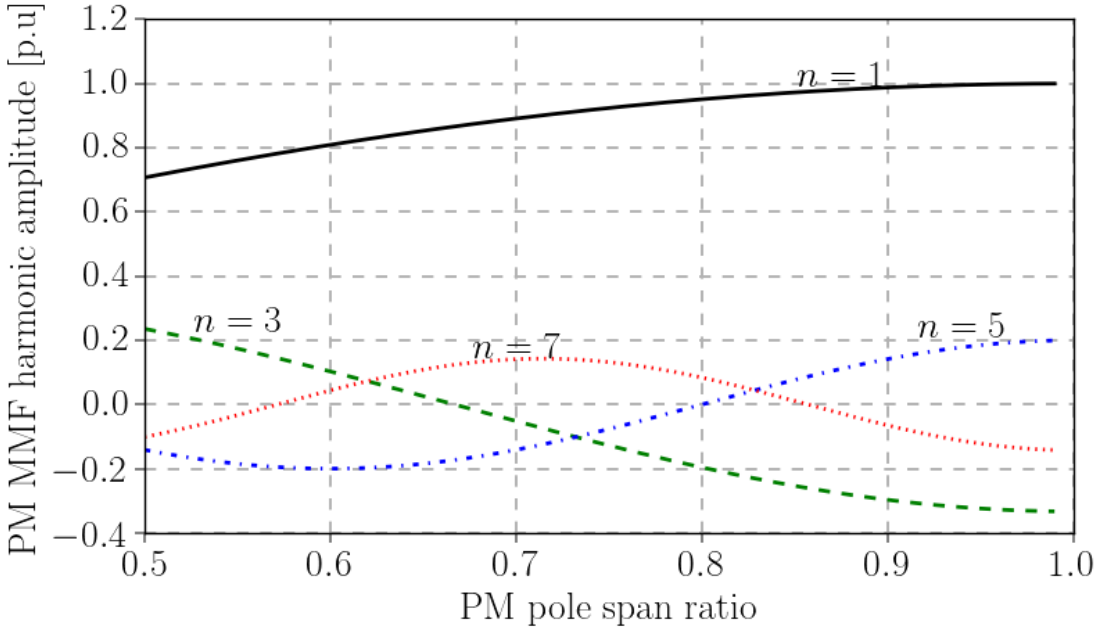

Figure 2.2: MMF harmonic magnitudes in uniform air gap as a function of PM pole span.

seventh harmonics' magnitudes are both close to zero at k_{PM} equal to 0.83. This is an interesting design point of PM pole pitch to minimize the two harmonics simultaneously even-though the third harmonic magnitude is still existing. Thus, some PM rotor MMF harmonic orders can theoretically be eliminated by only adjusting k_{PM}.

In order to assess the characteristics of the PM air-gap flux density (B_g), further assumptions are taken, that the stator has slot-less structure, and that the rotor and stator ferromagnetic material components have infinite permeability. This results in an perfectly uniform relative air-gap permeance with effective air-gap length defined from the combination of the physical air-gap and radial PM thickness as:

$$g' = g + \frac{h_m}{\mu_r} \tag{2.5}$$

where g is the physical clearance between the stator and the PMs. Then the air-gap flux density along the circumferential distance is the product of the constant air-gap permeance and the PMs' MMF, expressed as:

$$B_g(\theta, \theta_r) \cong \sum_{n=1,3,5,\ldots}^{\infty} \frac{\mu_o}{g'} \vec{M}_{r,n} \frac{h_m}{\mu_r} \cos\{np_r(\theta - \theta_r) - \theta_i\} \tag{2.6}$$

Considering the mechanical rotational speed of the permanent magnet rotor (ω_r), the position of the B_g waveform would also vary with time as its harmonics travel at an equivalent angular electrical velocity (ω_e). In this case, Eqn. 2.6 will now become,

$$\begin{aligned} B_g(\theta, t) &\cong \sum_{n=1,3,5,\ldots}^{\infty} \frac{\mu_o}{g'} \vec{M}_{r,n} \frac{h_m}{\mu_r} \cos\{np_r(\theta - \omega_r t) - \theta_i\} \\ \omega_e &= p_r \frac{d}{dt}\theta_r = p_r \omega_r \end{aligned} \tag{2.7}$$

All the rotor PMs' flux density harmonics rotate in the same direction, but only the major-harmonic (fundamental) has synchronous speed relative to the rotor, and thus

contribute to useful torque or flux linkage. The higher order, asynchronous harmonics are not of any significant importance as they are usually the source of rotor core losses. Although a simplified expression like Eqn 2.6 provides easy and quick understanding of the concept, it is not suitable for quantitative analysis purpose. A more accurate equation for a multi-pole external PM rotor was developed in [143], and is given below:

$$\begin{aligned} B_{rg}(r,\theta) \cong & \sum_{n=1,3,5,\ldots,}^{\infty} \frac{-\mu_o M_n}{\mu_r} \frac{np}{(np)^2-1} \\ & \times \left\{ \frac{(np-1)\left(\frac{R_m}{R_r}\right)^{2np} + 2\left(\frac{R_m}{R_r}\right)^{np-1} - (np+1)}{\frac{\mu_r+1}{\mu_r}\left[1-\left(\frac{R_s}{R_r}\right)^{2np}\right] - \frac{\mu_r-1}{\mu_r}\left[\left(\frac{R_s}{R_m}\right)^{2np} - \left(\frac{R_m}{R_r}\right)^{2np}\right]} \right\} \\ & \times \left[\left(\frac{r}{R_m}\right)^{np-1} + \left(\frac{R_s}{R_m}\right)^{np-1}\left(\frac{R_s}{r}\right)^{np+1}\right] \cdot \cos\left\{np_r(\theta-\theta_r)\right\} \\ \cong & \sum_{n=1,3,5,\ldots,}^{\infty} K_B(n) \cdot f_{Br}(r) \cdot \cos\left\{np_r(\theta-\theta_r)\right\} \end{aligned} \tag{2.8}$$

with all the parameters demonstrated on Fig. 2.3, and the similar expression for a multi-pole internal PM rotor is also provided in the same reference.

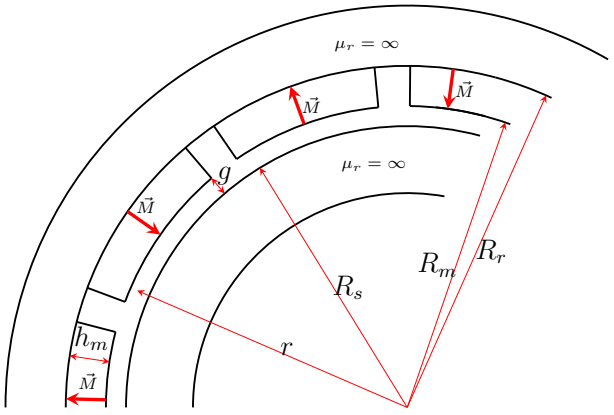

Figure 2.3: Parameters for equation. 2.8

2.2 Air-gap Permeance of Slotted Stator

The presence of slots on air-gap side surfaces of ferromagnetic regions of the machine influences the radially directed magnetic air-gap permeance. This influence comes in the form of an average air-gap permeance reduction and distribution variation. In surface-mounted PM rotor, the permeance variation along the angular periphery of the air-gap is mainly due to the open stator slots, since the PMs have relative permeability value close to unity. The linearized typical geometry of a PMV machine is shown in Fig. 2.4. In this case, the stator teeth work both as a magnetic flux path and as flux modulators that introduces the higher harmonics of the air-gap permeance. For the sake of simplicity in the analysis,, the stator slots are assumed to be fully open. This assumption is not

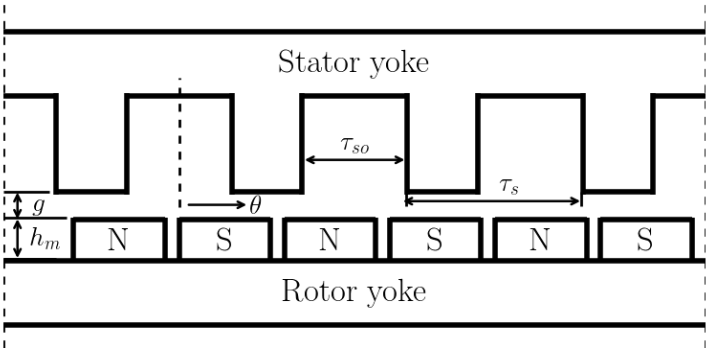

Figure 2.4: Linearized and simplified typical geometry of a PMV machine

far from the actual design points since PMV machines are usually equipped with wide to fully-open slots to enhance the modulation effect.

Assuming that the rotor surface is smooth, the relative permeability of iron regions is infinite, this permeance fluctuation is normally periodic with the stator slot pitch angle for evenly spaced slots. With the stator slot axis taken as the origin of the stator coordinate system, the permeance function is typically described using the following Fourier series function proposed in [144–146]:

$$\begin{aligned}
\Lambda(\theta) \cong\ & \Lambda_0 - \sum_{v=1,2,3,\ldots}^{\infty} \Lambda_v \cos(vQ_s\theta) \\
\Lambda_0 =& \frac{\mu_o}{g'}\left(1 - 1.6\beta\frac{\tau_{so}}{\tau_s}\right) \\
\Lambda_v =& \frac{\mu_o}{vg'}\frac{2\beta}{\pi}\left[\frac{0.78125}{0.78125 - 2\left(\frac{v\tau_{so}}{\tau_s}\right)^2}\right]\sin\left(1.6v\pi\frac{\tau_{so}}{\tau_s}\right)
\end{aligned} \tag{2.9}$$

where Λ_0 and Λ_v are the average and the specific magnitude of the v^{th} harmonic permeance coefficients obtained from a conformal mapping method, the parameters, τ_s and τ_{so} are respectively the slot pitch and slot opening as illustrated on Fig. 2.4. Furthermore, the coefficient β is determined by the relation [30; 144; 145]:

$$\beta = \frac{1}{2} - \frac{1}{2\sqrt{1 + \left(\frac{\tau_{so}}{2g'}\right)^2}} \tag{2.10}$$

where g' in Eqns. 2.9 and 2.10 is the equivalent air-gap length given by Eqn. 2.5. Both the average(Λ_0) and $v^{th}(\Lambda_v)$ harmonic magnitudes depend on the value of β, which in turn is a function of slot-opening to air-gap ratio $(\frac{\tau_{so}}{g'})$ as shown in Fig. 2.5.

Moreover, Eqn. 2.9 clearly reveals that Λ_0 and Λ_v are the functions of both the ratio of slot-opening to slot-pitch $(\frac{\tau_{so}}{\tau_s})$ and the ratio of slot opening to effective air-gap length $(\frac{\tau_{so}}{g'})$. This is illustrated in Fig. 2.6 for Λ_0 with a few different effective air-gaps and for Λ_v with PM radial length equal to 3 mm, bolstering an idea that the above mentioned parameters play an integral role in modulation effect of stator teeth. It should also be noted that the two graphs in Fig. 2.6 are normalized with different base values since the higher order permeance harmonics' amplitude are much smaller than that of the zeroth

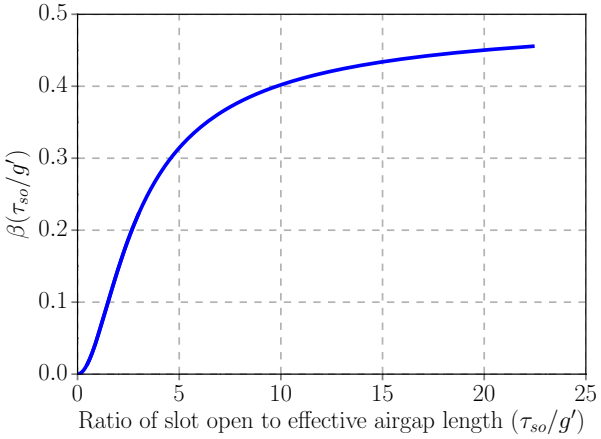

Figure 2.5: Parameter $\beta(\frac{\tau_{so}}{2g'})$

harmonic. An almost linear decrease of Λ_0 is observed as the slot opening ratio increases while Λ_1 increases to its peak value before a slight drop. Furthermore, an increase in effective air-gap length results in reduction of average permeance magnitude (Λ_0).

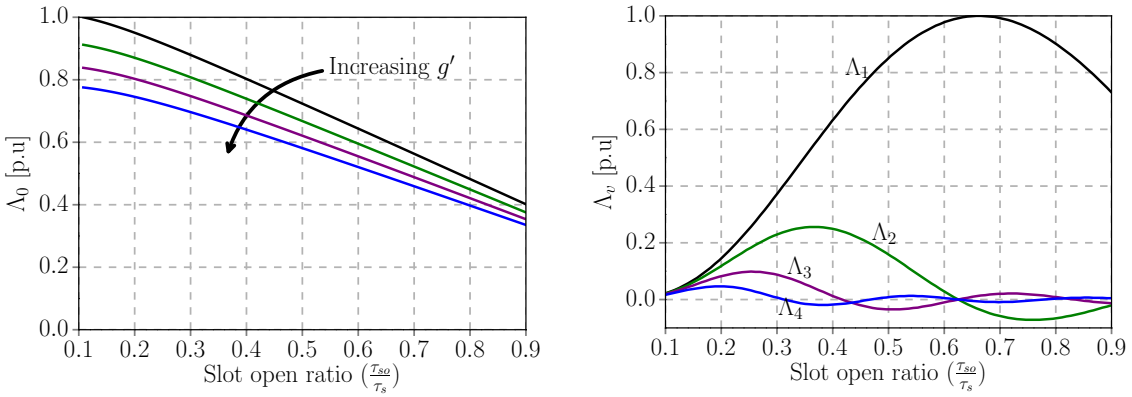

Figure 2.6: Relative air-gap permeance harmonics' variation with the ratio of slot opening to slot pitch: (a) average (b) higher order.

With very small slot opening ratios ($\frac{\tau_{so}}{\tau_s} < 0.3$), the second and third harmonics (Λ_2 and Λ_3) amplitudes are proportionately noticeable relative to that of the first harmonic (Λ_1), whereas this tendency changes for large slot opening ratios above 0.5, whereby they become insignificant in comparison to Λ_1 [144]. Thus, up to some extent, Λ_0 and Λ_1 amplitudes' values are considerably more dominant relative to other higher harmonics at larger slot-opening ratios. Particular interest is to be given to a point where $\frac{\tau_{so}}{\tau_s} = 0.625$, as this implies that all higher harmonics are theoretically non-existent, except the first (Λ_1) which is approximately at its peak. Basically, this could be a desired condition for the flux modulation concept since only the average and first slot harmonics are important. In general, the slot opening ratio is usually set to be more than 0.5 in PMV machines, hence the higher order harmonics can be neglected.

The relative air-gap permeance waveforms for three different slot opening ratios as predicted by Eqn. 2.9 are shown in Fig. 2.7, and their harmonic spectra are also shown

in Fig. 2.8. It can be clearly seen that slotting has significant effect on the permeance waveform, since the wider the slot opening becomes, the larger the permeance magnitude decreases. In addition, the higher order ($v \geq 2$) harmonic amplitudes are significantly smaller than those of the constant and fundamental harmonics. It can also be realized that all other harmonic orders are much lower compared to the zeroth-order, and at τ_{so}/τ_s equals to 0.625 there are no higher harmonic orders above 1.

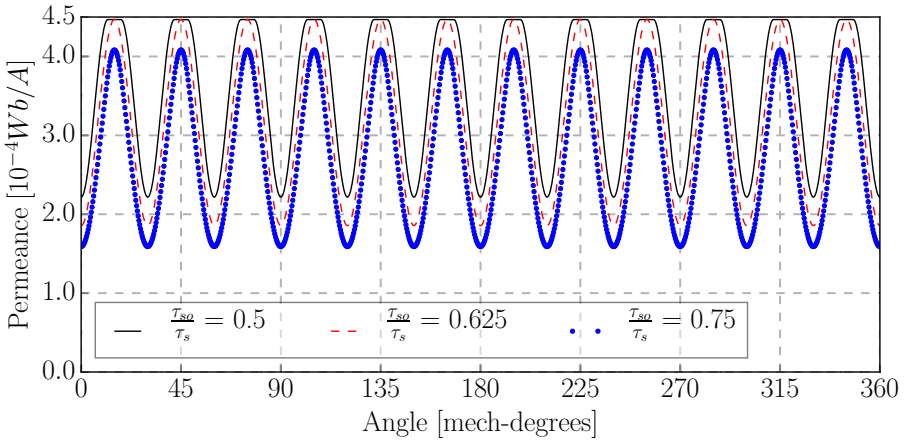

Figure 2.7: Relative air-gap permeance variation along air-gap periphery.

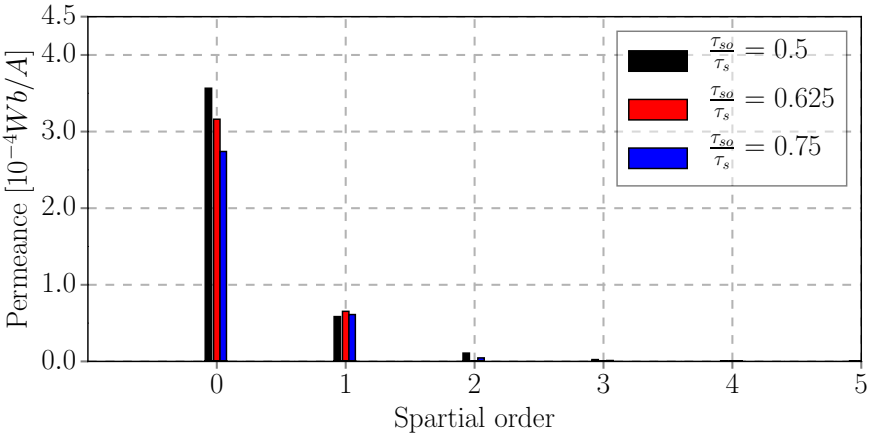

Figure 2.8: Relative air-gap permeance spatial orders

2.3 Magnetic Flux Modulation Concept

As a member of the flux-modulated machines family, the PMV machine relies on the principle of the flux modulation for its operation. The basic magnetic flux modulation principle is usually derived by assuming the following ideal conditions:

- Infinite permeability of ferromagnetic material components.
- Radial and uniformly magnetized PMs with $\mu_r \approx 1$.

In simplest terms, the theoretical flux modulation concept can generally be illustrated by Fig. 2.9, whereby the original 4 pole-pair field harmonic is transformed by the 6 pole-pair permeance harmonic into 2^{nd} and 10^{th} field harmonic orders in addition to the initial one.

Thus, a second magnetic field exciter component can be designed to have either 2 or 10 magnetic pole-pairs in order to match and engage with the initial one.

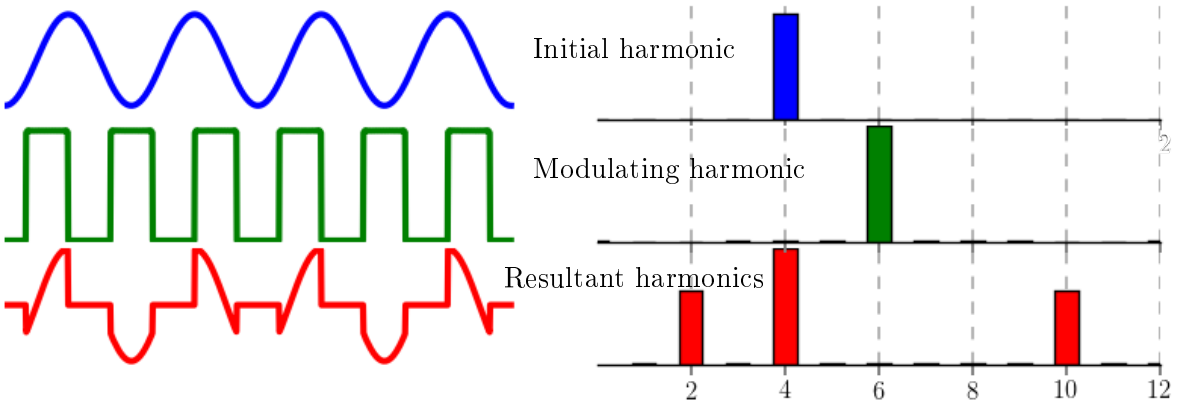

Figure 2.9: Illustration of ideal magnetic flux modulation process and spectrum shifting.

While maintaining the similar assumptions previously mentioned, the flux modulation principle in PMV machines can be explained from the flux modulated CMG. This is because the operation concept is practically similar between them, although it is easier to be described with reference to CMG than in PMV machines. The structure layout of a flux-modulated CMG with radially magnetized PMs is shown in Fig. 2.10. It has three main parts, being the outer rotor with larger number of PM pole-pairs (p_{r_l}) and the inner rotor with smaller number of PM pole-pairs (p_{r_h}). The third part consists of a ring of an uniformly spaced ferromagnetic segments situated between the two PM rotors, having a p_{fm} pole-pieces. The three components have the mechanical angular speeds of $\pm\omega_{r_l}$, $\pm\omega_{r_h}$ and $\pm\omega_{fm}$ for the outer PM rotor, the inner PM rotor and the flux modulator respectively. The positive rotational speed indicates the clockwise direction while the negative indicates the anti-clockwise rotation since the components are free to rotate in any of the two directions.

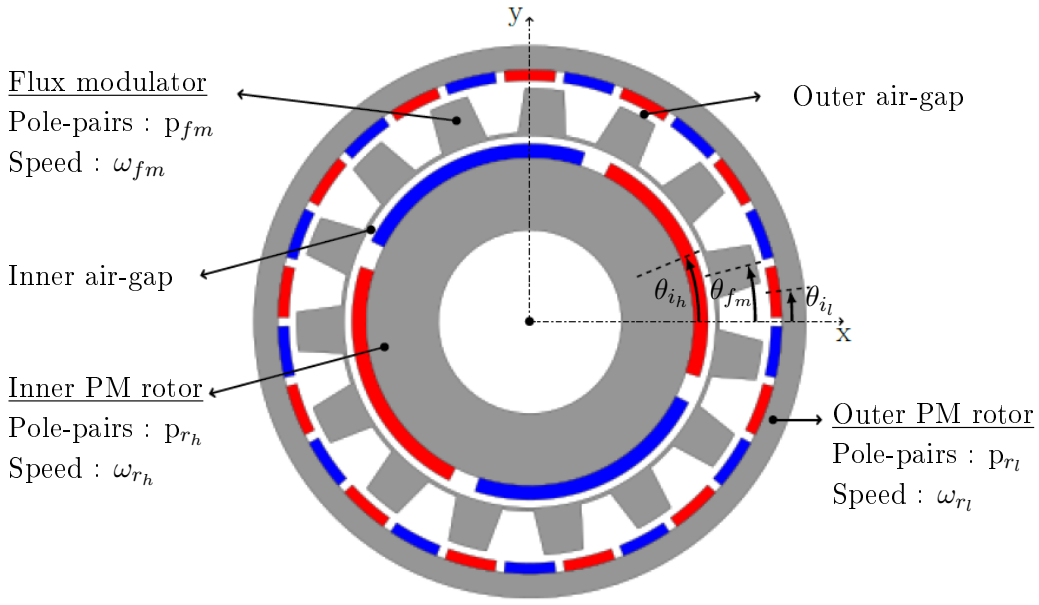

Figure 2.10: Structure of radial flux modulated coaxial magnetic gear.

Considering a single PM rotor and the slotted flux-modulator (stator), the magnetic flux density in the air-gap (B_g) can be obtained from the magneto-motive force and the permance functions. Thus, B_g can be expressed as the product of the Eqns 2.3 and 2.9 as defined in Eqn. 2.11, which describes the magnetic field modulation effect.

$$\begin{aligned}
B_g(\theta,t) \cong\ & F_{PM}(\theta,t) \times \Lambda(\theta,t) \\
\cong & \left[\sum_{n=1,3,5,\ldots}^{\infty}\left(\vec{M}_{r,n}\frac{h_m}{\mu_r}\right)\cos\left(np_r(\theta-\omega_r t)-\theta_i\right)\right]\times\left[\Lambda_0-\sum_{v=1,2,3,\ldots}^{\infty}\Lambda_v\cos(vp_{fm}(\theta-\omega_{fm}t)-\theta_{fm})\right] \\
\cong & \sum_{n=1,3,5,\ldots}^{\infty}\Lambda_0\left(\vec{M}_{r,n}\frac{h_m}{\mu_r}\right)\cos\left\{np_r(\theta-\omega_r t)\right\} \\
& -\frac{1}{2}\sum_{n=1,3,5,\ldots}^{\infty}\sum_{v=1,2,3,\ldots}^{\infty}\Lambda_v\left(\vec{M}_{r,n}\frac{h_m}{\mu_r}\right)\cos\left\{(vp_{fm}\pm np_r)\theta-(vp_{fm}\omega_{fm}\pm np_r\omega_r)t+(\theta_{fm}\pm\theta_i)\right\}
\end{aligned} \tag{2.11}$$

For a CMG or the PMV machine, there are two sources of magnetic fields, being the two PM sets on the rotors or a PM rotor and a stator armature. Therefore, the modulation effect on the fields produced by each excitation source can be separately analyzed and then combined using superposition principle to obtain the resultant fields in the two air-gaps. Furthermore, in order to simplify the equation, only the fundamental component of PM MMF (F_{PM1}), the average (Λ_0) and first order (Λ_1) harmonic components of permeance are used on the flux modulation principle explanation. This is also because the other higher order harmonic components have insignificant magnitudes as has been previously shown. Considering Eqn. 2.11 and supposing that only the PM set on the inner rotor is active, the flux density distribution in the outer air-gap close to the outer-rotor is approximated as:

$$\begin{aligned}
B_{g_h}(\theta,t) &\cong \left[F_{PM1_h}\cos\left\{p_{r_h}(\theta-\omega_{r_h}t)+\theta_{i_h}\right\}\right]\times\left[\Lambda_0-\Lambda_1\cos\left\{p_{fm}(\theta-\omega_{fm}t)-\theta_{fm}\right\}\right] \\
&\cong \overbrace{\Lambda_0 F_{PM1_h}\cos\left\{p_{r_h}(\theta-\omega_{r_h}t)+\theta_{i_h}\right\}}^{B_{h_0}} \\
&\quad -\overbrace{\frac{1}{2}\Lambda_1 F_{PM1_h}\cos\left\{(p_{fm}+p_{r_h})\theta-(p_{fm}\omega_{fm}+p_{r_h}\omega_{r_h})t+(\theta_{fm}+\theta_{i_h})\right\}}^{B_{h_+}} \\
&\quad -\overbrace{\frac{1}{2}\Lambda_1 F_{PM1_h}\cos\left\{(p_{fm}-p_{r_h})\theta-(p_{fm}\omega_{fm}-p_{r_h}\omega_{r_h})t+(\theta_{fm}-\theta_{i_h})\right\}}^{B_{h_-}}
\end{aligned} \tag{2.12}$$

where F_{PM1_h} is the fundamental harmonic of F_{PM} produced by the inner-rotor PMs with p_{r_h} pole-pairs.

Similarly, if only the outer rotor PM set is active, the magnetic flux density on the inner air-gap closer to the inner PM rotor is approximated as follows:

$$\begin{aligned} B_{g_l}(\theta,t) &\cong [F_{PM1_l}\cos\{p_{r_l}(\theta-\omega_{r_l}t)+\theta_{i_l}\}]\times[\Lambda_0-\Lambda_1\cos\{p_{fm}(\theta-\omega_{fm}t)-\theta_{fm}\}] \\ &\cong \overbrace{\Lambda_0 F_{PM1_l}\cos\{p_{r_l}(\theta-\omega_{r_l}t)+\theta_{i_l}\}}^{B_{l_0}} \\ &\quad -\overbrace{\frac{1}{2}\Lambda_1 F_{PM1_l}\cos\{(p_{fm}+p_{r_l})\theta-(p_{fm}\omega_{fm}+p_{r_l}\omega_{r_l})t+(\theta_{fm}+\theta_{i_l})\}}^{B_{l_+}} \\ &\quad -\overbrace{\frac{1}{2}\Lambda_1 F_{PM1_l}\cos\{(p_{fm}-p_{r_l})\theta-(p_{fm}\omega_{fm}-p_{r_l}\omega_{r_l})t+(\theta_{fm}-\theta_{i_l})\}}^{B_{l_-}} \end{aligned} \tag{2.13}$$

where F_{PM1_l} is the fundamental harmonic of F_{PM} produced by the outer-rotor PMs with p_{r_l} pole-pairs.

According to the expressions in Eqns. 2.12 and 2.13, the modulated flux density from each PM rotor is composed of the three main components described below:

- The fundamental component that is rotating at the synchronous speed and has exactly the same number of pole-pairs as their original exciting PM rotor.
- One harmonic component with asynchronous speed, same rotational direction but different number of pole-pairs to the parent exciting PM rotor, referred to as the positive rotating harmonic component.
- Another harmonic component with asynchronous speed, opposite rotational direction and different number of pole-pairs to the parent exciting PM rotor, referred to as the negative rotating harmonic component.

A summary of the resultant air-gap magnetic flux densities is provided in Table 2.1, where the harmonic magnitudes, pole-pair numbers and angular speeds are indicated.

Table 2.1: Modulated rotor PMs' magnetic flux densities in the two air-gaps.

Region	Comp.	Amplitude	Pole-pair	Angular speed*	Angular speed†
Outer air-gap	B_{h_0}	$\Lambda_0 F_{PM1_h}$	p_{r_h}	ω_{r_h}	ω_{r_h}
	B_{h_+}	$\frac{1}{2}\Lambda_1 F_{PM1_h}$	$p_{fm}+p_{r_h}$	$\frac{(p_{fm}\omega_{fm}+p_{r_h}\omega_{r_h})}{(p_{fm}+p_{r_h})}$	$\frac{(p_{r_h}\omega_{r_h})}{(p_{fm}+p_{r_h})}$
	B_{h_-}	$\frac{1}{2}\Lambda_1 F_{PM1_h}$	$p_{fm}-p_{r_h}$	$\frac{(p_{fm}\omega_{fm}-p_{r_h}\omega_{r_h})}{(p_{fm}-p_{r_h})}$	$\frac{(p_{r_h}\omega_{r_h})}{(p_{fm}-p_{r_h})}$
Inner air-gap	B_{l_0}	$\Lambda_0 F_{PM1_l}$	p_{r_l}	ω_{r_l}	ω_{r_l}
	B_{l_+}	$\frac{1}{2}\Lambda_1 F_{PM1_l}$	$p_{fm}+p_{r_l}$	$\frac{(p_{fm}\omega_{fm}+p_{r_l}\omega_{r_l})}{(p_{fm}+p_{r_l})}$	$\frac{(p_{r_l}\omega_{r_l})}{(p_{fm}+p_{r_l})}$
	B_{l_-}	$\frac{1}{2}\Lambda_1 F_{PM1_l}$	$p_{fm}-p_{r_l}$	$\frac{(p_{fm}\omega_{fm}-p_{r_l}\omega_{r_l})}{(p_{fm}-p_{r_l})}$	$\frac{(p_{r_l}\omega_{r_l})}{(p_{fm}-p_{r_l})}$

* Mechanical angular speeds when all the three components are rotating.
† Mechanical angular speeds when the modulating ring is stationary.

In order for magnetic steady torque transmission to occur between the two components, some of the intrinsic requirements are that the fields must have same pole-pair

number and angular speed. With that said, it is obvious that the fundamental harmonic components of the two PM rotors may never directly engage with each other to produce any useful torque ($p_{r_h} \neq p_{r_l}$). The logically available possibilities in this regard entails that the fundamental harmonic component of one PM rotor engages with the modulated harmonic components of the other PM rotor. Hence, the combination of pole-pair numbers that interacts to produse a meaningful torque transmission are as follows:

$$p_{r_h} = \left| p_{fm} \pm p_{r_l} \right| \quad \text{or} \quad p_{r_l} = \left| p_{fm} \pm p_{r_h} \right| \tag{2.14}$$

On further expansion and re-arranging of Eqn. 2.14, the pole-pair numbers of the inner- and outer-rotors that satisfy the torque transmission mechanism should comply with one of the following relationships:

(1) $p_{fm} = p_{r_l} + p_{r_h}$
(2) $p_{fm} = p_{r_l}$ - p_{r_h}
(3) $p_{fm} = p_{r_h}$ - p_{r_l}

The third condition is in contradiction to the initial assumption that the inner rotor PM pole-pair number is smaller than that of the outer PM rotor. In principle, it is still a valid option except that it only swaps the roles of the two PM rotors, and replaces the second condition. Consequently, the PM rotor pole-pair combinations in flux-modulated CMG boils down to the two choices below:

$$\begin{aligned} & p_{fm} = p_{r_l} + p_{r_h} \\ \Rightarrow\ & p_{fm}\omega_{fm} = p_{r_l}\omega_{r_l} + p_{r_h}\omega_{r_h} \end{aligned} \tag{2.15}$$

$$\begin{aligned} & p_{fm} = p_{r_l} - p_{r_h} \\ \Rightarrow\ & p_{fm}\omega_{fm} = p_{r_l}\omega_{r_l} - p_{r_h}\omega_{r_h} \end{aligned} \tag{2.16}$$

The first choice (Eqn. 2.15) is generally favored over the second since it normally produce better performance relative to that defined by Eqn. 2.16. Even though the three components have been treated as if they are all simultaneously rotating, the conventional practical designs have one component fixed stationary while the other two are rotating. That is, either the modulating ring or the PM rotor with a high pole count is kept stationary and the other two components serve as the input and output terminals of the CMG.

In accordance with Eqn. 2.15, if the modulator is kept stationary ($\omega_{fm} = 0$), the speed relationship between the two PM rotors is expressed as:

$$\begin{aligned} & p_{r_h}\omega_{r_h} = -p_{r_l}\omega_{r_l} \\ \Rightarrow\ & G_r = \frac{\omega_{r_h}}{\omega_{r_l}} = -\frac{p_{r_l}}{p_{r_h}} \qquad \text{or} \qquad G_r = -\left(\frac{p_{fm}}{p_{r_h}} - 1\right) \end{aligned} \tag{2.17}$$

On the other hand, if the PM rotor with a high pole count is kept stationary, the speeds of the modulating ring and the inner PM rotor are related by:

$$\begin{aligned} & p_{fm}\omega_{fm} = p_{r_h}\omega_{r_h} \\ \Rightarrow\ & G_r = \frac{\omega_{r_h}}{\omega_{fm}} = \frac{p_{fm}}{p_{r_h}} \qquad \text{or} \qquad G_r = \left(\frac{p_{r_l}}{p_{r_h}} + 1\right) \end{aligned} \tag{2.18}$$

The speed ratios in Eqns. 2.17 and 2.18 represents the CMG gearing ratio (G_r), which is also a factor between the steady-state torques experienced by the rotating components. The minus sign in Eqn. 2.17 means the two PM rotors will rotate in opposite directions, whereas the inner PM rotor and the modulating ring rotate in the same direction as denoted by Eqn. 2.18. In addition, there is a magnitude difference of one between the gear ratios in these two conditions, with the fixed modulator case resulting in lower G_r.

In order to demonstrate the flux-modulation principle, an example of flux densities in the two air-gaps of the flux-modulated CMG with p_{r_h}=2, p_{r_l}=13 and p_{fm}=15 are shown in Figs. 2.11 and 2.12. Looking into the outer air-gap when only the inner rotor PMs are active (Fig. 2.11), there is $p_{fm}\pm p_{r_h}$ harmonics observed in addition to p_{r_h}. In the same manner, when only the outer rotor PMs are active (Fig. 2.12), the $p_{fm}\pm p_{r_l}$ and p_{r_l} order harmonics also exists in the inner air-gap. Therefore, when both PM sets are active at the same time, Eqn. 2.15 suggests that $p_{fm}-p_{r_h}$ will match with p_{r_l} on the outer air-gap while $p_{fm}-p_{r_l}$ will engage with p_{r_h} in the inner air-gap to result in steady torque transmission.

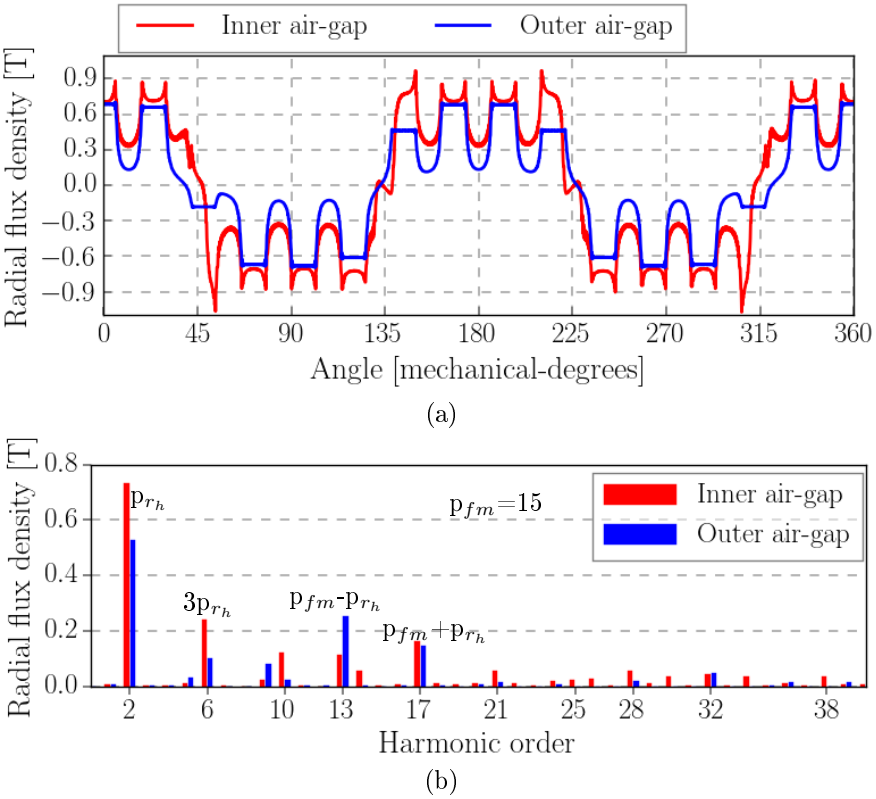

Figure 2.11: Radial flux density in the air-gaps produced by the inner rotor PMs: (a)waveforms, and (b) harmonic spectrum.

2.4 Magnetic Field Modulation in PMV Machines

The PMV machine operation relies on the same flux-modulation principle described for a CMG, and the similarity between them was explained by Qu *et al* [99]. The only difference is that the inner PM rotor in CMG (Fig. 2.10) is replaced by a stator with 3-phase alternating current in order to generate rotating fields. An alternative way to look at

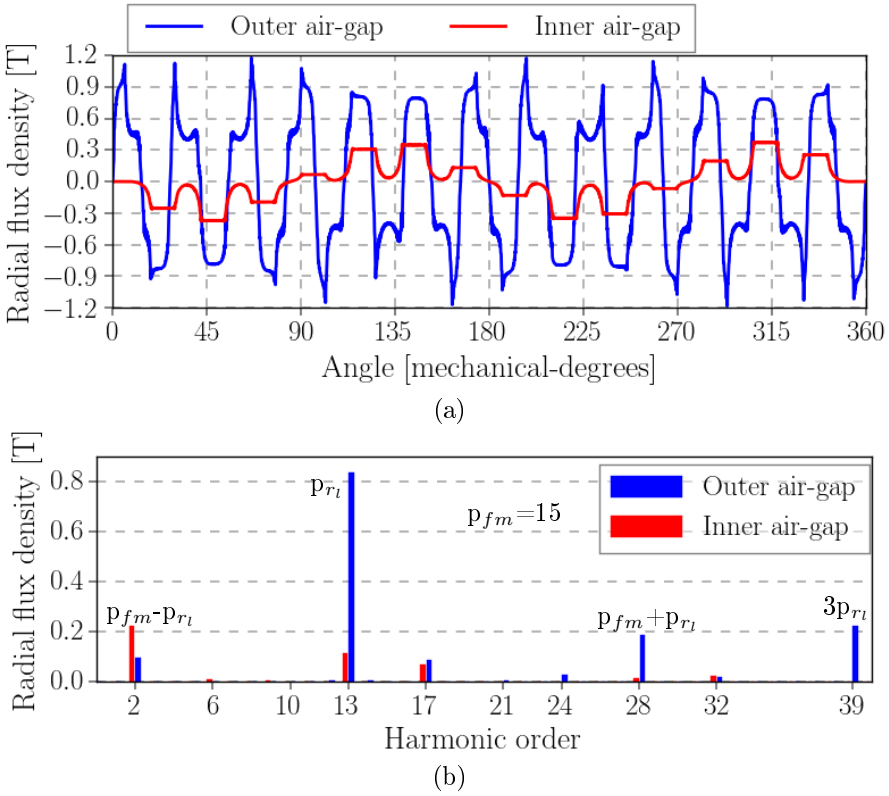

Figure 2.12: Radial flux density in the air-gaps produced by the outer rotor PMs: (a)waveforms, and (b) harmonic spectrum.

the PMV machine structure is that it is developed from a conventional synchronous PM machine by introducing the flux-modulating ring between the stator and PM rotor. Thus, in resemblance to the CMG, the essential task of the flux-modulator is to modulate the low-speed rotating field of the PM rotor and the high-speed field of the stator winding. Consequently, the fundamental MMF harmonic of the stator is able to interact with the modulated lower order harmonic component from the PM rotor, whereas the fundamental harmonic of the PM rotor interacts with the modulated high order harmonic from the stator. A basic configuration of the PMV machine is shown in Fig. 1.15. Further structure simplification and possibly the performance improvement are achieved by removing the inner air-gap through merging the stator teeth with the flux modulator into one component as presented by Figs. 1.16 and 1.17.

Based on the classical synchronous machine theory, the two electromagnetic fields can produce the steady torque if and only they have the same pole-pair numbers and speed. Since the number of stator armature and PM rotor magnetic poles are always different in PMV machines, the flux-modulator is the key to provide a specific air-gap permeance function and ultimately transforms the magnetic pole numbers and their speeds. The foregoing discussion of the flux modulation in PMV machines considers the case where the flux-modulating pieces are merged with- and have the same number as the stator teeth (p_{fm}=Q_s and $\omega_{fm} = 0$). In other words, the teeth of the stationary stator performs the flux modulation function instead of having an additional modulating-ring.

Assuming that the balanced three-phase pure sinusoidal currents are feeding in a machine running at a steady state operation, the total rotating air-gap MMF (F_C) due

to the stator armature currents can be represented as:

$$F_C(\theta,t) = \frac{3}{2}F_{C1}\left\{\begin{array}{l}\sum\limits_{n=1,7,13,\ldots,}^{\infty}\frac{K_{wn}}{n}\cos\{n\mathrm{p}_s\theta-(\omega_e t-\alpha)\}\\ +\sum\limits_{n=5,11,17,\ldots,}^{\infty}\frac{K_{wn}}{n}\cos\{n\mathrm{p}_s\theta+(\omega_e t-\alpha)\}\end{array}\right\} \qquad (2.19)$$
$$F_{C1} = \frac{2\sqrt{2}IN_{ph}}{\mathrm{p}_s\pi}$$

where F_{C1}, p_s and θ are the amplitude of the fundamental component of F_C, the stator pole-pairs and air-gap mechanical angular position, respectively, while I, α and ω_e are the rms amplitude, the initial angle and the electrical angular frequency of the current, respectively.

Eqn. 2.19 includes infinite number of harmonic components. Since the terms with higher orders have insignificant magnitudes relative to the major terms, they may be ignored. Thus, for analysis purposes, it is sufficient to deal with the fundamental and first order slot harmonics components, hence the MMF due to stator coil currents can be written as:

$$F_C(\theta,t) \cong \frac{3F_{C1}K_{w1}}{2}\left\{\begin{array}{l}\cos\{\mathrm{p}_s\theta-(\omega_e t-\alpha)\}+\\ \frac{1}{\frac{Q_s}{\mathrm{p}_s}-1}\cos\{(Q_s-\mathrm{p}_s)\theta+(\omega_e t-\alpha)\}-\frac{1}{\frac{Q_s}{\mathrm{p}_s}+1}\cos\{(Q_s+\mathrm{p}_s)\theta-(\omega_e t-\alpha)\}\end{array}\right\} \qquad (2.20)$$

With the prior knowledge of air-gap flux density due to the rotor PMs as previously described in Eqn. 2.11 for a CMG and noting that the stator is not rotating, an open-circuit air-gap flux density distribution for a PMV machine can similarly be evaluated as:

$$\begin{aligned}B_{PM}(\theta,t) &\cong [F_{PM1}\cos\{p_r(\theta-\omega_r t)+\theta_i\}]\times[\Lambda_0-\Lambda_1\cos(Q_s\theta)]\\ &\cong \overbrace{\Lambda_0 F_{PM1}\cos\{p_r(\theta-\omega_r t)+\theta_i\}}^{B^1_{PM}}\\ &\quad -\overbrace{\frac{1}{2}\Lambda_1 F_{PM1}\cos\{(Q_s+p_r)\theta-p_r\omega_r t+\theta_i\}}^{B^2_{PM}} - \overbrace{\frac{1}{2}\Lambda_1 F_{PM1}\cos\{(Q_s-p_r)\theta+p_r\omega_r t+\theta_i\}}^{B^3_{PM}}\end{aligned} \qquad (2.21)$$

Comparing Eqns. 2.20 and 2.21 and bearing in mind the relation between the numbers of magnetic pole-pairs and stator teeth or flux modulator pieces ($Q_s = p_r \pm \mathrm{p}_s$), it can be seen that there are three B_{PM} terms, each having similar spacial period to one of the terms in coil current MMF:

- $\frac{1}{2}\Lambda_1 F_{PM1}\cos\{(Q_s-p_r)\theta-p_r\omega_r t\} \iff \frac{3}{2}F_{C1}K_{w1}\cos\{\mathrm{p}_s\theta-(\omega_e t-\alpha)\}$
- $\Lambda_0 F_{PM1}\cos\{p_r(\theta-\omega_r t)\} \Longleftrightarrow \frac{3}{2}F_{C1}K_{w1}\frac{1}{\frac{Q_s}{\mathrm{p}_s}-1}\cos\{(Q_s-\mathrm{p}_s)\theta+(\omega_e t-\alpha)\}$
- $\Lambda_0 F_{PM1}\cos\{p_r(\theta-\omega_r t)\} \Longleftrightarrow \frac{3}{2}F_{C1}K_{w1}\frac{1}{\frac{Q_s}{\mathrm{p}_s}+1}\cos\{(Q_s+\mathrm{p}_s)\theta-(\omega_e t-\alpha)\}$

Consequently, the third term of B_{PM} have equal harmonic order that rotates synchronously with the fundamental component of coil current MMF. It should also be realized that the fundamental harmonic of stator armature have opposite rotational direction

to the PM rotor since it couples with the negatively rotating B_{PM}^{3} component. Similarly, the first term of B_{PM} is synchronous to the second term of the slot harmonics of coil current air-gap MMF if $Q_s = p_r + \mathrm{p}_s$. Otherwise if $Q_s = p_r - \mathrm{p}_s$, the first term of B_{PM} would interact with the third stator MMF component. Thus, the engagement of two field harmonic components results in steady torque transmission between the rotor and stator, even-though the two parts have different number of fundamental pole-pairs.

Again, in order to verify the approximation of flux modulation effect described by Eqn. 2.21, the open circuit flux density waveforms of a 10 pole-pair PM rotor and 12 stator teeth representing flux modulation pieces for a machine shown in Fig. 2.13 are presented in Fig. 2.14. A fairly good agreement is observed between the analytical equation and FEM results, and it can be seen that the air-gap magnetic flux density now has three main components. Thus, in addition to the original 10 pole-pair harmonic, the two other relatively smaller flux density harmonics are produced having the orders of 2- and 22-pole-pairs. Accordingly, the stator would have to be designed to have 2 or 22 armature electromagnetic pole-pairs to engage in torque transmission with the PM rotor.

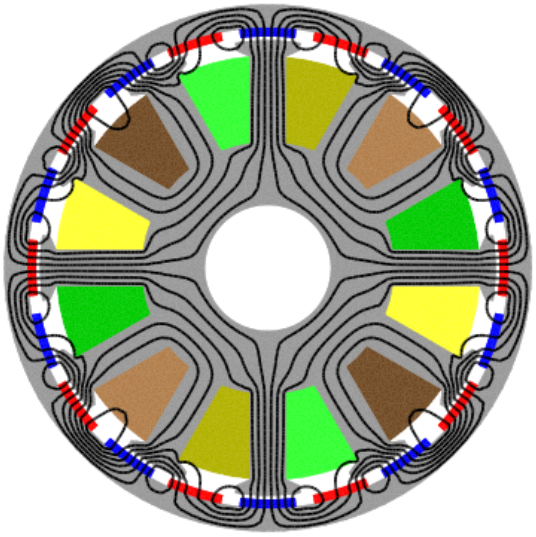

Figure 2.13: PMV machine with 12-slots and 2-stator pole-pairs showing open circuit flux lines

The per phase open circuit flux linkage is extracted by integrating the air-gap flux density due to PMs, and this is given by:

$$\begin{aligned}
\lambda_{ph}(\theta_r) &= \frac{N_{ph} r_g l_{stk}}{q} \sum_{k=0}^{q-1} \left[\int_{\theta_i + k\alpha_T}^{\theta_i + k\alpha_T + \frac{\pi}{p}} B_{PM}(\theta, \theta_r) d\theta \right] \\
&= \frac{K_{w1} N_{ph} D_g l_{stk}}{q} \sum_{k=0}^{q-1} \left[\frac{B_{PM0}}{p_r} - \frac{B_{PM1}}{2} \left\{ \frac{1}{p_r - Q_s} + \frac{1}{p_r + Q_s} \right\} \right] \sin\left\{ p_r(\theta - \theta_r) \right\} \\
&\Rightarrow B_{PM0} = F_{PM1} \Lambda_0 \quad \text{and} \quad B_{PM1} = F_{PM1} \Lambda_1
\end{aligned} \tag{2.22}$$

where D_g, l_{stk} and θ_i are the air-gap diameter, machine stack length and initial angular position of each phase winding, respectively. The change of flux-linkage with respect to

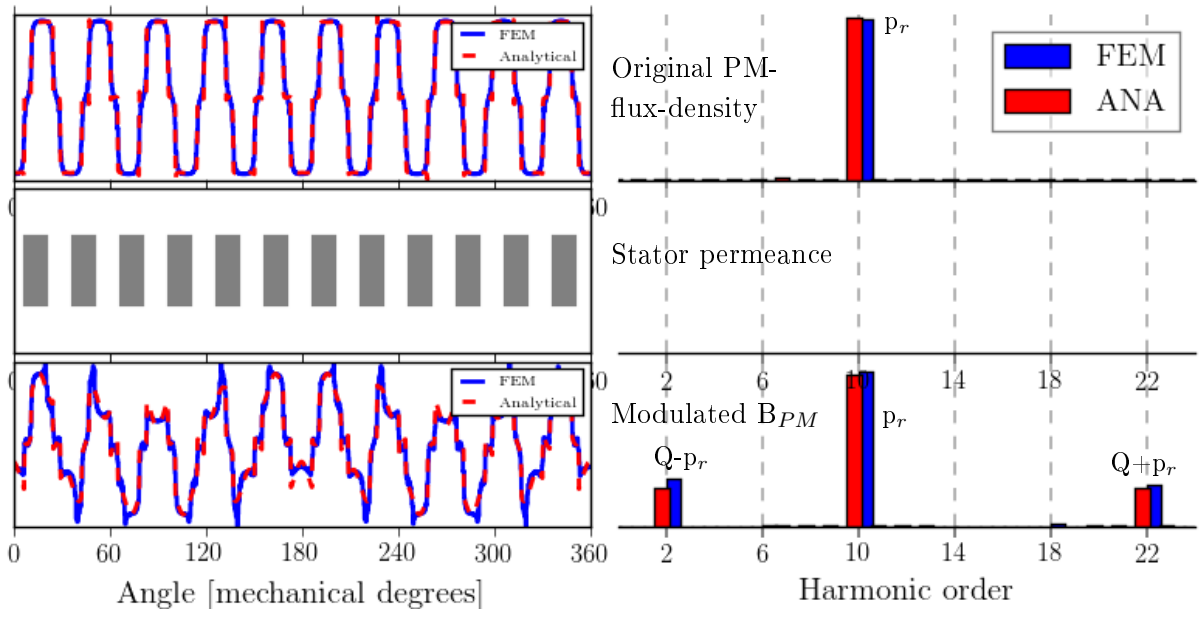

Figure 2.14: Open circuit air-gap magnetic flux density waveforms and their spectra before and after modulation process.

time results into the induced electro-motive force (EMF).

$$
\begin{aligned}
e_{ph}(t) &= \frac{d\lambda_{ph}(\theta_r)}{dt} = \frac{N_{ph}D_g l_{stk}}{q}\sum_{k=0}^{q-1}\left[\frac{B_{PM0}}{p_r} - \frac{B_{PM1}}{2}\left\{\frac{1}{\pm \mathrm{p}_s} + \frac{1}{Q_s + p_r}\right\}\right]\frac{d}{dt}\sin\left(p_r\theta_r + p\theta_i\right) \\
&= \frac{K_{w1}N_{ph}D_g l_{stk}}{q}\sum_{k=0}^{q-1}\left[B_{PM0} - \frac{B_{PM1}}{2}\left\{\frac{p_r}{\pm \mathrm{p}_s} + \frac{p_r}{p_r + Q_s}\right\}\right]\cos\left(p_r\omega_r + \mathrm{p}_s\theta_i\right) \\
&\cong \frac{K_{w1}N_{ph}D_g l_{stk}}{q}\sum_{k=0}^{q-1}\left[B_{PM0} \mp \frac{B_{PM1}}{2}\left\{\frac{p_r}{\mathrm{p}_s}\right\} - \frac{B_{PM1}}{2}\left\{\frac{p_r}{p_r + Q_s}\right\}\right]\cos\left(p_r\omega_r + \mathrm{p}_s\theta_i\right) \\
&\text{with} \quad \frac{d}{dt}\theta_r = \omega_r
\end{aligned}
\tag{2.23}
$$

The presence of three voltage constituents is now evident in the developed open circuit voltage expression. The first term is equivalent to the component found in classical synchronous PM machines, while the second and the third terms are due to the vernier effect. The existence of second and third components of Eqn. 2.23 differentiates PMV machines from the conventional PM synchronous machines. Moreover, the second term can be either positive or negative depending on the choice of the stator armature and rotor PM pole-pair number, while the third term is always negative. It should also be noted that the amplitude of B_{PM1} is much lower than that of B_{PM0}, mainly because it depends on the first order air-gap permeance that is small compared to the zeroth order permeance as shown in Fig. 2.6. Since the third back-EMF term is a product of the small valued B_{PM1} and the ratio $\frac{p_r}{p_r+Q_s} < 1$, its effect is generally negligible, and it can be disregarded in the analysis. In contrast, the product of B_{PM1} and the rotor-to-stator pole-ratio highly boosts the back-EMF's second term and makes it more significant relative to the first one. With the pole-pairs' and stator-slots' numbers chosen according to $p_r - Q_s = -p_s$, the first two EMF components in Eqn. 2.23 add up together contributing to larger voltage production compared to the regular synchronous PM machine. As a result, the PMV

machine's induced back-EMF magnitude consist of the two major terms that are usually referred to as the conventional and additional components, described in Eqn. 2.24.

$$E_{ph_{rms}} \cong \frac{K_{w1} N_{ph} D_g l_{stk}}{\sqrt{2}} \omega_r \left[F_{PM1} \times \left(\Lambda_0 + \frac{\mathrm{p}_r}{\mathrm{p}_s} \frac{\Lambda_1}{2} - \frac{\mathrm{p}_r}{\mathrm{p}_r + \mathrm{Q}_s} \frac{\Lambda_1}{2} \right) \right]$$

$$\cong \frac{2\sqrt{2} B_r}{\pi \mu_r} K_{w1} N_{ph} D_g l_{stk} \omega_r \left[\overbrace{\frac{h_m}{g'} \left[1 - 1.6\beta \frac{\tau_{so}}{\tau_s} \right]}^{\mathrm{K_{conv}}} + \overbrace{\frac{h_m}{g'} \frac{\beta}{\pi} \left[\frac{0.78125}{0.78125 - 2\left(\frac{\tau_{so}}{\tau_s}\right)^2} \right] \sin\left(1.6\pi \frac{\tau_{so}}{\tau_s}\right) \left[\frac{\mathrm{p}_r}{\mathrm{p}_s} - \frac{\mathrm{p}_r}{\mathrm{p}_r + \mathrm{Q}_s} \right]}^{\mathrm{K_{add}}} \right] \tag{2.24}$$

A further inspection of Eqn. 2.24 reveals that K_{conv} and K_{add} are the two terms playing key roles in PMV's operation, and they can greatly be affected by the variables D_g, l_{stk}, h_m and $c_o = \frac{\tau_{so}}{\tau_s}$ as also evident from Eqns. 2.9 and 2.10. The characteristics of K_{conv} and K_{add} with various values of PM thickness and slot opening ratio are respectively provided in Figs. 2.15 and 2.16 for a small PMV machine with a fixed diameter of 100 mm, 40 mm active stack length, 10 rotor PM pole-pairs, 12 stator slots and 0.8 mm physical air-gap length. In Fig. 2.15, K_{conv} is improved with an increase in PM thickness for each specific $(\frac{\tau_{so}}{\tau_s})$, whereas it gets reduced with an increase in slot opening ratio. This tendency can be explained from Fig. 2.6(a) and Eqn. 2.9 where the negative term of Λ_0 indicates an increase of effective air-gap length when the slot opening ratio increases. But, the effect of increasing h_m has more impact on increasing F_{PM1} than decreasing Λ_0, which ultimately leads to improved K_{conv}.

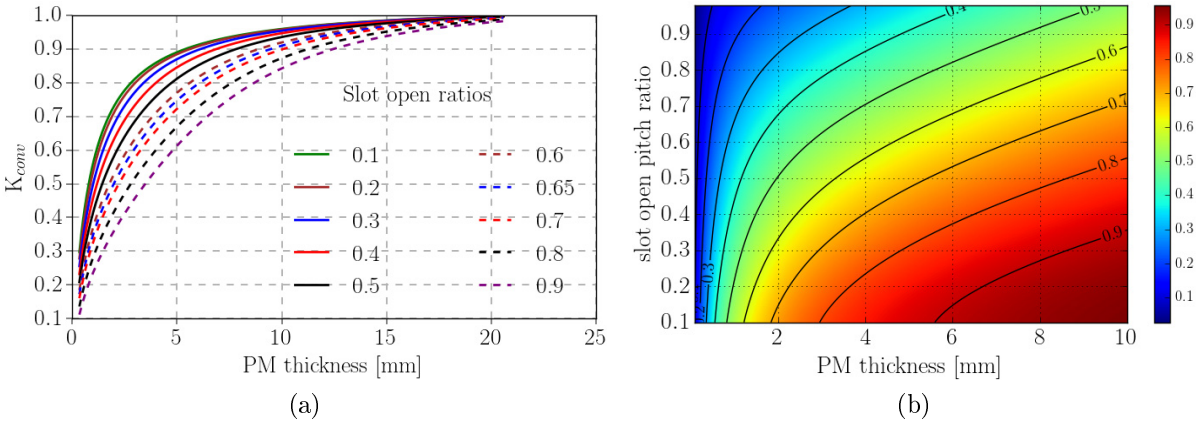

(a) (b)

Figure 2.15: Variation of K_{conv} with PM thickness and slot opening ratio: (a) K_{conv} at discrete $\frac{\tau_{so}}{\tau_s}$ as a function of h_m (b) heat map of K_{conv} against $\frac{\tau_{so}}{\tau_s}$ and h_m.

On one side, Fig. 2.16 shows a completely different tendency of K_{add} in comparison to that of K_{conv}. At first, K_{add} rapidly increases with an increment of PM thickness and reaches its peak point at a specific h_m value, after which it keeps on becoming smaller with larger PM thickness. Moreover, the similar increasing and decreasing tendencies of K_{add} are also observed with respect to increasing slot opening ratio. At this point, it should be remembered that K_{add} is a function of the first order permeance harmonic Λ_1 which is inversely proportional to PM thickness according to Eqn. 2.9, and also shows an upward and downward trend with respect to increasing slot opening ratio as illustrated in Fig. 2.6(b). That is, in a similar manner to Λ_1 in Fig. 2.6(b), which reaches its apex value at $c_o = 0.625$, K_{add} levels off with an increasing effective air-gap length (g') to achieve its best values at $\frac{\tau_{so}}{\tau_s} = 0.5\text{-}0.7$.

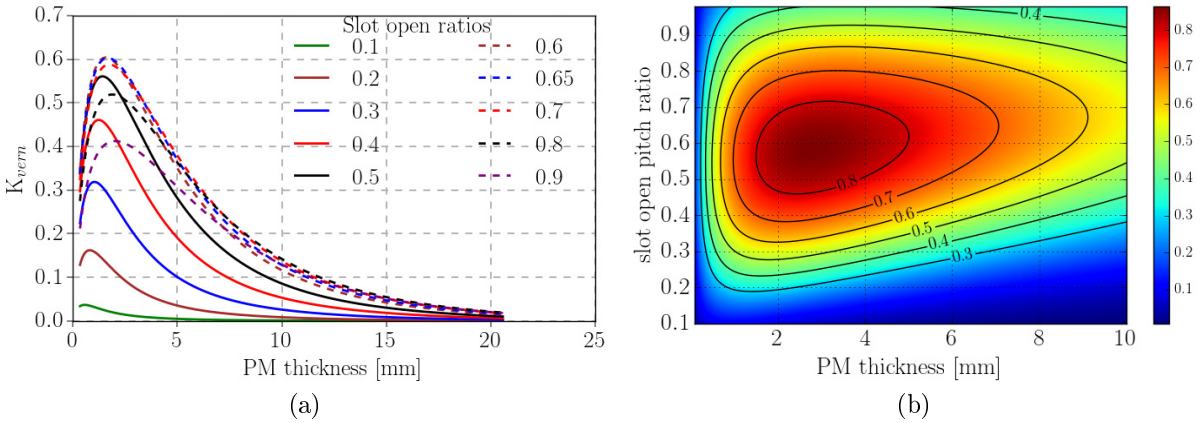

(a) (b)

Figure 2.16: Variation of K_{add} with PM thickness and slot opening ratio: (a) K_{add} at discrete $\frac{\tau_{so}}{\tau_s}$ as a function of h_m (b) heat map of K_{add} against $\frac{\tau_{so}}{\tau_s}$ and h_m.

Consequently, the sum of K_{conv} and K_{add} gives K_{vern} term which reflects the combination characteristics of its constituents terms, shown by Fig. 2.17. Furthermore, it can be clearly seen that K_{vern} also reaches its maximum value at a specific h_m, but saturates at a slightly lower value with further increasing h_m. In other words, K_{vern} mainly resembles K_{add} at lower PM thicknesses while it acts like K_{conv} at relatively larger h_m values.

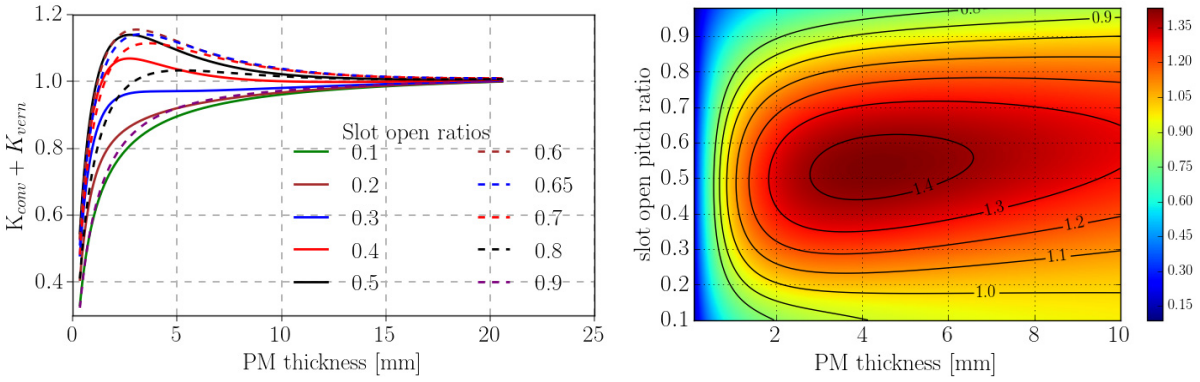

(a) (b)

Figure 2.17: Variation of K_{conv} plus K_{add} with PM thickness and slot opening ratio: (a) K_{conv} plus K_{add} at discrete $\frac{\tau_{so}}{\tau_s}$ as a function of h_m (b) heat map of K_{conv} plus K_{add} against $\frac{\tau_{so}}{\tau_s}$ and h_m.

This is due to the fact that as the PMs gets thicker, the effect of fundamental permeance gets reduced because of larger effective air-gap length, and the zeroth permeance remains as the only major component, leading to K_{vern} getting closer to K_{conv}. That is, too big effective air-gap renders a weakened modulation effect of the air-gap flux density. This suggests that the optimal PM thickness of PMV machines will likely be smaller than that required by the conventional synchronous PM machines for the same output performance, hence it has the potential for a comparatively lower PM material usage.

In any electrical machine, the air-gap electromagnetic torque relates to the stator winding currents and the back-EMF. With the induced back EMF known from Eqn. 2.23, and assuming that the machine is running at steady-state speed with pure sinusoidal currents,

the air-gap electromagnetic torque for a three-phase PMV machine is then formulated as shown below:

$$\begin{aligned} T_g &= \frac{3I_{ph}E_{ph}}{\omega_r} = 3I_{ph}\frac{2\sqrt{2}B_r}{\pi\mu_r}K_{w1}N_{ph}D_g l_{stk}\left(K_{conv}+K_{add}\right) \\ &= \frac{\sqrt{2}B_r}{\mu_r}K_{w1}K_s D_g^2 l_{stk}\left(K_{conv}+K_{add}\right) \\ \text{with} \quad K_s &= \frac{6N_{ph}I_{ph}}{\pi D_g} \end{aligned} \tag{2.25}$$

where K_s and A_s are the linear current density in $[\frac{kA}{m}]$ and active conductor area in a slot, respectively. The back-EMF waveform has a significant influence on the torque performance, hence the same arguments discussed in the preceding paragraphs for E_{ph} are still valid in this case. Therefore, with the two torque components reflected in Eqn. 2.25, the PMV machine has a good potential for higher torque density than the conventional synchronous PM machines at optimal PM thickness.

Neglecting the end-winding resistance and leakage reactance, the power factor (PF) is evaluated as a function of synchronous inductance and PM flux linkage as expressed in Eqns. 2.26 and 2.27. It can be clearly seen from this equation that a G_r factor also appears to proportionately increase the reactance, which adversely affects the power factor. Considering the case whereby the same stator configuration is being used for a conventional synchronous machines, this is a different scenario since the G_r factor is absent in the synchronous reactance of conventional PMSM, resulting into the realization of higher power factor. Then PF of the PMV machine can be calculated by applying the trigonometric functions. Therefore, a poor power factor is a consequence of relatively increased operating frequency and synchronous reactance of the PMV machine.

$$\begin{aligned} L_{gs} &= \frac{\pi\mu_o N_{ph}^2 l_{stk} D_g}{4p_s^2 g}K_{w1} \\ X_{sg} &= \omega_r p_r L_{gs} = \frac{p_r}{p_s}\frac{\pi\mu_o N_{ph}^2 l_{stk} D_g}{4pg}K_{w1} \end{aligned} \tag{2.26}$$

$$\begin{aligned} \text{PF} = cos(\varphi_v) &= \frac{E_{ph}+R_{ph}I_{ph}}{\sqrt{(\omega_r p_r L_{gs})^2+(E_{ph}+R_{ph}I_{ph})^2}} \\ &= \frac{1}{\sqrt{1+\left(\frac{\omega_r p_r L_{gs}}{E_{ph}+R_{ph}I_{ph}}\right)^2}} \end{aligned} \tag{2.27}$$

2.5 Basic Stator Configurations of Single Air-gap PMV Machines

In single air-gap PMV machines, various PM rotor structures such as surface-mounted, inset, interior and Halbach arrays can all be used. The stator configuration or rather the type of employed winding arrangement leads to several PMV machine types. Based on

this idea, the three most common PMV machines are shown in Fig. 2.18 and named as follows:

1. Conventional overlap winding PMV machine (OW-PMV).
2. Split-tooth concentrated winding PMV machine (Split-tooth PMV).
3. Two-slot pole-pitch winding PMV machine (Two-slot PMV).

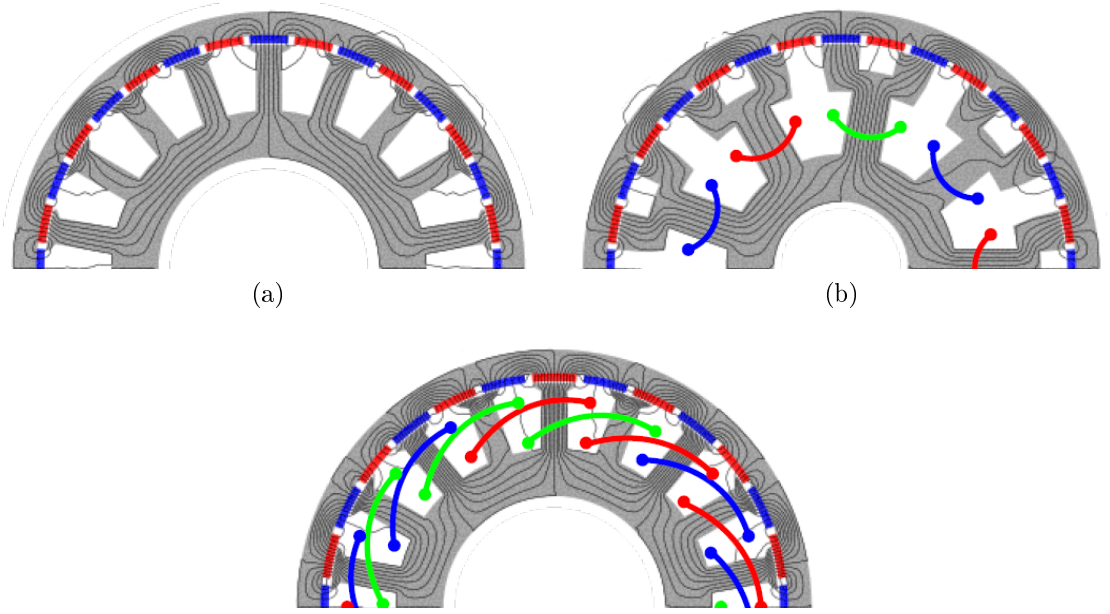

Figure 2.18: Common stator configurations showing winding arrangements and open circuit flux lines: (a) OW-PMV, Q_s =p_{fm}=18, p_s=2, p_r=16, (b) split-tooth PMV, Q_s=9, p_{fm}=18, p_s=2, p_r=16 and (c) two-slot PMV, Q_s =p_{fm}=18, p_s=4, p_r=14.

AC rotating machines' stator windings are generally designed with the aim of generating air-gap MMF distribution having predominant sinusoidal fundamental component while the higher-order space harmonics are minimized. This is even more important in PMV machines because the fundamental harmonic is further modulated into several other harmonics including the desired working component. The winding MMF distribution was defined in Eqn. 2.19 from which it can be realized that all the triplen harmonics are non-existent in a star connected three-phase armature windings. These harmonics have magnitudes that are inversely proportional to their order and they travel at different rotational speeds around the air-gap.

Conventionally, all the harmonics rotating in the same direction as that of the fundamental harmonic are said to be rotating in positive-direction (forward), hence their speeds (including that of the fundamental) are assigned positive sign. On the contrary, the series of harmonics going in opposite direction to the fundamental are said to be in negative-direction (backward) and their speeds will take the negative sign. For a three-phase machine, the rotational direction alternates between the harmonics, and it can be determined from the harmonic order as follows:

$$\begin{aligned} &\text{Positive:} && n = 6k+1 && k = 0,1,2,3,... \\ &\text{Negative:} && n = 6k-1 && k = 1,2,3,... \end{aligned} \tag{2.28}$$

The coil MMF harmonic orders corresponding to the first-order slot-harmonics generally occurs at $n = \frac{Q_s}{p_s} \pm 1$, and all other harmonics with higher orders than this are usually less significant. Moreover, in a similar analogy to Eqn. 2.28, for this slot-harmonic pair, the higher order rotates in the same direction as the fundamental component, while the lower order rotates in the opposite.

In Eqns. 2.19, 2.23 and 2.25, a winding factor (K_{wn}) appears to be one of the notable factors that affects the induced EMF and air-gap torque. This means the type of stator winding arrangement also needs careful consideration in regard to the expected voltage and torque qualities.

But before proceeding into the winding factor calculation methods, a number of parameters has to be defined so they can help with the analysis method. To start with, any electrically balanced rotating machine can always be reduced to its smallest independent number of electrically equivalent poles and slot sections called base windings, denoted by t. If the number of such repeatable sections is greater than one, it means they can be connected in either series or parallel to form a full functional winding since their individual voltages and currents are similar in terms of magnitude and phase. The number of base sections/windings (t) is calculated by determining the greatest common divisor (gcd) of the slots number and pole-pairs.

$$\mathrm{t} = \gcd(\mathrm{p}_s, \mathrm{Q}_s) \tag{2.29}$$

As a result, the number of base slots and pole-pairs for a double-layer winding can be calculated as:

$$\begin{aligned} \mathrm{Q}_s^{'} &= \frac{\mathrm{Q}_s}{\mathrm{t}} \in N \qquad \text{and} \qquad \mathrm{p}_s^{'} = \frac{\mathrm{p}_s}{\mathrm{t}} \in N \\ N &= \text{integer} \end{aligned} \tag{2.30}$$

If the number of slots per phase in a base section is even, such windings are said to be of first grade, whereas if it is odd, then the winding is called second grade.

$$\begin{aligned} \frac{\mathrm{Q}_s^{'}}{\mathrm{m}} &= \in N_{even} \longrightarrow \text{first grade} \\ \frac{\mathrm{Q}_s^{'}}{\mathrm{m}} &= \in N_{odd} \longrightarrow \text{second grade} \\ \mathrm{m} &= \text{phase number} \end{aligned} \tag{2.31}$$

Depending on whether the number of slots per pole per phase (q) is an integer or a fraction, the windings can be defined as either integral or fractional slot, respectively.

$$\begin{aligned} \mathrm{q} &= \frac{\mathrm{Q}_s}{2\mathrm{p}_s\mathrm{m}} = \mathrm{k} + \frac{\mathrm{t}}{\mathrm{p}_s} \\ \mathrm{k} &= \text{integer} \end{aligned} \tag{2.32}$$

If q is larger than or equal to one, the winding is said to be overlapping, and it can further be classified into overlap-integral or overlap-fractional. If q is strictly more than one, several coil-ends per phase are assigned to two or more adjacent slots. This means they are now distributed and there is a slight phase shift between such group of coils even though they belong to one phase. In addition, the phase coils can be configured

to span either a full or a fraction of the pole-pitch by shifting their coil ends relative to their supposedly original slot positions. On the contrary, if q is less than one, the winding is always non-overlapping. Usually, tooth concentrated configurations are used in this type of winding, which gives a coil-span of one slot. For a symmetrical 3-phase integral slot windings, t is always equivalent to the number of pole-pairs (t=p_s), hence the base windings comprises only a single pole-pair (p_s'=1) and base slots $Q_s'=\frac{Q_s}{p_s}$. Accordingly, the lowest order of field harmonic created by an integral slot windings is the fundamental harmonic. On one hand, fractional slot windings generate more harmonics, and even have sub-harmonics with orders less than the fundamental if the machine periodicity (t) is less than p_s.

The winding distribution factor (k_d) is defined as the ratio between the geometrical and arithmetic sum of the phasors of one phase winding [147; 148].

$$\begin{aligned} k_d &= \frac{\sin\left(\frac{q_{ph}}{2}\frac{\alpha_{ph}}{2}\right)}{\frac{q_{ph}}{2}\sin\left(\frac{\alpha_{ph}}{2}\right)} && \text{if } q_{ph} \text{ even} \\ k_d &= \frac{\sin\left(q_{ph}\frac{\alpha_{ph}}{4}\right)}{\frac{q_{ph}}{2}\sin\left(\frac{\alpha_{ph}}{4}\right)} && \text{if } q_{ph} \text{ odd} \\ \text{where } \alpha_{ph} &= \frac{2\pi}{Q_s/t} \end{aligned} \tag{2.33}$$

The pitch factor is used to account for the number of slots spun by one coil throw in a phase. Since one coil needs a minimum of two slots for its forward and return current paths, the lowest value of the coil-span is 1, and can be achieved in tooth concentrated windings. Therefore, tooth concentrated windings have a pitch factor of 1 by default, while the distributed winding can achieve a maximum of 1 or less. The pitch factor (k_p) is approximated by [147; 148]:

$$\begin{aligned} k_p &= \sin\left(\frac{\frac{2\pi p_s y_q}{Q_s}}{2}\right) \\ y_q &= \text{round}\left(\frac{Q_s}{2p_s}\right) \end{aligned} \tag{2.34}$$

The winding factor is simply the product of the distribution and the pitch factor. The distribution of a group of coils belonging to one phase per pole along the stator periphery, and/or the use of short pitched coils are the two major factors affecting the value of the winding factor. One of the importance of the winding factor is the fact that the value of the machine's average electromagnetic torque is proportional to its fundamental component while the machine's torque quality depends on higher order components. Therefore, it is always desirable to have a fundamental winding factor component (K_{w1}) as close to one as possible in order to maximize the machine's induced voltage and average torque capabilities. On the other hand, the higher order harmonic components of the winding factor ($K_{wn}; n \geq 2$) are required to be at minimum to have a smooth running machine.

Apart from many other existing physical structure modifications, the winding short pitching is one technique that is normally employed to improve the voltage and torque qualities in the overlap winding PMV machines. However, this strategy is not always applicable to tooth concentrated winding PMV machines. Since tooth concentrated windings

are inherently rich in harmonics, Split-tooth PMV are also characterized by high voltage and torque ripples. A fairly clear approach to calculate the winding factors for this type of winding was provided by Skaar and Nilssen, and concluded that based on the value of q, a feasible region for reasonable winding factors would be $\left(\frac{1}{4} < \mathrm{q} < \frac{1}{2}\right)$. [149]. Furthermore, this study showed that in pole/slot combinations with $\mathrm{Q}_s{=}2\mathrm{p}_r{\pm}1$ and $\mathrm{Q}_s{=}2\mathrm{p}_r{\pm}2$, the radial flux machines utilizing this winding arrangement have balanced air-gap radial forces.

Based on this observation, the two-slot pole pitch windings were developed, and their implementation on PMV machines was demonstrated by several researchers including Wang *et al* among others [150]. This type of winding is obtained by just doubling the number of slots from the one slot-pitch winding conventional PM machines. The purpose of doubling the slot number with no change in initial armature poles is to create a bigger numerical difference between them, and this gives more design flexibility which can easily satisfy Eqn. 1.6. This then results in a new range of q values with no negative influence on winding factor, i.e. $\left(\frac{1}{2} < \mathrm{q} < 1\right)$, and other advantages from their original one slot-pitch are retained. Most of the single slot-pitch combinations always gives feasible two slot-pitch windings except those with the basic ratio $\frac{\mathrm{Q}_s}{2\mathrm{p}_s}{=}\frac{3}{2}$. Considering all the applicable conditions in developing this type of winding, the gear ratio of PMV machine utilizing it is defined by Eqn. 2.35. It can be clearly seen that the G_r is confined within a region of $(2 < \mathrm{G}_r < 5)$, and converges to 3 as the stator winding pole-pair number is increased, shown in Fig. 2.19.

$$\mathrm{G}_r = 3 \pm \frac{2}{\mathrm{p}_s} \qquad \text{and} \qquad \mathrm{G}_r = 3 \pm \frac{4}{\mathrm{p}_s} \qquad (2.35)$$
$$\text{with} \quad \mathrm{p}_s > 2$$

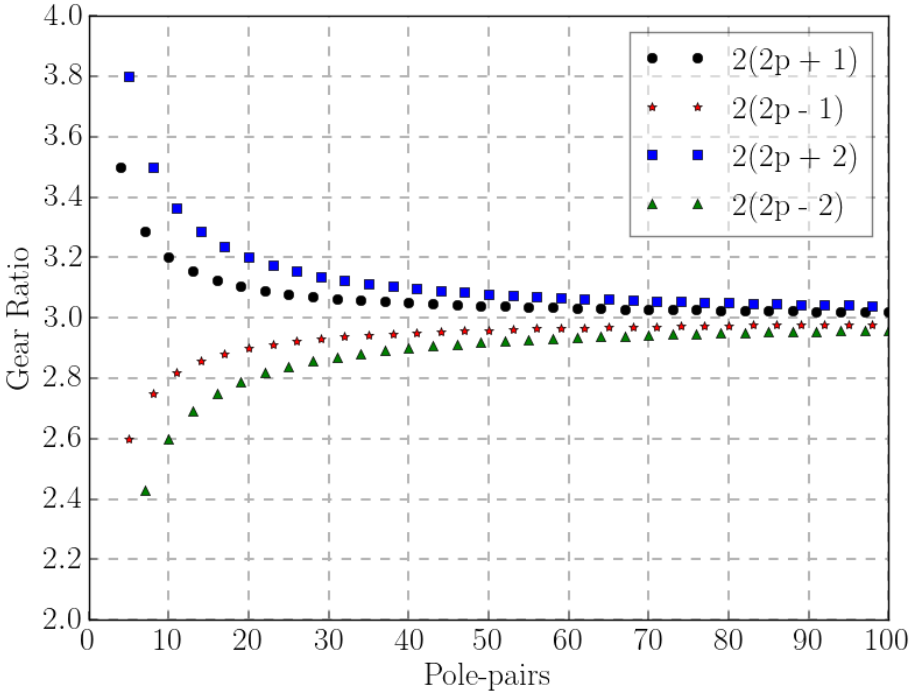

Figure 2.19: Gear ratios of two slot-pitch PMV machines

Chapter 3

Field-Circuit Model of PM Vernier Machines

The coupled field-circuit model of PM vernier machines is described in detail in this chapter, which is an essential tool for the design and performance analysis of this type of machines.

3.1 Equivalent Circuit Model

The output performance of the PMV machine is calculated with equations derived from the fundamental per phase equivalent circuit, shown in Fig. 3.1. As displayed on this generator mode circuit, e_m is the induced electromotive force (EMF), R_ϕ, U_ϕ and I_ϕ are the phase resistance, terminal voltage and phase current, respectively. In order to account for the core and magnet eddy-current losses, a shunt resistance R_{cm} is also included. Since the electromagnetic analysis is done in 2D-FEM, the synchronous inductance is split into L_m and L_e, which represents the main and end-winding inductances, respectively.

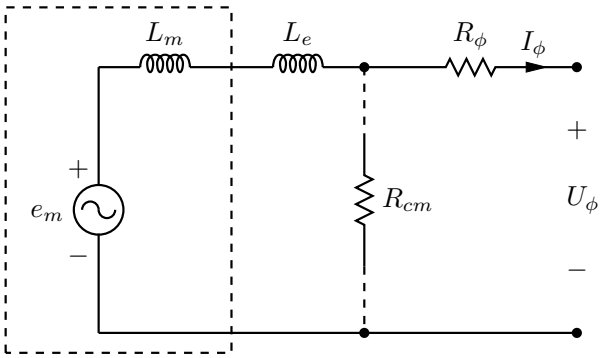

Figure 3.1: Per-phase equivalent circuit.

All the equivalent circuit parameters enclosed by the dashed lines in Fig. 3.1 are readily obtained from the 2D FE model. The analytical calculations of the remaining parameters is described in subsequent sub-sections.

Because the air-gap flux linkages are also deduced from the 2D FE model, the time-dependent stator induced EMF is computed by taking derivative with respect to time,

while the terminal voltage can be obtained from Kirchhoff's voltage law.

$$\begin{aligned} e_m &= \frac{d\lambda}{dt} \\ \Rightarrow U_\phi &= e_m - I_\phi \frac{d(L_m + L_e)}{dt} - I_\phi R_\phi \end{aligned} \tag{3.1}$$

To avoid the complications in doing the machine performance calculations in the time domain, the instantaneous 3-phase output quantities are projected onto the dq0-axis rotor reference frame through the use of dq0 transformation matrix defined as [151]:

$$\mathrm{K_{dq0}} = \frac{2}{3}\begin{bmatrix} \cos\theta & \cos\left(\theta - \frac{2\pi}{3}\right) & \cos\left(\theta + \frac{2\pi}{3}\right) \\ -\sin\theta & -\sin\left(\theta - \frac{2\pi}{3}\right) & -\sin\left(\theta + \frac{2\pi}{3}\right) \\ \frac{1}{2} & \frac{1}{2} & \frac{1}{2} \end{bmatrix} \tag{3.2}$$

In order to apply this transformation matrix, it is assumed that the machine is on steady-state operation, which will accordingly result in constant dq0 values. Further assumptions are that the machine may not be heavily saturated in its core regions and that it must have negligible harmonics with fair-enough sinusoidal EMF waveforms. The importance of these assumptions in regard to surface-mounted PM machines is that if the iron parts are not over-saturated, then there is no significant internal asymmetry in such regions, and this results in direct- and quadrature-axis inductances being approximately equivalent. In addition, for a 3-phase star (Y) connected armature windings at balanced conditions, there is no zero-sequence dq0 component, hence the dq0 and dq terms will be used interchangeably throughout the rest of this document.

To further simplify the application of dq-transformation matrix, one phase (for instance, phase-A) is normally used as a reference phase and its axis has to be magnetically aligned with the rotor positive d-axis. In this way, only the armature current angle has to be adjusted to get the required torque loading of the machine. For instance, when the current angle is 90 electrical degrees, it means the armature and rotor electromagnetic fields are totally out of phase with each other and that will result in maximum torque attainable by the machine. For surface-mounted PMV machine, in dq-reference frame, this would mean that the d-axis current magnitude is zero and the q-axis current is at its maximum.

The dq-axis steady-state equivalent circuits fixed to the rotor reference frame corresponding to the phase circuit in Fig. 3.1 are provided in Fig. 3.2. From these circuits, the steady-state dq-axis voltage equations can be expressed as:

$$\begin{aligned} V_d &= -\lambda_q \omega_r + L_e I_q \omega_r - I_d R_\phi \\ V_q &= \lambda_d \omega_r - L_e I_d \omega_r - I_q R_\phi \\ V_s &= \sqrt{\frac{V_d^2 + V_q^2}{2}} \end{aligned} \tag{3.3}$$

A combination of FEM solutions and analytical equations is used to calculate the dq-axis synchronous inductances given by:

$$\begin{aligned} L_d &= \frac{\lambda_d - \lambda_m}{-I_d} + L_e \\ L_q &= \frac{\lambda_q}{-I_q} + L_e \end{aligned} \tag{3.4}$$

During the maximum torque control of the machine, I_d is usually kept to zero and I_q set to maximum current value in order to obtain the best machine torque output. In this case, L_d is taken to be equivalent to L_q as the use of $I_d = 0$ would result in mathematically infinite L_d value. The dq-axis current components are also deduced from the circuit as follows:

$$\begin{aligned} I_{d1} &= I_d + \frac{E_d}{R_{cm}} \\ I_{q1} &= I_q + \frac{E_q}{R_{cm}} \\ I_{s1} &= \sqrt{\frac{I_{d1}^2 + I_{q1}^2}{2}} \end{aligned} \tag{3.5}$$

With the equivalent circuit and other associated parameters known, the air-gap electromagnetic power and developed average electromagnetic torque can also be computed from the general equations:

$$\begin{aligned} T_{EM} &= \frac{3}{2} G_r p_s \left(\lambda_d I_{q1} - \lambda_q I_{d1}\right) \\ P_{EM} &= T_{EM} \frac{2\pi}{60} n_s \end{aligned} \tag{3.6}$$

In the generator mode of operation, the difference between the electromagnetic power and mechanical power at the machine shaft is due to rotational losses and shunt field losses. On the other hand, the electromagnetic power differs from the output electric power at the machine terminals by the armature copper losses. That is, numerical addition of the developed air-gap power and the sum of rotational and shunt field losses will yield in the shaft mechanical input power, while subtraction of armature losses from it gives the generator output power. The output electrical power consists of useful active power and reactive power, both of which can be approximated from the phase circuits in Fig. 3.2:

$$\begin{aligned} \text{Active Power:} \quad & P_{out} = \frac{3}{2}(V_d I_d + V_q I_q) \\ \text{Reactive Power:} \quad & Q_{out} = \frac{3}{2}(V_d I_q - V_q I_d) \\ \text{Apparent Power:} \quad & S_{out} = \sqrt{\frac{P_{out}^2 + Q_{out}^2}{2}} \end{aligned} \tag{3.7}$$

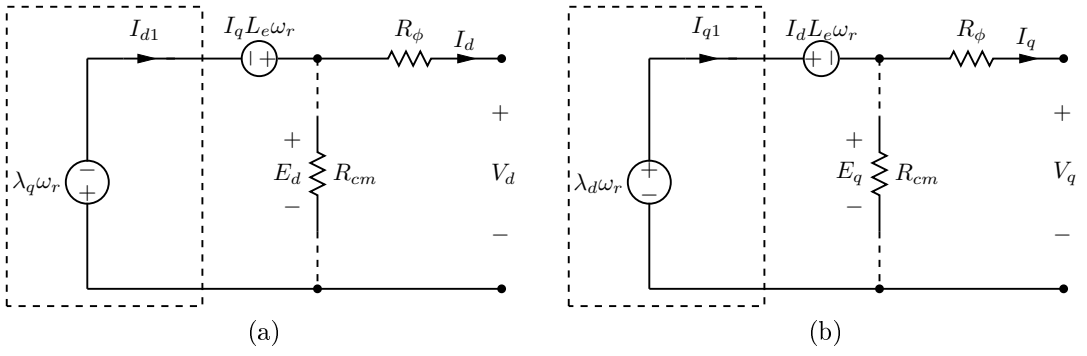

Figure 3.2: Rotor reference frame equivalent circuits (a) d-axis and (b) q-axis.

Subsequently, the power factor (PF), which is a function of phase angle difference between the output voltage and current, is given by the equation below:

$$\mathrm{PF} = \left| \left(\frac{P_{out}}{S_{out}} \right) \right| \tag{3.8}$$

The power flow model for a generator mode of operation described in the preceding paragraph is summarized below:

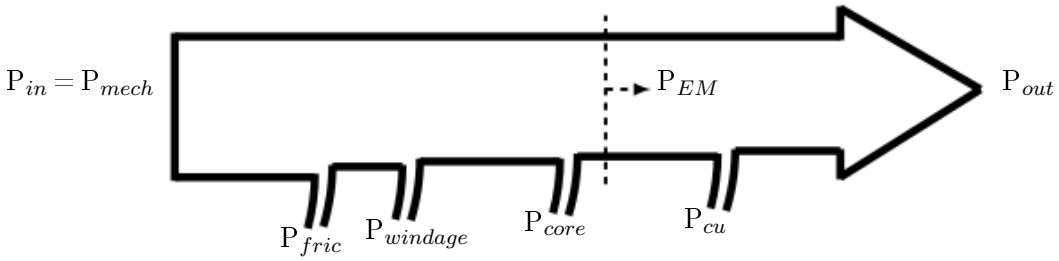

Figure 3.3: Generator mode power flow diagram.

During the design optimization stage, the windage and frictional losses which constitute to mechanical losses are ignored in order to simplify the problem. Also, the core losses as used in the above equation includes both the PM eddy current loss and total iron losses. Consequently, the efficiency only considers the frequency dependent core losses and copper losses.

$$P_{cu} = 3I_s^2 R_\phi \tag{3.9}$$

Finally, the efficiency (η) of the machine is simply:

$$\eta_{\%} = \frac{P_{out}}{P_{in}} \times 100 \tag{3.10}$$

3.1.1 Field circuit model parameters

Ignoring the conductor skin effect on the basis of the assumption that the used stator armature conductors have small diameters, the per phase temperature dependent armature resistance is calculated from the well-established equation:

$$\begin{aligned} R_{ph} &= \frac{2N_{ph}\rho_T(l_a + l_e)}{n_a \frac{A_{co}}{z}} \\ \text{with } A_{co} &= ff \times A_{slot} \end{aligned} \tag{3.11}$$

where l_a and l_e are the machine active stack and coil single-side end-winding lengths, respectively, n_a is number of parallel circuits and z is the number of conductors per slot. The active conductor area (A_{co}) is calculated from the available slot area (A_{slot}) and the slot fill-factor (ff). The realizable value of (ff) is usually in the range of 0.30 - 0.60 for round conductors. Better slot fill-factor values are easily achieved for larger machines whereas it gets to the low end for small machines especially those with over-lapping winding stators. The conductor material resistivity (ρ_T) at temperature T_c is obtained from the following equation:

$$\rho_T = \rho_{20} \{1 + Y_T(T_c - 20)\} \tag{3.12}$$

where Y_T and ρ_{20} are respectively the specific conductor material thermal coefficient and resistivity at 20°C. For the designs considered in this document, a 99.5 % IACS copper is used as the coil conductor material, with the properties: $\rho_{20} = 17\times10^{-9}\,\Omega$m and $Y_T = 0.0089\,\mathrm{K}^{-1}$. It is assumed that the coils will be operating at a temperature of $T_c = 80°$C.

The stator coil's end-winding length (l_e) depends on several parameters such as, the type of stator coil winding (overlapping or non-overlapping), number of stator coil layers (single or double), end-winding shape and the size of the stator diameter. Various equations have been proposed to approximate (l_e) as can be found in [142] and [147]. The equation employed here was adopted from [142] as it had a good accuracy compared to the practical dimensions from one previously built prototype with overlapping windings.

$$l_e = (0.083p_s + 1.217)\frac{p_s D_{out} - h_t}{2p_s} + 0.02 \quad [\mathrm{m}] \tag{3.13}$$

where D_{out} and h_t are the stator outer diameter and radial tooth height, respectively.

There exists several analytical methods for estimating the end-winding leakage inductance [152]. Based on the classical boundary value equations of a three dimensional end-coil, and on assumption that the coil is surrounded by iron boundaries on all its sides, Honsinger proposed a method for overlap distributed windings in [153]. Most of these equations presented in the literature have limited accuracies within their varying conditions. This further supports the idea that the 3D-FEM is presently still the best method, as pointed out in [152]. But, due to the fact that the preliminary designs are done in 2D-FEM in this study, an analytical equation was implemented to account for the end-winding leakage inductance [142].

$$L_{le} = \frac{2\mu_o N_{ph}^2 l_e}{pq} P_{le} \tag{3.14}$$

The specific end-winding leakage permeance P_{le} is given by Eqn. 3.15, valid for double-layer, low voltage, small and medium machines [142].

$$P_{le} \cong 0.34q(1 - \frac{2}{\pi}\frac{w_c}{l_e}) \tag{3.15}$$

where w_c is the coil pitch.

The field-circuit model employed in this study require the stator's three-phase currents as some of their inputs. In order to make sure that the machine is still within the recommended limits of its designed cooling methods during the operation, the current can be specified either in terms of the current-density (J) or calculated from the copper loss constraints. The latter method requires both the permitted rated copper loss (P_{cu}) limits and per-phase equivalent resistance be known in advance. Then, the rms current amplitude is computed from Eqn. 3.16.

$$I_s = \sqrt{\frac{P_{cu}}{3R_{ph}}} \tag{3.16}$$

For the former method, the standard current density value associated with a specific cooling technique is used, for instance, 3 - 5 A/mm^2 for natural air-cooling. The exact

rms amplitude of the current flowing in each series conductor is provided by the following equation :

$$I_s = J\frac{A_{slot} \times ff}{z} \tag{3.17}$$

The current space-phasor can be represented as illustrated in Fig. 3.4, and defined by:

$$\begin{aligned} \hat{I} &= \sqrt{2}I_s\angle\theta = I_d + jI_q \\ I_d &= I\cos\theta \quad \text{and} \quad I_q = I\sin\theta \end{aligned} \tag{3.18}$$

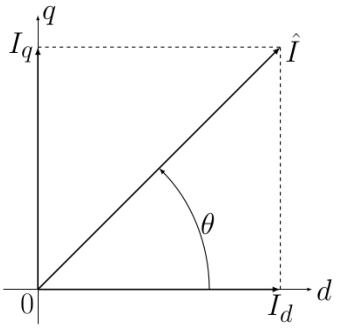

Figure 3.4: dq-axis currents' space phasor diagram.

For surface-mounted PM rotor machines, the current angle is usually set to $\theta = 90°$ electrical degrees when the machine is operating at its maximum torque and assumed to be on the constant torque region. These conditions result in $I_d = 0$ and $I_q = \hat{I}$, which also comes with further assumption that the load connected to the generator is balanced and purely resistive. Consequently, the machine's d- and q-axis inductance are almost equal as well. With the current magnitude and angle known, the instantaneous three-phase currents (i_{abc}) can be calculated from the (I_{dq}) by the use of inverse (K_{dq0}) transformation.

$$\begin{aligned} i_{abc} &= [K_{dq0}^{-1}][I_{dq}] \\ i_{abc}(t) &= \sqrt{2}I_s\cos(\omega_e t - \theta - i\frac{2\pi}{3}); \quad i = 0,1,2 \quad \text{for phase a,b,c respectively.} \end{aligned} \tag{3.19}$$

Therefore, the three-phase winding currents are set in the stator coil-windings in FEA program, with the rotor's positive direct axis perfectly aligned with the stator's chosen reference phase axis (normally phase 'A').

Core losses are a function of flux density magnitude, volume of iron material within a machine and mainly the rate of change of flux density. In addition, the considered component's material properties also plays a huge role on the resultant core losses. To slightly simplify the problem, the core regions material properties' dependency on temperature was neglected. Thus, at any given input speed, pole/slot combinations with a higher frequency are likely to have higher losses than others. Using the multi-step static FEA, the core losses are approximated by employing the Steinmetz based equation (Eqn. 3.20) [154; 155]. Since this model equation uses flux variation and magnitude deduced from several independent static solutions, it gives satisfactory accuracy albeit much faster compared to transient FEM simulations.

$$P_c = \frac{1}{T}\int_0^T C_{SE}\left|\frac{dB}{dt}\right|^{\alpha}|\Delta B|^{\beta-\alpha}\,dt \tag{3.20}$$

where T is the period, ΔB is the peak-to-peak flux densiy, C_{SE}, α and β are the lamination material loss model coefficients. On the other side, the FEM package used for transient simulations implements a core loss model that is different to the one presented above, although it is still based on Steinmetz principles as well.

$$P_c = K_h f^{\alpha} B^{\beta} + K_e (fB)^2 \tag{3.21}$$

the coefficients K_h, α, β and K_e are all material dependent and can therefore be obtained from manufacture's or supplier's data sheets. From this equation, the joule losses due to eddy currents in the rotor PMs are also catered for. The inclusion of the PM eddy current losses in PMV machine's loss analysis is necessary since they add a significant percentage to the total frequency dependent losses. This is because there is abundance of the air-gap field components which do not rotate in synchronism with the rotor, created by the modulation effect of the slots' permeance. Besides that, the armature winding MMF distribution also has a fast-rotating lower-order space harmonics than those of the PMs, which adds more to the PM eddy current losses since they act as sub-harmonics. With the core losses having been determined, the stator core resistance (R_{cm}) can be calculated from a rearranged version of ohm's law equation as:

$$R_{cm} = \frac{3{E_a}^2}{P_c} = \frac{3}{2}\frac{(-\lambda_q \times \omega_r)^2 + (\lambda_d \times \omega_r)^2}{P_c} \tag{3.22}$$

3.2 Finite Element Modeling

As discussed in section 3.1, a combination of FEM and classical machine equivalent electric circuit modeling is used to analyze a PMV machine. The two FEM packages employed to create this design environment are SEMFEM and MagNet version - 7.8. SEMFEM is an in-house developed FEM program that is faster and includes other features unavailable in MagNet, although it is limited to only static 2D FE simulations. But its capability is extended by creating simultaneous multi-step static simulation solutions in order to obtain some FE results that would otherwise need transient solvers. MagNet is an numerical analysis software from Mentor Graphics that can process magnetic or electromagnet fields solutions, and capable of dealing with both 2D and 3D FE static and transient simulations [156]. In a case where a considered pole/slot combination of a PMV machine has a periodicity, only a section of such a machine is modeled by employing periodic boundary conditions to reduce the solving time.

Modeling of an electric machine in FEM involves three stages listed below:

- Pre-processing
- Processing
- Post-processing

Pre-processing: This is the user-intensive part performed at the beginning of the FEM modelling process where the machine is divided into its respective regions such as the rotor, air-gap and stator according to the geometrical structure. In some instances, it also includes drawing of the machine's components for visual purposes. It entails the three major tasks being the component/region material definition, cross sectional area/volume mesh generation and problem definition. The proper setting of each components' material

properties is a very important step especially for materials with non-linear characteristics which implements the BH-curve fit. For the foregoing design, this is somehow simplified by the fact that most materials required for candidate machines were already available in the material library of the employed FEM packages. Besides that, both packages also allowed creation of a new material or modification of an existing material into customized properties by the user whenever the need arose.

On the other hand, in order to enhance the accuracy of the FEM solution, the finite elements' (mesh) size has to be adjusted to a proper level. This is because the mesh size does not only affect the degree of solution accuracy but also determine the simulation speed of the machine. That is, finer mesh gives more accurate results but also takes longer time to complete solving. Thus, the compromise between these two contradicting requirements was found by setting finer mesh in the air-gaps and other regions with expected large flux gradient, while larger mesh elements were defined where the flux is with less changes. For transient solvers, the choice of the time step also has an influence on the simulation results' accuracy especially on the field harmonics, cogging torque and torque ripples. In the same manner as the mesh size, bigger time step values finishes quicker with less accurate results while smaller time steps yields more accurate results but with longer solution time. One way to speed up the transient solvers in steady state operation is to simulate the machine only up to one-sixth of the total period since the electromagnetic performance characteristics starts to repeat after that.

To complete the model definition, correct boundary conditions were applied so that the simulation solution will be valid. In most cases, the PMV machine exhibits a magnetic/electrical periodicity of at least two (2), hence only a basic section of the machine was modeled with relevant periodic boundary conditions (even or odd) applied on the right and left sides of cross section of radial flux machine. In addition, an air-box was added on the inner-most and outer-most radii to represent an artificial outer boundaries with Dirichlet boundary conditions defined on its surfaces. Figure 3.5 shows some of the FEM model settings for this stage where a dense mesh can be observed around the air-gap regions and a more relaxed mesh on the stator slot regions.

Processing: The simultaneous solving of linear and/or non-linear partial differential equations on each individual mesh element is performed to find the magnetic vector potential variations. As it has been stated before, the speed and accuracy of this step mainly depends on the input data and settings done on the pre-processing step.

Post-processing: After the processing step is done, the extraction of the FEM solution results with more interest on quantities such as flux densities, flux linkages, torques and others, is carried out. This information is particularly used to calculate the machine performance characteristics.

The FEM modeling process and performance calculation are summarized in Fig. 3.6. Python script is used as the interface to interact with FE programs by sending pre-processing commands and extracting the solution results, as well as the data processing environment in the post-processing stage. The input and output data are stored in an external tab delimited text (.txt) file for later analysis and to make it accessible to any other programs outside the current platform, as will be shown in the optimization section.

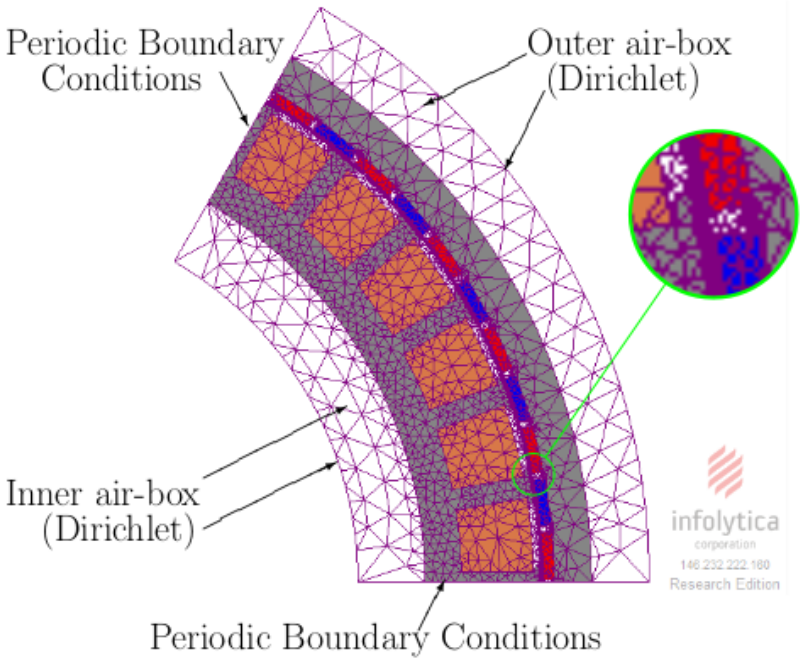

Figure 3.5: PMV machine cross section with mesh.

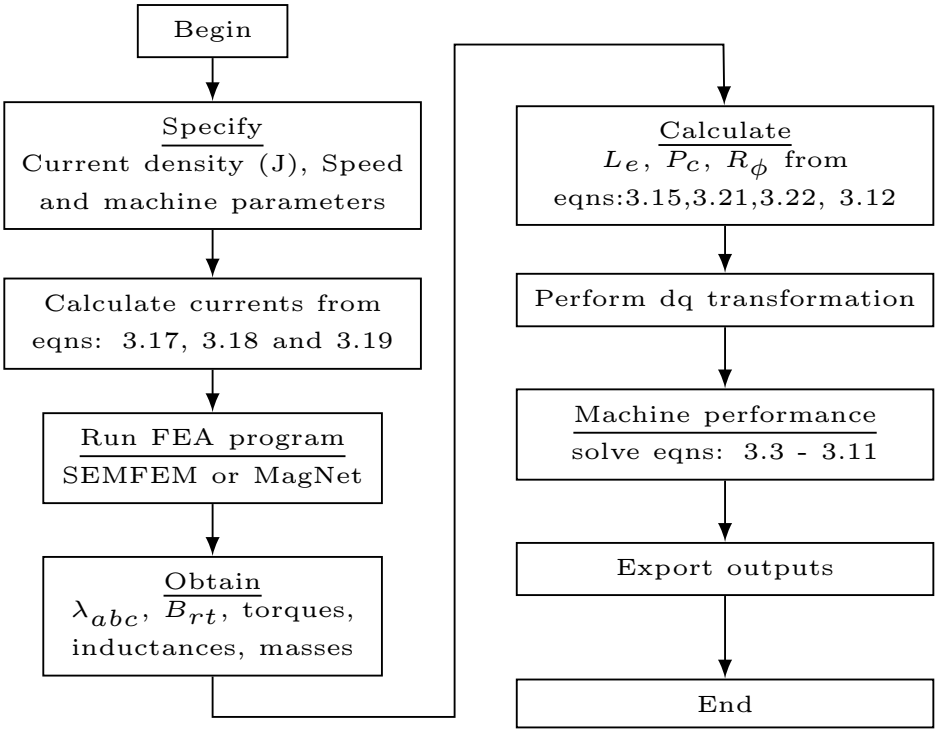

Figure 3.6: FEM flow diagram.

3.2.1 Calculation of flux linkages

In the two used FEM packages, the formulation of flux linkage calculations is derived from the fundamental concepts of magnetic field by using the Maxwell equations, which

are presented in their differential form below:

$$\text{Gauss' Law:} \quad \nabla \cdot \mathbf{D} = \rho \tag{3.23}$$

$$\text{Faraday's Law:} \quad \nabla \times \mathbf{E} = -\frac{\partial \mathbf{B}}{\partial t} \tag{3.24}$$

$$\text{Ampere's Law:} \quad \nabla \times \mathbf{H} = \mathbf{J} + \frac{\partial \mathbf{D}}{\partial t} \tag{3.25}$$

$$\text{Magnetic flux continuity:} \quad \nabla \cdot \mathbf{B} = 0 \tag{3.26}$$

with the symbols defined as:

$\mathbf{B}$ = Magnetic flux density
$\mathbf{D}$ = Electric flux density
$\mathbf{E}$ = Electric field strength
$\mathbf{H}$ = Magnetic field strength
$\mathbf{J}$ = Current density

Equation 3.26 denotes the fact that magnetic poles always exist in pairs, hence magnetic flux lines will also form closed curves. For the quasi-static magnetic field approximations, the displacement current part of Eqn. 3.25 is zero ($\frac{\partial \mathbf{D}}{\partial t} = 0$), and this reduces it to:

$$\nabla \times \mathbf{H} = \mathbf{J} \tag{3.27}$$

Considering the magnetic fields in the medium other than the permanent magnet material, the relationship between magnetic flux density and magnetic field intensity is given as:

$$\mathbf{B} = \mu_r \mu_0 \mathbf{H} = \mu \mathbf{H} \tag{3.28}$$

where $\mu_r = 1$ in free space.

Based on Eqn. 3.26, the solving of the Maxwell equations is begun by expressing the magnetic flux density in terms of another vector named magnetic vector potential ($\mathbf{A}$), through the following equation:

$$\mathbf{B} = \nabla \times \mathbf{A} \tag{3.29}$$

Now, substituting Eqn. 3.29 and the re-arranged form of Eqn. 3.28 into Eqn. 3.27, we get:

$$\frac{1}{\mu} \nabla \times \nabla \times \mathbf{A} = \mathbf{J} \tag{3.30}$$

which can be expanded into an easier form as:

$$\nabla(\nabla \cdot \mathbf{A}) - \nabla^2 \mathbf{A} = \mu \mathbf{J} \tag{3.31}$$

For further simplification of Eqn. 3.30, $\nabla \cdot \mathbf{A}$ is chosen to be zero, that is $\nabla \cdot \mathbf{A} = 0$, which result into a much shortened equation:

$$\nabla^2 \mathbf{A} = -\mu \mathbf{J} \tag{3.32}$$

In Cartesian coordinates system, $\nabla^2 \mathbf{A}$ is represented in matrix form as:

$$\nabla^2 \mathbf{A} = \begin{vmatrix} \mathbf{i} & \mathbf{j} & \mathbf{k} \\ \frac{\partial^2}{\partial x^2} & \frac{\partial^2}{\partial y^2} & \frac{\partial^2}{\partial z^2} \\ \mathbf{A}_x & \mathbf{A}_y & \mathbf{A}_z \end{vmatrix} = -\mu \mathbf{J} \tag{3.33}$$

$$\Rightarrow \left[\frac{\partial^2 \mathbf{A}_z}{\partial y^2} - \frac{\partial^2 \mathbf{A}_y}{\partial z^2}\right] \mathbf{i} - \left[\frac{\partial^2 \mathbf{A}_z}{\partial x^2} - \frac{\partial^2 \mathbf{A}_x}{\partial z^2}\right] \mathbf{j} + \left[\frac{\partial^2 \mathbf{A}_y}{\partial x^2} - \frac{\partial^2 \mathbf{A}_x}{\partial y^2}\right] \mathbf{k} = -\mu \mathbf{J} \tag{3.34}$$

In the two dimensional analysis defined in the XY-plane, both the current and magnetic vector potential are only in the z-direction ($\mathbf{J}_x$=$\mathbf{J}_y$=0 & $\mathbf{A}_x$=$\mathbf{A}_y$=0), meaning only the derivatives with the z-component remains valid while all other derivatives vanishes. This gives a much shortened form of Eqn. 3.34:

$$\left[\frac{\partial^2 \mathbf{A}_z}{\partial y^2} - \frac{\partial^2 \mathbf{A}_z}{\partial x^2}\right] = -\mu \mathbf{J}_z \tag{3.35}$$

Therefore, the equation to be solved in 2D-FE analysis can be represented as:

$$\nabla^2 \mathbf{A}_z = -\mu \mathbf{J}_z \tag{3.36}$$

Again, in the 2D finite element analysis, a model to be solved is discretized into small areas called elements, which altogether form a mesh spread throughout the model's total surface area. The approximation of magnetic vector potential in each of the elements is expressed as:

$$\mathbf{A}_z(x,y) = \sum_{j=1}^{n} \alpha_j(x,y) \mathrm{A}_j^e \tag{3.37}$$

where n is the number of individual element's nodes, $\alpha_j(x,y)$ is the specific element's shape function and A_j^e is the unknown potential value of each node per element. In SEMFEM, the first order elements having three nodes and a triangular shape are used in the approximation of vector potential. Consequently, this gives:

$$\mathbf{A}_z(x,y) = \sum_{j=1}^{3} \alpha_j(x,y) \mathrm{A}_j^e \tag{3.38}$$

On the other side, MagNet provides options for both first and higher order elements. In the case of higher order elements, hierarchic shape functions are used and the finite element approximation becomes:

$$\mathbf{A}_z(x,y) = \sum_{j=1}^{3} \alpha_j(x,y) \mathrm{A}_j^e + \sum_{j=1}^{n-3} \alpha_j^h(x,y) \mathrm{A}_j^h \tag{3.39}$$

with α_j^h and A_j^h being the additional hierarchic shape functions and the node-less parameters coupled to a considered element, respectively.

Iterative methods such as Newton-Raphson method are used to solve for the unknown magnetic vector potential ($\mathbf{A}$) and eventually the magnetic flux density ($\mathbf{B}$). The magnetic flux (φ) is then obtained by the integration of the flux density over a surface area of interest.

$$\varphi = \int_S \mathbf{B} \cdot ds \tag{3.40}$$

For a coil of N-turns, with each turn linking a flux and excluding the end-winding regions, the flux linkage is the sum of the flux for the total number of coils turns.

$$\lambda = \mathrm{N} \int_S \mathbf{B} \cdot ds \tag{3.41}$$

$$\Rightarrow \text{with N = number of coils turns} \tag{3.42}$$

3.2.2 Torque calculation

As previously described by Eqn. 3.6, the air-gap average electromagnetic torque is expressed as a function of the stator winding currents and the flux linkages. This approximation provides a fairly accurate result in static analysis. Alternatively, there are other torque calculation methods implemented in either transient or multiple-step static analysis that enable torque ripple or cogging torque calculation estimations. This is because in these cases, the rotation of one of the machine components tends to distort the elements in air-gap region. Hence the torque calculation techniques need to be able to account for the torque at each time-instant of component rotation. Two methods are available in SEMFEM that facilitates the movement of the finite element meshes applied in static time-stepped simulations [157]:

- Air-gap element (AGE) technique
- Moving-band (MB) solver

In the AGE method, Fourier series expansion is used to express the magnetic vector potential in Eqn. 3.37, from which the air-gap field is analytically solved within some boundary conditions. Maxwell stress tensor method is then employed to calculate the torque from the series representation as follows:

$$\mathrm{T} = \frac{\mathrm{L}}{\mu_0} \int_{\theta_1}^{\theta_2} r^2 \mathrm{B}_r \mathrm{B}_\theta d\theta \tag{3.43}$$

where L is the machine stack length.

The moving-band solver implements the Coulomb's virtual work method to calculate both the forces and torques on a moving body. It is a highly accurate method that utilizes the principle of virtual works by integrating the fields over virtually deformed elements situated between the stationary and moving parts. The integration over virtually distorted domain is usually asserted in terms of localized coordinates instead of global ones. For each static step, the torque expression used in this method is given by:

$$\mathrm{T} = \frac{\mathrm{L}}{\mu_0} \sum_{e=1}^{N_{mb}} \int_{\Omega_e} \left(-\mathbf{B}^{\mathbf{T}} \mathbf{G}^{\text{-}\mathbf{1}} \frac{\partial \mathbf{G}}{\partial \theta} + \frac{1}{2} \frac{\mathrm{B}^2}{|\mathbf{G}|} \frac{\partial \mathbf{G}}{\partial \theta} \right) \mathrm{d}\Omega \tag{3.44}$$

where $\mathbf{B} = (\mathrm{B}_x, \mathrm{B}_y)$, $\mathrm{B} = \|\mathrm{B}\|$, $\mathbf{G}$ is the Jacobian matrix of the global nodal coordinates with respect to local element coordinates, $|\mathbf{G}|$ is the determinant of $\mathbf{G}$, Ω_e is an individual element's area, and N_{mb} the number of moving band elements. Performance comparison between these two techniques as implemented in SEMFEM for magnetically geared PM machines was also done by Gerber and Wang [157]. The authors concluded that MB solver is relatively fast and accurate for obtaining the average torque, whereas the AGE is more suitable for cogging and ripple torques but at the expense of high computational cost.

On its part, MagNet uses a tunable Maxwell stress method to compute the forces and torques on the components of an analyzed model [158]. It defines two or more different components as a set of connected regions separated, and each completely enclosed by the virtual air material. The torque calculation formulation in this case is developed from the conventional Maxwell stress tensor method as demonstrated by McFee *et al* [159].

Chapter 4

Design Optimization of PMV Machines

In this chapter, the FEA based design optimization of permanent magnet vernier machine is described. In spite of the fact that they can be more time consuming than analytical methods, the 2D-FEA is used as a machine modeling tool during the design optimization stage as they are comparatively more accurate, which justifies their choice over the former. As discussed in the previous chapters, the PMV machine has an internal magnetic gearing effect. Hence, in addition to the normal steps followed in the design of a conventional PMSM, it is imperative to decide on the value of the gearing ratio that will render acceptable torque quality for a PMV machine, which will also be able to achieve high torque density concurrently. Consequently, a number of different machine candidates were investigated in order to select suitable pole/slot combinations, which will fairly satisfy the application requirements. Furthermore, the optimization procedure and employed algorithms are briefly explained in order to provide a good understanding of how the final machine dimensions were established. Lastly, the simulated performance of one selected optimum PMV machine is also presented and compared to that of an existing PMSM machine.

4.1 Employed Optimization Algorithms

There are different optimization techniques available, which in most instances, are grouped as *gradient-based* and *non-gradient based* algorithms. The latter group is generally praised of its high reliability to reach a global optima, though it can be time and memory expensive for a very large sets of optimization variables. Gradient-based algorithms are time efficient, but are likely to be trapped in local optima due to their direct dependence on the function gradient at each step. To ensure that a global optimum is obtained under these techniques, final results obtained from multiple optimization iterations with different starting points are expected to be within a fine margin. Considering that a large number of pole/slot combinations need to be investigated for different PMV machines, a gradient-based algorithm, namely, *Modified Method of Feasible Directions* (MMFD) was implemented at the initial stages of the optimizations [63].

Most gradient based optimization methods are usually designed to implement only one objective function at a time. That means if there is a need to simultaneously optimize more than one objectives, they have to be combined into a single function defined as a weighed sum of individual objectives. But this approach has a drawback in that some objectives may not be completely optimized as they mainly depend on the magnitude of the

weight coefficients assigned to them relative to others. Therefore, in the foregoing design, a single objective MMFD was used to conduct initial screening of candidate machines to be optimized. Once this was achieved, a multi-objective optimization whereby an objective function is defined as a vector of two or more performance indexes was performed on a few selected machines by utilizing the *Non-Dominated Sorting Genetic Algorithm-II* (NSGA-II). That is, all elements of vector objective function are simultaneously optimized to find a set of variables satisfying all the inequality or equality constraints imposed on the search space. This gives a cluster of solutions from which we can select the best optimized points called *pareto optimals*. A pareto front can then be obtained by plotting a set of pareto optimals in an objective space of two elements of vector objective function. It gives a boundary between the feasible and infeasible design options. For instance, a PMV machine optimized for two performance indexes, being total active mass and efficiency, under certain constraints not mentioned in this example, was found to have a solution space plotted in Fig. 4.1.

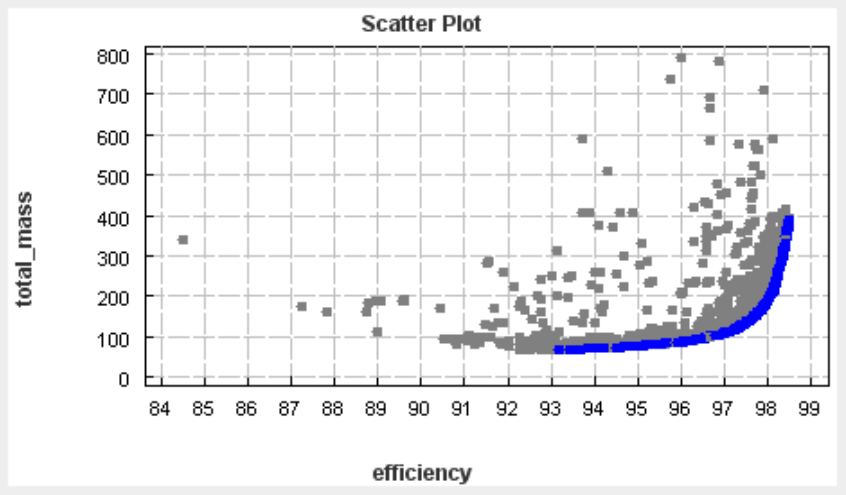

(a)

Figure 4.1: Pareto front example

All the points in this graph represent feasible designs, whereas the blue colored points form the pareto front. That is, there can be no other designs that will dominate those points that lie along the pareto front line. In addition, the same pareto front provides a clear picture of the design trade-offs between the two chosen performance indexes, revealing that improvement of one element comes at the deterioration of the other. Thus one good design point can be picked on the pareto front line according to the specific design requirements and further evaluations done on it.

4.1.1 Method of modified feasible directions

Basically, MMFD is a typical modification on the fundamental theory of the method of feasible directions, which has the advantages of conceptual simplicity, solution feasibility and computational efficiency [63]. It relies heavily on using the gradients of smooth objective functions and the constraints to iteratively improve the design to better state than previously. From the the beginning step, the MMFD optimization process requires a set of initial design variables, and the objective function is evaluated from them. It is time efficient if such an initial design is feasible, otherwise more time is needed in driving the

optimizer back to the feasible region. At each process iteration (k), the objective function and inequality constraints are evaluated on the current design variables. Then the crucial constraints at that step are identified. The objective function's and constraints' gradients are very helpful information for the determination of a search direction. If there are no active or violated constraints, the Fletcher-Reeves conjugate method (Eqn. 4.2) or the "direction of steepest descent" (Eqn. 4.1) defined by the negative gradient vector may be used to speed up the process. The latter is used at the initial stages of the process while the former is applied at any stage where the condition holds. But when the active constraints are met, the optimizer strives to find a search direction that improves the design while going in parallel to the constraint.

$$S^k = -\nabla F(X^{k-1}) \tag{4.1}$$

$$S^k = -\nabla F(X^{k-1}) + \beta S^{k-1}, \tag{4.2}$$

where β is a scalar used in direction finding process.

$$\beta = \frac{\left|\nabla F(X^{k-1})\right|^2}{\left|\nabla F(X^{k-2})\right|^2}$$

After the search direction is obtained, the constraints' gradients are used to estimate the reasonable value of the distance or step (α^*) to be moved in that determined direction. The design variables are then updated with the new values that lead in a direction towards the optimum while also being tangential to or moving away from the constraints. This optimization process represented by the flow diagram in Fig. 4.2, continues iteratively until the objective function is completely minimized/maximized, the maximum number of iterations is exceeded or there are no more feasible solutions.

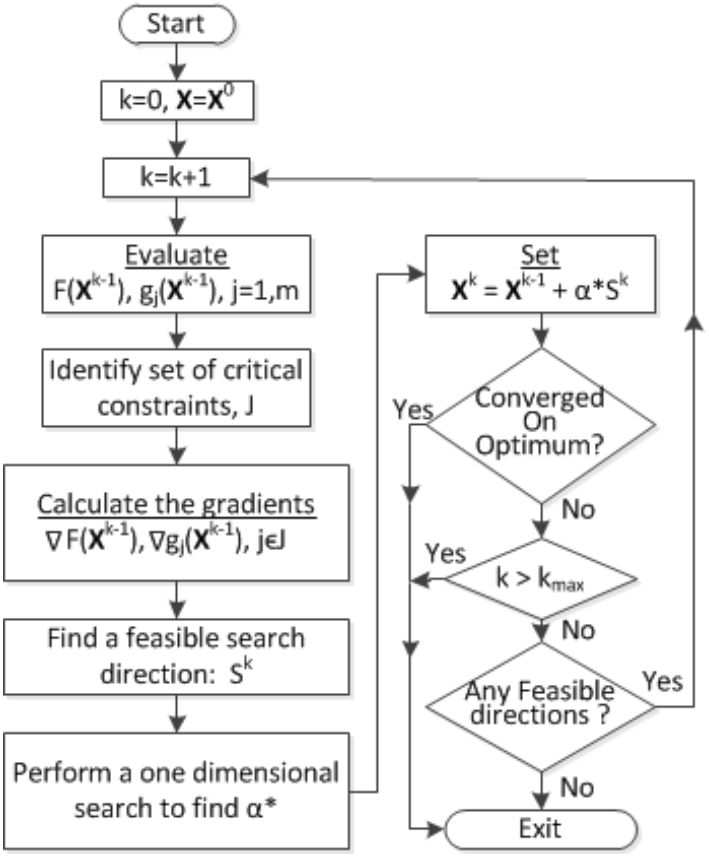

Figure 4.2: MMFD flow diagram [63].

4.1.2 Non-dominated sorting genetic algorithm II

The NSGA-II is a powerful multi-objective search evolutionary algorithm proposed by Deb *et al* [64; 65], that uses an elitism preserving approach and a fast sorting procedure to find solutions converging towards Pareto-optimal set. Actually, it can also be regarded as an intelligent advancement of a simple probabilistic genetic algorithms (GA) that utilizes a better selection operator to obtain diverse and uniformly spread solutions.

A general NSGA-II procedure begins by creating an offspring population (Q_t) of the same size as the parent population (P_t), and combining them to form a large pool of population (R_t) with twice the size of (P_t). Then the R_t population is classified by non-dominated sorting approach, where each individual member of R_t is ranked on the basis of its non-dominance relative to other members. The best non-dominated individuals belong to the first front of non-domination level, and the subsequent fronts are orderly

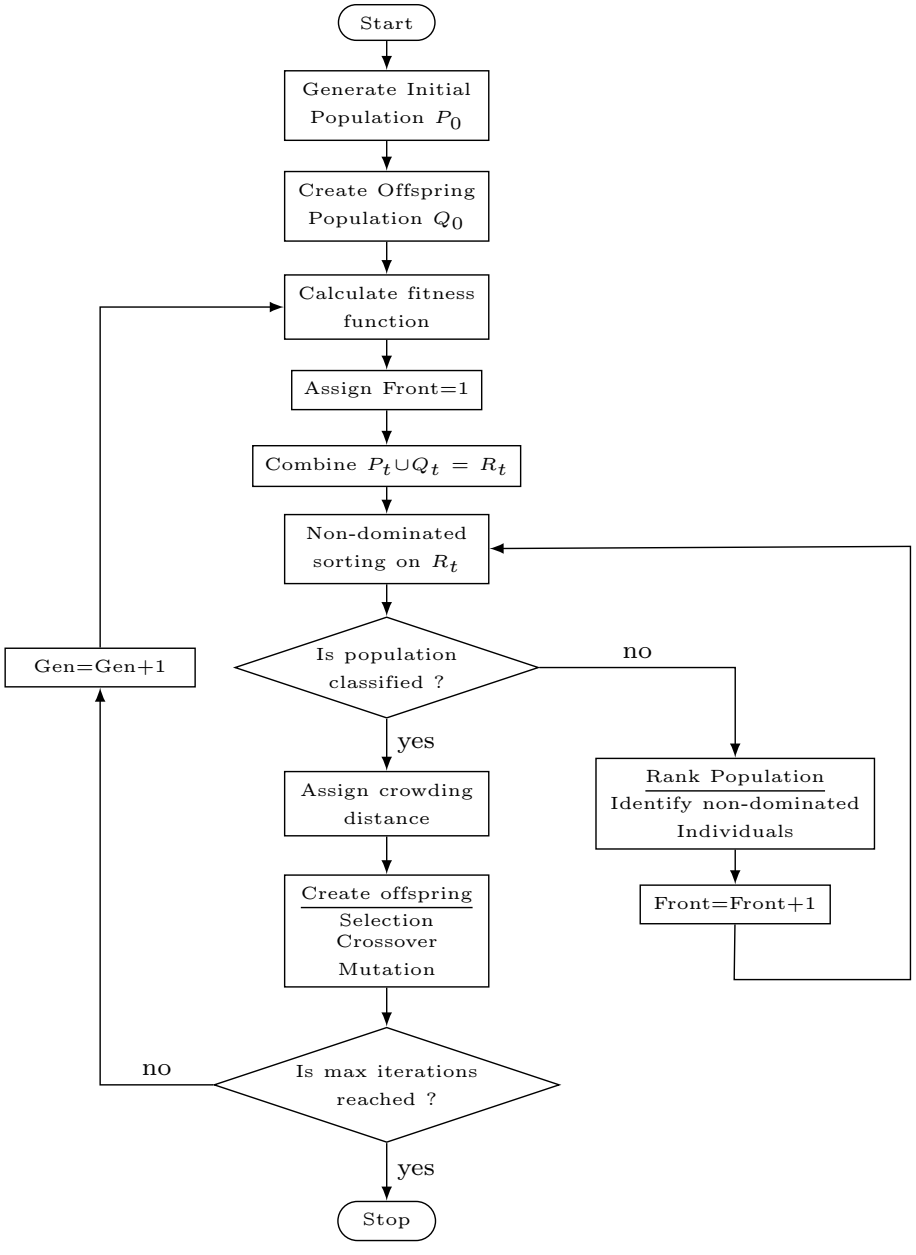

Figure 4.3: NSGA-II flow diagram [63–65].

filled with the solutions of the lower ranks. In most cases, the solutions in the first and second fronts are automatically selected into the new population set (P_{t+1}). Since the aim is to reproduce a new set P_{t+1} with equivalent size to that of P_t out of larger R_t set, not all the solutions in the lower ranked fronts will be included. If the maximum size of P_{t+1} is not yet reached, a more sophisticated selection is applied on the lower ranked fronts to take few and non-crowded solutions from them. The NSGA-II process is schematically summarized in Fig. 4.3.

4.2 PMV Machine Topologies Considered

Permanent magnet vernier machines can be realized into various structure configurations characterized by different performance merits. The surface-mounted rotor PM machines are probably the most common relative to other PM arrangements such as inset, interior, spoke and Halbach types, which may add more mechanical complexity in manufacturing. For PMV machines, design variations are largely brought by the design of three main components, being the rotor, flux-modulator and armature winding layout. The study in this dissertation focused only on the single-stator and single-rotor PMV machine types with radially magnetized surface-mounted PM outer rotor and without additional PMs mounted on the stator as shown in Fig. 4.4, namely:

- Conventional PMV machine (overlap-winding) (Fig. 4.4 a)
- Split-tooth PMV machine (tooth concentrated winding) (Fig. 4.4 b)
- Separate modulator PMV machine (tooth concentrated winding) (Fig. 4.4 c)

Since the machines are outer-rotor topologies and are to be operating at relatively low speeds, the centrifugal forces will not be an issue. The PMV machine design with

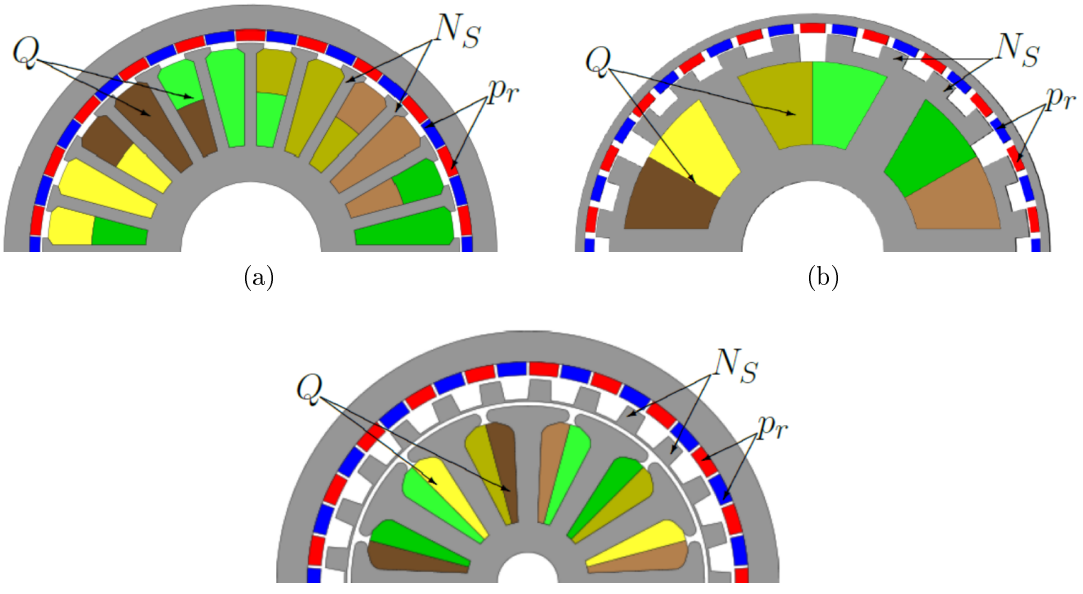

Figure 4.4: Considered PMV machine types: (a) conventional overlap-winding PMV (b) tooth concentrated winding, split tooth PMV (c) tooth concentrated winding, separate modulator PMV.

distributed overlapping stator winding (Fig. 4.4 a) is referred as the conventional type of PMV machine in this dissertation. Its stator teeth works both as main flux path and flux modulating pieces. Whilst the distributed windings enjoy certain advantageous properties such as less harmonics in EMFs and good winding factor etc., a major drawback is the long end-windings that may incur more copper losses. An alternative is to use tooth concentrated windings, although their rich harmonic content is also a problem (Figs. 4.4 b and 4.4 c). In Fig. 4.4 (c) the air-gap between the stator and modulating pieces in separate modulator PMV machine is magnified to only illustrate the fact that the two pieces are different components. In practical cases, there may be a tiny gap in that region due to the mechanical imperfections resulting from assembling of two laminated pieces, and that may add some additional magnetic reluctance. However, there are also exceptional arrangements where that air-gap length has to be kept big enough to allow free rotation between those components.

It should also be realized that while the number of stator slots or teeth (Q_s) is the same as the number of modulating pieces (N_s) in conventional overlap-winding PMV, this is a different case in the other PMV machine types. In tooth concentrated-winding machines, the number of modulator pieces is chosen with regard to Eqn. 1.5, as is the case with the number of stator teeth in overlap-winding machine. The designer further has to separately choose the number of stator slots, which in combination with the stator pole-pairs, will have the best possible winding factor, as outlined in other studies for this winding type [149; 160]. In addition, the number of stator slots must be a factor of the modulator pole-pieces in tooth-split PMV machine. However, this restriction can be removed by adopting the separate modulator tooth concentrated winding PMV structure, since the modulator and stator are two separate components.

All the investigated pole/slot combinations are provided in Tables 4.1 and 4.2 for overlap-winding and tooth concentrated (both split-tooth and separate-modulator) PMV machines, respectively. Considered machine designs were selected to have gearing ratios spanning from 5 up to 20 increasing in steps of 3, and the number of stator pole-pairs are 1, 2 and 3. This is to ascertain a wider range of gear ratios is uniformly covered with a reasonable number of pole/slot combinations.

Table 4.1: Investigated pole-slot combinations for overlap-winding PMV machines.

	Pole-ratio = 5			**Pole-ratio = 8**			**Pole-ratio = 11**			**Pole-ratio = 14**			**Pole-ratio = 17**			**Pole-ratio = 20**		
$\mathbf{p_s}$	**Q**	$\mathbf{p_r}$	**q**	**Q**	$\mathbf{p_r}$	**q**	**Q**	$\mathbf{p_r}$	**q**	**Q**	$\mathbf{p_r}$	**q**	**Q**	$\mathbf{p_r}$	**q**	**Q**	$\mathbf{p_r}$	**q**
1	6	5	1.0	9	8	1.5	12	11	2.0	15	14	2.5	18	17	3.0	21	20	3.5
2	12	10	1.0	18	16	1.5	24	22	2.0	30	28	2.5	36	34	3.0	42	40	3.5
3	18	15	1.0	27	24	1.5	36	33	2.0	45	42	2.5	54	51	3.0	63	60	3.5

Table 4.2: Investigated pole-slot combinations for tooth concentrated-winding PMVMs.

	Pole-ratio = 5				**Pole-ratio = 8**				**Pole-ratio = 11**				**Pole-ratio = 14**				**Pole-ratio = 17**				**Pole-ratio = 20**			
$\mathbf{p_s}$	**Q**	$\mathbf{N_s}$	$\mathbf{p_r}$	**q**	**Q**	$\mathbf{N_s}$	$\mathbf{p_r}$	**q**	**Q**	$\mathbf{N_s}$	$\mathbf{p_r}$	**q**	**Q**	$\mathbf{N_s}$	$\mathbf{p_r}$	**q**	**Q**	$\mathbf{N_s}$	$\mathbf{p_r}$	**q**	**Q**	$\mathbf{N_s}$	$\mathbf{p_r}$	**q**
1	3	6	5	0.5	3	9	8	0.5	6	12	11	1.0	3	15	14	0.5	9	18	17	1.5	3	21	20	0.5
2	6	12	10	0.5	9	18	16	0.75	12	24	22	1.0	15	30	28	1.25	6	36	34	0.5	21	42	40	1.75
3	9	18	15	0.5	9	27	24	0.5	18	36	33	1.0	9	45	42	0.5	27	54	51	1.5	9	63	60	0.5

In each machine type, the investigated models have the same maximum external dimensions' limits, with the difference between them being the slot-pole numbers and relevant stator configurations.

4.3 Optimization Procedure and Specifications

The numerical optimization of electrical machines may be seen as the recursive process, whereby a machine is repeatedly analyzed and evaluated for an output performance. The parameters of the machine are continuously adapted to achieve an improved objective function, and keeping it within some defined dimensional or characteristic constraints. This section describes the design specifications and design procedure for optimizing PMV machines. Two optimization algorithms are utilized, i.e., MMFD and NSGA-II. This is summarized by the flow diagram in Fig. 4.5. For every candidate machine to be optimized, the performance and geometrical constraints have to be known well in advance. Then the machine information such as rotor pole-pair number, winding data and materials used for every component have to be properly defined.

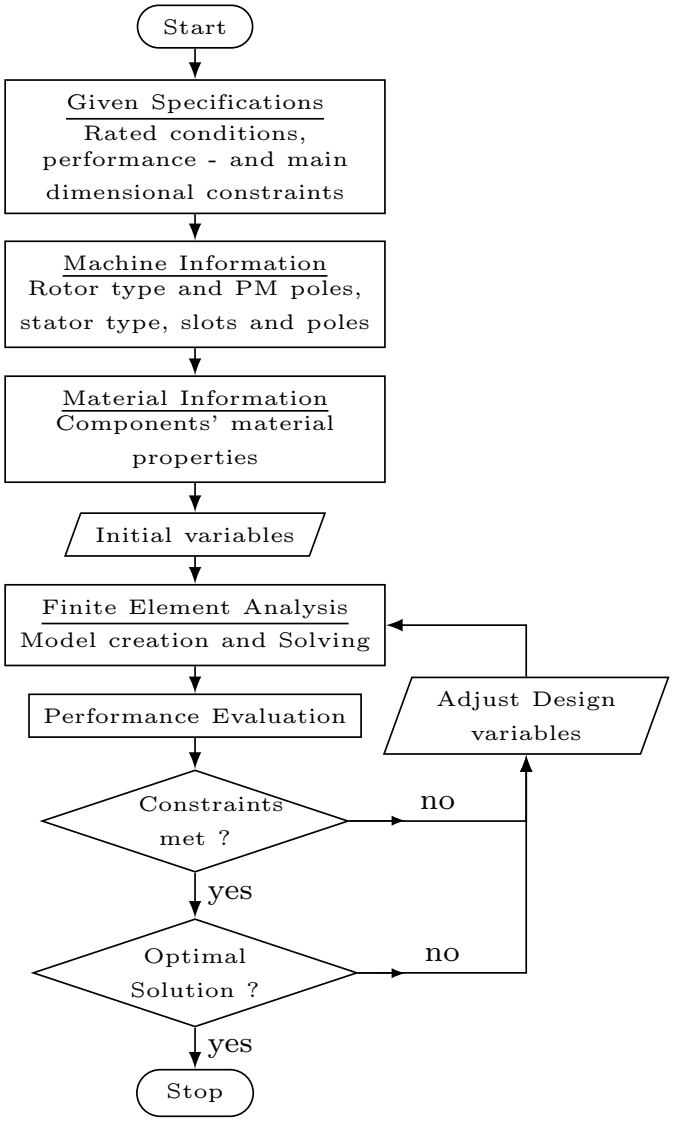

Figure 4.5: Summary of optimization procedure

4.3.1 Optimization procedure

The optimization of a PMV machine is a non-linear constrained problem that depends on many variables such geometrical parameters, components' material properties and target application specifications. In order to determine the optimum values of these parameters, an optimization problem has to be converted into a mathematical statement with an objective function that can be minimized or maximized within certain constraints. For the foregoing task, a dedicated optimization environment was realized for the design of PMV machines which consists of the following three packages:

- VisualDOC version - 7.2 from VR&D Inc.
- SEMFEM - In-house developed FEM program.
- MagNet version - 7.8 from Mentor (previously owned by Infolytica Corporation).

VisualDOC is an optimization suite from VR&D Inc. that provides and executes the selected optimization algorithm on the given problem. This is achieved by coupling it with the FEM analysis program through the external files that acts as interlink between them [63]. In this case, the two chosen algorithms are MMFD and NSGA-II as already explained in the preceding paragraphs. Figure 4.6 demonstrates how the three software tools were integrated together and used to create a design environment. During the optimization process, the machine analysis was performed with a 2D FE solver at a maximum load point of the rotor and armature current angle, and SEMFEM was chosen over MagNet for this purpose because of its relatively fast solving speed.

As illustrated on the figure, VisualDOC iteratively directs inputs to and retrieves outputs from SEMFEM while also evaluating their performance compliance to the defined constraints. As a final calibration step, a 3D-FE static solver in MagNet is used to verify static performance of every optimum solution from VisualDOC, and a 2D-FE transient

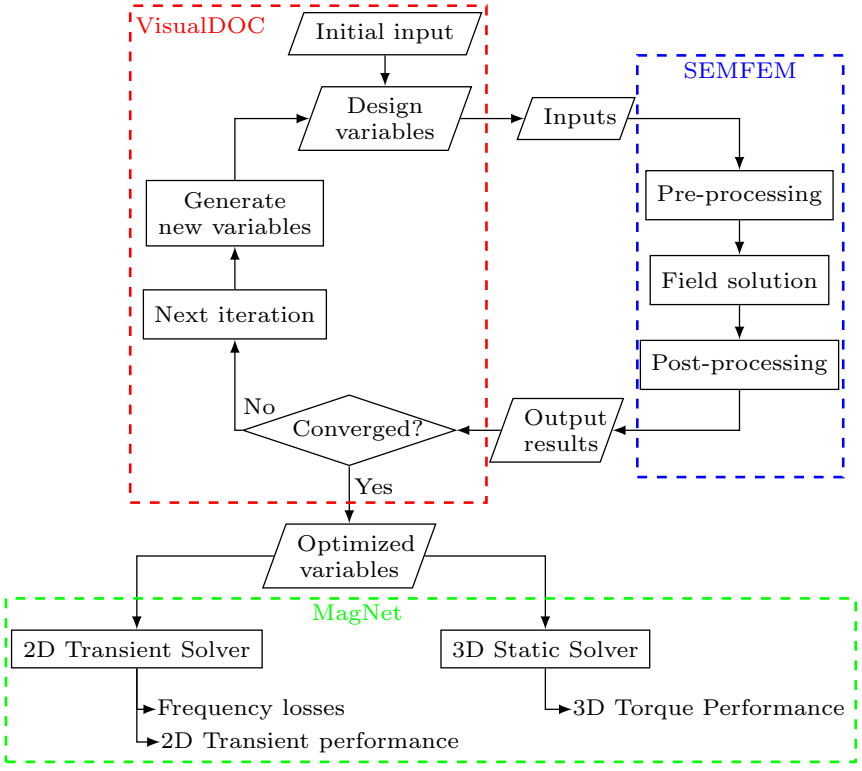

Figure 4.6: Optimization flow diagram.

simulation is further done to computing the core and PM losses and analyze the transient performance.

The aim of the overall optimization process was to attain the best geometrical dimensions that will result in the optimal values of the objective function. To account for various requirements in wind generator applications, the foregoing PMV machine design optimization objective has the following four indexes which are important design considerations for these applications.

- Total active material mass.
- Required PM mass.
- Volumetric size.
- Power factor.

The total electromagnetic active machine weight and PM masses are important as they are closely related to the machine's cost, especially the PM material since it is the most expensive material per unit mass. At this design stage, it would be a more complicated task to approximate the mass of the support structure, hence that is excluded on the calculation of total mass. On the other hand, both the machine's total mass and volume have an impact on its portability considering the fact that it has to be installed on the tower. For a PMV machine, it is of utmost interest to optimize the power factor to the best possible value while maintaining other constraints. This is because PMV machines generally have lower power factor than conventional PM synchronous machines.

Even though there are several parameters to be optimized, only one or utmost two objective indexes were selected to be executed at a time, for MMFD and NSGA-II respectively. The remaining ones would be treated as constraints together with specifications of the machine. These main parameters that define the objective search space for each considered machine are provided in Table 4.3. For the comparative purposes, a previously designed PMSM machine was used as the benchmark to be analyzed with the best designed PMV machine [161]. In order to do a fair comparison study on these two machines, the rated operating speed and output power were kept equal as 150 rpm and 15 kW, respectively.

Table 4.3: Main specifications for the optimized machines.

Parameter	Value
Output power (kW)	15
Air-gap length (mm)	1.5
Slot-fill factor	0.35 - 0.5
Operating speed (rpm)	150
Aspect ratio ($\frac{L}{D}$)	0.05 - 0.7

L = active stack length, D = total diameter.

The constrained optimization problem was formulated as follows:

$$\begin{aligned} \text{Minimize:} \quad & F(\mathbf{X}) = \mathbf{Y} \\ \text{Subject to:} \quad & \eta \geq 94\% \\ & J \leq 5\,\text{A/mm}^2 \\ & \text{PF} \geq 0.6 \end{aligned}$$

where $\mathbf{X}$ represents the vector of geometric variables in Figs. 4.7 and 4.8 with angle ratios defined in Eqn. 4.3, and $\mathbf{Y}$ is one or a set selected of objective functions. All the machines are intended to operate under the natural air-cooling conditions, consequently, the armature conductor current density (J) is limited to $5\,\mathrm{A/mm^2}$. It should also be noted that the temperature and material characteristics were kept constant throughout the optimization process. Due to the fact that some of the machines use overlapping windings, the stator slot-filling factor was also limited to 0.35 - 0.5, which is practically fair considering the challenges met in such winding type manufacturing while also ensuring that the conductor material is efficiently utilized. During the optimization process, core-losses, end-winding length, end-winding's inductance and resistances were calculated using analytical equations so that their effect can be included in the performance evaluation deduced from 2D FEA static solutions at post-processing. Thus, both the efficiency and power factor calculations have included the effect of end-windings.

$$\begin{aligned} \theta_{pm\_p} &= \frac{\pi}{p_r}; \quad \theta_{sp} = \frac{2\pi}{Q_s}; \quad \theta_{mp} = \frac{2\pi}{N_s}; \quad \sigma_{pm} = \frac{\theta_{pm\_s}}{\theta_{pm\_p}} \\ \sigma_s &= \frac{\theta_s}{\theta_{sp}}; \quad \sigma_{so} = \frac{\theta_{so}}{\theta_s}; \quad \sigma_{mo} = \frac{\theta_{mo}}{\theta_{mp}}; \quad \sigma_{mi} = \frac{\theta_{mi}}{\theta_{mp}} \end{aligned} \tag{4.3}$$

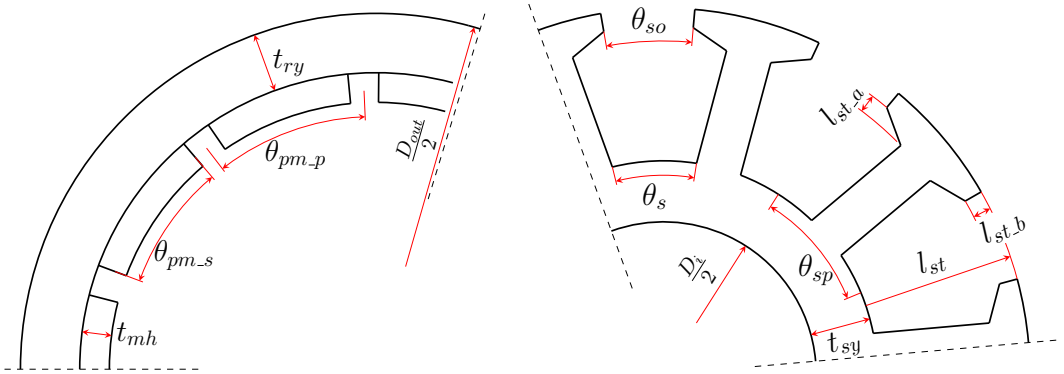

Figure 4.7: Geometric optimization variables: (a) rotor for all PMV machines (b) conventional overlap-winding PMV stator.

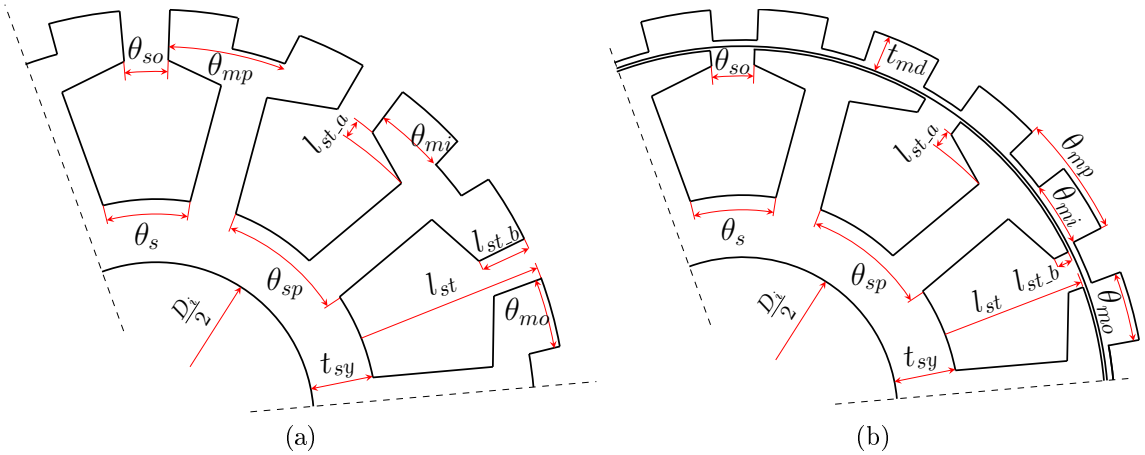

Figure 4.8: Geometric optimization variables: (a) tooth concentrated, split tooth PMV stator (b) tooth concentrated, separate modulator PMV stator.

A vector of geometric design variables shown by Figs. 4.7 and 4.8 are further explained in Table 4.4 together with their range limits; all length dimensions are in millimeters. As for the PMs, the upper limits on lengths and pole-arcs are set to reduce the leakage flux between adjacent PMs. On the other hand, the minimum lengths for any other component including the PMs is set to ensure their mechanical integrity so that they can be easily manufactured.

Table 4.4: List of geometric design variables and their ranges.

Description	var.	min	max	Units
Outer diameter	D_{out}	200	650	mm
Inner diameter	D_i	100	-	mm
Stack length	L_{tsk}	50	650	mm
Rotor yoke thickness	t_{ry}	5.0	-	mm
Rotor PM thickness	t_{mh}	1.5	-	mm
Modulator thickness	t_{md}	2.5	-	mm
Stator yoke thickness	t_{sy}	5.0	-	mm
Stator tooth thickness	t_{st}	2.0	-	mm
Stator tooth length	l_{st}	10.0	-	mm
Stator tooth base thickness	l_{st_b}	1.5	-	mm
Stator tooth additional thickness	l_{st_a}	1.5	-	mm
Modulator pole pitch ratio (outer)	σ_{mo}	0.30	0.90	-
Modulator pole pitch ratio (inner)	σ_{mi}	0.30	0.90	-
PM span to pole-pitch ratio	σ_{pm}	0.60	0.95	-
Slot angle to pitch ratio	σ_s	0.40	0.95	-
Slot opening pitch ratio	σ_{so}	0.10	1.0	-

4.4 Optimization Results

In PM vernier machines, the choice of number of stator slots and rotor pole-pairs is very important as this will determine the machine's speed gearing ratio (G_r) and operating frequency at any given input speed. This is one contrast to PMSM where the rotor poles is ideally chosen based on the operating frequency alone. Generally, the suitable G_r can be chosen on the basis of the intended/required speed and/or torque conversion factor, while also taking into consideration the predicted torque ripple characteristics of each pole-slot combination. It has been reported that cogging or ripple torque effects can be minimized by choosing fractional G_r, at the expense of lower average or stall torque [162].

As a preliminary design exercise, a number of 3 kW PMV machines were optimized in order to choose suitable candidates for pole/slot combination. The range of considered pole-slot combinations is given in Tables 4.1 and 4.2, with the objective being to minimize total electromagnetic active mass. All the machines must have an output power of 3 kW with at least 90 % efficiency at the rated operating speed of 150 rpm, and without the power factor constraint. The goal here was to just get an indication of how the pole/slot combination would affect the design, but not necessarily aiming to get the absolute best machine in every aspect of performance. Therefore, in addition to minimizing mass, the

power factor and torque ripple were the two other optimization output responses to be observed. It should be noted that these two output variables are not directly optimized, but they are just being assessed during the process. The minimum requirements and constants applicable to all candidate machines are given in Table 4.5.

Table 4.5: Specifications for the small PMV machines.

Parameter	Value
Output power (kW)	3
Output efficiency (%)	90
Air-gap length (mm)	0.8
Slot-fill factor	0.45
Operating speed (rpm)	150
Aspect ratio ($\frac{L}{D}$)	0.05 - 0.7

L = active stack length, D = total diameter.

The total electromagnetic active masses as a function of the gear ratios for the three PMV machine configurations are quantitatively compared in Fig. 4.9. It can be observed that as the gear ratio increases, the total active mass initially decreases before this downward trend ceases at certain gear ratio, after which the mass stays constant or even increase again. The reason for this, is that the higher gear ratio means large number of rotor pole-pairs, which encourages excess PM leakage flux and consequently the poor performance. In addition, higher gear ratio also implicates high operational frequency for the same input speed, which results in increased core losses. Since the minimum efficiency requirement has to be fulfilled in the optimization, a design with high core loss would respond by increasing the rotor and stator yokes to reduce flux density magnitudes in the affected regions, leading to heavier designs.

Another noticeable trend is that combinations with p_s =1 generally lead to the heaviest designs due to their thick stator and rotor yokes. For overlap-winding machines with stator magnetic pole-pairs equal to 2 and 3, the mass begins to be constant at G_r of 11 and upwards, whereas it slowly increases for tooth concentrated machines. It can also be noted that the results in Fig. 4.9 partly differs to the analytical equations' based predictions which neglects the effect of component partial saturation and flux leakage.

When considering the power factor, Fig. 4.10 shows that it doesn't necessarily follow a uniform trend against the rising gear ratio, although on average, most machines on the high end have lower power factor than those on the lower side of the G_r scale. This phenomenon can be better explained by the simplified power factor expression (Eqn. 2.26), whereby the pole-ratio appears on the denominator of the equation [43]. Consequently, it can be realized that the power factor has an indirect inverse proportionality to the gear ratio. Furthermore, this may also be attributed to the fact that larger G_r values have more flux leakage and higher operating frequency which in turn give rise to synchronous reactance, hence the lower power factor.

Doing the comparison between the three machine types, overlap winding PMV machines shows better power factor relative to the other two machine types. This is because the tooth concentrated winding machines have more magnetic reluctance due to

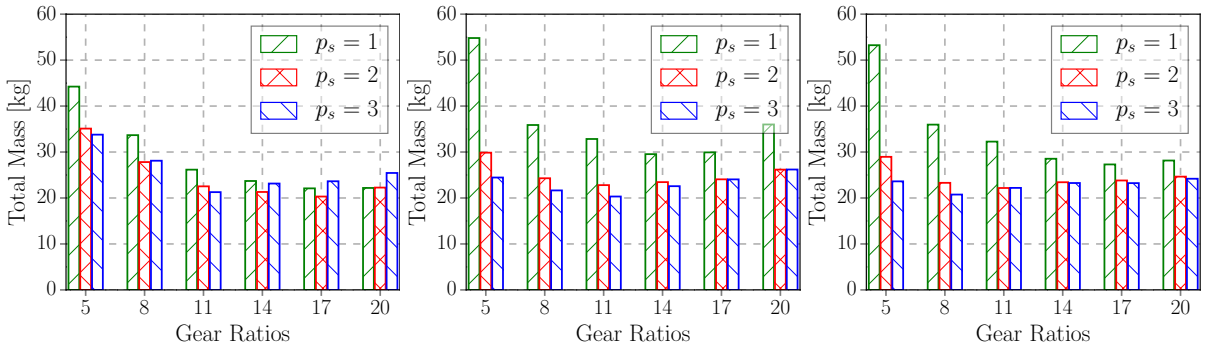

(a) Conventional overlap-winding (b) Tooth-concentrated, split-tooth (c) Tooth-concentrated, separate-modulator

Figure 4.9: Total active mass vs gear ratio for 3 kW machines.

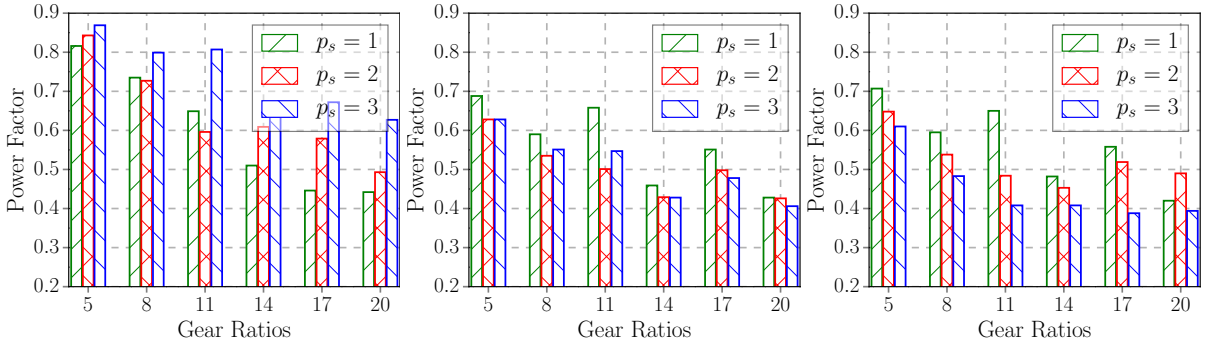

(a) Conventional overlap-winding (b) Tooth-concentrated, split-tooth (c) Tooth-concentrated, separate-modulator

Figure 4.10: Power factor vs gear ratio for 3 kW machines.

the modulating pieces situated in-between the rotor and stator. Besides, most of the tooth concentrated-winding machines listed in Table 4.2 are characterized by poor winding factor. This situation could be mitigated by choosing the armature configuration with better winding factors, but the choice in this regard gets very limited when the PMV machine pole/slot combinations rules are taken into account. In general, the results in Fig. 4.10 demonstrate that the PMV machines' power factor at this output power capacity can hardly reach above 0.8, yet it can go as low as 0.4. Thus, the G_r does not only improve on the machines' torque capacity, but also scales up the reactance as proved by (Eqn. 2.26), leading to poor power factors. Therefore, continuous increase of pole-ratio would eventually lead to the significant decrease of power factor.

Concerning Fig. 4.11, it is interesting to see how the percentage ripple torques are so small for most of the overlap winding PMV machines without any measure being applied to minimize them. This inherent feature, coming about as a result of high lowest common multiple (LCM) between stator pole-pairs and slot numbers is one strong advantage of this machine types. On the other hand, the combinations with G_r equals to 5 have the highest torque ripples across all the three machine types. The tooth concentrated winding PMV machines show significant torque ripple with most of them above 5% mark, and this is to be expected since this type of winding is well known to be rich in magnetic field harmonics.

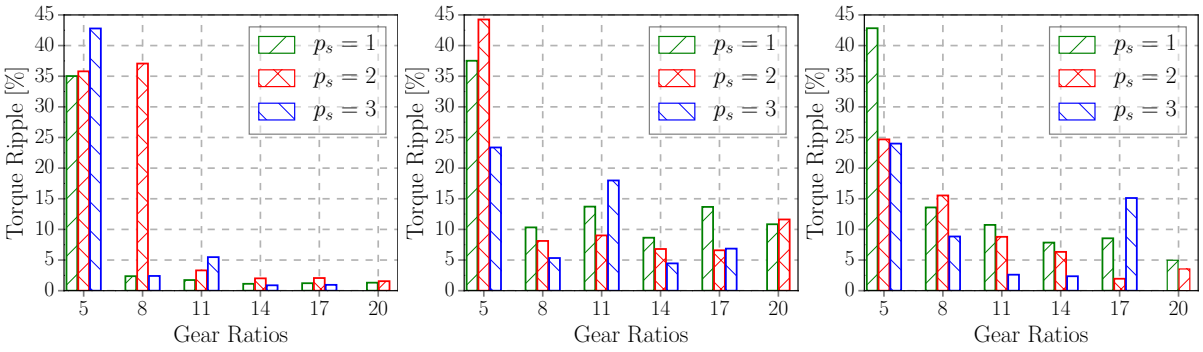

(a) Conventional overlap-winding (b) Tooth-concentrated, split-tooth (c) Tooth-concentrated, separate-modulator

Figure 4.11: Torque ripple vs gear ratio for 3 kW machines.

The findings from the 3 kW machines are also corroborated by the results from the 15 kW machine optimizations presented in Figs. 4.12, 4.13 and 4.14. In this case, the minimum power factor constraint was now active and many pole/slot combinations appear to be on the threshold. At this power level, the impact of low power factor and efficiency constraint seems to be having a direct influence on the optimum design for each combination. This is more apparent in tooth-concentrated winding machines where some of the combinations on the lower scale of the gear ratio (Gr = 5 and 8) could not even meet these constraints, hence omitted from the graphs.

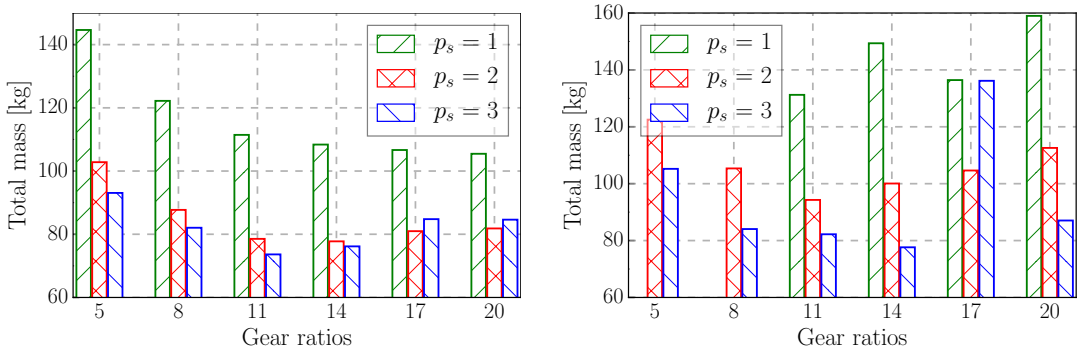

(a) Conventional overlap-winding (b) Tooth-concentrated, split-tooth

Figure 4.12: 15 kW machines' total active mass vs gear ratio.

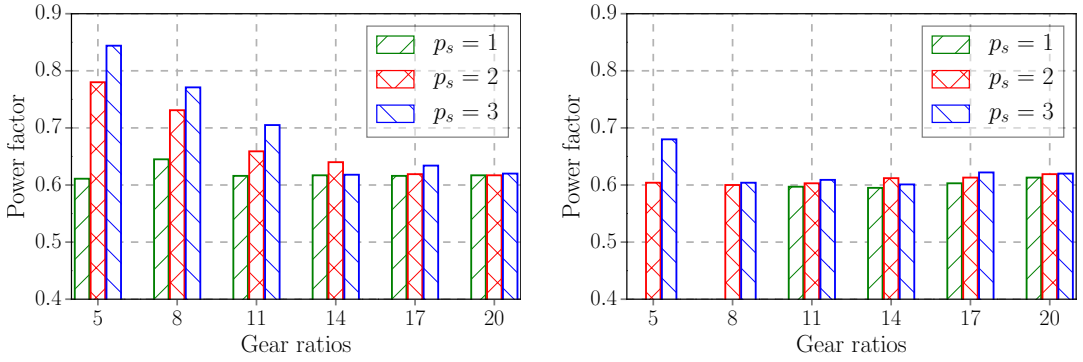

(a) Conventional overlap-winding (b) Tooth-concentrated, split-tooth

Figure 4.13: 15 kW machines' power factor vs gear ratio.

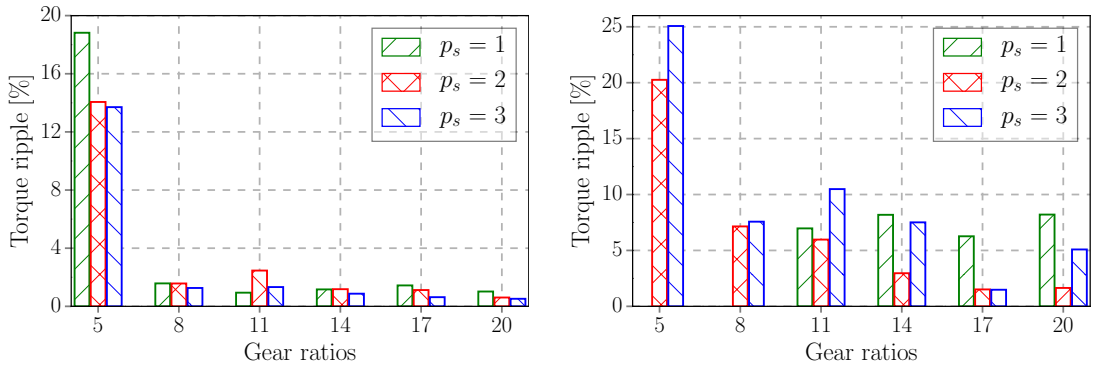

(a) Conventional overlap-winding (b) Tooth-concentrated, split-tooth

Figure 4.14: 15 kW machines' torque ripple vs gear ratio.

4.5 Selected Optimum Design for 15 kW PMV Machine

According to the results obtained on the preceding 3 kW and 15 kW PMV machines' optimizations, the most favorable PMV configuration among the three examined types was found to be the overlap-winding PMV as it generally possesses better power factor and lower torque ripples. Moving onto the 15 kW machine, it was realized during the optimization process that the total active mass also varies rapidly with the aspect ratio. Therefore, the influence of this variable on total active mass at a 15 kW level was investigated on machine with $p_s = 3$, $p_r = 33$ and $Q = 36$. As can be read from Fig. 4.15, the PMV's mass is high at very low aspect ratios, but this tends to decrease with increasing (L/D) values. From 0.4 to 0.6 the mass remains almost constant, which means an aspect ratio close to 0.4 would be a good choice for this machine since the minimum mass is obtained from this region while no benefits are offered beyond it.

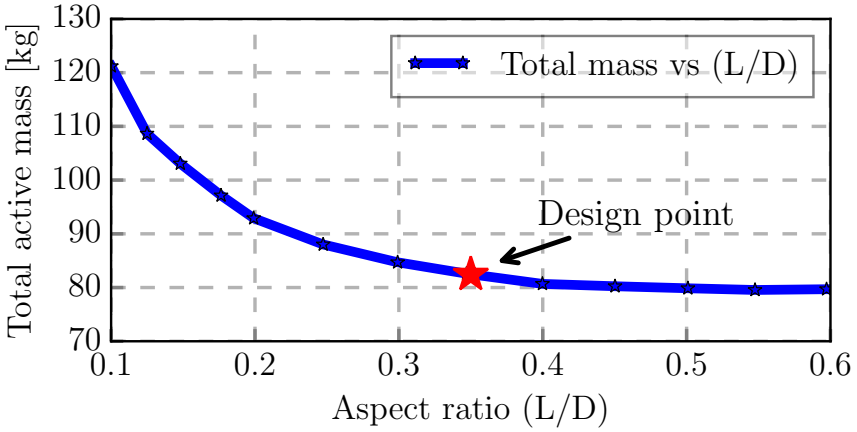

Figure 4.15: Total active mass as a function of aspect ratio

Another relation to explore was the total active mass versus PM mass. While the overall weight of the machine is an important aspect for the intended application, the cost per kilogram of PM mass is usually high, hence it has a significant contribution to the cost of the machine. The plot of the relationship between these two masses is provided in Fig. 4.16, and it shows that small PM material usage renders the heaviest machine. But with the increase of the PM mass, the total active mass rapidly decreases before it gets stagnant at 4.0 kg of PM mass and beyond. According to this graph, the highest PM mass required for this machine type and output capacity, would be around 5.5 kg, with the total active mass being just over 80 kg. This is arguably an advantage for the PMV machine when compared to the normal PM synchronous machines as the later usually require more PM material.

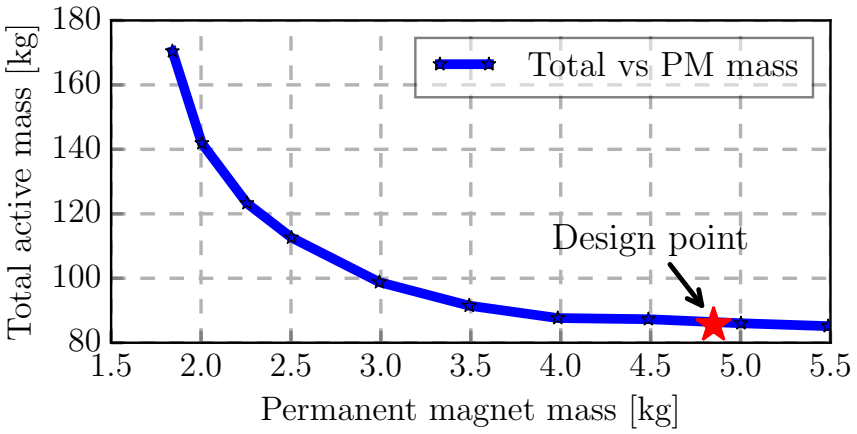

Figure 4.16: Total active mass as a function of PM mass

NSGA-II was also implemented as a non-gradient based optimization strategy for the multi-objective design. Figure. 4.17(a) shows the Pareto-front found between efficiency and total active mass defined as the two objectives, where the trade-offs can be clearly seen. It shows that the total active mass increases in accordance with increasing efficiency. The reason behind this is that, to improve on the efficiency, both the core and copper losses have to be lowered, and that can easily be achieved by having thicker yokes (more core mass) and more winding mass. But with this increase of mass, the efficiency can only be improved up to a certain level, after which it remains almost constant. The graphs dictates that there can be no other design points that can have higher efficiency than the boundary indicated by the Pareto-front for this machine type with the previously defined specifications. It was also important to investigate the feasibility of improving on the power factor of PMV machine since it normally ranges on the lower side of the scale. As it was done with efficiency, the Pareto-front line was drawn between the power factor and total active mass in Fig. 4.17(b).

Figure. 4.17(a) also compares the two strategies from gradient based- and non-gradient based optimization methods which were actually used to obtain Pareto-fronts. MMFD has few optimal points with lower efficiency than NSGA II due to its susceptibility to be trapped within local optima, whereas NSGA-II is most likely to find global optimums. Even though NSGA-II usually takes long computational periods, it is chosen over MMFD since it thoroughly explores most of the design points in the search space.

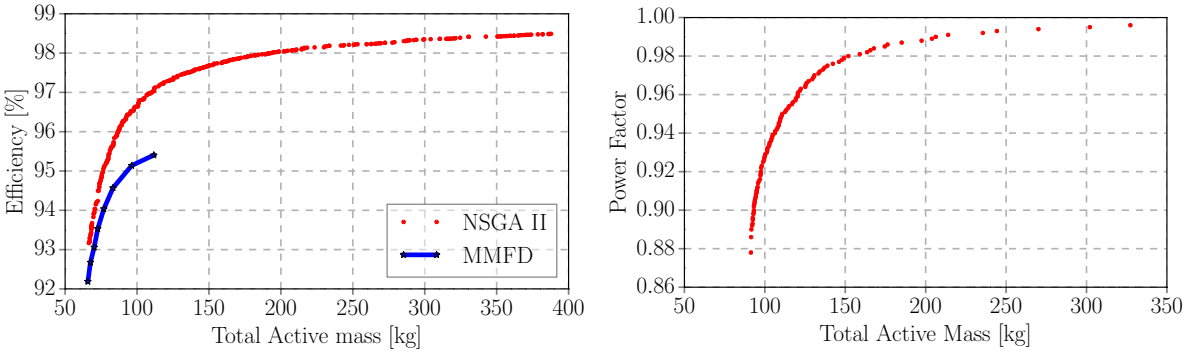

(a) (b)

Figure 4.17: Total mass vs.: (a) efficiency and (b) power factor.

The main properties of the selected PMV and benchmark PMSM machines are described on Table 4.6 and their cross sections provided in Fig. 4.18. In addition, the two generators' detailed dimensional parameters are also given in Table 4.7.

Table 4.6: Compared machine properties.

Parameter	PMSM	PMVM
Stator slots	48	36
Winding poles	40	6
Rotor poles	40	66
Rated frequency (Hz)	50	82.5
Winding type	Tooth concentrated	Overlapping

Table 4.7: Machines' dimensional parameters.

Parameter	PMSM	PMVM
Outer diameter (D_{out})	655 mm	433 mm
Stack length (L_{stk})	125 mm	151 mm
Rotor yoke height (t_{ry})	8.3 mm	13.6 mm
Rotor magnet height (t_{mh})	5.5 mm	3.9 mm
Magnet pole span (σ_{pm})	0.84	0.88
Air-gap length (g)	2 mm	1.5 mm
Stator yoke height (t_{sy})	6.7 mm	13.6 mm
Stator slot angle ratio (σ_s)	0.51	0.74
Slot opening ratio (σ_{so})	1.0	0.82
Stator tooth length (l_{st})	41.0 mm	27.96 mm

Regarding the comparison of the two machines, an estimation of the active volumetric machine size can be given by the total diameter (D_{out}) and active stack length (L_{stk}). While the active volume of the PMV is about 60% of that of the PMSM, the total volume of the PMV machine is close to 72% of the PMSM when taking into account their respective end-winding overhang. Even though the PMV has about 50% more armature winding mass than the PMSM, due to its long end-winding, it still has slightly less overall total active mass than its counterpart. Moreover, it uses approximately 30% less PM material than that of PMSM. Output efficiencies are almost equal since this was the

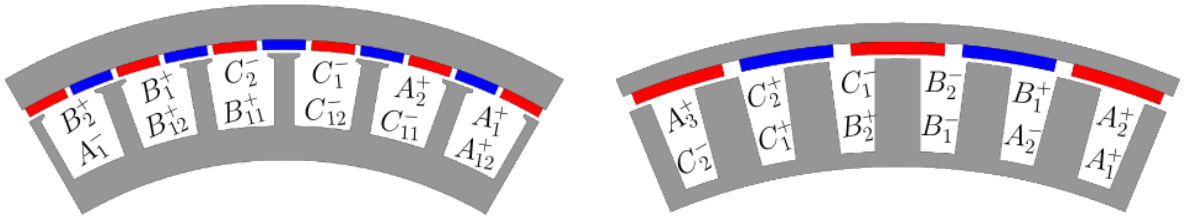

(a) (b)

Figure 4.18: Cross sections of compared PM machines: (a) PMVM (b) PMSM.

minimum requirement constraint for the design optimization. The PMSM has a high power factor, which is normal for synchronous PM machines, whereas the PMVM has a much lower PF of 0.78. This is a known disadvantage for PMVMs, and with the above indicated power factors, it can result in a converter system cost increase of about \$24 based on the prices of SEMIKRON IGBT power modules. As a result, the PMVM's lower cost merit will be somewhat discounted since the total sum of the generator and converter costs will end up being similar between these two systems. Cogging and torque ripple are two other critical factors in PM machines, as they can affect the machine's starting capability and also create adverse mechanical vibration and noise. The PMV machine has smaller cogging torque and smoother torque output than that of the PMSM as evidenced in Figs. 4.19 and 4.20. Nonetheless, both torque quality performances are within acceptable margin for this size of machine torque rating. The properties and performance comparison of the two machines is summarized by Table 4.8.

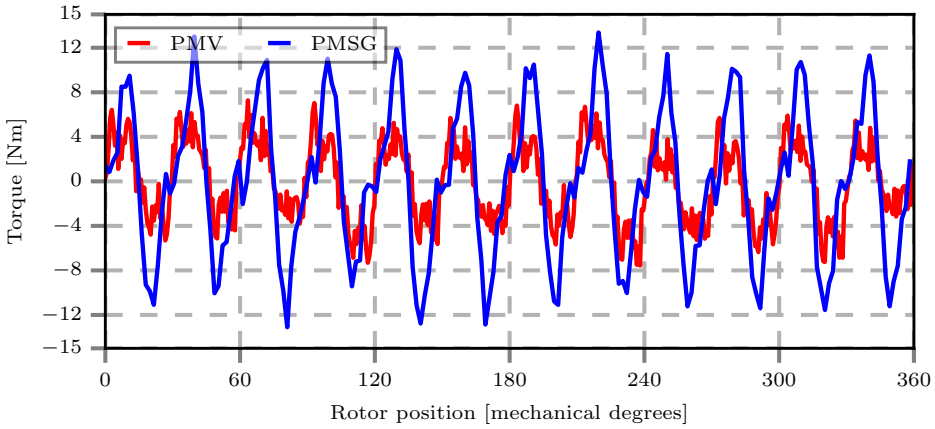

Figure 4.19: PMV and PMSG machines' cogging torques based on FEA.

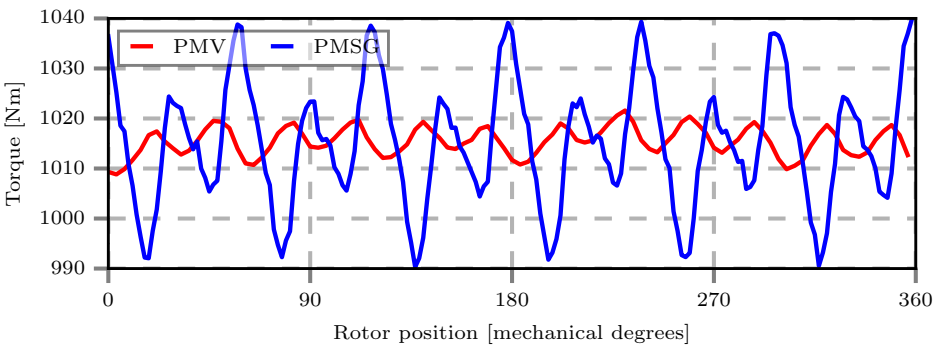

Figure 4.20: FEA based output torque comparison between PMV and PMSG machines.

Table 4.8: Comparison of PMSM and PMVM.

Parameter	**PMSM**	**PMVM**
Maximum torque (T_{avg})	1000.0 Nm	1014.0 Nm
Torque ripple (T_{rip})	3.42 %	1.25 %
Cogging torque (T_{cogg})	2.34 %	1.66 %
Winding losses (P_{cu})	588.48 W	480.4 W
Core losses (P_{core})	252.19 W	320.9 W
PM losses (P_{PM})	109.31 W	155.47 W
Output power (P_{out})	15.0 kW	15.4 kW
Efficiency (η)	94.44 %	94.2 %
Power factor (PF)	0.97	0.78
Torque density	23.7 KNm/m^3	45.6 KNm/m^3
Torque per mass	11.2 Nm/kg	12.0 Nm/kg
End-winding overhang	23 mm	66 mm
Inner diameter (D_i)	528 mm	313 mm
PM_{mass} ($50/kg)	7.0 kg	4.85 kg
$Core_{mass}$ ($2/kg)	62.44 kg	45.08 kg
$Winding_{mass}$ ($6.67/kg)	20.16 kg	34.49 kg
$Total_{mass}$	89.6 kg	84.42 kg
Total active material cost	$ 609	$ 563

Both the PMV and PMSM machines were designed at their rated operating point conditions. However, it is also important to know the performance characteristics of these machines beyond their rated speed conditions, as they are both designed for variable speed operation with power electronic converter grid connection. Hence, this calls for an analysis of their power capability characteristics over a wide operational speed range. Considering their power factor differences, PMV and PMSG would need different converter sizes for operation. For this comparison, a 20 kVA converter with a line-to-line voltage limit of 400 V is used for both machines. The converter voltage and current limits are indicated in by Fig. 4.21, whereby it can also be seen that the current limit is around 29 A.

With the above mentioned voltage and current constraints, the torque-speed and power-speed curves are presented by Fig. 4.22. In the constant torque region, both machines have equal torque performance, but the PMV machines has a higher torque over a wider speed range beyond the rated speed. In a similar way, their power performances is very close before the rated speed is reached, but the PMV machines can maintain rated power output over a wide speed range. In Fig. 4.23, the machines efficiencies are closely matched as this was the minimum design constraint during the optimization. It is worth noting that the PMV machine's power factor is significantly less than that of PMSM, but it improves once the machine reaches higher speed, with a slight increasing efficiency too.

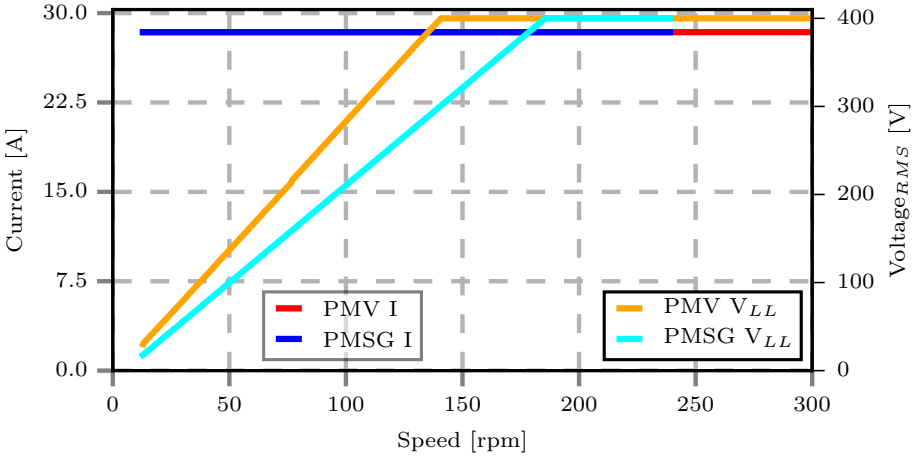

Figure 4.21: Machines' current and voltage traces corresponding to a similar converter rating.

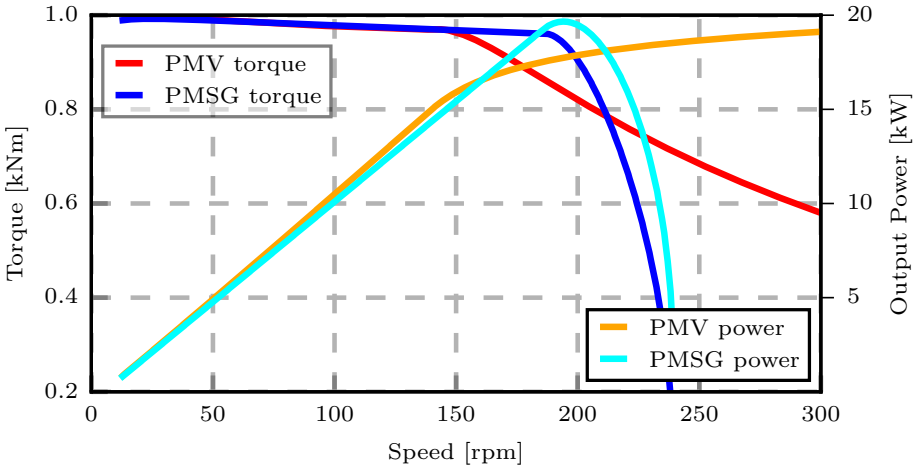

Figure 4.22: Power and torque curves versus generator speeds.

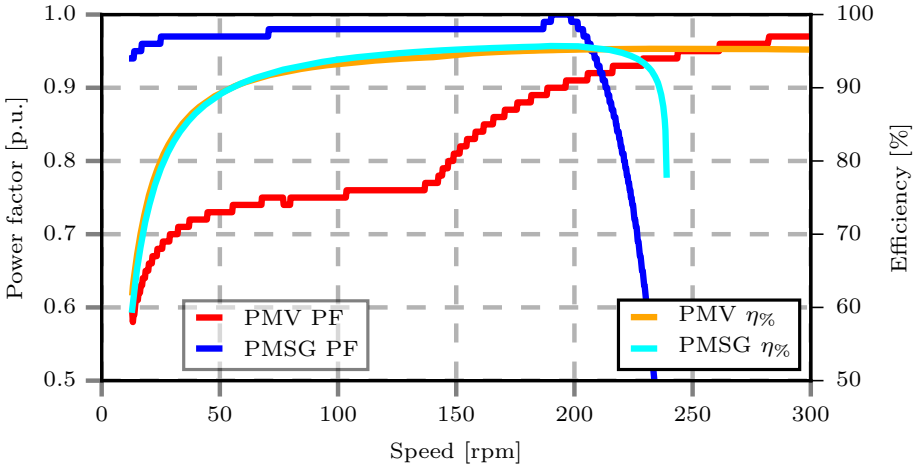

Figure 4.23: Efficiency and power factor performance versus generator speeds.

Chapter 5

Mechanical Design, Construction and Testing of PMV Machine Prototype

In order to practically verify the theoretical operating principle and validate the formulated FE-based optimal design approach, a 15 kW PMV machine prototype was built. The key dimensions that describe the constructed PMV machine are provided in Table 5.1. Figure 5.1 shows the machine's open-circuit flux line distribution, no-load and full-load flux density shaded-plots. The stator and rotor yokes have maximum flux density magnitudes of approximately 1.5 T and 1.7 T respectively, while the over-saturated regions appears on the edges of teeth base. In this chapter, the mechanical design, construction and experimental evaluation of the prototype PMV machine are described in detail.

Table 5.1: Prototype machines' dimensional parameters.

Parameter	Value
Stator slots (Q)	36
Winding pole-pairs (p_s)	3
Rotor pole-pairs (p_r)	33
Winding type	Overlapping
Outer diameter (D_{out})	433 mm
Stack length (L_{stk})	151 mm
Rotor yoke height (t_{ry})	13.6 mm
Rotor magnet height (t_{mh})	3.9 mm
Magnet pole span (σ_{pm})	0.88
Air-gap length (g)	1.5 mm
Stator yoke height (t_{sy})	13.6 mm
Stator slot angle ratio (σ_s)	0.74
Slot opening ratio (σ_{so})	0.82
Stator tooth length (l_{st})	27.96 mm

5.1 Machine Components and Construction

Both the stator and rotor iron cores are made of a non-grain oriented fully processed type of electrical steel of grade M400-50A. The core laminations have a thickness of 0.5 mm each, cut with laser technology to maintain a good accuracy of the dimensions. A total

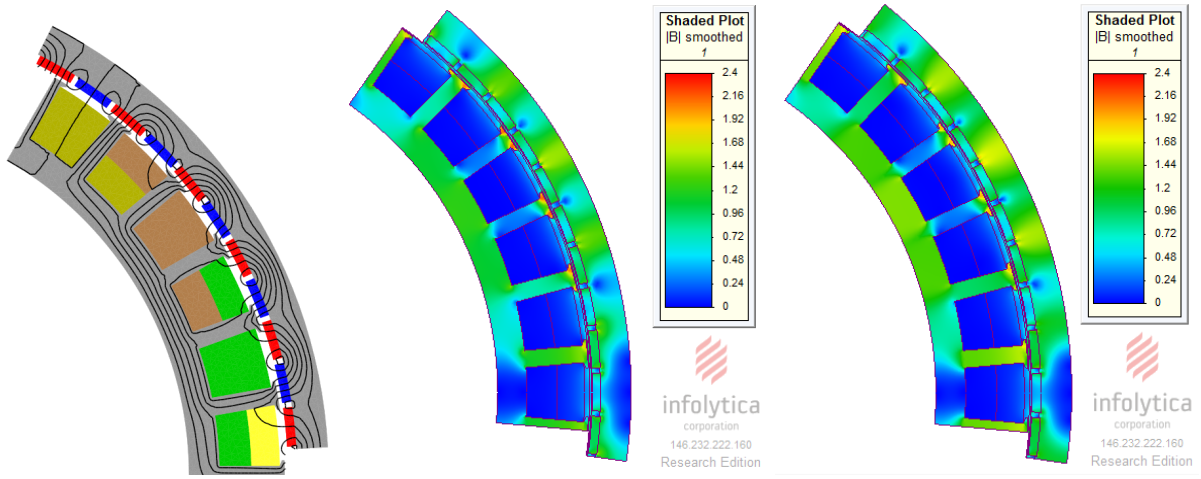

(a) (b) (c)

Figure 5.1: Prototype machine ($1/6^{\text{th}}$) FEM simulation results: (a) Open-circuit flux lines, (b) Open-circuit flux density and (c) Full-load flux density.

of 290 laminations were stacked together to have an axial machine active core length of 151 mm, achieving an iron stacking factor of 96 %. The stack of laminations are held and pressed by using a number of rods through the holes, which are located towards the external and internal edges for rotor and stator, respectively. The material properties of the above mentioned active core material are summarized in Table 5.2.

Table 5.2: Stator and rotor core lamination material properties.

Property	Value
Material grade designation	M400-50A
Lamination thickness	0.5 mm
Mass density	7700 kg/m^3
Core loss @ 1.5T & 50Hz	3.57 W/kg
@ 1.5T & 100Hz	9.82 W/kg
Resistivity	42 $\mu\Omega$cm
Relative permeability @ 1.5T	1050
Thermal conductivity	25 W/(m °C)
Specific heat capacity	490 J/(kg °C)

5.1.1 Stator winding layout

Double-layer overlapping three-phase winding are used in the stator, which is short-pitched by 1-slot as illustrated by Fig. 5.2. This stator pole-pitch shorting reduces the resultant MMF fifth order harmonic and also reduce the end-winding resistance, thereby improving on the efficiency.

Each stator coil has 9 turns of round copper conductors and one conductor is made up of 13 parallel wire strands. All the coils in one phase are connected in series such that their induced EMFs will be summed up, making a total of 12 coils per phase. Even though the prototype relies on natural air-convection as a cooling method, the designed

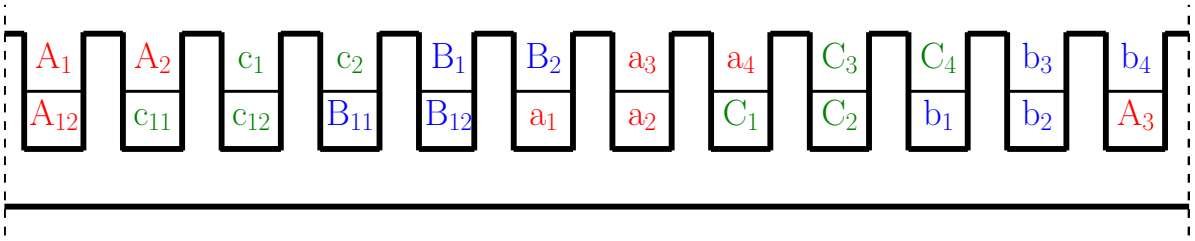

Figure 5.2: Illustration of winding arrangement for one third of a stator cross section, representing one stator magnetic pole-pair.

rated current density is relatively low and the winding temperatures are not expected to exceed 150 °C at full load, hence a thermal class F of conductor insulation material was found suitable to be used. Furthermore, the winding coils and stator laminations are electrically isolated from each other by using Nomex paper slot liner, which also works as the cushion to protect the windings from the sharp lamination edges. An epoxy resin was added in the slots to affix the coils onto the stator laminations and make them one body. The achieved slot filling factor for the prototype machine is 0.36.

5.1.2 PM rotor

In surface-mounted PM rotors, there has to be a mechanism applied to ensure that the PMs are securely fixed in one position on the rotor core surface. Amongst many methods available for fixing PMs which may include screwing, use of non-magnetic bandage or retaining ring, an adhesive has been found adequate in the foregoing design. That is because the external rotor type is being used, which means the rotational centrifugal forces have no adverse effect as they naturally pushes the PMs against the rotor core surface instead of pulling them off. The employed adhesive is a 1 : 0.4 mixture of two components epoxy glue, namely, Aerontec's Araldite epoxy AV 138 and hardener HV 998, respectively. This mixture is a very strong adhesive if given enough curing time of at least 24 hours at room temperature, and it retains its strength at working temperatures of up to 150 °C. Necessary precautions were also taken to make sure that the gluing surface areas are free of oil or grease that could weaken the bond strength, and an adhesive layer of thickness 0.05-0.10 mm was enough to provide a greatest lap shear strength. Table 5.3 summarizes the technical data of the used epoxy mixture.

Table 5.3: Description of the Araldite glue mixture used to stick PMs.

Property	Value
Adhesive designation	AV 138 & HV 998
Mix color	Grey
Density	1.65-1.75 g/cm^3
Mix viscosity @ 25 °C	80000-100000 mpa
Flash point	>104 °C
Thermal expansion coefficient	67.0 K^{-1} · 10^{-6}
Cure time @ 23 °C	24 hrs
Lap shear strength @ 23 °C	13 N/(mm^2)
@ 150 °C	18 N/(mm^2)

Besides the use of glue to fix the PMs, the small protruding pieces were made on the surface of the rotor core to create some grooves for inserting the PMs. These tiny pieces work as guides to ensure that the PMs are uniformly distributed along the circumference of the rotor bore during the insertion process, and also assists to avoid the PMs dislocation due to repulsive and/or attractive forces between themselves. The lamination protrusions were made shorter enough to limit the flux leakage while also being long enough to shield the PMs from any tangential movement. A picture of stacked pieces of rotor laminations where the mentioned protrusions can be seen is shown in Fig. 5.3. The height of the tips is about 0.5 mm, which is a way less than the PM radial thickness.

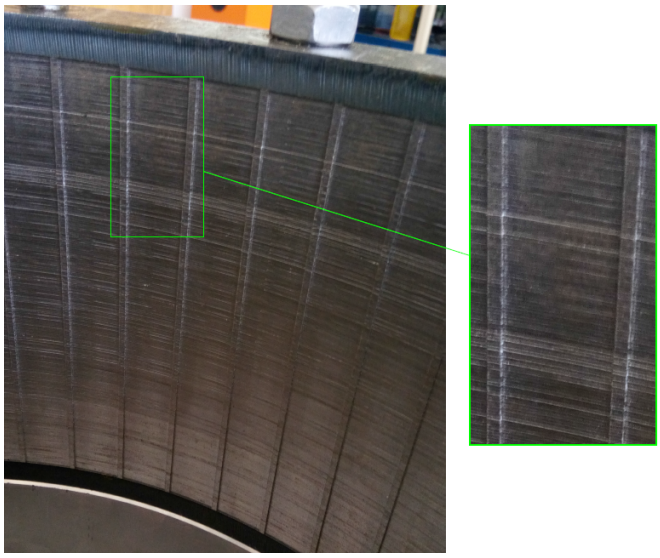

Figure 5.3: Rotor core lamination protrusions.

It has been shown in the previous chapters that in PMV machine's operation, the armature windings' fundamental MMF harmonics will always have lesser pole number than the PM rotor, so, the torque is developed through the interaction of only one of the modulated higher order stator MMF harmonic with the PM's MMF. This means that the stator fundamental harmonic MMF and the other higher order modulated space harmonics (rotating at different speed and/or direction to that of the PM rotor) are just the loss inducing components in the PMs and other parts of the rotor. At elevated operating frequencies the high eddy current losses in PMs may cause excessive heating, thereby exposing them to risk of irreversible partial demagnetization.

In surface-mounted PM machines, the circumferential segmentation of the PMs have proven to be most effective method of the eddy current loss reduction. But this method could not be easily applied in the current design owing to the small available PM pole-pitch that would render some mechanical complexities during the assembly. Therefore, only the axial PM segmentation was applied as a measure to alleviate the induction of PM eddy current losses. Even though this technique may not be as effective as the circumferential segmentation, it can still provide a substantial loss reduction [163; 164]. The axially segmented PMs are shown in Fig. 5.4, whereby each rotor pole has been divided into two axial segments.

With regards to the PM material, the grade N48H of sintered Neodymium Iron Boron (NdFeB) was selected because it has high magnetic remanence (B_r) and large BH energy

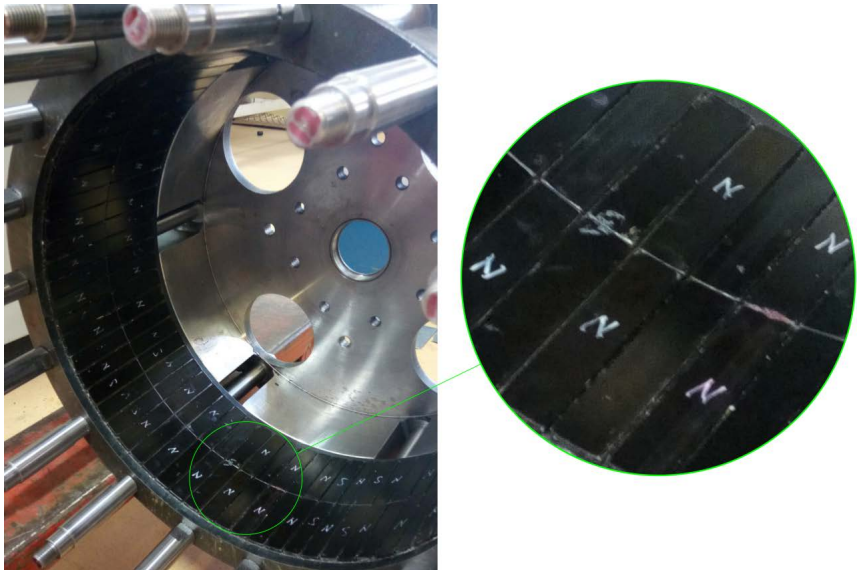

Figure 5.4: Axially segmented rotor PMs.

product. In addition, the temperature rating H was chosen for the PMs to alleviate the risk of partial demagnetization due to high temperature effects. The technical data of the selected NdFeB PMs is summarized in Table 5.4, which shows a maximum working temperature up to 120 °C is allowed for these PMs. Hence their safety relative to temperature effects alone is guaranteed as they are expected not to exceed 100 °C during the machine operation. Besides, the PMs are epoxy coated to protect them from corrosion as well.

Table 5.4: PM material technical data.

Property	Value
Material grade designation	N48H
Remanence (B_r)	13.7 kGs
Maximum BH energy product	46.26 MGO
Recoil permeability @ 20, 80, 150 °C	1.038, 1.040, 1.044
Coercivity @ 20, 80, 150 °C	-1065478, -987337, -894392 A/m
Mass density	7500 kg/m^3
Electrical resistivity @ 20 °C	$1.8e^{-06}$ Ωm
Specific heat capacity	460 J/(kg °C)
Thermal conductivity	7.6 W/(m °C)

5.1.3 Machine assembling

The prototype PMV machine consists of two main components being the stator and the PM rotor, allowing it to retain the relatively simple structure of single-rotor single-stator type machines. The development of these two components from their individual basic constituent parts is separately shown in Fig. 5.5 for the rotor and Fig. 5.6 for the stator. Then their integration into one full functional machine is illustrated in Fig. 5.7 together with a longitudinal cross section showing their arrangement. Two bearings are fitted between the shaft and the rotor support plates from each side of the stator while the

stator is fixed by the key onto the shaft. Detailed production drawings, materials and dimensions of the components are described in the Appendix A.

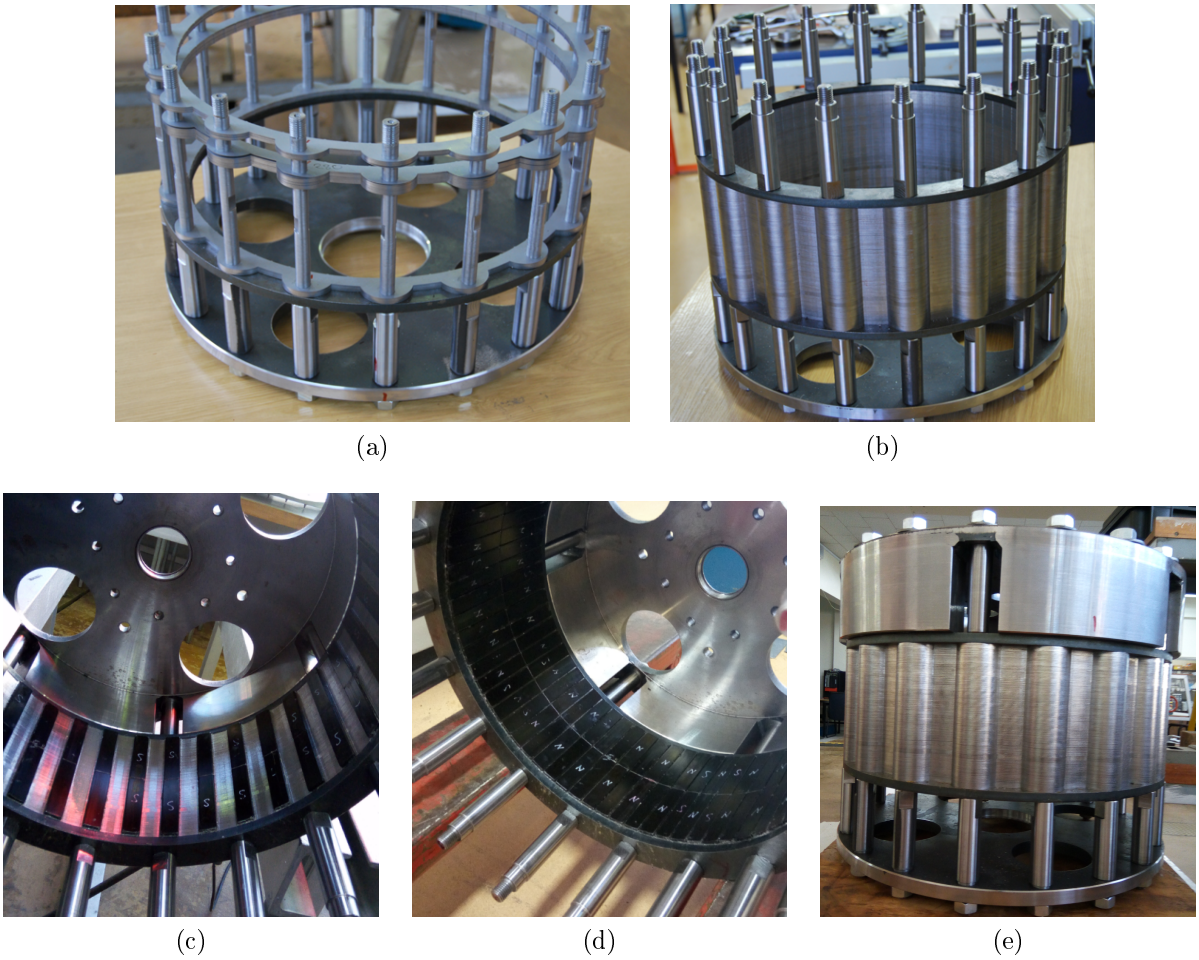

Figure 5.5: Rotor construction: (a) stacking laminations onto the rods (b) complete stack of laminations pressed with end-rings (c) inserting first set of PMs (d) all sets of PMs are mounted (e) full PM rotor and its support structure.

Rotor core was constructed by sliding the lamination pieces onto the rotor rods and pressing them by the stack end-rings through bolting mechanism as shown by Fig. 5.5 (a) and (b). Each rod is made up of three sections. The middle section goes through the lamination stack and the two other sections are then tightly screwed in from both sides to press the laminated stack just like in nut and bolt system. In addition, the two end sections of the rods also acts as the spacers between the rotor magnetically active core and the end-plates, creating more axial space for the stator end-windings. In Fig. 5.5(c), a set of same polarity PMs is stuck on the bore surface of the rotor lamination stack and the glue is given enough curing time before the adjacent PMs can be inserted. In Fig. 5.5(d) the rotor has all the PMs mounted and the full rotor with support structure is given in Fig. 5.5(e).

The fabrication process of the distributed overlapping winding stator of the machine is illustrated in Fig. 5.6. A stack of stator core laminations fixed on the stator end-plate on one side by means of the rods is shown in Fig. 5.6(a). After the required number of

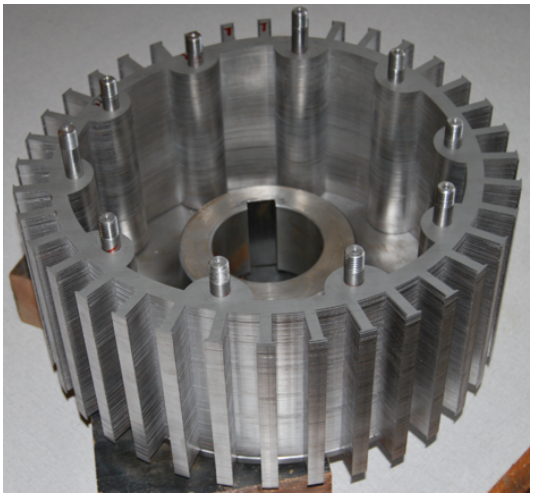

(a)

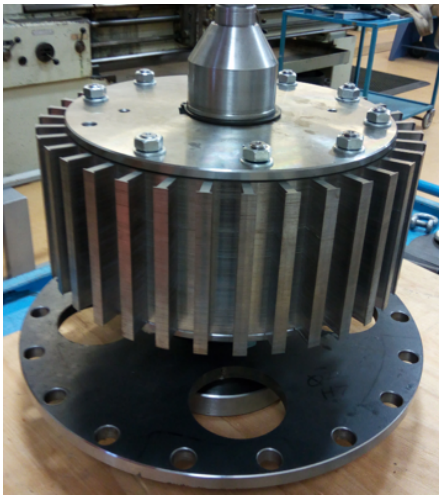

(b)

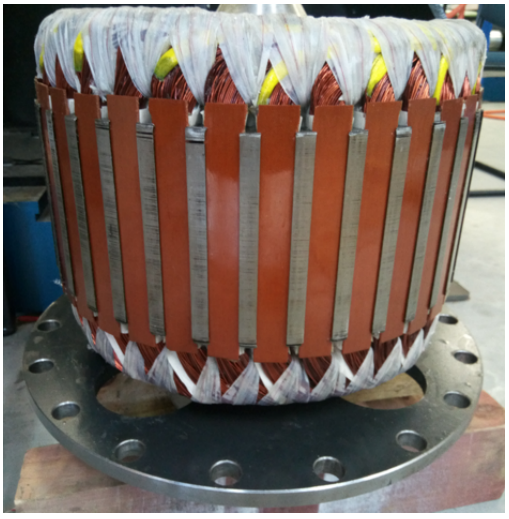

(c)

(d)

Figure 5.6: Assembling of stator: (a) stacking laminations onto the rods (b) complete lamination stack pressed with end-plates and mounted on the shaft (c) side view of wound stator with distributed overlapping windings (d) top view of end-winding overhang.

the laminations was pushed in, the second end-plate was also brought in and the stack tightly compressed by nuts (Fig. 5.6b). The shaft was subsequently inserted in the center of the end-plates and serves as the axle. It has a key to keep the stator stationary and cyclips are put on either side to stop any axial displacement. Stator coils were then neatly wound and epoxied as shown by Figs. 5.6 (c) and (d).

After the fabrication of the rotor and stator were completed, the full PMV machine was finally assembled as depicted by Fig. 5.7(a). Removable copper strips were inserted in the air-gap to suppress the effect of strong attraction forces between the two components and protect the PMs from being scratched or smashed by the stator core. A finished PMV machine is shown in Fig. 5.7(b) mounted on the test bed. The mechanical alignment and configuration of the machine's integral parts is displayed by Fig. 5.7(c). A slim encoder shaft runs from the driving end of the rotor through the middle of the main shaft to the supported side to provide the rotor's speed and position tapping point.

(a)

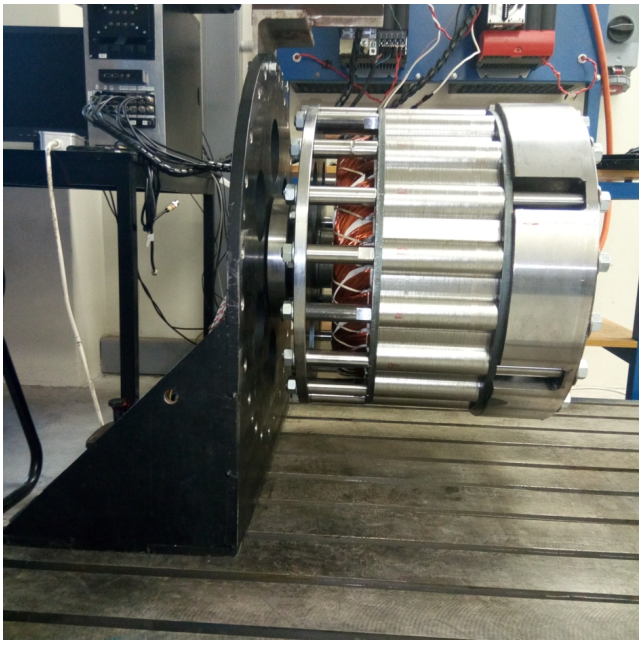

(b)

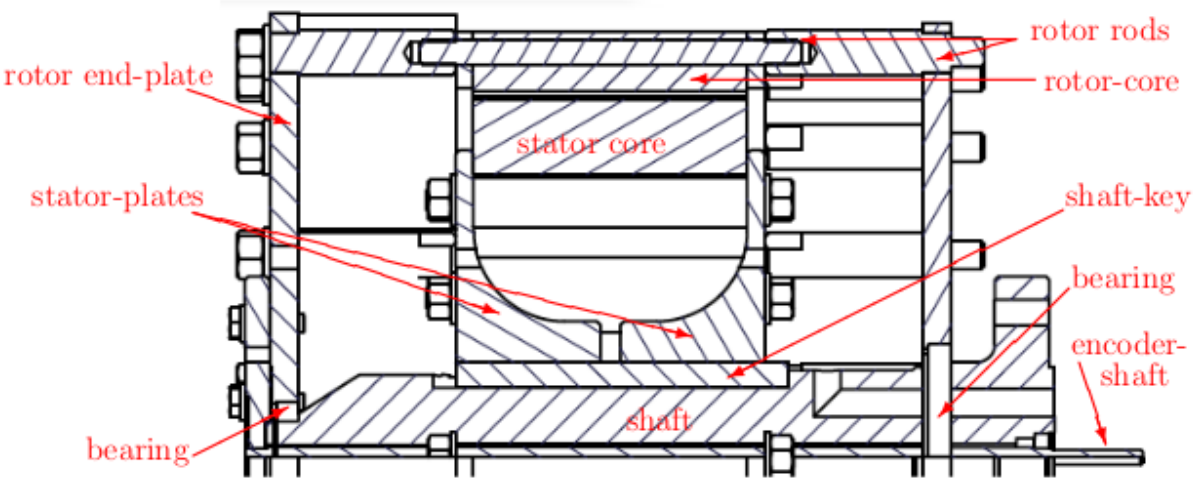

(c)

Figure 5.7: Machine assembling: (a) inserting the stator into the rotor (b) PMV machine on the test bench (c) longitudinal cross section of machine structure (winding not shown).

It can also be seen from Fig. 5.7 that all of the machine components rest on the main shaft that is supported from only one side. This clearly calls for a stress analysis to assess the extent of possible shaft deformation and determine if it will be strong enough to support all that load. A free body diagram in Fig. 5.8 illustrates the contact points of the forces endured by the shaft. The components' weight exerts a gravitational force while the magnetic torque applies a twisting moment.

Figure. 5.9 provides the analysis results performed by Autodesk Inventor. It shows that the safety factor is 2.74, and that is acceptable considering the fact a minimum factor of two is often satisfactory. The von-Misses stress analysis further indicates that the experienced pressure is well within the shaft material's capability.

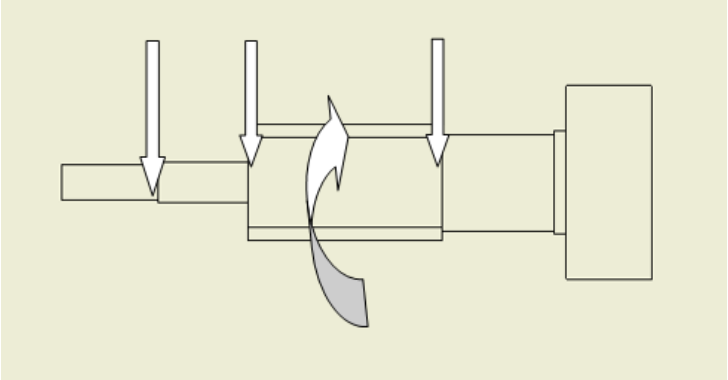

Figure 5.8: Free body diagram of the shaft showing the forces distribution.

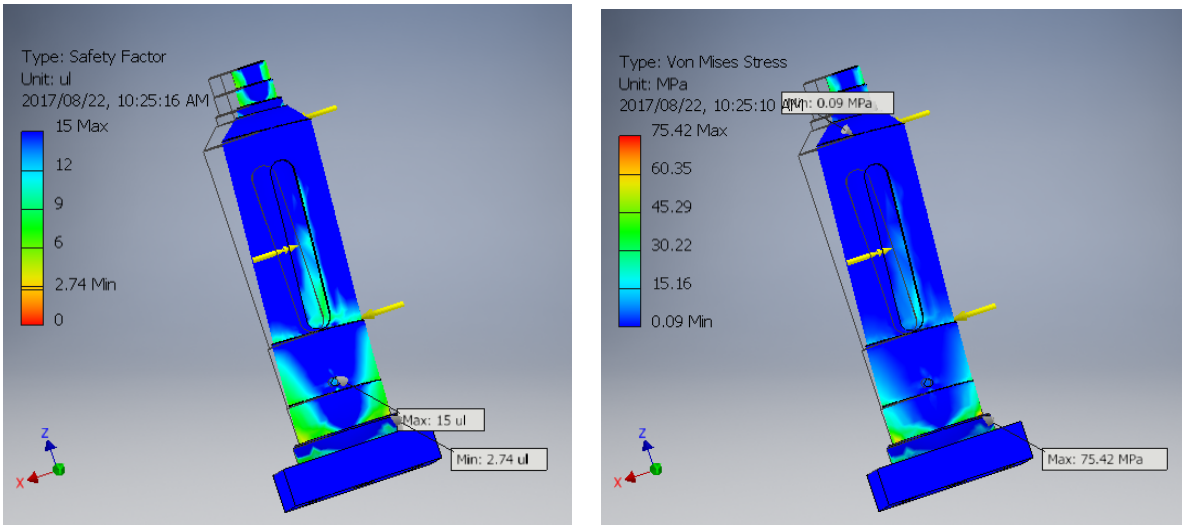

(a) (b)

Figure 5.9: Shaft analysis: (a) safety factor (b) von-Misses stress analysis.

5.2 Experimental Evaluation

Several laboratory tests were carried out on the developed PMV prototype machine to practically evaluate its performance. Since the PMV machine was operated as a generator, a 45 kW three-phase induction machine was used as a prime mover to emulate the wind turbine input by driving the prototype at a desired speed and providing required input power. The no-load tests were firstly conducted to characterize the prototype, and the load tests were also done to fully investigate the PMV machine performance. A description of the test bench set-up and instrumentations used to conduct the experiments is given in this section. Then the prototype PMV machine's experimental results are subsequently presented, with some comparison to related FEM based results made where possible.

5.2.1 Test bench set-up

Figure 5.10 shows a schematic representation explaining the experimental test set-up while the picture of the actual set-up is given by Fig 5.11 for the no-load tests. It consists of the following pieces of equipment:

- 45 kW Induction machine
- AC drive - Allen-Bradely PowerFlex 750s
- Torque sensors - Lorenz DR 2212 (2000 Nm) and DR 3000 (500 Nm)
- Voltage probes - Tektronix P5205 differential probe
- Tektronix TDS 3014C phosphorous digital oscilloscope
- Computer, voltmeters, 3-phase switch and connection cables

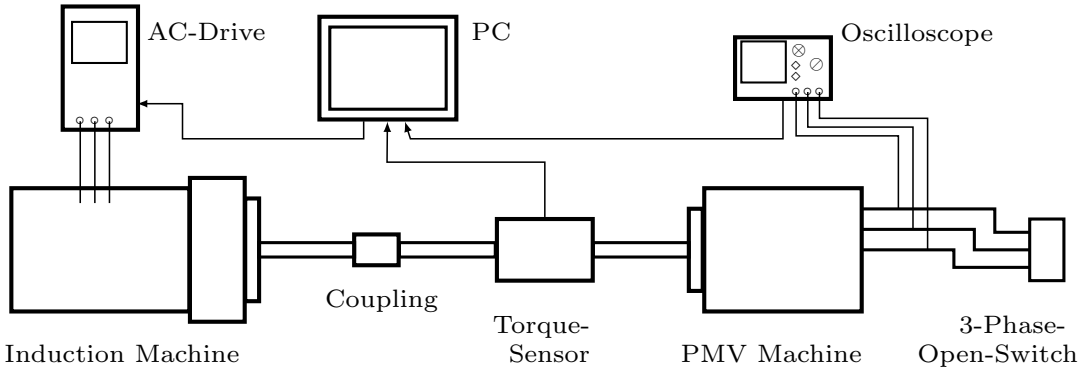

Figure 5.10: Schematic diagram of open-circuit test set-up.

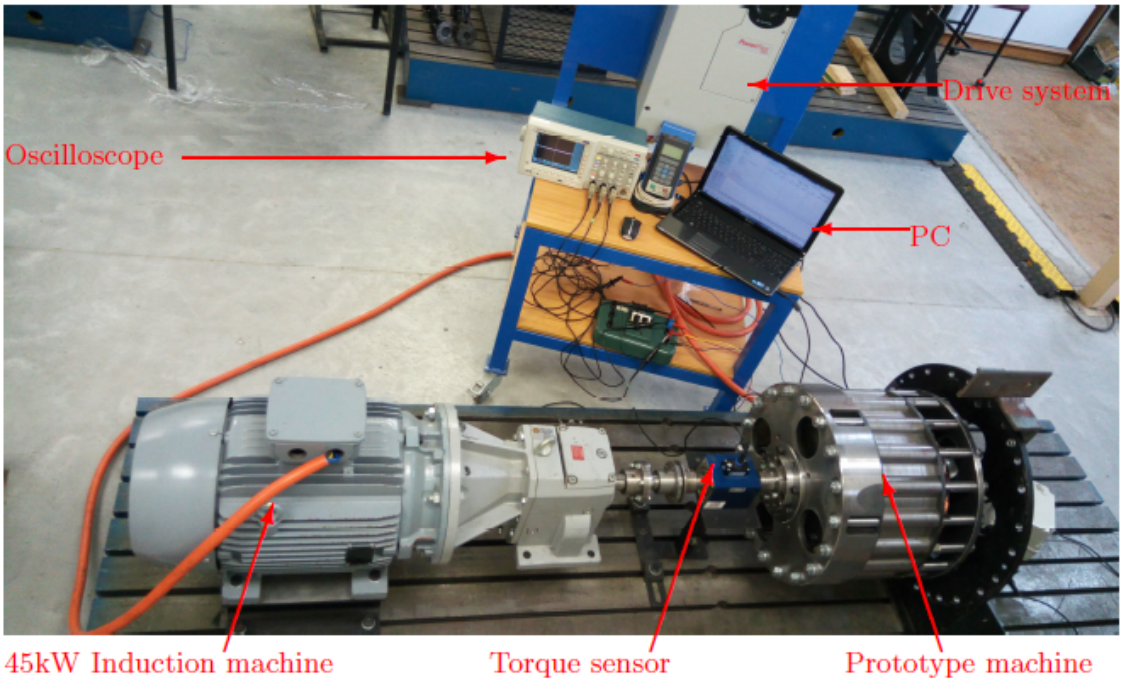

Figure 5.11: Experimental set-up for open-circuit tests.

The prime mover (induction machine) is connected to the prototype PMV machine via flexible coupling. A 500 Nm torque sensor is placed between the two machines so that

it can be used to measure the input power and speed to the prototype. An Allen-Bradely PowerFlex 750s variable frequency AC drive is used to control the induction machine to a required input speed via a PC interface. Voltage probes were used to continually measure the output voltage from the prototype machine terminals and log it into the digital oscilloscope. All the data logged into the oscilloscope is simultaneously saved and retrieved after the test for further analysis.

5.2.2 DC phase resistance

The machine's phase winding resistance was measured by employing a simple circuit shown in Fig. 5.12. A variable DC voltage source was used to inject a constant current into each phase winding while the current through and the voltage across the phase coils were being simultaneously read. The resistance value was calculated as the ratio of voltage to current as presented in Table 5.5. The measurements were conducted at an ambient room temperature of 25 °C. Due to the resistance being temperature dependent, resistance equation that implements the winding material's temperature coefficient can be used to determine the resistance value at an expected winding operating temperature.

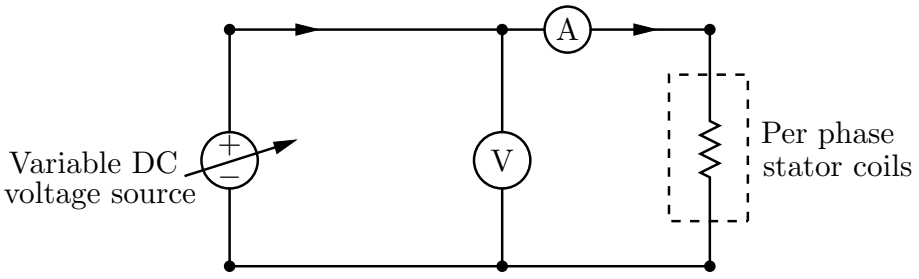

Figure 5.12: Phase DC resistance measuring circuit.

All the three-phase windings are balanced as there is insignificant percentage difference between their impedance values. Also, the obtained practical readings are about 4% lower than the analytically predicted resistance of 0.146 Ω, suggesting that the stator end-windings' lengths were over-estimated during the design phase as they appear shorter than predicted.

Table 5.5: Stator winding DC resistance data.

Phase A			Phase B			Phase C		
V	I	R = $\frac{V}{I}$	V	I	R = $\frac{V}{I}$	V	I	R = $\frac{V}{I}$
0.144	1.00	0.144	0.136	1.00	0.136	0.141	1.00	0.141
0.286	2.02	0.142	0.272	2.02	0.135	0.283	2.00	0.142
0.429	3.01	0.143	0.402	3.00	0.134	0.417	2.98	0.140
0.565	4.00	0.141	0.538	4.01	0.134	0.558	4.00	0.140
0.702	4.99	0.141	0.669	5.00	0.1338	0.700	5.04	0.139
Ave. R(Ω)		0.142			0.135			0.140

5.2.3 Cogging torque

In the operation of the PM-excited and slotted iron-cored machines such as the current PMV design, cogging torque plays an adverse role as it affects the machine's starting ability. This is particularly relevant to wind energy applications as the developed torque of wind turbines under start-up conditions is relatively low. Thus, the high cogging torque in a wind generator may lead to a complete failure of starting up [165]. In addition, the cogging torque manifests itself by creating the machine's internal vibration and producing acoustic noise. Hence it is usually preferred to be at minimum in any machine design. The set-up shown in Fig. 5.13(a) was used to measure the starting cogging torque of the PMV machine, and its diagram illustration is included in Fig. 5.13(b). By slowly moving the rotor-connected torque-beam vertically upwards, the rotor position is varied in small discrete steps. In that way, the influence of the transient losses and other related effects to the measurements can be avoided since the rotor movement was done in very small static steps. The torque sensor records both the rotor angular position and experienced torque at each step.

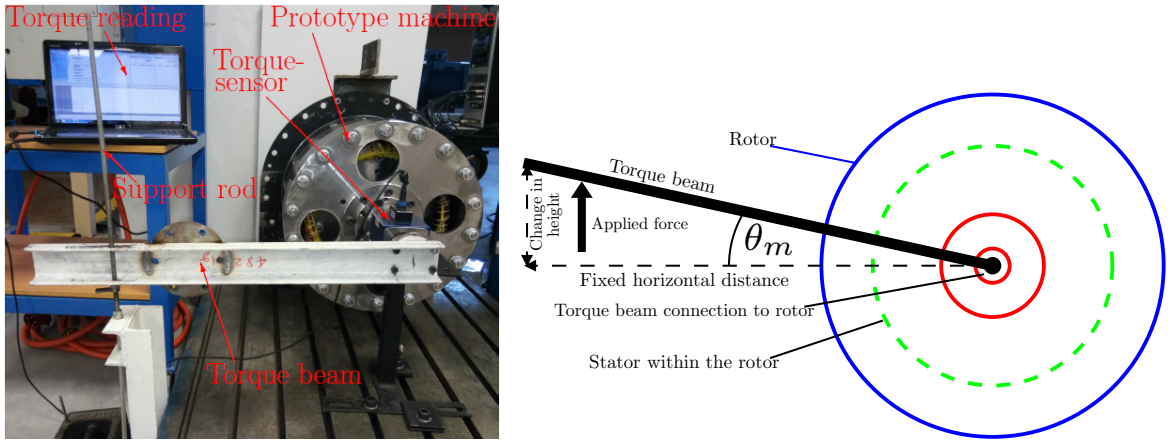

(a) (b)

Figure 5.13: Test set-up for cogging torque measurement.

The measured and FE predicted cogging torque waveforms are compared in Fig. 5.14, where it can be seen that the obtained practical cogging torque is significantly higher than the FEA based results. The deviation comes as a consequence of cogging torque's sensitivity to variations in PM properties and mechanical tolerance issues in the rotor assembly process. Amongst them, the most critical irregularities include the rotor eccentricity, the PM misplacement and dimensional variations [166; 167].

The effects of rotor eccentricity and PM misplacement are indicated by simulation results in Fig. 5.15. With the rotor axis displaced from that of the stator by a distance of one third of the air-gap length, the peak cogging torque is 50 Nm. On one side, shifting three PMs from their ideal placement positions by 6% of the PM width gives a cogging torque magnitude of 15 Nm. It may not be easy to know which imperfection contributes the most to the observed difference in Fig. 5.14 because all the assembly and/or manufacturing variations' effects could occur concurrently. Even though the experimental cogging torque is much higher than the FEA value, it is still within the acceptable range as its peak value is just under 2% of the average rated torque.

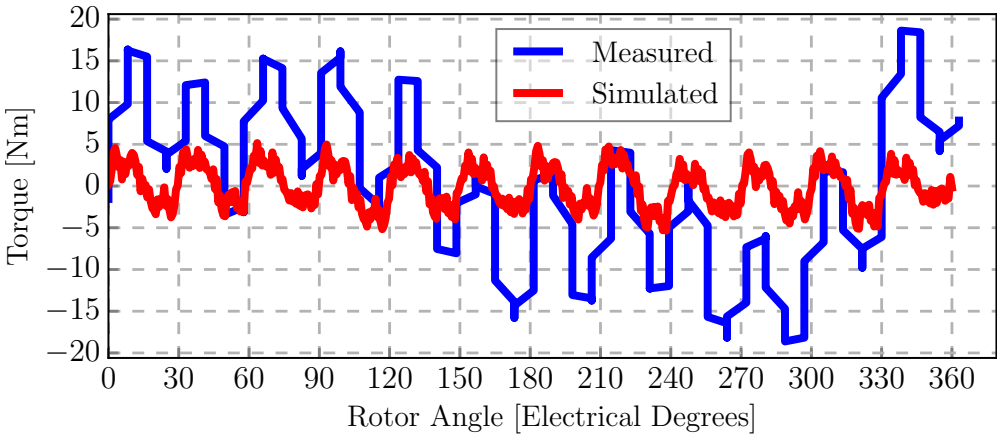

Figure 5.14: Cogging torque as a function of rotor angular position.

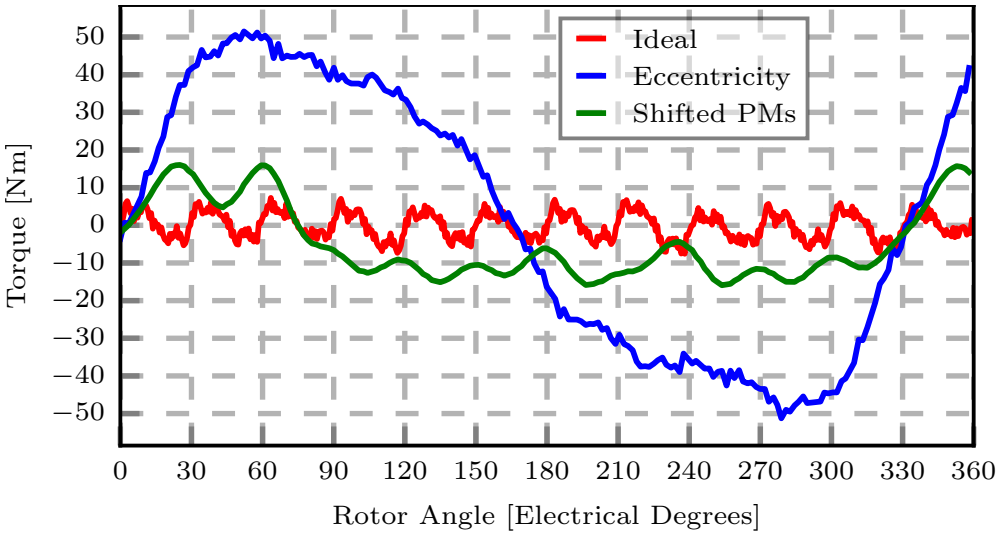

Figure 5.15: Effects of possible construction imperfections on cogging torque.

5.2.4 Open circuit tests

The no-load tests were performed on the prototype PMV machine to experimentally examine its characteristics of the induced back-EMF, determine the mechanical and no-load magnetic losses, and compare them with the FEA predicted values. In this test, the prototype machine was driven by the prime-mover at a constant speed while the output terminals of the star connected phase windings were kept open-circuited.

These tests were carried out at several steps of speeds up to at least twice the rated speed. The profile of an open-circuit line-to-neutral back-EMF waveform at rated speed of 150 rpm and their harmonic spectrum are given in Fig. 5.16 and Fig. 5.17, respectively, for both the experimental measurements and FEA predicted values. It can be observed that the three-phase voltages are well balanced and uniformly distributed from each other indicating that the rotor PMs are evenly magnetized and properly mounted on the rotor yoke, and that the stator coils were correctly wound.

The voltage waveforms are almost sinusoidal with the presence of small third order harmonics developing slightly flattened voltage waveform tops. Thus the small presence of the third harmonic causes a minor decrease in fundamental harmonic. In terms of

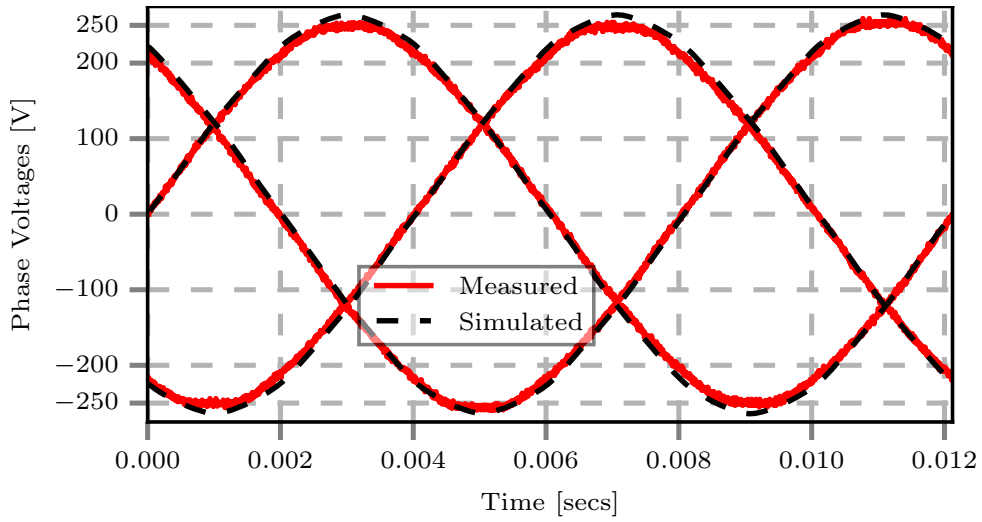

Figure 5.16: Open-circuit phase voltage waveforms at rated speed.

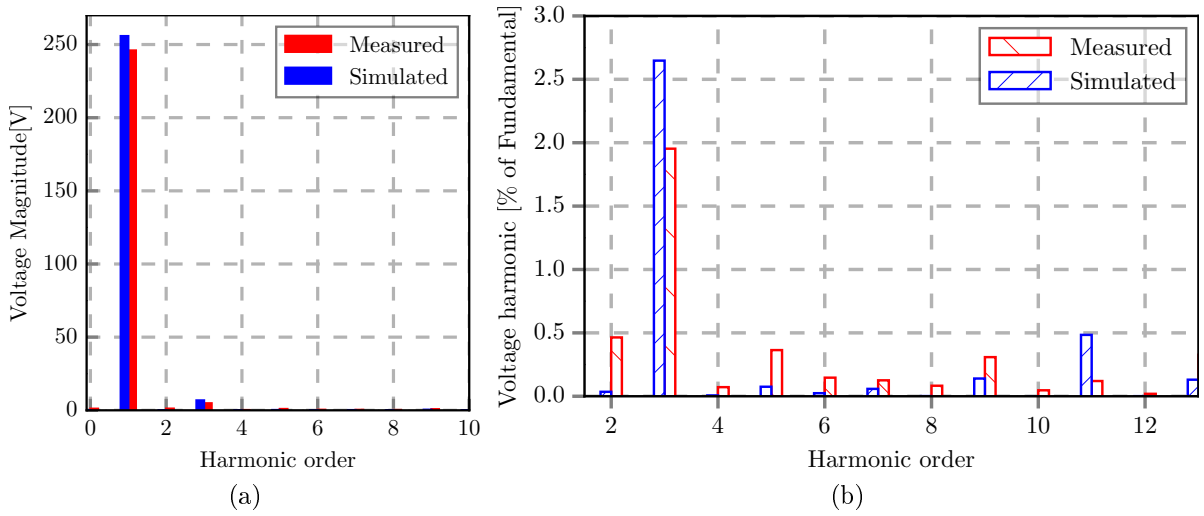

Figure 5.17: Open-circuit phase voltage harmonic spatial order: (a) voltage magnitude and (b) higher order voltage harmonics expressed as a percentage of fundamental harmonic magnitude.

percentages, the higher order harmonics in the measured and simulated voltages are all less than 3%. Therefore, the minimum harmonic content clearly proves that the machine has a good voltage quality. This low harmonic presence in the open-circuit voltage is attributed to the fact that the machine has a distributed winding type with a short-pitched arrangement to suppress some potential higher order harmonic amplitudes. Furthermore, the experimental results' magnitude are slightly smaller than the 2D FEA predicted values by a difference of less than 5%. The reason for this minor difference relies on a number of factors such as an axial flux leakage, manufacturing tolerances and the components' material imperfections, which are not accounted in the 2D FE analysis. At this rated speed, the EMF waveforms have a period of 12.12 ms indicating an operating frequency of 82.5 Hz. For an armature winding with electromagnetic pole-pairs number of three, this serves as a validation of the magnetic gearing effect present between the rotor and stator, and agrees with the operation principle.

A number of tests were performed at various operating speeds to reveal the machine's open-circuit induction constant with respect to the speed. Figure. 5.18 depicts the graph of phase RMS back-EMF as a function of input rotor speed. A linear relationship of voltage to rotor speed can be clearly seen with a good correlation of the experimental and the FEA based results at lower speeds. However, there is a slight difference emerging between the two values as the speed increases. This is because of the reduced magnetic permeability of the machine active components' materials as it saturates at higher frequencies. Apart from the minor discrepancies between the experimental and FEA values of the back-EMF, there is a satisfactory correlation between the two results, confirming a good agreement between the prototype and FE modelled PMV machine.

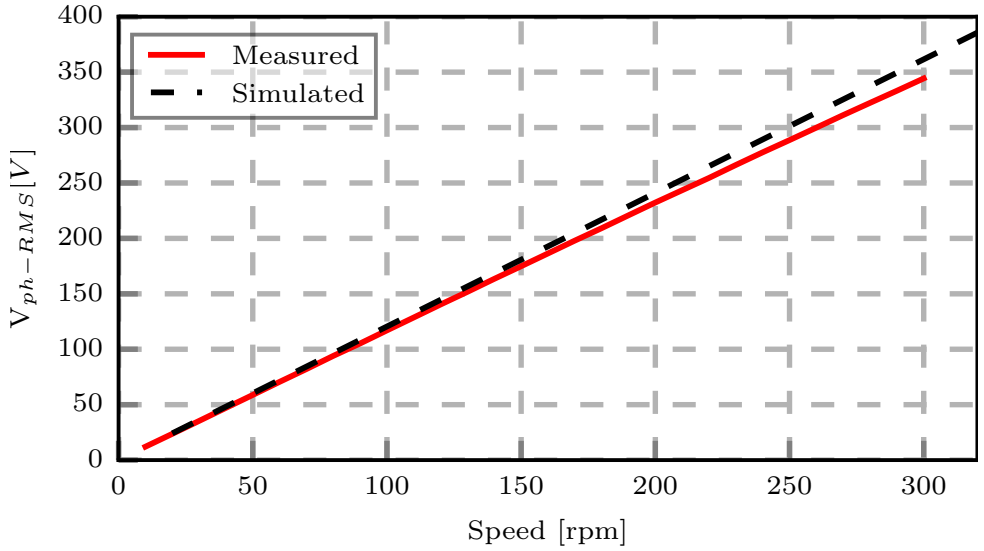

Figure 5.18: Open-circuit voltage versus rotor speed.

The machine's no-load input power and the associated driving torque were also investigated at various speeds, and the obtained results are plotted in Fig. 5.19. This power constitutes the prototype's no-load power losses, which include the mechanical losses, eddy-current and hysteresis losses in both the electromagnetically active and non-active components. In order to separate the bearing friction and rotor windage losses from the others, the machine was pre-assembled without PMs and tested. That means all the frequency dependent losses were excluded since there was no excitation, and only mechanical related losses were present. However, it was later realized that this method is not completely reliable because the bearing losses were undermined as there were no machine internal forces which usually pre-load the bearings thereby increasing their losses. Therefore, the obtained results in this regard may not be very accurate.

The total loss graph rapidly increases at higher speeds because of the core eddy-current loss component that is a function of squared frequency. The measured total losses correlate reasonably well with the sum of the measured bearing and simulated frequency dependent losses up to rated frequency. However, at higher frequencies, the discrepancy between the measured and predicted total losses becomes more significant. As shown in Fig. 5.19, the PM losses and eddy current losses in the stator conductors located in open slots have also been accounted for in the predicted total loss. The remaining discrepancy between the measured and total of approximated losses is likely due to (i) the inaccuracy of the implemented core loss model at higher frequency [168–170], (ii) underestimated

mechanical losses as previously mentioned, and (iii) the leakage flux induced losses in supporting structure since the simulations were only done in 2D FEM.

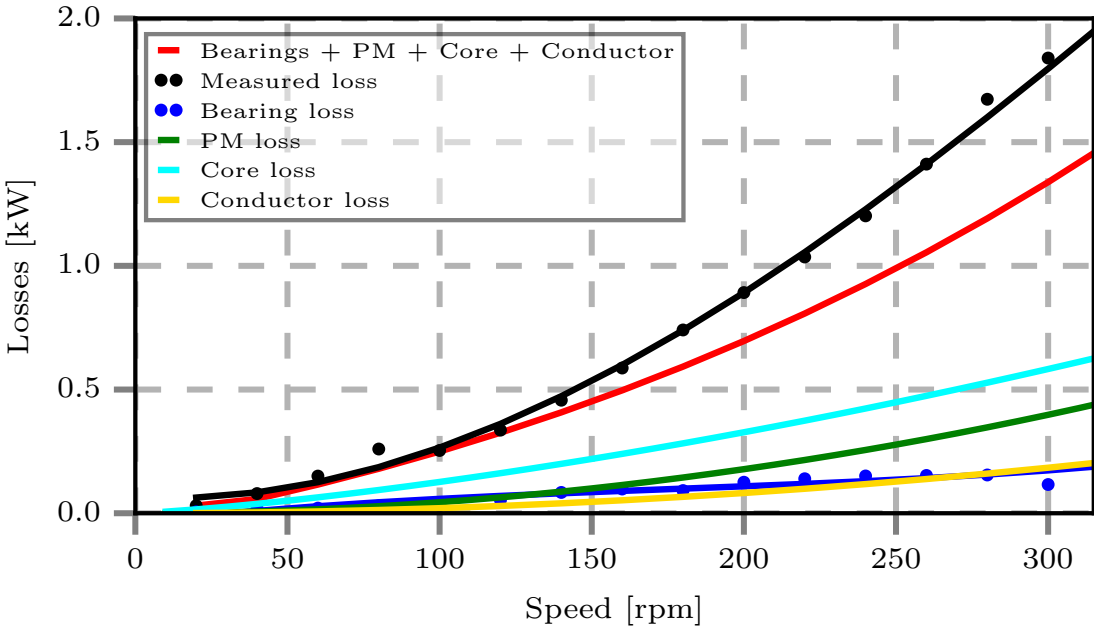

Figure 5.19: No load losses as a function of rotor speed.

5.2.5 Load tests

A drive system consisting of the induction machine as a prime mover to the prototype, and the SEW back-to-back converter for power conditioning and circulation was implemented for studying the loaded performance of the PMV machine in generator mode. Due to the low torque ratings of the induction machine, a 1 : 7.6 ratio mechanical gearbox was used to step-up its output torque to satisfy the torque requirements of the prototype PMV machine at rated conditions.

A field oriented control strategy based on the dq-theory in rotor reference frame is used to achieve the maximum torque at each stator current loading. This is performed with the aid of the position encoder attached to the rotor shaft, providing the controller with the rotor's speed and angular position at any time instant. With this feedback information known, the reference phase's orientation is controlled to always remain aligned on the rotor's direct axis, while the stator's current angle is adjusted to obtain maximum torque. The stator's angle is typically around 90 electrical degrees at operating speeds below and including the rated speed for best torque result, but it gradually changes beyond that speed.

A test set-up diagram is provided on Fig. 5.20, while the picture of the actual laboratory testing arrangement is shown in Fig. 5.21. The operating testing conditions were heavily restricted by both the converter's voltage limitations and the prime mover's torque-speed capabilities, which lead to the prototype PMV machine being tested at speeds in the narrow range of 110 rpm up to 150 rpm only.

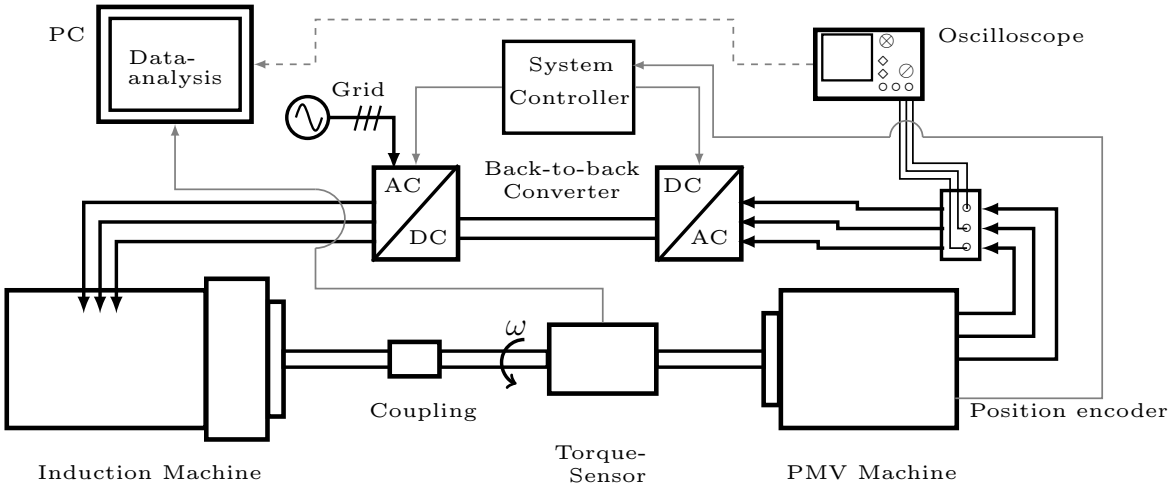

Figure 5.20: Schematic diagram of test set-up for loaded conditions.

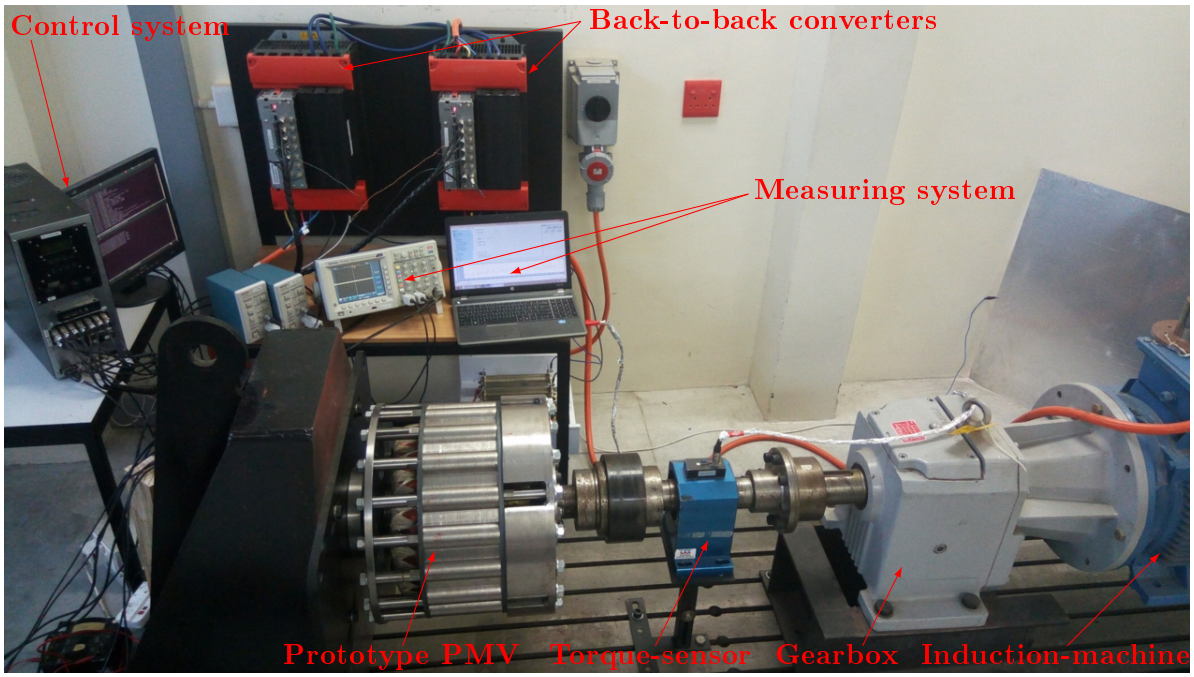

Figure 5.21: Experimental set up for loaded tests.

The measured voltage and current waveforms at steady-state generator operation are shown in Fig. 5.22. The output current is sinusoidal with the amplitude of 44.5 A, whereas the PWM inverter line-to-line voltage displays a rectangular shape. In addition, it can be seen from the figure that the current is lagging the reference voltage, which is a clear indication that the PMV machine's power factor is not high.

The torque profile of the machine as a function of the stator current loading is presented in Fig. 5.23. The machine is able to deliver a torque with magnitude slightly above 1 kNm at less than 3 A/mm^2 current density, which means that the armature losses and the stator heat generation will be confined to reasonable values. At the rated torque operation, the ripples are just about 4%, meaning the rotor is running smoothly. The good torque quality is also attributed to the short pitching of the stator winding which reduced the 5^{th} order harmonic fields.

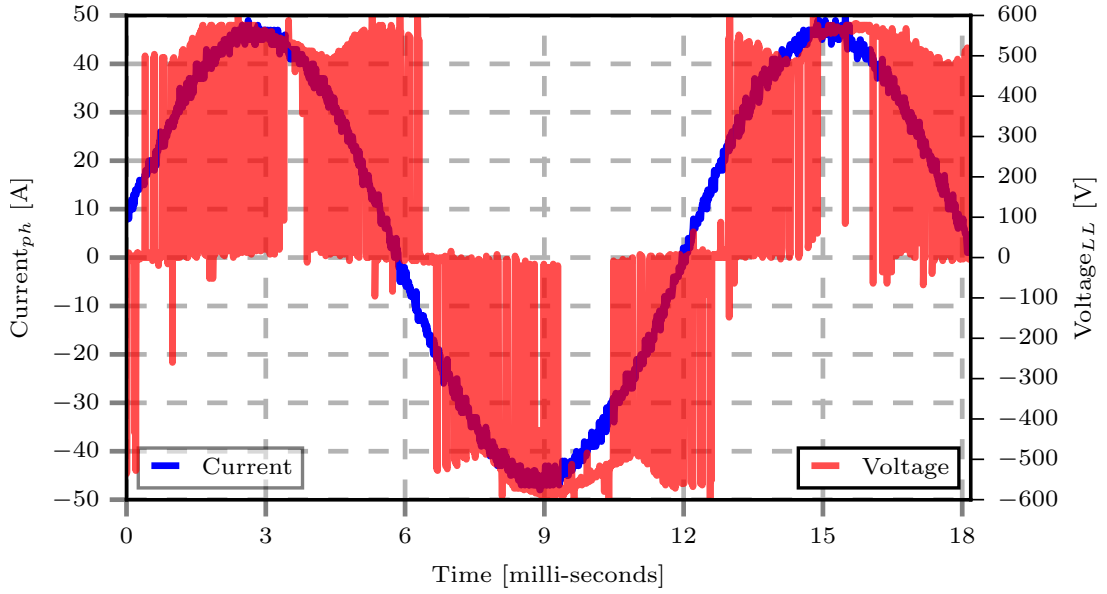

Figure 5.22: Measured phase current and line-to-line voltage at 150 rpm.

Figure 5.24 shows the active output power at 110 rpm , 130 rpm and 150 rpm, reaching a maximum of 15.2 kW at rated load current and speed. This result is a good indication that a machine is able to deliver the expected output at rated operating conditions.

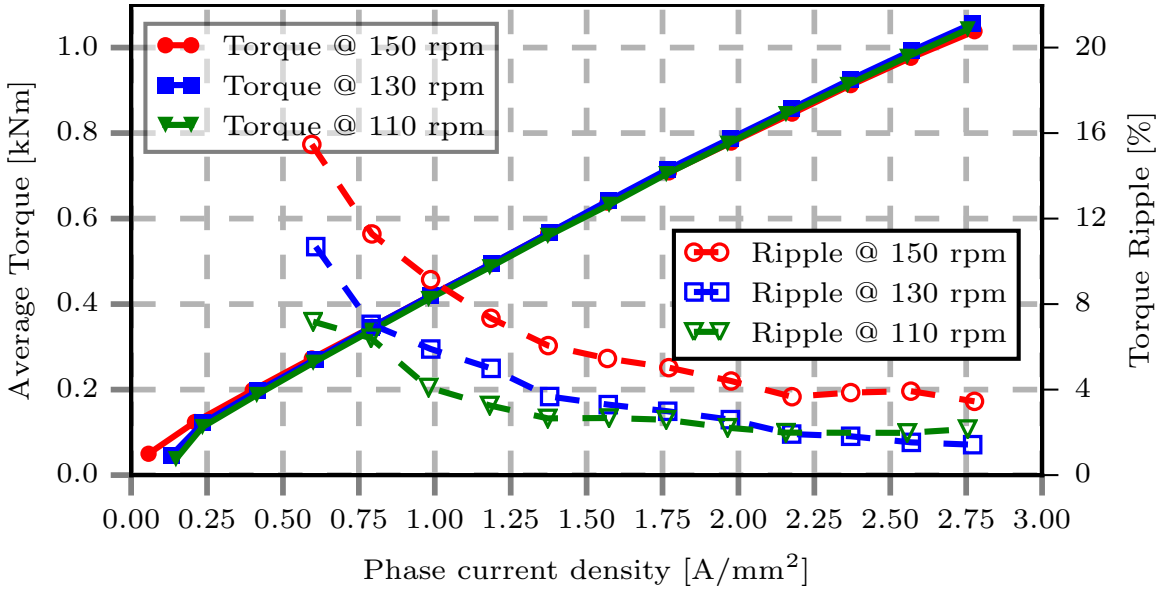

Figure 5.23: Torque characteristics as a function of phase current.

On the other side, the obtained experimental power factor shown in Fig. 5.25 deviates from the FEA predicted result of 0.78 as only 0.71 could be achieved at rated conditions. Due to the overwhelming practical no-load losses indicated in Fig. 5.19, the PMV machine's efficiency is also reduced from 94% to just above 93% as shown by Fig. 5.26. The observed differences between the simulated and measured results are due to the constructional imperfections and inaccurate approximations of certain parameters during the FEA

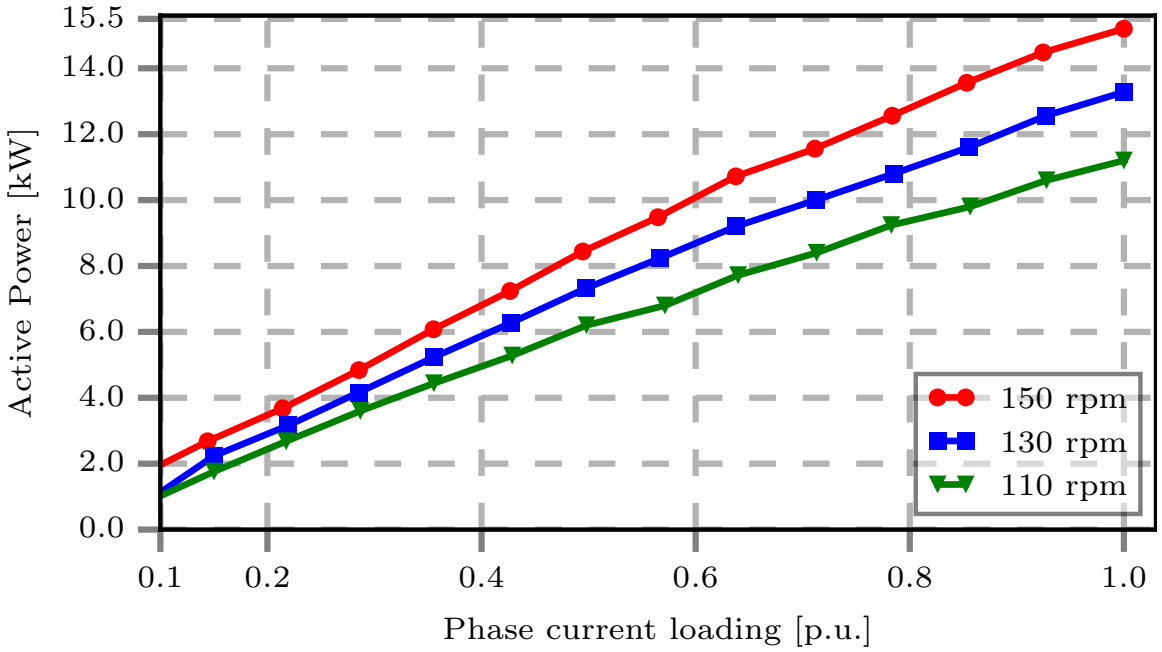

Figure 5.24: Active power as a function of phase current.

modeling. These include the end-winding leakage inductance, temperature and harmonic effects on the losses incurred by the laminations and PMs.

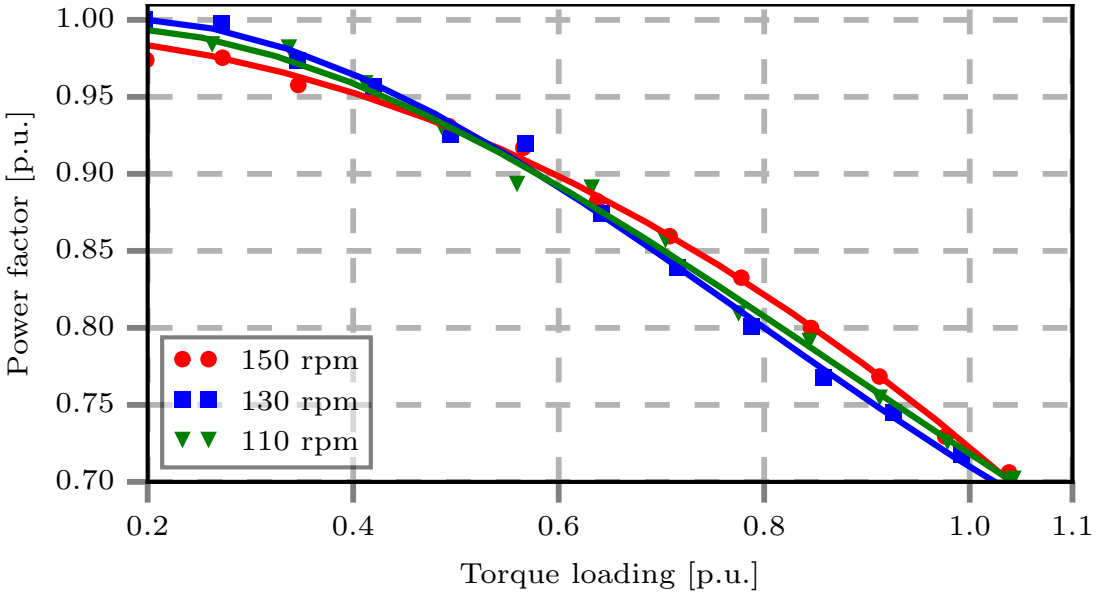

Figure 5.25: Experimental power factor.

The PMV machine prototype is again shown in Fig. 5.27 together with the benchmark PMSG prototype, where their comparative size approximation can also be observed. While the PMSG has a relatively shorter stack and winding overhang axial length, the PMV has a smaller diameter, and ultimately less volume. Since the two machines have an equivalent torque output, it implies that the PMV machine's torque density is superior to that of the PMSG. Fig. 5.28 illustrates that the measured cogging torque of PMV is smaller than that of the PMSG.

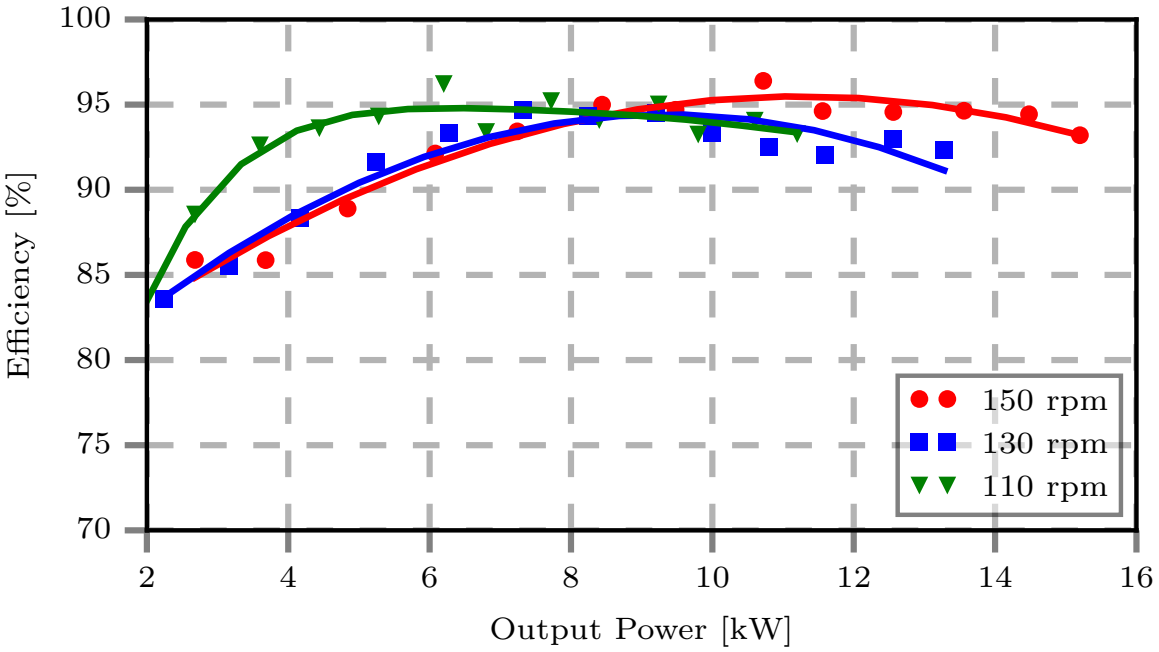

Figure 5.26: Efficiency at increasing power for two constant rotational speeds.

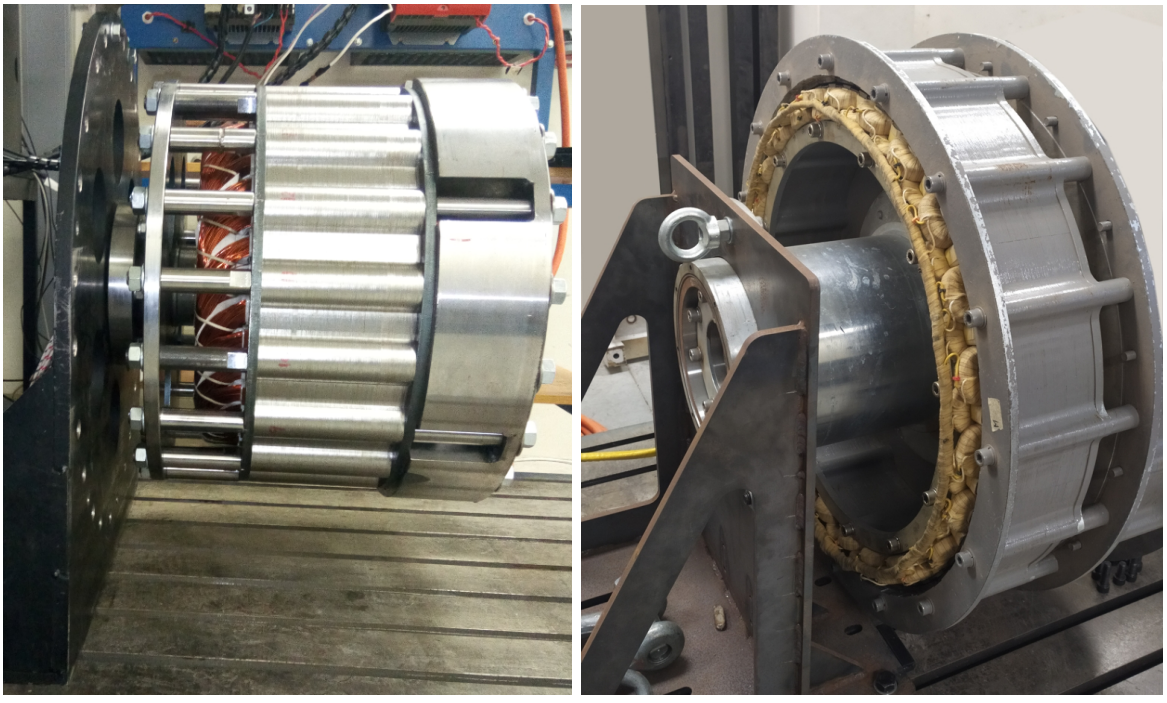

(a) (b)

Figure 5.27: Machine prototypes: (a) PMV machine (b) PMSG machine.

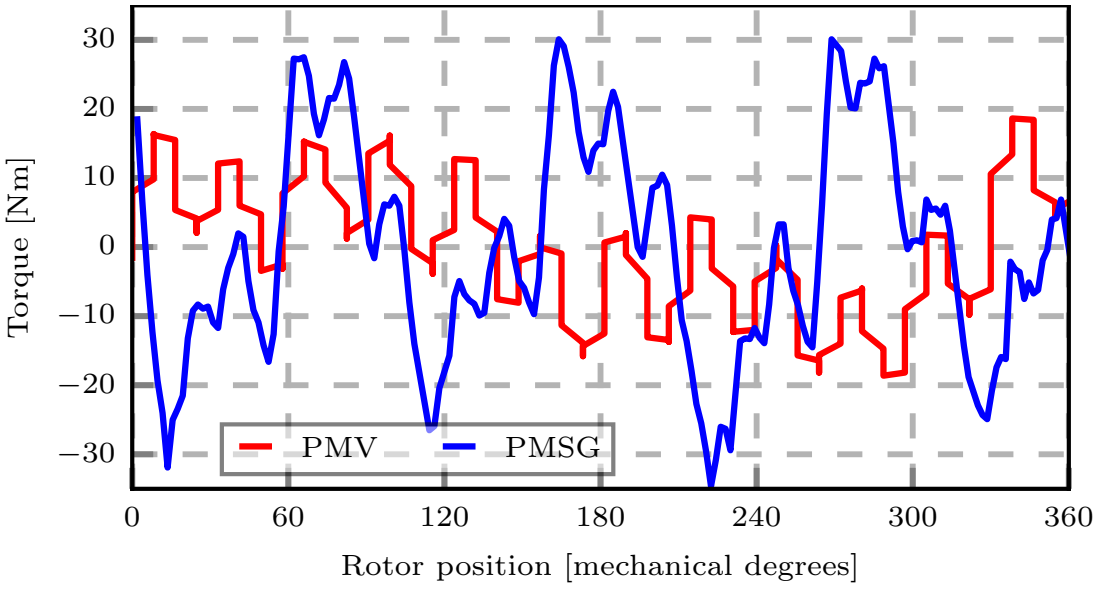

Figure 5.28: Measured cogging torque comparison.

Chapter 6

High Power PMV Machines: Design and Evaluation

This chapter aims at studying the feasibility of implementing the PMV machines at a utility scale wind energy applications. To achieve this goal, a 3 MW PMV machine will be designed and evaluated against a conventional PMSM machine of similar power ratings. For modern large wind turbines, the increasing in size and weight has made it more challenging to lift and mount a nacelle onto the top of the tower. Thus, a key design objective of wind turbine manufacturers is to reduce the size and weight of the nacelle and its contents. Amongst various criteria factors available for comparing wind generator topologies, the electromagnetic active material weight, total volume and cost were chosen as the indexes of main interest. That's because the decrease in total volume relates to the compactness of the machine, and also indirectly improves on the volumetric torque density. On the other hand, the lighter machine is always a preferred choice in many applications including wind energy conversion, and the total active weight can be easily translated into the machine's cost estimation if the price per-kilogram of each constituent material is known.

As in the previous chapters, it should be noted that the mechanical integrity of each component is not simultaneously optimized or continually checked during the electromagnetic optimization process, but, where applicable, the minimum dimensions are set as constraints to ensure manufacturability. Furthermore, the mechanical support structure of the machine is not considered in either total mass or volume. The generator input speed and output efficiency are set to be equal across all the designed machines to create a common ground for comparison. The torque ripple and cogging torque are other important parameters to be observed during the process, but they are not directly optimized.

6.1 Design Specifications

There is a substantial amount of research regarding the PMV machines in the literature with majority of it firmly supported by the developed and tested prototypes. However, most of it focuses on sub-kilowatt machine designs. This leads to the analysis and even comparison of these machine types being limited to within small-scale applications only, leaving much desire of knowledge about large machines' potential. Accordingly, in this chapter, the PMSMs are used as a reference guide to a number of main parameters' ranges that could be applicable to a certain output level of generator, such as input speed, oper-

ating frequency, total outer diameter and stack length, etc. So, a summary of literature on PMSMs specifically in regard to their active material weight and volume composition is given before the performance specifications for the PMV machines can be drawn.

Since the optimization objectives are concerned with the reduction of active material weight and volume, a presentation of these characteristic parameters for a PMSM is given in Fig. 6.1 as obtained from the literature. This is done for a 1 MW, 3 MW and 5 MW machine output levels to indicate their characteristic relationship against rating up-scaling as well. As these machines were optimized by different researchers based on various specifications, constraints and algorithms, there is a bit of variance in their performance at each rated level. Hence the ranges in the figure indicate the dispersion of active weight and volume highlighting the minimum and maximum values as obtained from the relevant literature, and sometimes the distribution is not necessarily uniform within that range. By considering their averages, both the active material weight and volume shows somewhat linear trend against the machine power rating. Furthermore, it appears from Fig. 6.1 that about 16.5 tons mass and 20 m^3 volume are deemed reasonable for a 3 MW direct-drive PMSM generator. Even though an air-gap radius would be more logical to consider for these radial flux machines as it relates more closely to the torque rating, the total volume was instead used to indicate the approximate space requirement of the machines.

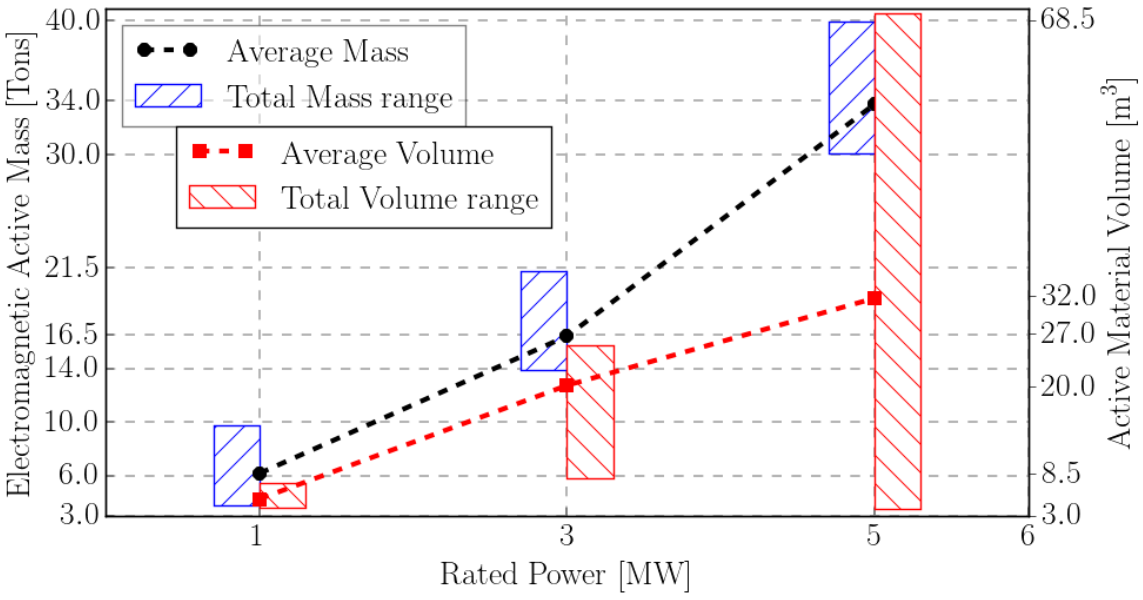

Figure 6.1: Total active mass and volume of PMSM as function of power rating found from the literature [66–73].

A break down of different material types contributing to the machines' active weights provided in Fig. 6.1 is also shown by Fig. 6.2. As seen in the figure, the lamination mass is always the most dominant as it takes at least 60 % of the total mass. It should be noted that for the winding mass and volume, the type of the stator winding arrangement plays a major role when the end-winding mass is included in the active mass estimation. For instance, the over-hang winding weight of the overlapping stator type may double the total winding mass in short stacked machines as opposed to that of tooth concentrated winding type which would add just a small portion. On the other hand, the PM material contributes the least percentage mainly because of its smaller volume requirement relative

to other material types and also because of its slightly lower mass density. On the same note, the higher mass share taken by the lamination material also means that it occupies the biggest volume because it has slightly less mass density than the winding material (copper). Therefore, Fig. 6.2 shows that the lamination material is the main deciding factor on the PMSM machine's active weight.

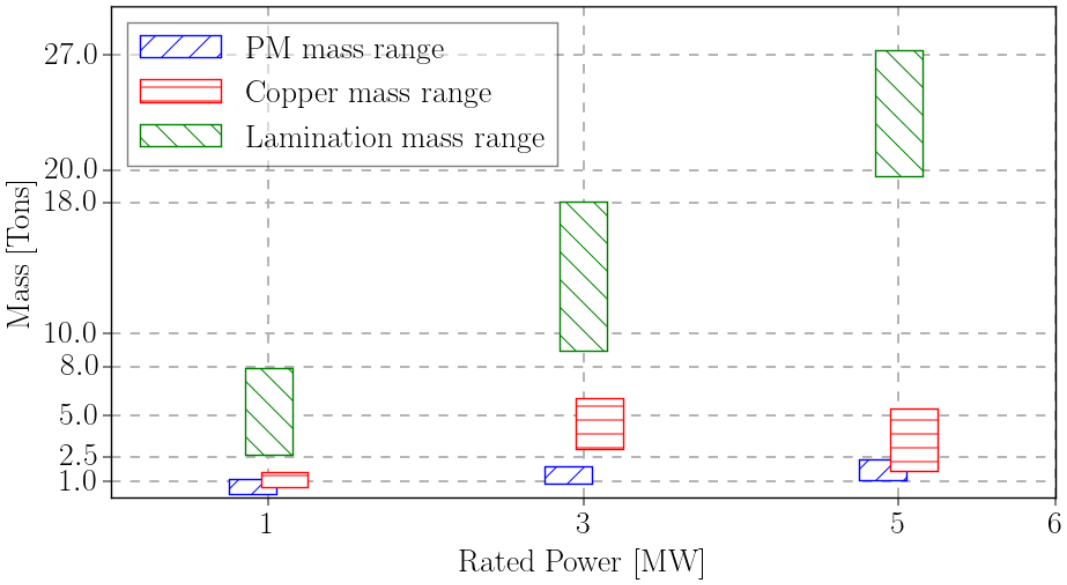

Figure 6.2: Different active material weight distribution vs. power rating of PMSM [66–73].

In order to estimate the cost of the active materials in PMSM machine, the specific cost of each material has to be known. But, it can be a bit tricky to find reliable values because the material cost may vary with different suppliers and material grades. It gets even tougher for the PM material as the prices fluctuate more significantly [171]. Therefore, the figures provided in Table 6.1 are rough approximations of the material prices used in this study, which may be slightly different to the market values. Based on the cost-per-kilogram indicated in Table 6.1, the cost distribution of the active materials is plotted in Fig. 6.3. It can be seen that, even though the PM material mass is the smallest, it has the largest share on the machine material cost. This means that minimizing the total mass as a whole may not be adequate to reduce the machine cost. The PM material may need to be specifically optimized for that purpose.

Table 6.1: Approximate costs of different materials for PMSM components [85].

Material	**Cost per kilogram ($/kg)**
Silicon steel (Lamination)	2.0
Copper (Winding)	6.67
Neodymium Iron Boron (PM)	50.0

Based on the information drawn from the available PMSM literature, the main design specifications are provided on Table 6.2. A minimum efficiency of 94 % is specified for 300 kW machines or less, while 95 % is required for 1 MW machines and above. As the output capacity of the machine is increased to the mega-Watt level, the available wind speed distribution, generator physical size and that of turbine blades dictates the rated speed be decreased accordingly and the frequency should follow similar trend to limit the

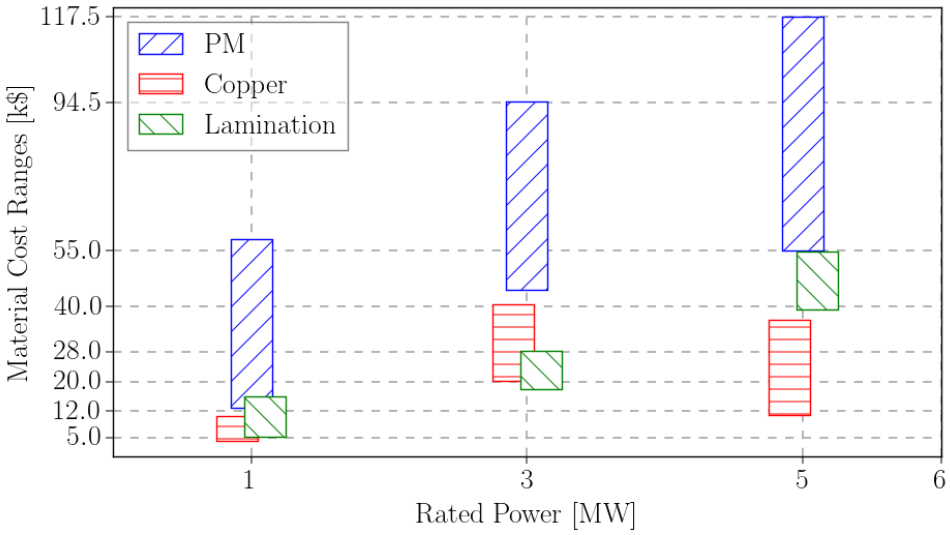

Figure 6.3: Material cost breakdown vs. power rating [66–73].

core-losses. Theoretically, larger air-gap radius would also be needed to accommodate high number of poles and handle large input torque from the blades. But factors such as available nacelle size, manufacturing and logistic constraints put the upper limits as to how large a machine can be. So, the total outer diameter (D_{out}) of active volume is considered in this case to give an approximate size of machine, and the air-gap radius will be determined by the optimization variables. It is assumed that no special cooling methods will be implemented for the machines, hence an armature current density of $5\,A/mm^2$ is set to be the upper limit as for a natural convection air-cooled machine. Considering the fact that surface-mounted PMs are used on the rotor, a reasonable air-gap length corresponding with machine size should be selected to reduce strong magnetic attraction forces between the stator and rotor and make it easier to maintain uniform length around the circumference during construction. It is generally selected to be around 0.1 % of the total diameter.

Table 6.2: Main design specifications of machines at different power levels [66–73].

Parameter	60 kW	300 kW	1 MW	3 MW
Maximum diameter (m)	1.2	2.5	3.5	5.0
Air-gap length (mm)	3.0	4.0	4.0	5.0
Rated speed (rpm)	80	50	30	20
Efficiency (%)	≥94	≥95	≥95	≥95
Current density (A/mm^2)	≤5	≤5	≤5	≤5

A list of candidate pole-slot combinations for each category of the output power capacity is provided on Table 6.3. The pole-slots are selected based on the input speed and the expected rated frequency. As indicated on the table, the combinations are further grouped into two frequencies. The lower frequency corresponds to that of a conventional direct-drive PMSM at each power level while the other one matches that of the medium speed PMSM with single-stage gearbox. The basic idea behind this, is to evaluate the performance of the PMV machine when it is operated at the direct-drive and medium speed PMSM frequency conditions, with similar input speed and gear ratio. This is because a

PMV machine looks rather similar to a conventional direct-drive PMSM structurally, but it incorporates magnetic gearing principle in its operation.

Table 6.3: Investigated pole-slot combinations for distributed overlap-winding and two-slot pole-pitch concentrated PMV machines.

Power-rating	Average Frequency*	Stator slots (Q_s)	Stator(p_s) pole-pair	Rotor(p_r) pole-pair	Pole ratio	slots/pole /phase(q)
60 kW	40 Hz	36	8	28	3.5	0.75
		36	6	30	5.0	1.0
		36	4	32	8.0	1.5
		36	3	33	11.0	2.0
	60 Hz	60	14	46	3.29	0.71
		54	9	45	5.0	1.0
		54	6	48	8.0	1.5
		48	4	44	11.0	2.0
300 kW	30 Hz	48	13	35	2.69	0.62
		42	7	35	5.0	1.0
		45	5	40	8.0	1.5
		42	4	38	9.5	1.75
	60 Hz	96	23	73	3.17	0.70
		84	14	70	5.0	1.0
		81	9	72	8.0	1.5
		84	8	76	9.5	1.75
1 MW	30 Hz	84	20	64	3.2	0.70
		72	12	60	5.0	1.0
		75	10	65	6.5	1.25
		72	8	64	8.0	1.5
	60 Hz	162	40	122	3.05	0.68
		144	24	120	5.0	1.0
		135	18	117	6.5	1.25
		135	15	120	8.0	1.5

* The frequencies for some individual pole/slot combinations may differ to the indicated average values by ± 2 Hz.

- The rows highlighted in gray are the two-slot concentrated winding (CW) machines while all other combinations belong to the distributed overlap-winding (OW) machines.

6.2 Design Optimizations

It was realized during the initial stages of optimization for these large machines that the gradient-based algorithms were not sufficiently effective due to their tendency of getting stuck in local optimum points. This trouble persisted even when the multi-start method with several number of random starting points was being applied. An alternative was to use genetic based optimization algorithm. However, this technique is time consuming because it needs a large number of generations to obtain the best optimum solutions. Therefore, the two algorithms highlighted in chapter 4, that is the NSGA-II and MMFD are implemented at two sequential steps to obtain one best final solution.

In this hybrid optimization approach, the NSGA-II is initially used to determine the search region that is believed to contain the global optimum within it. Once in this general vicinity of the global optimum, the MMFD is used with the NSGA-II's results as the starting point to quickly locate the precise optimum point by further zooming into the solution area. That is, one best solution from NSGA-II can be used as an initial input to MMFD or a number of different final results including the best one can be used as starting points just like in multi-start method with gradient-based algorithms. In this way, the two algorithms are combined and efficiently employed to find a true optimum point within much reasonable time. That is because, since the MMFD started from an already improved point, it will quickly converge with less number of evaluation iterations than what would be required if NSGA-II would be used alone to find the very best point. Figure. 6.4 illustrates the work-flow of this optimization technique.

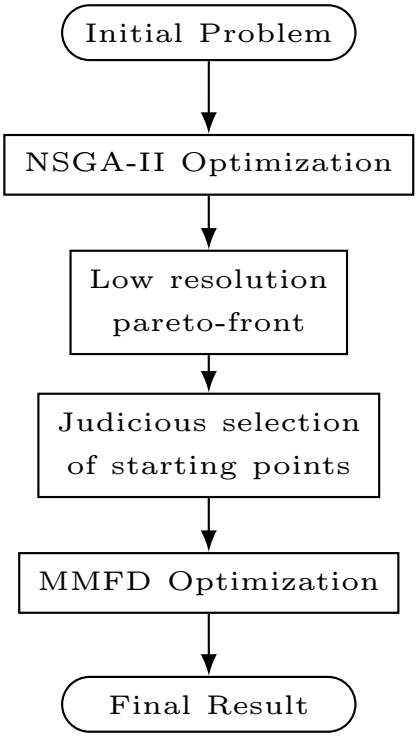

Figure 6.4: Hybrid optimization technique work flow.

In NSGA-II, a number of user-adjustable operators has to be fine tuned based on the characteristics of the optimization problem in order to enhance the algorithm's efficiency and reliability. The settings of these specific parameters are represented in Table 6.4 for the optimization of all machines from 60 kW to 3 MW studied in this chapter. A fixed initial population size of 60 was also used for all optimization trials. This value is five-times the number of optimizations variables and it was chosen based on the reason that according to NSGA-II theory, the population size has to be at least three-times the variable number to provide search space with adequate variable combinations. It should also be kept in mind that a too big populations size would drastically increase the number of solver evaluations and optimization time. The maximum number of generations was set to 600 for smaller machines up to 1 MW and increased to 1200 for 3 MW machines because the purpose of the NSGA-II in this case was just to identify the zone of global optimum but not to arrive at an absolute optimum point which would definitely need a

much larger value. The mutation probability was set to 0.0833, which is the reciprocal of the variables number (12) as per the relevant theory of NSGA-II as well [64].

Table 6.4: NSGA-II user adjustable parameters' set values.

Parameter	**Value**
Initial population size	60
Maximum iterations	600 - 1200
Probability of mutation	0.08333
Disindex of mutation	12
Probability of cross-over	0.99
Disindex of cross-over	16

A comparison of the two optimization techniques (i.e MMFD and NSGA-II) and a hybrid method is shown in Table 6.5. The computational performance is based on a desktop computer with an Intel Core i7, CPU @ 3.6 GHz and RAM of 16 GB. A typical solution time for the $1/40^{\text{th}}$ FE model is about 3 seconds, although it drastically varies during the optimization process depending on the available size of the area and mesh to be solved. If a single objective MMFD is implemented, the convergence time is very short (less than an hour) and the simulation iterations are not so many. But the final solution is only optimum on one objective. In addition, a final solution from the gradient-based MMFD depends heavily on the initial variables' values. NSGA-II requires much longer time and many simulation iterations to find a set of optimum solutions on multiple objectives. A hybrid method builds up from NSGA-II's quasi-optimum solutions to quickly converge to optimum point, hence it is more time efficient.

Table 6.5: Computational time indications of two optimization algorithms.

Objectives ⇒	❶ = Min[M_{tot}], ❷ = Min[M_{PM}], ❸ = Max[PF]							
	Initial	MMFD			NSGA-II	Hybrid	NSGA-II	Hybrid
		❶	❷	❸	❶&❷	❶&❷	❷&❸	❷&❸
Lamination mass	16.31	7.70	12.51	11.76	6.21	6.43	9.18	5.78
Copper mass	6.82	3.69	4.19	4.21	3.56	3.56	4.55	4.39
PM mass	1.58	1.13	0.73	2.00	0.90	0.93	1.02	1.09
Total mass	24.70	12.52	17.43	17.97	10.67	10.92	14.75	11.26
Power factor	0.50	0.49	0.41	0.75	0.49	0.49	0.57	0.52
Sim. iterations		792	698	579	221520	72450	180240	72614
Time (hours)		0.65	0.71	0.64	126.22	28.30	111.72	28.69

⇒All the mass values have units of tons.

6.3 Preliminary Optimizations Results

The PMV machines are designed and optimized for rated powers of 60 kW, 300 kW and 1 MW. A comparison is made of the power factor and the active weights of the overlapping-winding type machines, at a number of different gear ratios. This is to investigate the

relations between the gear ratios and the design objectives of large power PMV machines. Figures 6.5, 6.6 and 6.7 show how the active mass varies with the power factor for 60 kW, 300 kW and 1 MW designs, respectively. For most designs on either the lower or higher frequency, a small change in power factor results in a significant difference in total active mass.

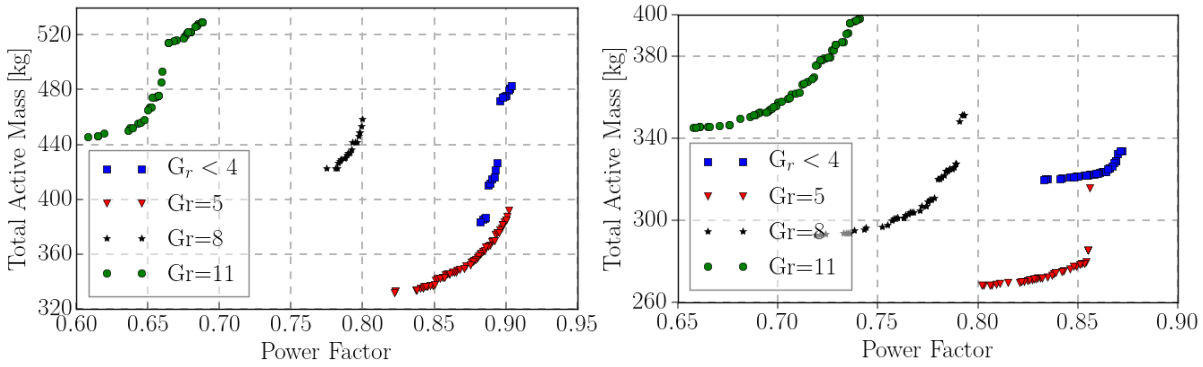

Figure 6.5: Total active mass versus power factor for 60 kW machine (a) at 40Hz and (b) at 60 Hz.

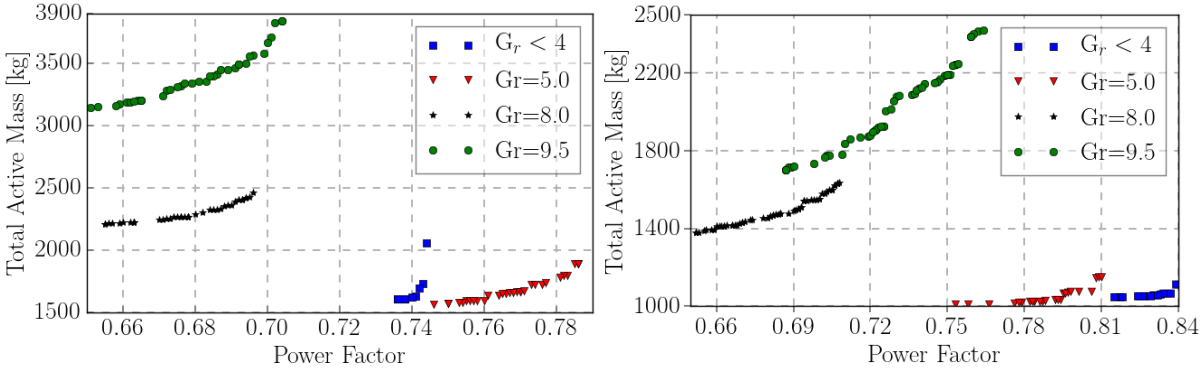

Figure 6.6: Total active mass versus power factor for 300 kW machine (a) at 30Hz and (b) at 60 Hz.

In distributed overlap winding (OW) machines with a gear ratio ($G_r \geq 5$), there is a decreasing tendency of mass while the power factor is improving, as the gear ratio is decreasing. These Pareto fronts clearly reveal the competing relationship between the active mass and power factor in PMV machines with the increasing output power capacity.

According to the optimization procedure explained earlier, the Pareto fronts are used to just indicate the regions of possible optimum designs, so a number of points are selected for further optimization using gradient-based algorithm to find an absolute optimum design for each pole-slot combination. The results from the second stage optimization are provided in Tables 6.6, 6.7 and 6.8 for 60 kW, 300 kW and 1 MW, respectively. Included in these tables are the machines' performance characteristics and their main dimensions. Both the stator and rotor yokes are always thinner in higher frequency designs compared to the lower one, and this is because lower frequency designs have smaller pole-pair number and wider pole-pitches. Hence thicker yokes would be necessary to provide larger area for

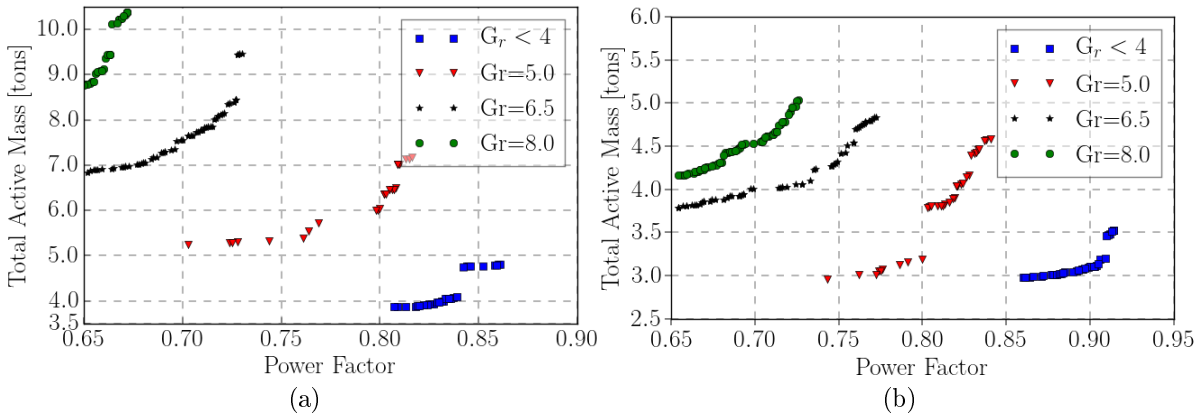

Figure 6.7: Total active mass versus power factor for 1 MW machine (a) at 30Hz and (b) at 60 Hz.

the flux return paths, thereby reducing the flux density and subsequently the core losses. Again, most machines have wide open slots to enhance the modulation effect, which also agrees well with theoretical predictions.

Table 6.6: Optimized parameters and some performance indications of investigated pole-slot combinations for 60 kW machines.

	Pole-ratio < 4		**Pole-ratio $= 5$**		**Pole-ratio $= 8$**		**Pole-ratio $= 11$**	
Parameters	**40 Hz**	**60 Hz**	**40 Hz**	**60 Hz**	**40 Hz**	**60 Hz**	**40 Hz**	**60 Hz**
Rotor yoke height (mm)	14.29	10.00	14.82	10.95	24.25	15.55	30.13	22.34
Rotor PM height (mm)	6.00	5.54	5.39	5.42	6.07	6.00	6.83	6.21
Stator yoke height (mm)	14.09	10.34	13.90	10.12	23.82	14.34	34.10	21.74
Stator tooth length (mm)	46.05	41.39	30.79	30.02	35.16	26.02	37.61	23.42
Magnet pole span	0.80	0.87	0.90	0.88	0.83	0.85	0.78	0.86
Slot opening ratio	0.70	0.64	0.66	0.69	0.84	0.75	0.95	0.75
Stator slot angle ratio	0.71	0.72	0.75	0.78	0.76	0.78	0.71	0.78
Outer diameter (m)	0.945	0.951	0.819	0.881	0.941	0.946	1.009	0.966
Stack length (m)	0.235	0.228	0.480	0.240	0.228	0.220	0.202	0.209
Inner diameter (m)	0.779	0.810	0.684	0.762	0.756	0.816	0.785	0.812
Power factor	0.81	0.83	0.75	0.76	0.67	0.70	0.66	0.66
Efficiency	94.64	94.66	94.50	94.63	94.77	94.73	95.16	94.84
Torque ripple (%)	1.00	0.61	13.62	10.64	0.74	0.86	1.06	1.12
Cogging torque (%)	0.60	0.36	3.46	9.20	0.33	0.35	1.09	0.86
Silicon steel mass (kg)	204.27	154.50	178.34	132.88	264.66	166.78	326.20	221.55
Copper mass (kg)	160.93	125.77	125.95	112.11	130.46	106.47	166.52	116.00
PM mass (kg)	24.04	23.94	23.94	22.92	24.00	24.03	24.06	24.00
Total active mass (kg)	389.24	304.21	328.23	267.91	419.12	297.31	516.78	361.55

The total volume excluding the over-hang winding axial length can be approximated from total diameter and stack length. In addition, most machines, especially at 1 MW level, have an aspect ratio of around 0.20 as depicted by Fig. 6.8, which means the stack

Table 6.7: Optimized parameters and some performance indications of investigated pole-slot combinations for 300 kW machines.

	Pole-ratio < 4		Pole-ratio $= 5$		Pole-ratio $= 8$		Pole-ratio $= 9.5$	
Parameters	**30 Hz**	**60 Hz**	**30 Hz**	**60 Hz**	**30 Hz**	**60 Hz**	**30 Hz**	**60 Hz**
Rotor yoke height (mm)	19.09	10.26	25.31	12.72	39.64	21.27	54.59	21.70
Rotor PM height (mm)	9.77	9.22	10.04	7.17	10.09	8.78	8.530	8.15
Stator yoke height (mm)	18.56	10.27	23.63	10.42	39.29	19.09	53.72	19.83
Stator tooth length (mm)	56.35	49.57	40.59	28.73	39.10	29.62	41.96	27.05
Magnet pole span	0.83	0.81	0.86	0.84	0.80	0.83	0.76	0.76
Slot opening ratio	0.64	0.60	0.69	0.68	0.75	0.82	1.00	1.00
Stator slot angle ratio	0.66	0.72	0.75	0.80	0.74	0.79	0.65	0.65
Outer diameter (m)	1.709	1.652	1.697	1.785	1.883	1.918	2.122	2.077
Stack length (m)	0.413	0.457	0.391	0.441	0.381	0.401	0.425	0.415
Inner diameter (m)	1.493	1.485	1.490	1.659	1.619	1.752	1.796	1.916
Power factor	0.73	0.72	0.70	0.72	0.65	0.65	0.66	0.65
Efficiency	95.55	95.52	95.30	95.38	96.65	95.67	96.69	95.77
Torque ripple (%)	2.35	0.41	15.23	15.33	0.89	0.61	0.64	0.59
Cogging torque (%)	0.17	0.10	5.58	8.93	0.18	0.34	0.39	0.29
Silicon steel mass (tons)	0.908	0.601	0.893	0.539	1.438	0.846	2.450	0.959
Copper mass (tons)	0.572	0.479	0.523	0.355	0.616	0.309	0.556	0.312
PM mass (tons)	0.130	0.130	0.130	0.110	0.130	0.129	0.130	0.130
Total active mass (tons)	1.610	1.209	1.546	1.004	2.184	1.284	3.136	1.401

lengths are always shorter relative to the diameters. This has an implication that the end-winding resistance and inductance effects will be more prominent in distributed OW winding machines with long over-hang winding lengths.

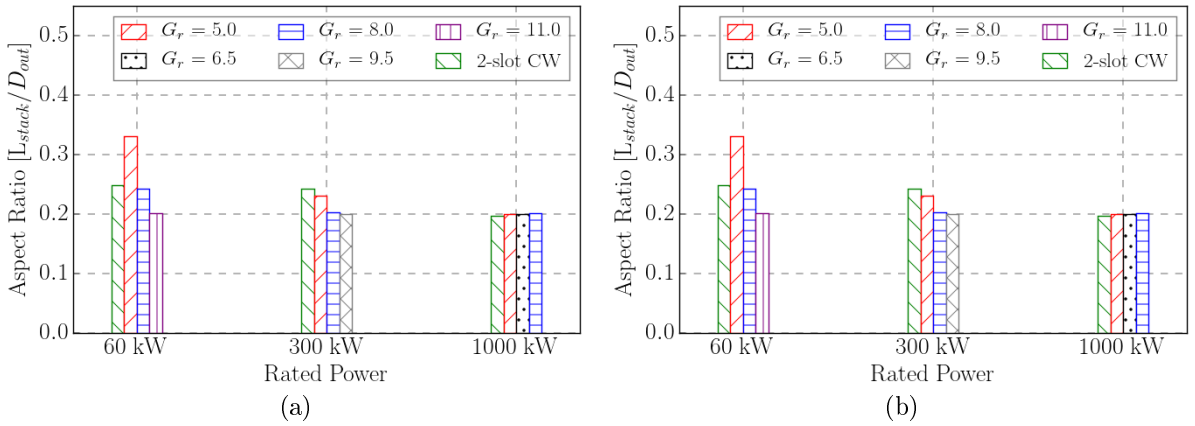

Figure 6.8: Aspect ratios of designed machines at different output power ratings (a) operating frequency at 30 Hz (b) operating frequency at 60 Hz.

Figures 6.9, 6.10 and 6.11 illustrate the trend of active mass and power factor as a function of gear ratios at two different frequencies. It can be clearly seen that the mass increases with the gear ratio while the power factor decreases. It should be remembered

Table 6.8: Optimized parameters and some performance indications of investigated pole-slot combinations for 1 MW machines.

	Pole-ratio < 4		Pole-ratio = 5		Pole-ratio = 6.5		Pole-ratio = 8	
Parameters	**30 Hz**	**60 Hz**	**30 Hz**	**60 Hz**	**30 Hz**	**60 Hz**	**30 Hz**	**60 Hz**
Rotor yoke height (mm)	19.80	10.94	25.12	13.16	37.73	17.73	45.16	19.11
Rotor PM height (mm)	12.31	8.16	9.88	9.11	10.84	9.58	11.77	8.81
Stator yoke height (mm)	31.28	10.00	22.99	12.63	40.78	19.97	35.84	17.31
Stator tooth length (mm)	43.92	32.08	33.63	27.09	42.62	30.52	40.79	23.930
Magnet pole span	0.86	0.86	0.89	0.86	0.83	0.87	0.84	0.90
Slot opening ratio	0.66	0.68	0.67	0.67	0.90	0.85	0.77	0.75
Stator slot angle ratio	0.71	0.73	0.79	0.82	0.69	0.74	0.73	0.74
Outer diameter (m)	3.039	3.283	3.295	3.301	3.339	3.430	3.198	3.500
Stack length (m)	0.600	0.657	0.659	0.660	0.668	0.694	0.642	0.719
Inner diameter (m)	2.844	3.153	3.104	3.172	3.075	3.275	2.907	3.353
Power factor	0.78	0.81	0.66	0.72	0.66	0.66	0.65	0.66
Efficiency	95.70	95.72	95.62	95.67	96.88	96.00	97.66	96.53
Torque ripple (%)	1.53	1.25	16.60	9.09	0.95	0.70	1.25	1.82
Cogging torque (%)	0.28	0.24	8.68	3.50	0.17	0.25	0.54	0.43
Silicon steel mass (tons)	2.156	1.531	2.849	1.551	4.550	2.349	4.75	2.554
Copper mass (tons)	1.152	0.892	1.281	0.82	1.205	0.876	1.662	0.924
PM mass (tons)	0.447	0.352	0.441	0.398	0.460	0.459	0.462	0.462
Total active mass (tons)	3.755	2.775	4.570	2.771	6.215	3.684	6.869	3.940

that the minimum constraint on power factor was set to 0.65 during the optimization, and higher gear ratio designs appear to be testing this threshold, giving an impression that it would likely go lower than that if the constraint was relaxed. The power factor gets worse with an increasing output power capacity while the total mass continues to rapidly increase. Hence, the considered pole/slot combinations at 1 MW were selected to have a pole-ratio of utmost 8 as there was no benefit of going higher than that. It is at this rated level that the two-slot concentrated winding (CW) machines with $G_r \leq 5$ appears to be more attractive in terms of power factor and light weight than the conventional distributed OW machines.

An indication of the average DD PMSM weight is also added on Fig. 6.11 for the purpose of comparing the PMV machines with it. Although not shown on the graph, it is assumed that the PMSM will generally have a power factor that is very close to unity. So, all the PMV designs in this figure have poor power factor comparing with the PMSM. But the distributed OW PMV machines with gear ratio of 5 and the 2-slot-pitch CW machines are much lighter than the DD PMSM. That is, there seems to be a tradeoff between the light weight and power factor in PMV machines.

Focusing onto the distributed OW machines in Fig. 6.11, it may appear as if the pole-slot combinations with gear ratio of 5 are still competitive relative to PMSM, a further look into their performance reveals that they have the highest torque ripples as highlighted in red on the performance tables, and rich EMF harmonics indicated by induced voltage harmonics in Fig. 6.12. The voltage distortion gets even worse as the machine is loaded.

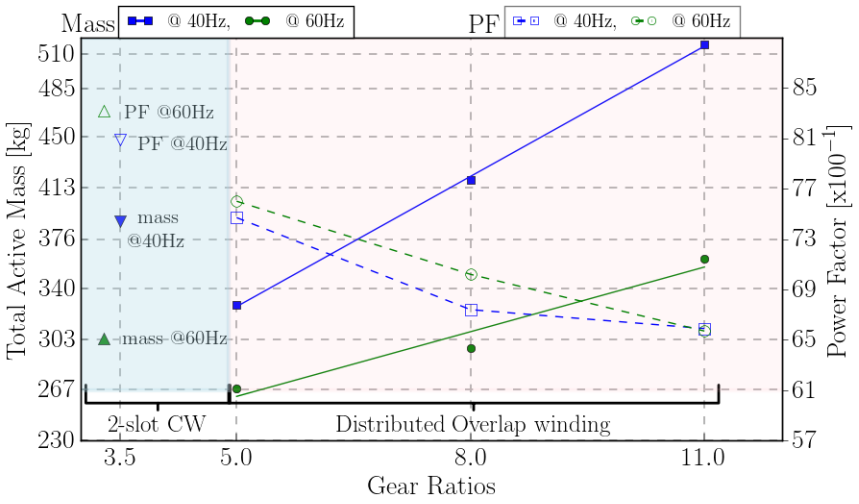

Figure 6.9: Total active mass and power factor vs. pole-ratio for 60 kW machines.

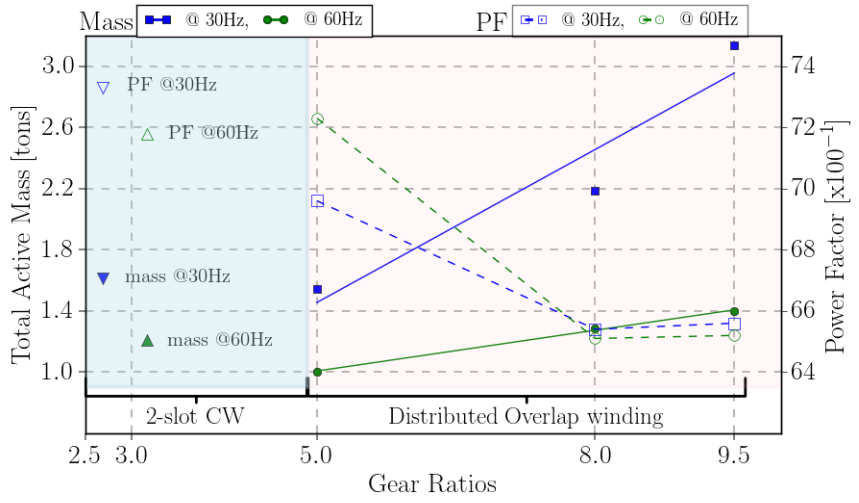

Figure 6.10: Total active mass and power factor vs. pole-ratio for 300 kW machines.

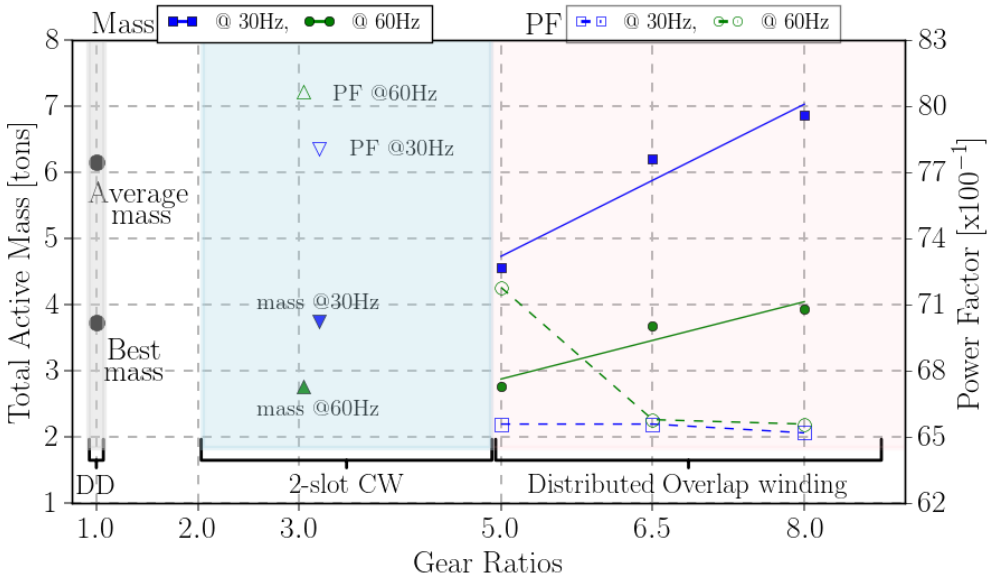

Figure 6.11: Total active mass and power factor vs. pole-ratio for 1 MW machines.

This shows that the 2-slot CW PMV machines are the only competitive options to be considered in power capacities larger than 1 MW.

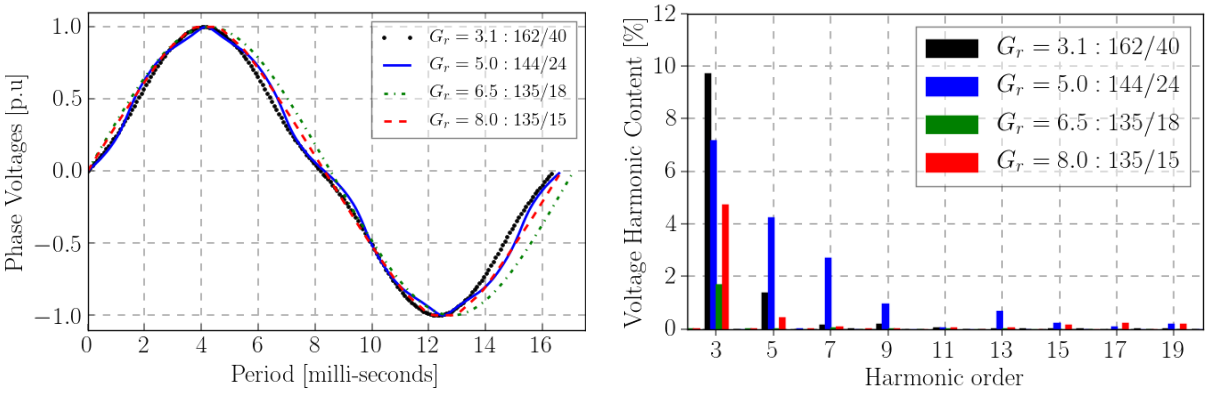

(a) (b)

Figure 6.12: Comparison of per-phase open circuit voltage characteristics of 1 MW designs (a) normalized voltage waveform magnitudes (b) higher order harmonic content percentage.

On the other hand, higher frequency designs are always lighter and have better power factors than their low frequency counterparts at any given gear ratio. Usually, the limit on frequency is imposed by the need to avoid excessive core losses. It was then found necessary to compare the two frequency groups' core-loss characteristics as displayed by Fig. 6.13(b) for 1 MW rating. At this power level, the conventional DD PMSM usually have an operating frequency of 30 Hz. But, looking at the PMV machines with 30 Hz and 60 Hz operating frequencies, there appears to be no significant differences between their resultant core losses. This is because designs with higher frequency comes out to have a much reduced iron volume which then helps to balance out the frequency dependent core-losses. This shows the potential of operating PMV machine at medium-speed frequency range at high power level.

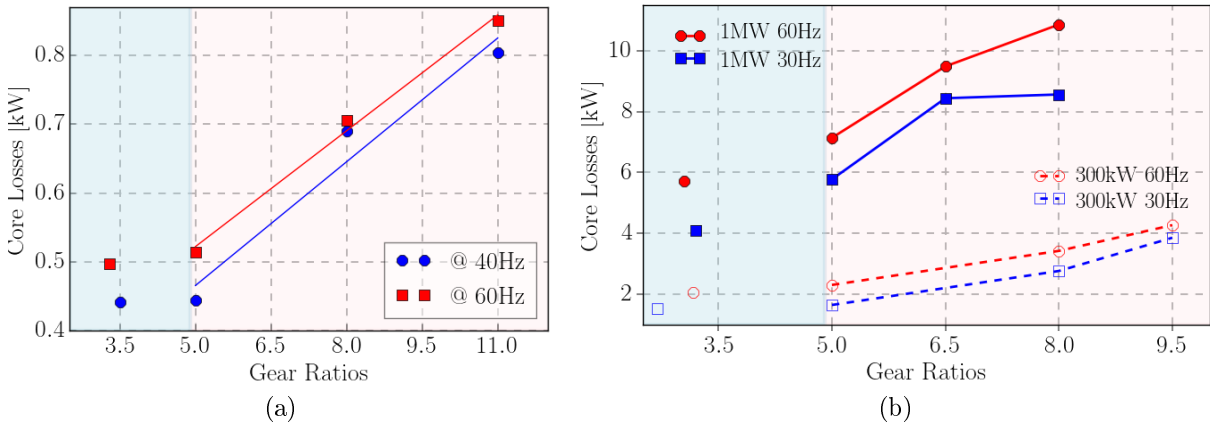

(a) (b)

Figure 6.13: Core losses at different frequencies vs. pole-ratio (a) 60 kW machines and (b) 300 kW and 1 MW machines.

6.4 3 MW PMV Machine Designs

It has been observed from the results of 1 MW machines that PMV machine designs with operating frequency similar to that of their conventional PMSG counterparts offer no significant benefits. Therefore, the decision was made to go for slot/pole combinations that operate at medium-speed frequency ($\approx$ 50 Hz) but with equivalent turbine input speed to the DD-PMSGs, since their core-losses are not so different. That is, in addition to the gearing ratio, the generators' rated speed and output frequency were also the main factors considered in selection of the slot/pole combinations as presented in Table 6.9.

Table 6.9: Investigated slot/pole combinations for 3 MW PMV machines.

Winding configuration	**2-slot concentrated**		**Distributed overlapping**		
Stator slots (Q_s)	270	276	240	240	225
Stator pole-pairs (p_s)	67	68	40	32	25
Rotor pole-pairs (p_r)	203	208	200	206	200
Pole-ratio (G_r)	3.03	3.06	5.00	6.50	8.00
Slots per pole per phase (q)	0.67	0.68	1.00	1.25	1.50
Rated frequency [Hz]	50.75	52.00	50.00	52.00	50.00

In order to verify if the chosen PMV machines would still be able to deliver the minimum efficiency requirement for a 3 MW output capacity, some test optimizations were run with a relaxed constraints on volume and PM material mass. Figure. 6.14 presents the Pareto-front of total active machine's weight as a function of their output efficiencies. It can be seen that there are design points available for all the combinations at efficiencies of 95 % and above, while their weights are still within the range of PMSGs. Although some design points get a little heavier, it seems possible to have an efficiency of more than 96 % and keep the active components' mass within the reasonable range. These results further confirms that the frequency dependent losses are not a major burden to the selected combinations' efficiency. However, there are other performance characteristics that needs to be explored during the design optimizations besides the output efficiency alone.

For the PMV machine, the power factor is one of the performance indexes that always need a special attention as it can come out to be detrimental if not properly designed. With that said, Fig. 6.15 shows the Pareto-front between the total active mass and power factor for the five PMV machine slot/pole combinations and having different gear ratios. During the optimizations, the upper limit to the PM material usage was set to be equal to the average PM mass requirement of the reference PMSGs indicated in Fig. 6.2, and the minimum efficiency was set to be 95 %. Since the PMV machines have similar input speeds to those of the PMSGs, this means a fairly similar ground is created for the comparison purposes in these two machine types to be presented later in this section. From the figure, the higher gear ratios seemingly lead to lower power factors and heavier total masses. Furthermore, it is realized that some of the PMV slot/pole combinations can lead to poor power factors with values less than 0.4. This further asserts the point that at output power capacities larger than 1 MW, it is always better to go for lower gear ratio if any benefits are to be obtained from this type of machine.

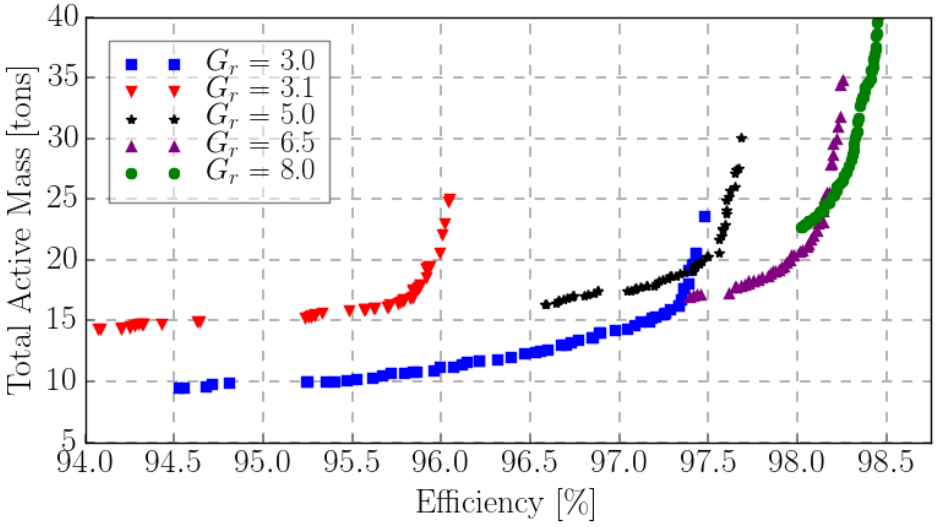

Figure 6.14: Total active mass vs. efficiency for 3 MW PMV machines.

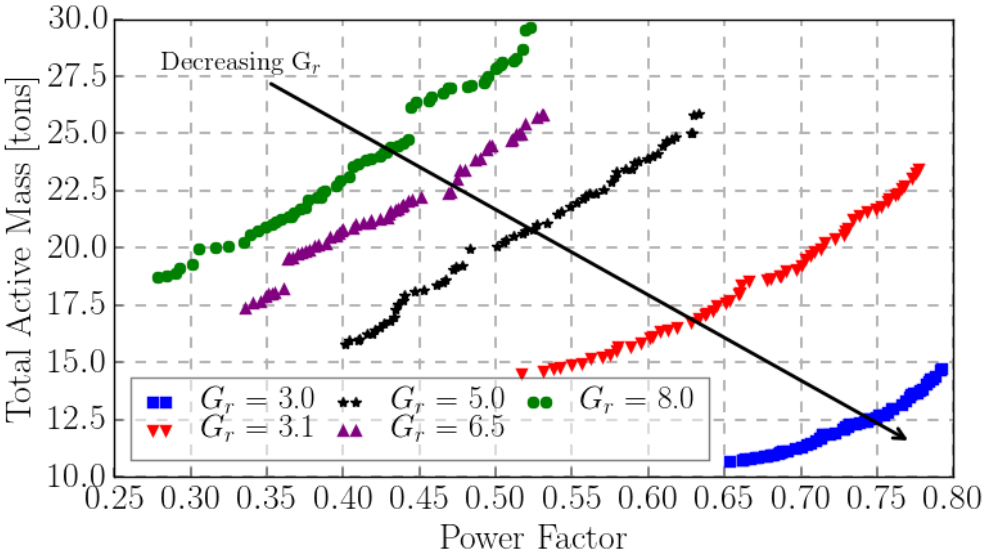

Figure 6.15: Total active mass vs. power factor for 3 MW PMV machines.

In order to compare the PMV machines with the PMSG, one design point for each slot/pole combination was taken from the Pareto-fronts given in Fig. 6.15 and further optimized. The objective in this case was to have a lighter and cheaper PMV machine with best possible power factor. Since the PM material has the highest cost-per-kilogram amongst all the constituent materials, the total machine cost was indirectly optimized by minimizing this material type. Therefore, machines' total mass was minimized at three values of the PM material content, namely 1.0, 1.4 and 1.9 tons. These points were of interest because the average PM content of the considered PMSGs from the literature is found to be around 1.4 tons, and the benchmark PMSG to be compared to the PMV machine has a PM mass of 1.9 tons. It was also decided to test if a PM mass content of PMV machines can be pushed further down to 1.0 tons.

The results are presented in Figs. 6.16 and 6.17, and on Tables 6.10 and 6.11, with the indicative costs of materials also included. Even though silicon steel used for machine cores has slightly lower mass density than winding copper, it appears to be the deciding

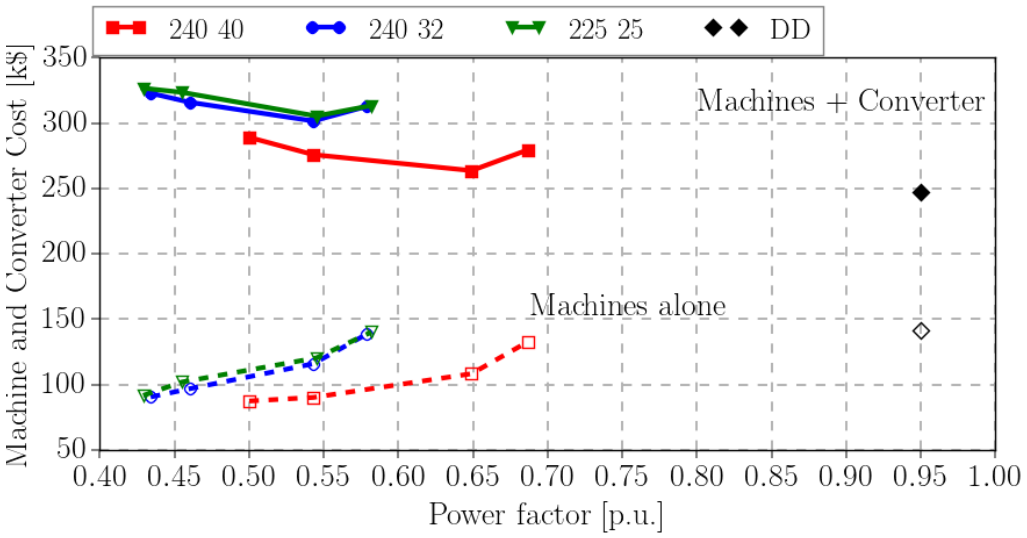

Figure 6.16: Comparison of machine and total system costs for distributed overlapping winding PMV machines.

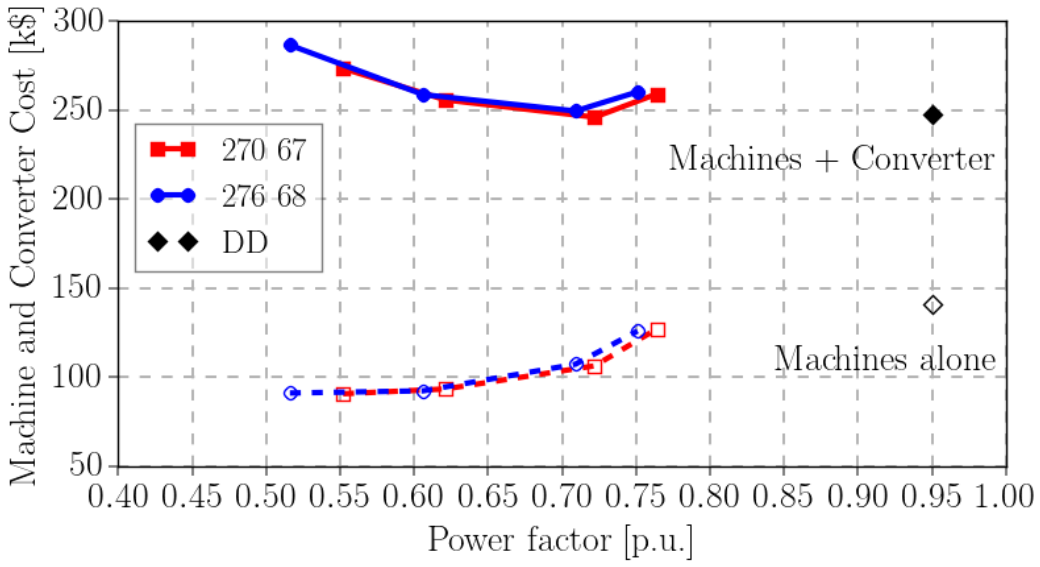

Figure 6.17: Comparison of machine and total system costs for 2-slot concentrated winding PMV machines.

factor when it comes to the total active mass because of its larger volume content in most of the designs. Thus, changing the PM mass has little effect on total active mass, but a significant change can be seen on the power factor. The machines' efficiencies are always higher than minimum constraint of 95 % even though the operating frequency is relatively high. Adding too much PM material renders an increasingly expensive machine while the power factor has small improvement, hence designs having less of this material are more favorable in terms of cost, yet their power factors are poor. Figs. 6.16 and 6.17 show that a cheaper machine with low power factor leads to an expensive system when the power converter costs are included. Thus, to select a good design, a best compromise has to be found between the machine cost and required converter cost.

Table 6.10: Mass and cost comparisons of 3 MW distributed overlap winding PMV machines at different PM mass constraints.

$Q_s/p_s/p_r$	**240/40/200**			**240/32/206**			**225/25/200**		
Pole-ratio	5.0	5.0	5.0	6.5	6.5	6.5	8.0	8.0	8.0
Material Mass contributions (tons)									
Rotor PM	1.00	1.39	1.83	1.00	1.40	1.85	1.00	1.40	1.85
Core iron	7.38	6.98	10.16	9.95	9.71	10.07	10.39	10.36	9.86
Winding copper	3.81	3.74	3.62	4.02	3.98	4.47	4.67	4.41	4.43
Total generator	12.19	12.11	15.61	14.97	15.09	16.39	16.06	16.17	16.14
Performance Information									
Efficiency (%)	96.81	97.06	97.14	96.85	97.08	97.41	97.54	97.77	97.82
Power factor	0.54	0.65	0.69	0.46	0.54	0.58	0.46	0.55	0.59
Machine cost distributions (k$)									
Rotor PM	50.0	69.5	91.5	50.0	70.0	92.5	50.0	70.0	92.5
Core iron	14.8	13.96	20.3	19.9	19.4	20.1	20.8	20.7	19.7
Winding copper	25.4	24.9	24.1	26.8	26.5	29.8	31.1	29.4	29.5
Total generator	**89.3**	**108.4**	**135.9**	**96.7**	**115.9**	**142.4**	**101.9**	**120.1**	**141.7**
PE converter	186.67	155.08	146.09	219.13	186.67	173.79	219.13	183.27	170.85
Total system	275.97	263.48	281.99	315.83	302.57	316.19	321.03	303.37	312.55

Table 6.11: Mass and cost comparisons of 3 MW 2-slot concentrated winding PMV machines at different PM mass constraints.

$Q_s/p_s/p_r$	**270/67/203**			**276/68/208**		
Pole-ratio	3.03	3.03	3.03	3.06	3.06	3.06
Material Mass contributions (tons)						
Rotor PM	1.00	1.39	1.80	1.00	1.39	1.87
Core iron	7.30	6.88	7.60	6.61	7.08	7.13
Winding copper	4.31	3.45	3.49	4.39	3.56	3.70
Total generator	12.61	11.72	12.89	12.00	12.03	12.70
Performance Information						
Efficiency (%)	96.09	95.91	96.13	95.98	95.93	96.30
Power factor	0.62	0.72	0.76	0.61	0.71	0.76
Machine cost distributions (k$)						
Rotor PM	50.0	69.5	90.0	50.0	69.5	93.5
Core iron	14.6	13.8	15.2	13.2	14.2	14.3
Winding copper	28.7	23.0	23.3	29.3	23.7	24.7
Total generator	**93.3**	**106.3**	**128.5**	**92.5**	**107.4**	**132.5**
PE converter	162.58	140.00	132.63	165.25	141.97	132.63
Total system	255.88	246.30	261.13	257.75	249.37	265.13

Figure 6.18 shows the mass distribution of the chosen designs and compares them to the benchmark PMSG. PMV machines with lower gear ratios have a good advantage in terms of total active weight, while there is not so much difference at high gear ratios. In

summary, designing for a lighter machine with reasonable power factor at this power rating, requires choosing a pole/slot combination with lower G_r. This is a slightly different trend to the sub-kilowatt machines where the lowest G_r values are not necessarily the best.

As illustrated in Fig. 6.19, the colour-coded mass scales of the investigated designs for different power ratings are indicated together with their respective gear ratios. Although the lightest designs are invariably associated with a low gear ratio of 5 for power rating up to 1 MW, the relationship between the mass and gear ratios is not very distinctive. However, at 3 MW output capacity, it becomes clear that the lowest G_r has lightest and highest G_r has heaviest mass.

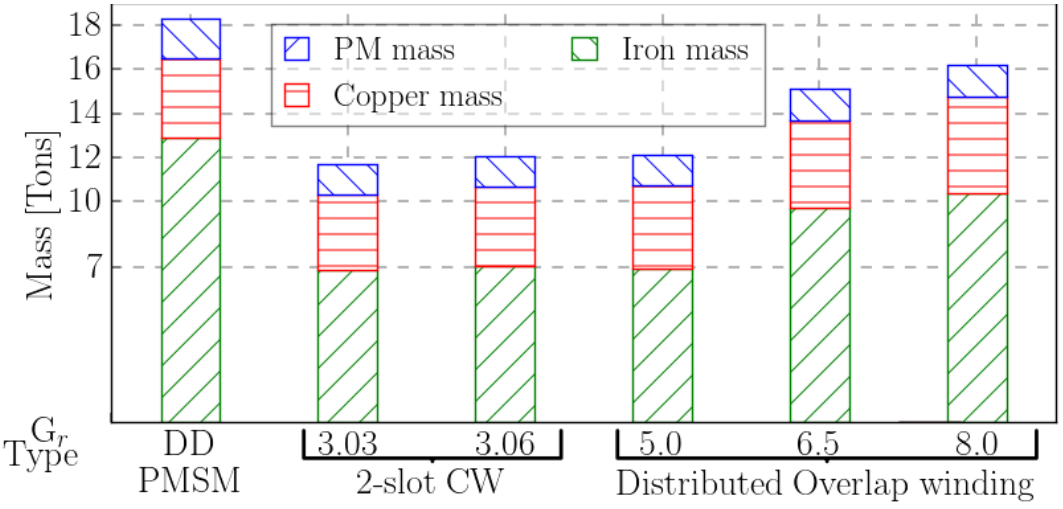

Figure 6.18: Comparison of active material weights of PMV machine and PMSM machine.

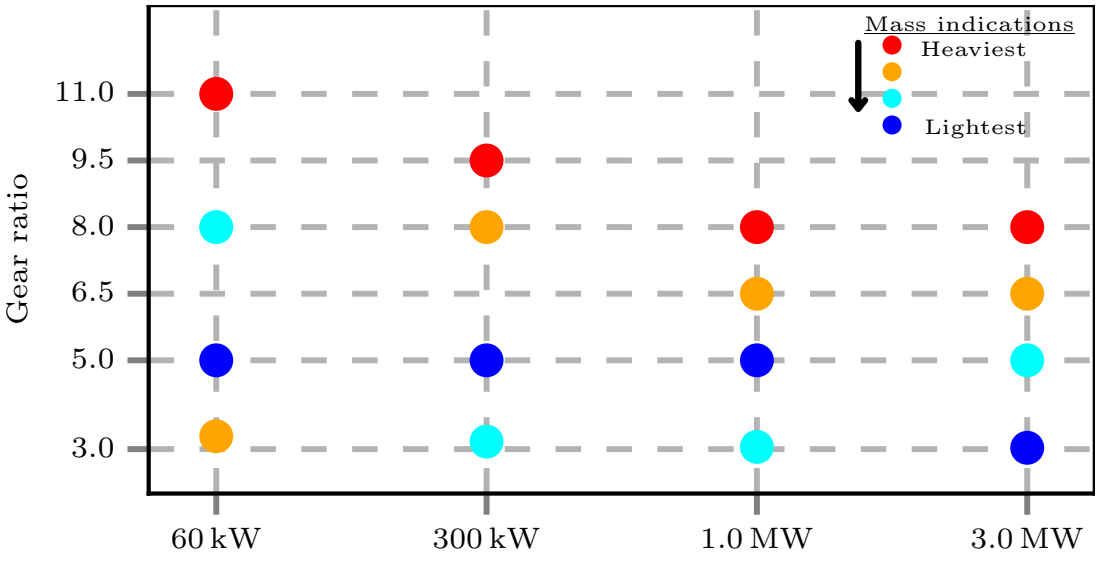

Figure 6.19: Total mass indications as a function of power ratings and gear ratios.

The results in Table 6.12 reveals that the PMV machine on its own can be lighter and cheaper than the PMSG. But when the power converter costs are considered, the overall system costs of PMVs become similar to those of DD PMSMs because of their

high converter rating requirement. It should be noted that a linear inverter costing model was assumed in this study, which may not necessarily reflect the true costs in industry. In the case that the inverter costs follow a stepped increasing pattern with regard to their MVA rating, the cost of PMV generator systems may become competitive for certain power levels. Furthermore, the PMV machines' power factor gets improved if the total volume is allowed to increase with longer stack lengths, but this will inevitably lead to large size machines, which are unfavorable.

Table 6.12: Mass and cost comparisons of different 3 MW PMSG ([66; 70]) and PMV machines.

Machine type	**DD PMSG**		**2-slot CW PMV**		**Distributed OW PMV**		
Rotor/Stator pole-ratio	1.0	1.0	3.0	3.05	5.0	6.5	8.0
Characteristic Information							
Output power (MW)	3.00	3.00	3.04	3.06	3.00	3.04	3.04
Efficiency (%)	95.0	-	95.91	95.93	97.06	97.08	97.77
Power factor	0.93	-	0.72	0.71	0.65	0.54	0.55
Average torque (kNm)	1910.0	-	2006.8	2020.5	1943.5	1981.5	1962.7
Total diameter (m)	5.000	5.00	5.000	5.000	5.000	5.000	5.000
Stack length (m)	1.300	1.190	1.403	1.399	1.378	1.377	1.372
Material Mass contributions (tons)							
Rotor PM	1.90	1.92	1.39	1.39	1.39	1.40	1.40
Core iron	10.30	11.70	6.87	7.08	6.98	9.71	10.36
Winding copper	3.12	3.31	3.45	3.56	3.74	3.98	4.41
Total generator mass	13.38	16.90	11.72	12.04	12.11	15.09	16.18
Machine cost distributions (k$)							
Rotor PM	95.00	96.00	69.50	69.50	69.50	70.00	70.00
Core iron	20.60	23.40	13.74	14.16	13.96	19.42	20.72
Winding copper	20.81	22.08	23.01	23.75	24.95	26.55	29.41
Total generator	**136.41**	**141.48**	**106.25**	**107.41**	**108.41**	**115.97**	**120.13**
PE converter	108.39	106.11	140.0	142.0	155.1	186.7	183.3
Total system	244.8	247.59	246.25	249.41	263.51	388.9	303.43

The dimensions and cross sections of these selected machines are respectively provided in Tables 6.13 - 6.18 and Figs. 6.20 - 6.25. It can be observed that the PMV machines have thin teeth, wide and shallow slots, which may explain why they have less iron content than the PMSGs.

Table 6.13: Optimized parameters for PMV machine: $Q_s/p_s/p_r = 270/67/203$

Dimension	value	Dimension	value
Outer diameter (m)	5.000	Rotor PM height (mm)	9.88
Stack length (m)	1.403	Stator tooth length (mm)	40.95
Inner diameter (m)	4.832	Magnet pole span	0.861
Rotor yoke height (mm)	14.60	Slot opening ratio	0.667
Stator yoke height (mm)	13.20	Stator slot angle ratio	0.674

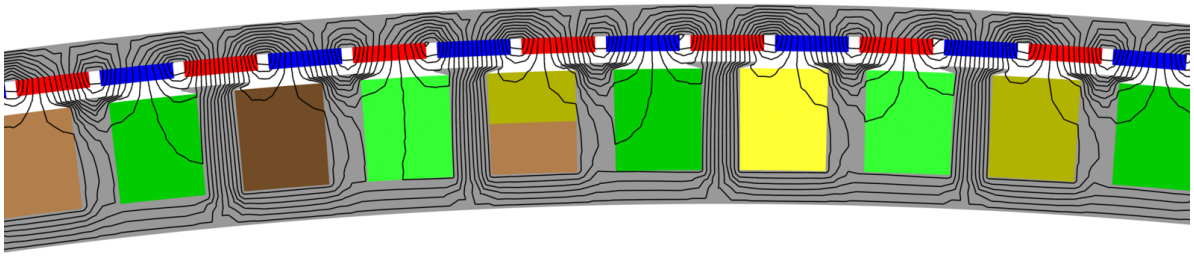

Figure 6.20: Cross-section ($1/27^{\text{th}}$) of 2-slot CW PMV machine with $Q_s/p_s/p_r = 270/67/203$.

Table 6.14: Optimized parameters for PMV machine: $Q_s/p_s/p_r = 276/68/208$

Dimension	value	Dimension	value
Outer diameter (m)	4.995	Rotor PM height (mm)	9.97
Stack length (m)	1.399	Stator tooth length (mm)	42.05
Inner diameter (m)	4.822	Magnet pole span	0.854
Rotor yoke height (mm)	14.98	Slot opening ratio	0.659
Stator yoke height (mm)	14.35	Stator slot angle ratio	0.686

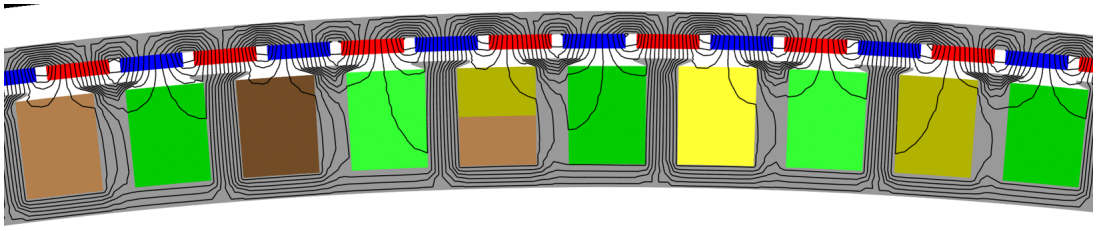

Figure 6.21: Cross-section ($1/28^{\text{th}}$) of 2-slot CW PMV machine with $Q_s/p_s/p_r = 276/68/208$.

Table 6.15: Optimized parameters for PMV machine: $Q_s/p_s/p_r = 240/40/200$

Dimension	value	Dimension	value
Outer diameter (m)	4.999	Rotor PM height (mm)	9.67
Stack length (m)	1.379	Stator tooth length (mm)	37.49
Inner diameter (m)	4.826	Magnet pole span	0.892
Rotor yoke height (mm)	17.77	Slot opening ratio	0.695
Stator yoke height (mm)	16.48	Stator slot angle ratio	0.780

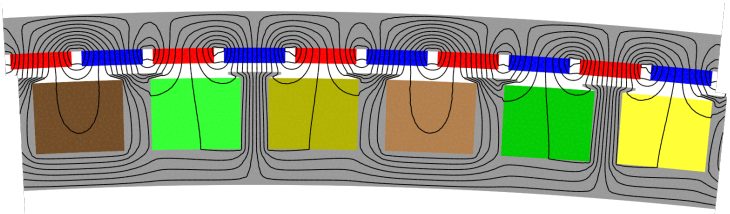

Figure 6.22: Cross-section ($1/40^{\text{th}}$) of distributed overlap-winding PMV machine with $Q_s/p_s/p_r = 240/40/200$.

Table 6.16: Optimized parameters for PMV machine: $Q_s/p_s/p_r = 240/32/208$

Dimension	value	Dimension	value
Outer diameter (m)	5.000	Rotor PM height (mm)	9.91
Stack length (m)	1.378	Stator tooth length (mm)	43.42
Inner diameter (m)	4.786	Magnet pole span	0.879
Rotor yoke height (mm)	23.80	Slot opening ratio	0.757
Stator yoke height (mm)	24.70	Stator slot angle ratio	0.741

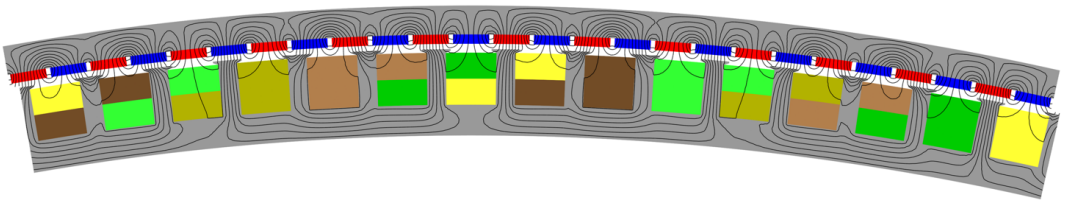

Figure 6.23: Cross-section ($1/16^{\text{th}}$) of distributed overlap-winding PMV machine with $Q_s/p_s/p_r = 240/32/208$.

Table 6.17: Optimized parameters for PMV machine: $Q_s/p_s/p_r = 225/25/200$

Dimension	value	Dimension	value
Outer diameter (m)	5.000	Rotor PM height (mm)	9.80
Stack length (m)	1.372	Stator tooth length (mm)	44.63
Inner diameter (m)	4.774	Magnet pole span	0.898
Rotor yoke height (mm)	27.65	Slot opening ratio	0.787
Stator yoke height (mm)	26.05	Stator slot angle ratio	0.769

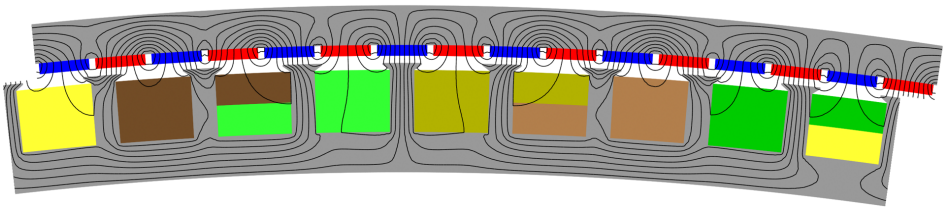

Figure 6.24: Cross-section ($1/25^{\text{th}}$) of distributed overlap-winding PMV machine with $Q_s/p_s/p_r$=225/25/200.

Table 6.18: Parameters of bench-mark PMSM machine: $Q_s/p_s/p_r = 192/80/80$ [66]

Dimension	value	Dimension	value
Outer diameter (m)	5.000	Rotor PM height (mm)	22.00
Stack length (m)	1.300	Stator tooth length (mm)	50.00
Inner diameter (m)	4.770	Magnet pole span	0.70
Rotor yoke height (mm)	20.00	Slot opening ratio	1.00
Stator yoke height (mm)	18.00	Stator slot angle ratio	0.59

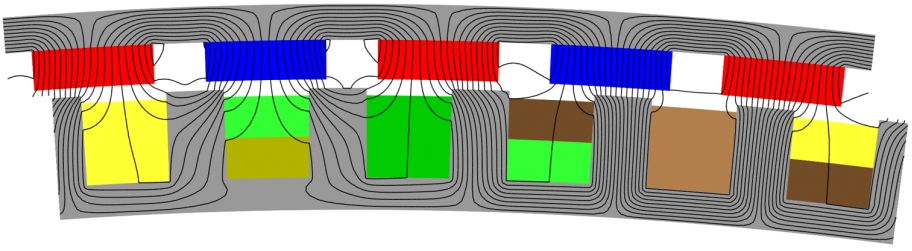

Figure 6.25: Cross-section ($1/32^{\text{th}}$) of tooth concentrated winding conventional PMSM bench-mark machine with $Q_s/p_s/p_r = 192/80/80$ [66].

Chapter 7

Conclusions

The work presented in this dissertation has focused on the analysis, optimal design and prototyping of Permanent Magnet Vernier machines for use in the wind generator applications. A number of topological variations in the PMV machine type were studied through the use of finite element analysis and numerical optimization in order to investigate its performance capabilities. The highlights of original work contributions and general conclusions drawn from this study are summarized in this chapter, together with the relevant recommendations proposed for the future research related to this machine type.

7.1 Research Contributions

In this dissertation, the research contributions and new work conducted can be summarized as follows:

- By a way of comparing the three most common single-stator and single-rotor PMV machine configurations, namely, the conventional overlap-winding, tooth-concentrated split-tooth and tooth-concentrated separate modulator PMV machines, it has been shown that OW-PMV machines are relatively superior in terms of the overall performance. The comparative design study focused mainly on the minimum electromagnetic active mass, better power factor and torque quality. While the tooth-concentrated winding type PMV machines usually boasts on good fault tolerance capability and less over-hang winding volume, the modulator segments situated in between the two field-exciting components adds a significant reluctance to the magnetic field path. This leads to a reduced magnitude of the working field harmonics, hence the low performance too. On the contrary, the OW-PMV machine has a shorter magnetic air-gap length and offers additional options like winding short pitching for improving on the necessary field harmonics, and ultimately improving on the torque magnitude and quality.

- The prototype development and laboratory testing of a 15 kW PMV machine has been reported in this dissertation. In the light of relatively scarce practical performance information relating to this machine type and power capacity, this work serves as a further practical confirmation to the feasibility of its industrial manufacturability for larger power ratings. Furthermore, a fair agreement between the measured and FEA predicted results not only validates the working principle, but it also demonstrates the excellent features possessed by the machine. However, further

evaluation of PMV machine benefits against its drawbacks needs to be performed in order to establish its distinct strengths against other existing technology.

- The comparison of PMV machine with a benchmark conventional PMSM has revealed its merits and shortcomings. It has been shown that an optimally designed PMV machine has considerably less PM material content, which can be logically translated to cheaper machine possibilities while maintaining higher torque density than its counterpart. With careful design and selection of pole/slot combination, a PMV machine with less cogging torque and generally good torque qualities can be easily achieved. Although the low power factor remains a major drawback for the PMV machine due to the implicated higher converter cost requirement, this burden can be subsidized by the cheaper machine cost resulting from reduced usage of expensive PM material in comparison to the PMSM. Therefore, a slight margin between the total cost of the system employing the two machine types can be expected.

- Through the performed multi-objective design optimization studies, it has been established that pole/slot combinations with higher gear ratios offer no substantial benefits. Even though it is not so apparent at a sub-kilowatt machine level, this observation becomes more clear with a shift to the utility-scale machine designs. That is, selecting a machine with higher gear ratio results in relatively inferior power factor, which implies increased converter size and cost. On one side, imposing a minimum power factor threshold sees the said combinations struggling to satisfy the constraints due to the relatively large flux leakage, hence un-attractive designs will be obtained.

- The PMV machine type has been mostly proposed for use in other purposes such as traction applications. But in this thesis, it has been demonstrated that it can perform well in wind power conversion application as well. From both the performance and economical perspectives, The PMV machine appears to be a potential alternative to the conventional synchronous PM generators.

- This work has further demonstrated that PMV machine can be considered as an intermediate drive train option between the gear-less (direct-drive) and single-stage mechanically geared (medium-speed) PM machines drive-trains. This is because, while being operated at direct-drive speed ratings, its performance gets more enhanced when its operating frequency is allowed to match with that of medium-speed machines due to the soft gearing inherent in them. Even though the increased core-losses are usually a deterring factor for designing PMSM at elevated frequencies, it seems not to be an alarming issue in this case, as the experienced core losses are within the range to those of direct-drive PM machines.

7.2 General Conclusions on PMV Machine Design

The general remarks and conclusions on the design and optimization of PMV machines through this research project are summarized in this section.

PMV machine theory: An effort was made to explain the basic theory of Permanent Magnet Vernier machine operating fundamentals. Simplified analytical equations were used to describe the electromagnetic air-gap MMF harmonic modulation

to realize the magnetic gearing principle. The analytic expressions were further expanded to define the concept of vernier effect between the PMs' and AC armature windings' MMF harmonics. From that, the intelligent utilization of magnetic field harmonics for stable torque transmission and power generation mechanisms were theoretically deduced. Although the physical structure of the PMV machine may sometimes look similar to that of the synchronous PM machine, understanding of the presented PMV machine basic principles provides better insight into its operation and can be used as a theoretical tool to choose the suitable pole/slot combinations and predict the preliminary performance of the machine.

Evaluation of performance parameters: Even though the simple analytical equations may be used to predict the general tendencies of machine dimensions and performance, the FEA remains an important tool for more accurate analysis. The hybrid approach, consisting of 2D finite element method and classical field circuit modeling was described and employed to analyze the PMV machine. In this method, the most important parameters such as magnetic field density and flux linkages, etc., are obtained from the FEM while the analytical equations (in conjunction with FEM results) are used to calculate the other performance parameters to fully characterize the machine. Formulation for these key parameters is provided for reliable and ease of machine evaluation. This approach achieves a good balance between the solution speed and precision, avoiding possibilities of inaccurate calculation which can easily give false performance implications.

Design optimization: A combination of gradient-based MMFD and stochastic NSGA-II algorithms were employed to optimize several PMV machines for a number of objectives, which include, among others, the maximum power factor, minimum PM mass and total active mass. It was revealed that selection of suitable pole/slot combinations carries an immense importance for obtaining a lighter machine design with satisfactory power factor. Three PMV machine topologies, being conventional overlap-winding machine, split-tooth concentrated winding and separate modulator winding machines were optimized and compared on the basis of the best power factor and minimum mass as well. Although the long end-winding lengths may be an obvious drawback, it was found that the distributed overlap-winding PMV machine is generally the best among them. This is because the two concentrated winding stator type PMV machines have rich harmonic content, which affects their torque quality. Moreover, the modulator component situated between the stator and rotor adds to the reluctance of magnetic flux path.

Prototyping and testing: The prototype development and testing of 15 kW optimized PMV machine is presented. With the currently lacking information regarding the manufacturing and practical performance of this size of PMV machine in literature, this laboratory prototyping acts to supplement the possibility of industrial production of this machine type. The experimental results obtained under the generator mode of operation serves to characterize the built machine and validate the FEA predicted performance. Some discrepancies exists between the measured and FEM results, and these are due to the construction imperfections and loss underestimation during the FEA design stage. It can be inferred that the end leakage effects, mechanical losses and eddy current loss induced in the support structure adds an unexpectedly significant portion of machine total losses.

7.3 Performance of PMV Machines

Comparison of PMV and PMSM machines: Comparison of the PMV machine with the conventional PM synchronous machine has been done in this study. In order to have a fair comparison platform, the input speed and volume maximum limits were kept similar between the two machine types. Although the PMV machine has lower power factor compared to that of PMSM, the two machine types have similar output efficiency capabilities. In addition, the PMV machine has potential for good torque quality and less voltage harmonic distortion, if suitable pole/slot combinations are selected. At small power level, the PMV machine boasts on lower volume and PM material requirement and offers higher mass torque density than the PMSM machine. While the lower PM material usage may translate to a lower cost machine, this advantage is offset by the cost of bigger converter capacity needed for a PMV machine, which at the end brings the total cost of the two systems to level up.

Mega-Watt level machine feasibility studies: An investigation study was conducted into the potential design of PMV machine at utility power scale wind energy conversion applications. It is shown that, at a mega-Watt power level, lower pole-ratios are more attractive to achieve optimum machines with reasonable total mass and power factor. Even though the PMV machine is designed to operate at a direct-drive generator speeds, its operating frequency may need to be in the same range as that of medium-speed generators in order to enhance its best potential. This implies that its inherent soft gearing effects makes it an intermediate alternative between the direct drive and medium-speed concepts. The study predicts that it is feasible and economically reasonable to develop a MW output level PMV generator for the wind power applications.

7.4 Recommendations

Based on the work conducted in this dissertation, some recommendations for future work are proposed as follows:

- It may be beneficial to conduct the thermal and demagnetization analysis of the machine to fully characterize its performance.
- It is believed that other major electromagnetic MMF harmonics that are not utilized in the gearing effect contribute to the loss generation. More studies on the air-gap MMF composition may help to determine their extend of adverse impact and possibilities of minimizing them.
- The iron loss, PM loss and conductor skin effect loss are aspects that needs further investigation to allow accurate efficiency estimation during the design stage.
- The electro-magnetically non-active support structure may need to be included in the early design stages for the complete machine optimization, mechanical integrity and cost estimation.
- Practical tests in the real wind turbine scenarios are necessary to establish the machine's reliability under actual environmental conditions.

Appendices

Appendix A

Prototype Component Drawings

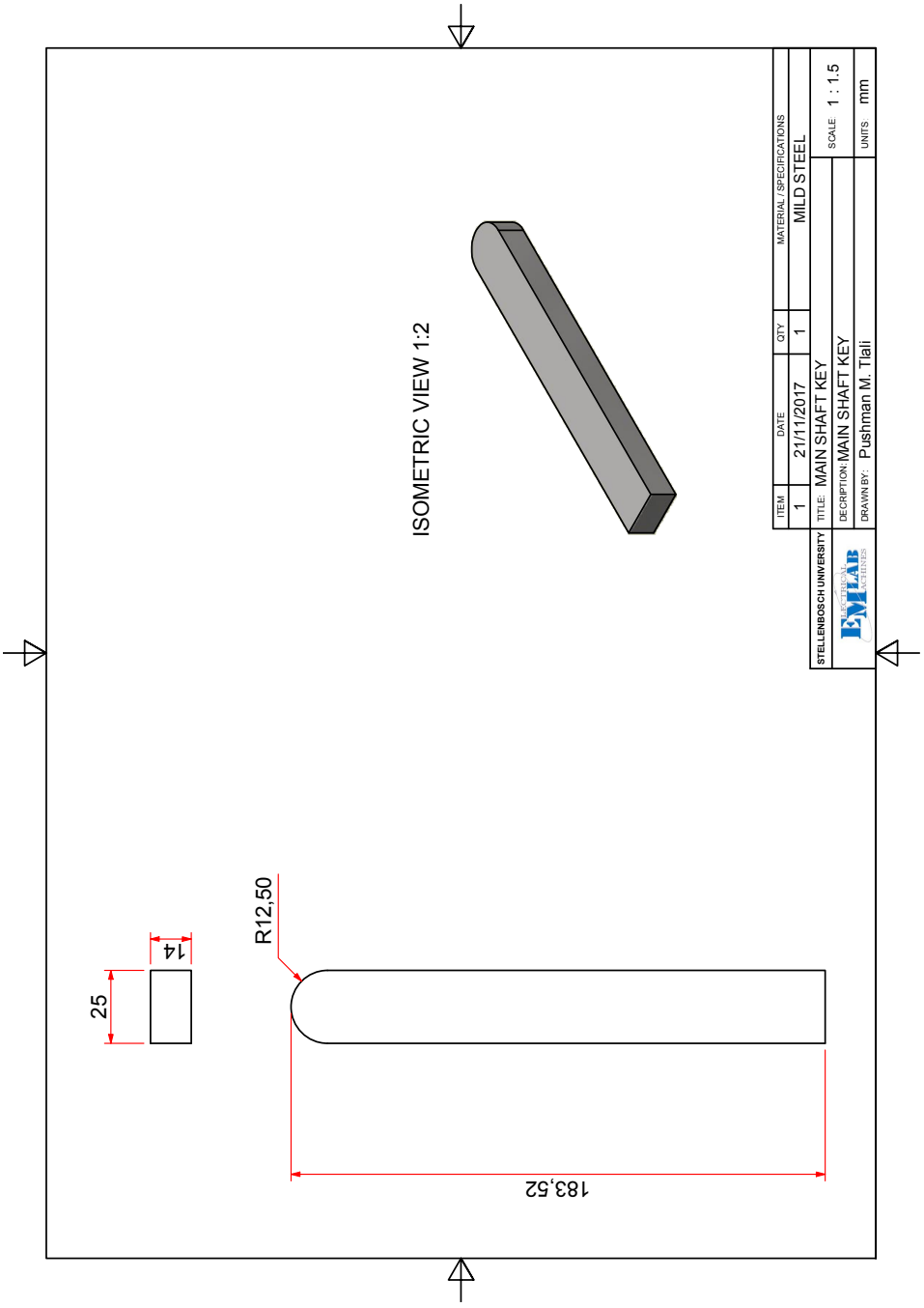

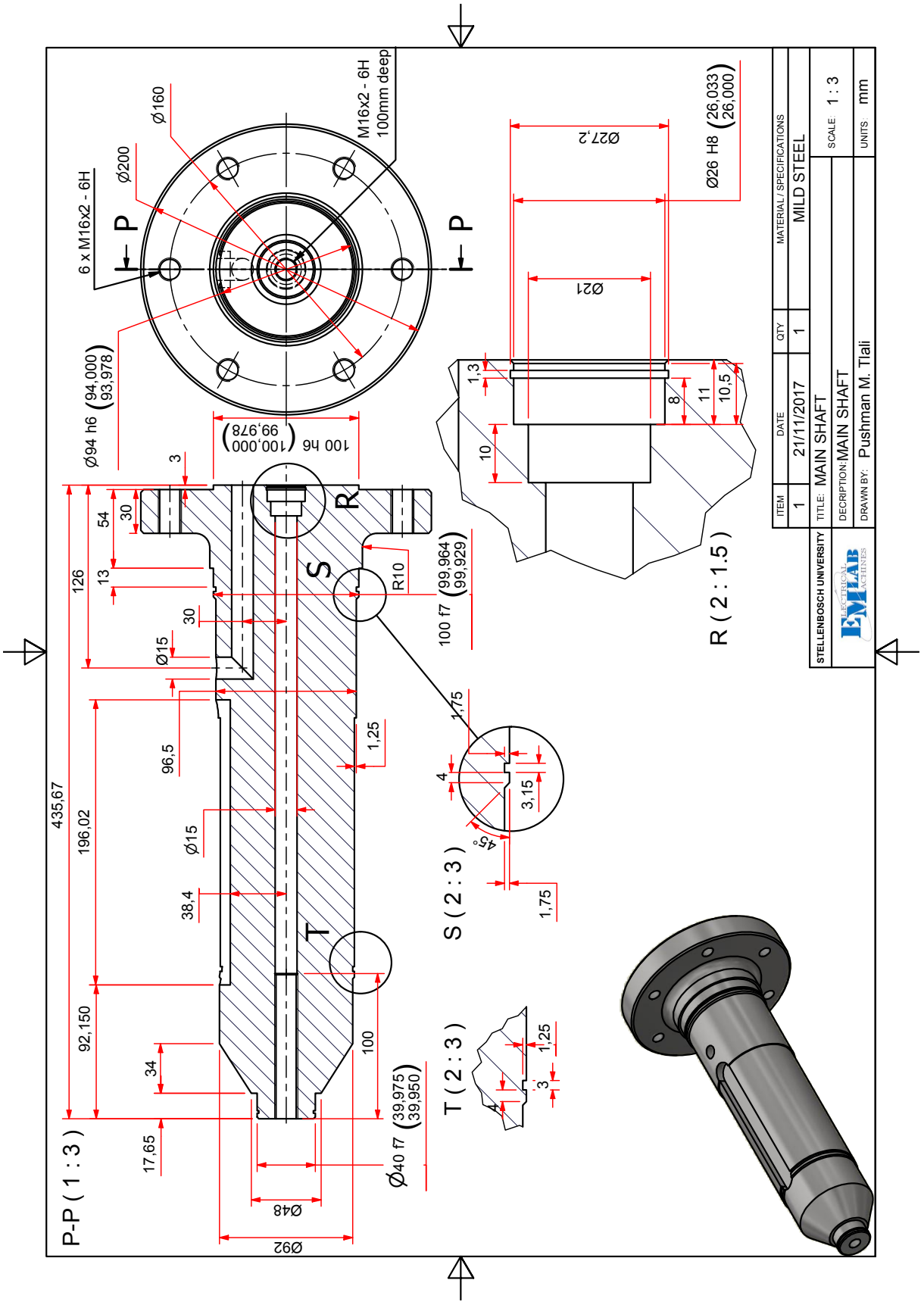

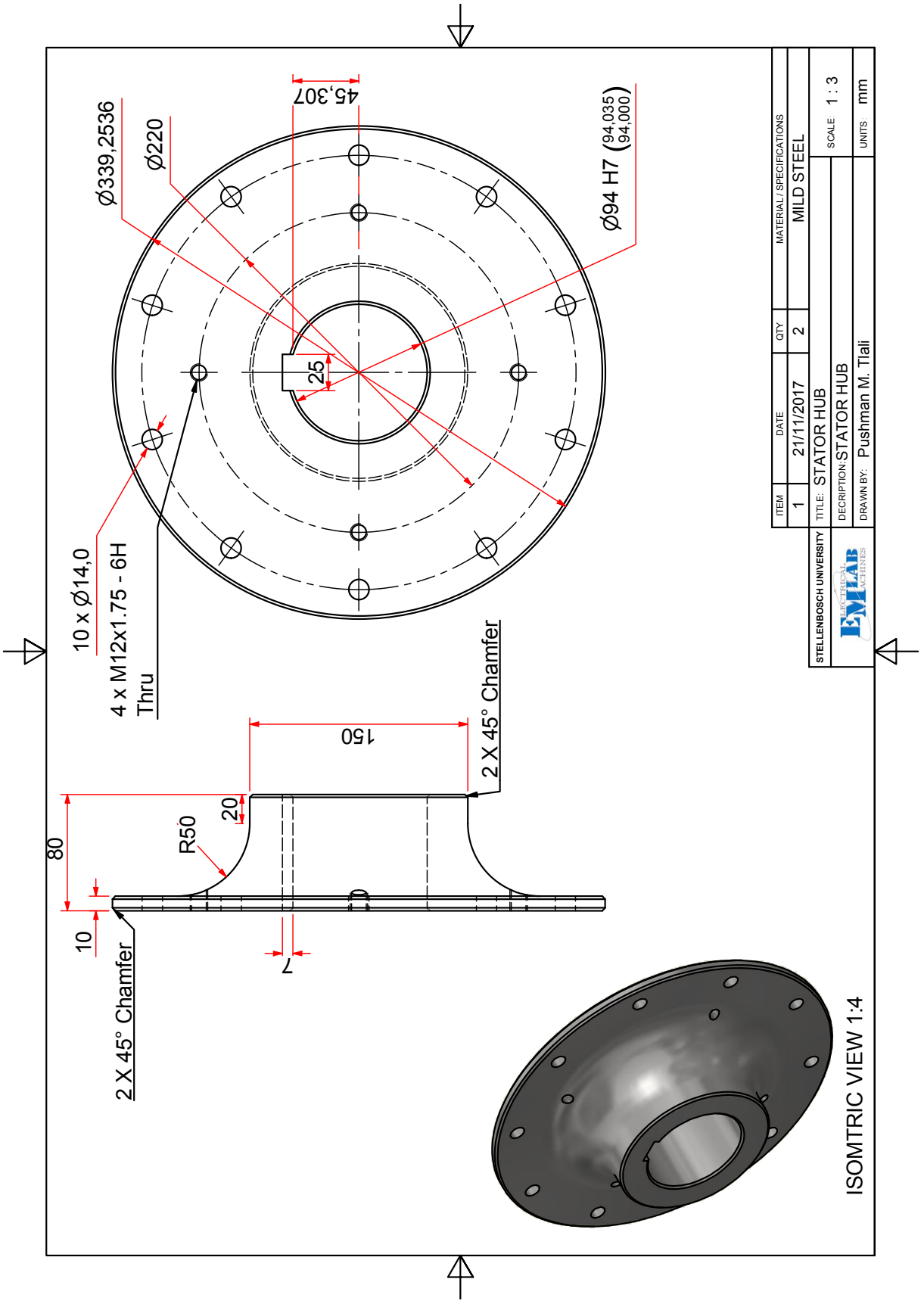

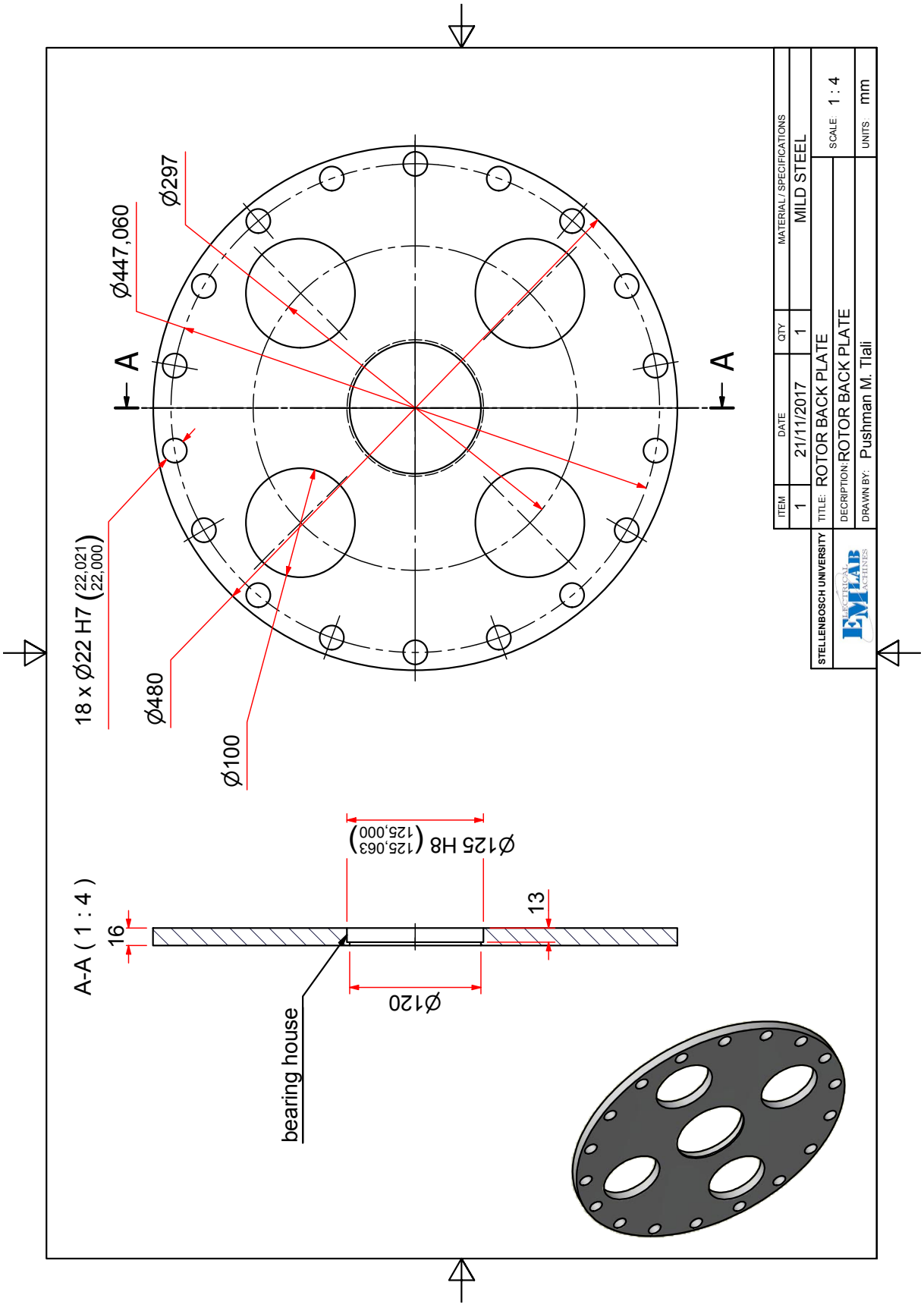

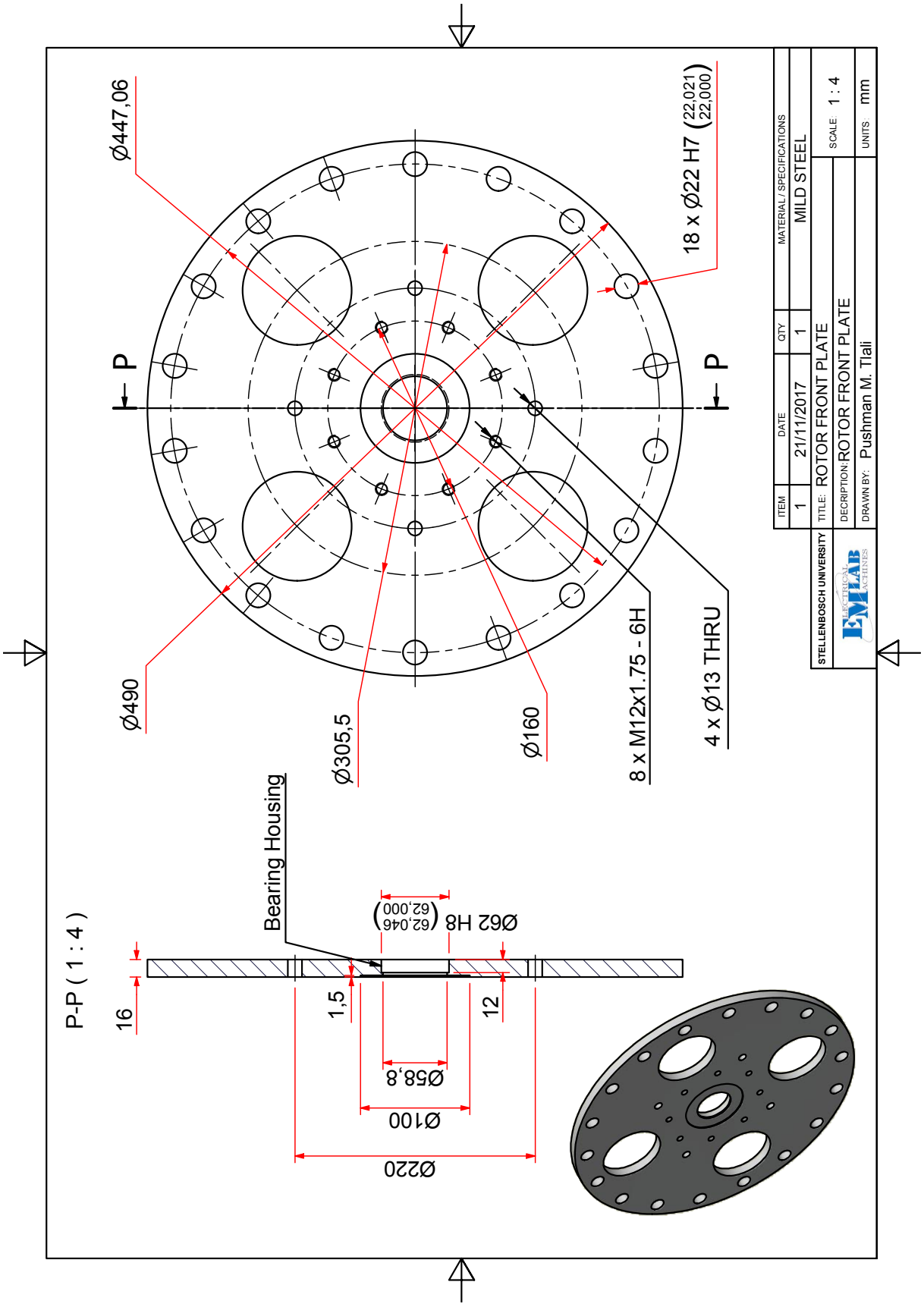

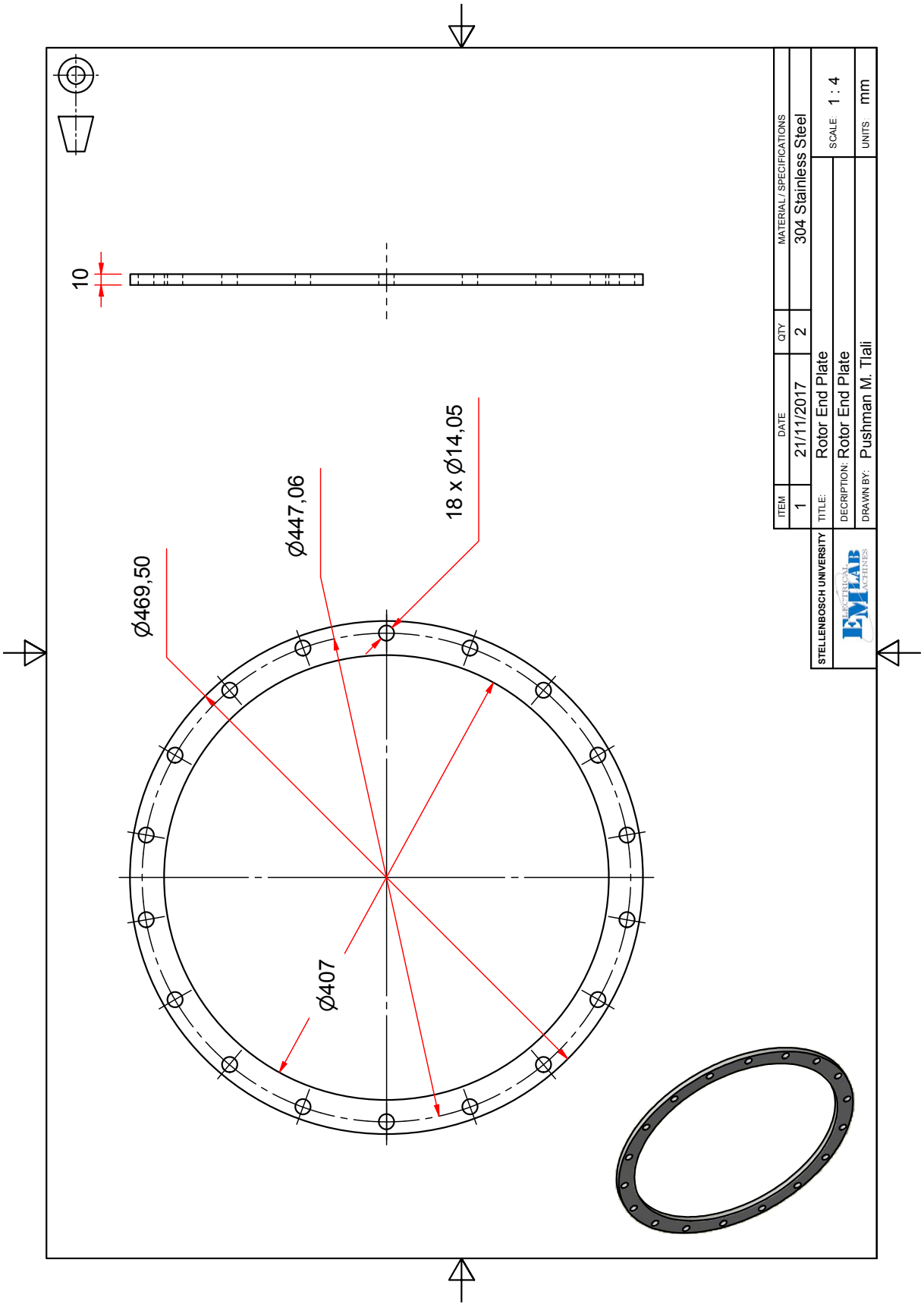

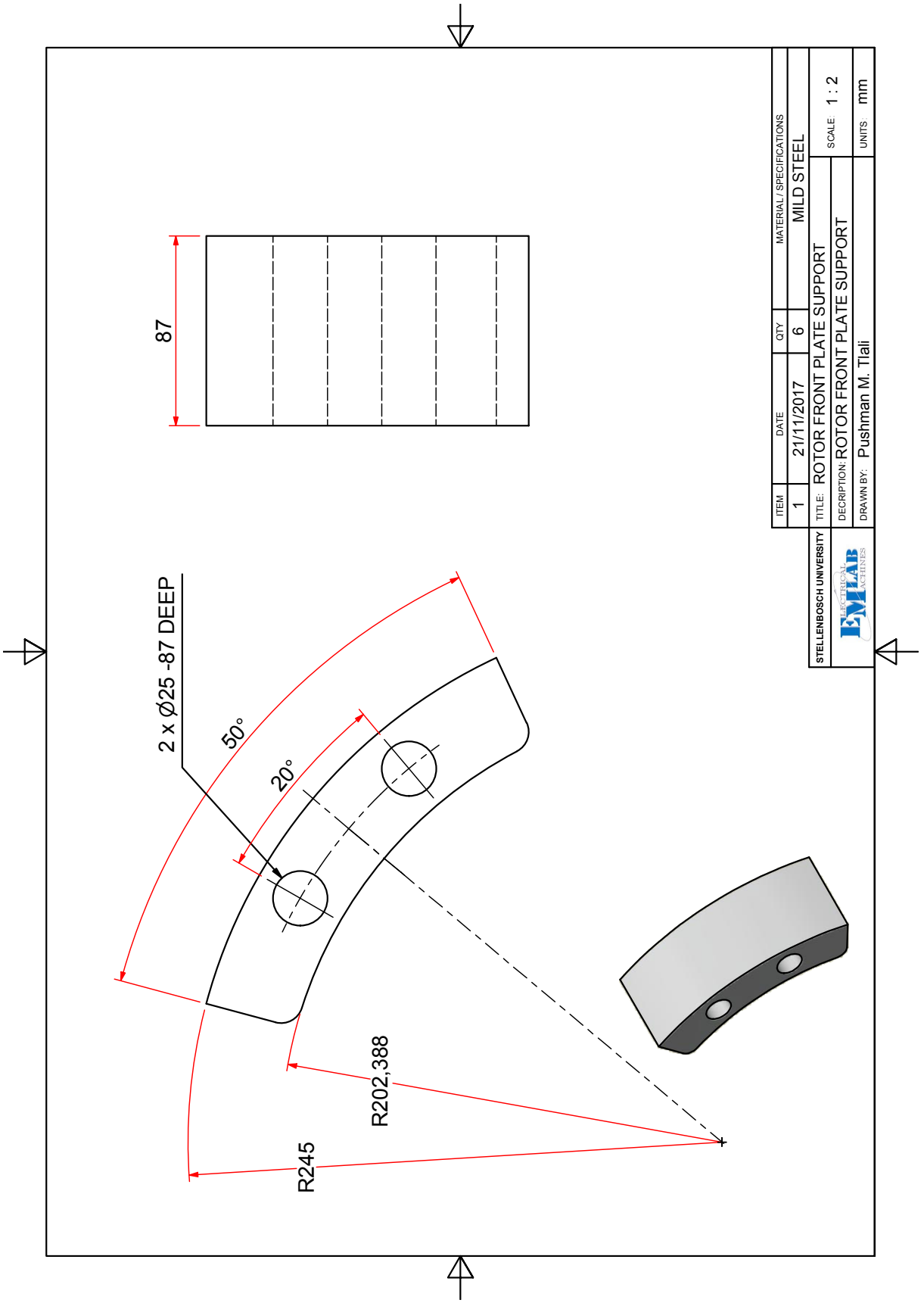

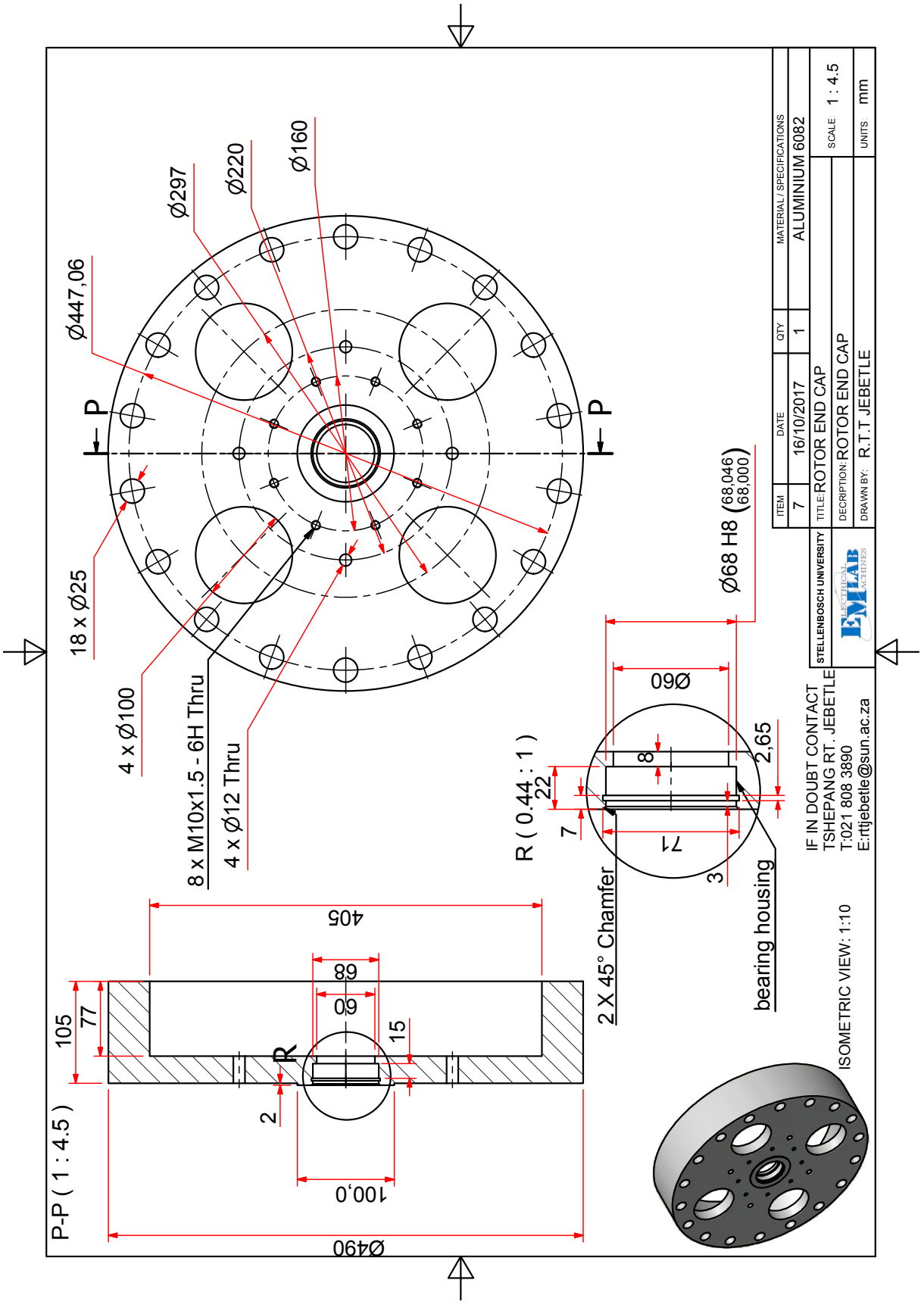

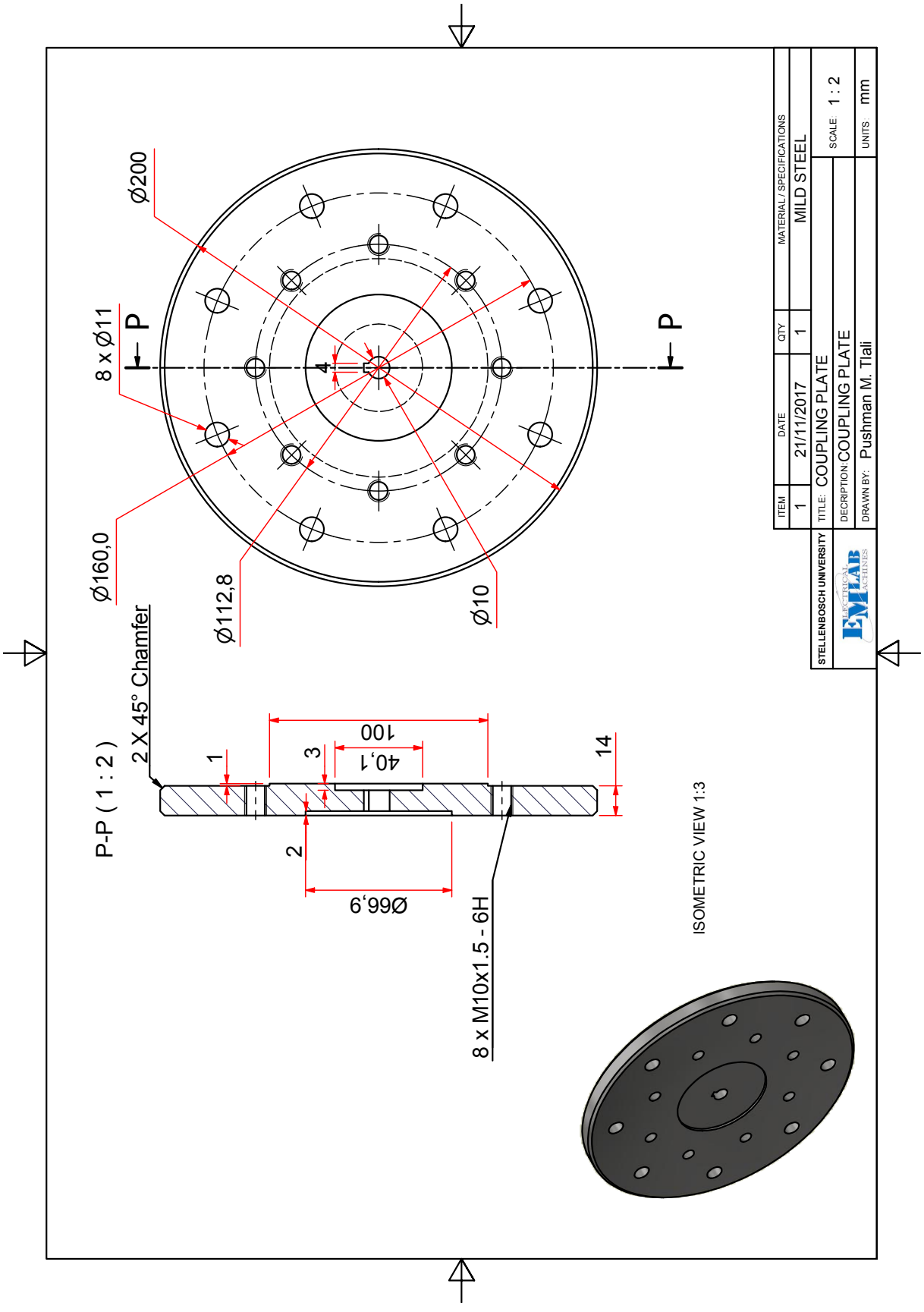

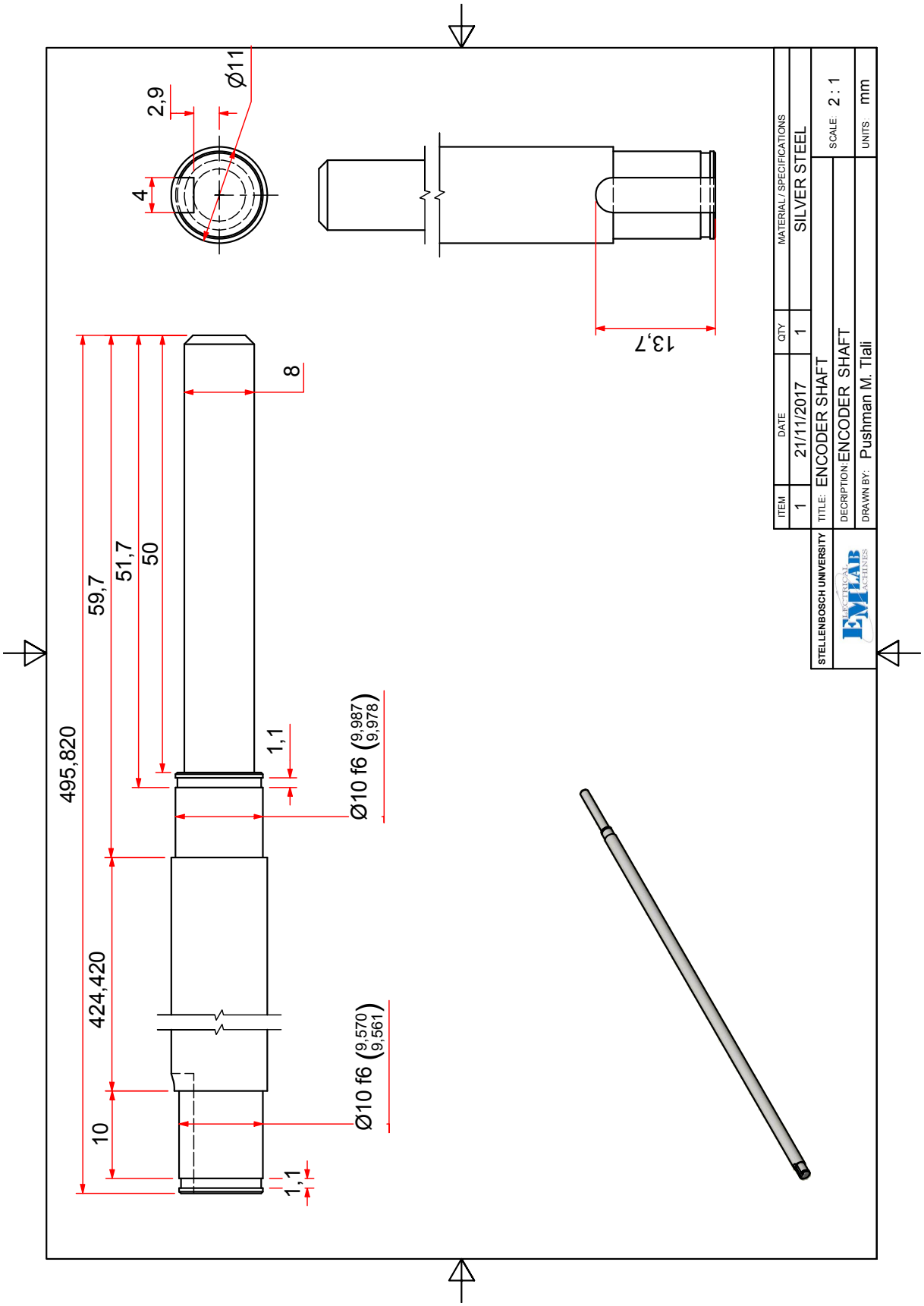

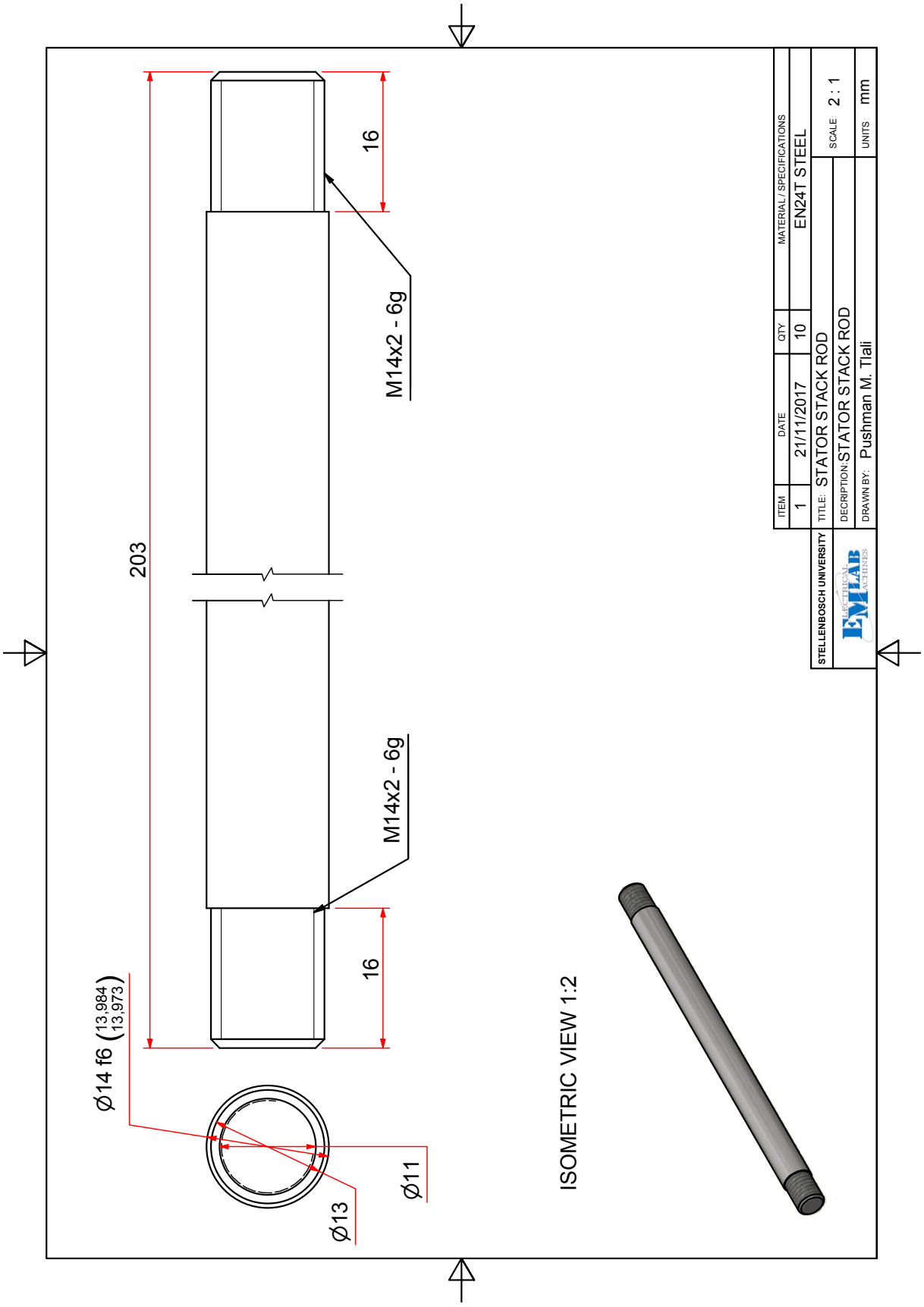

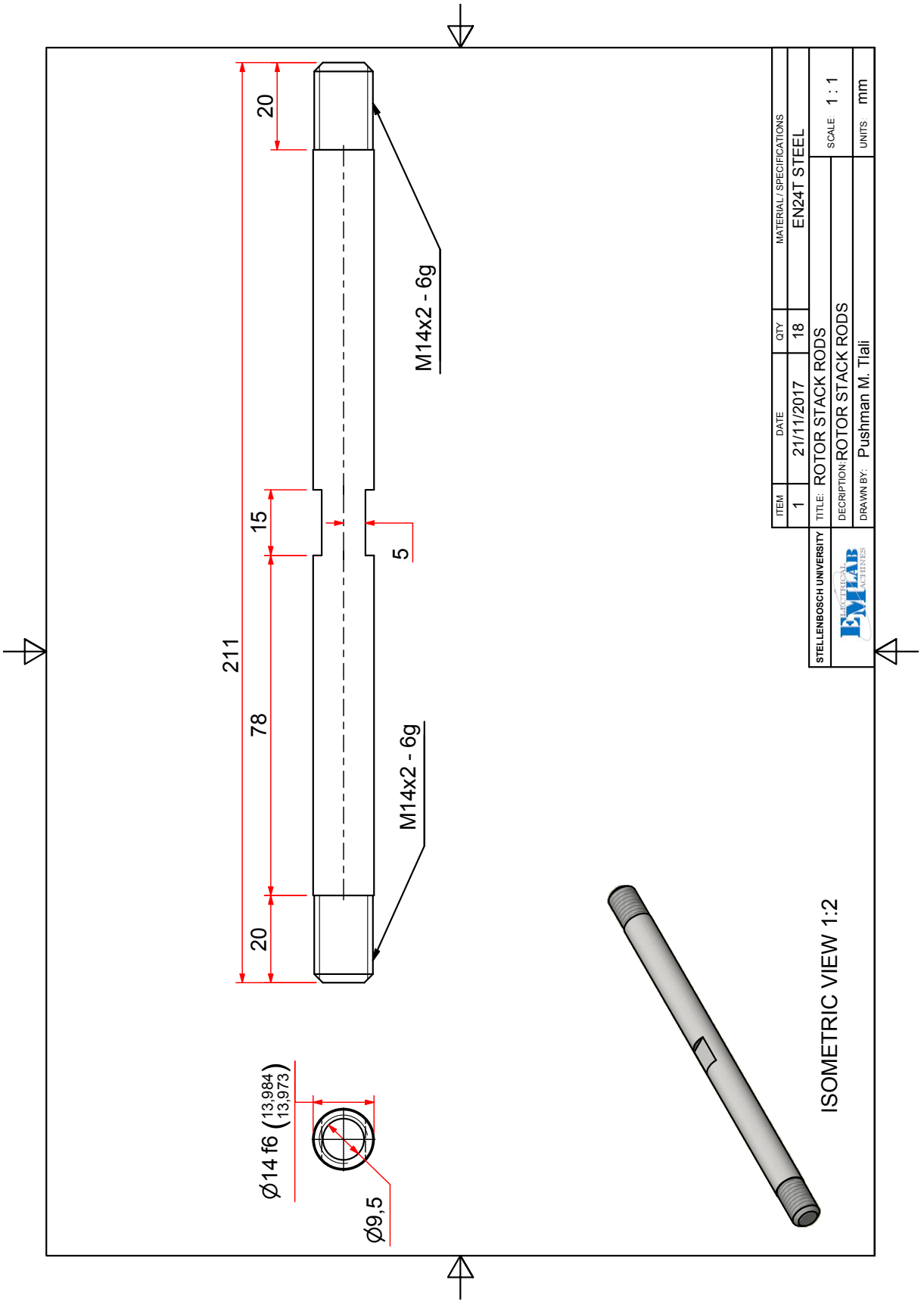

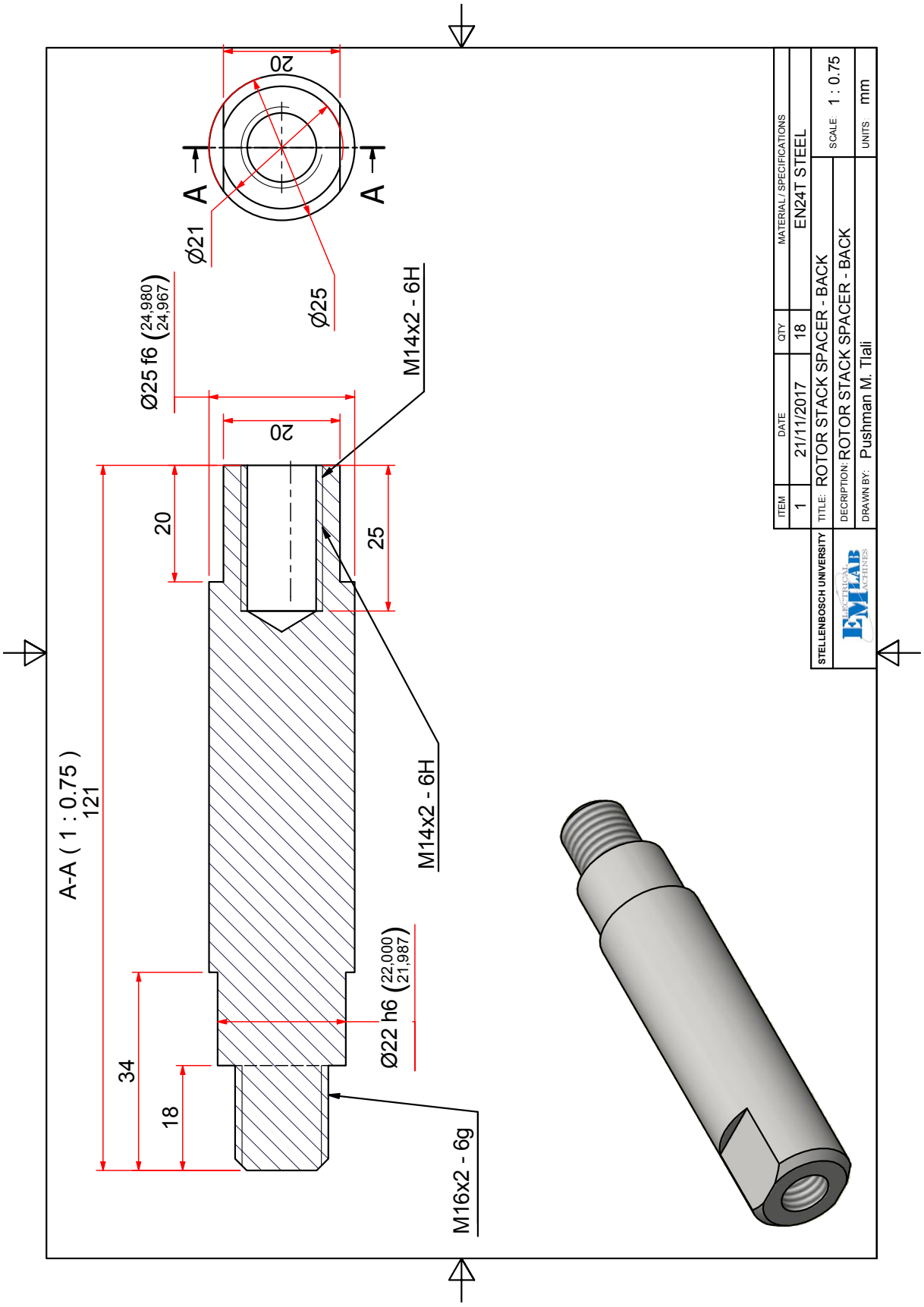

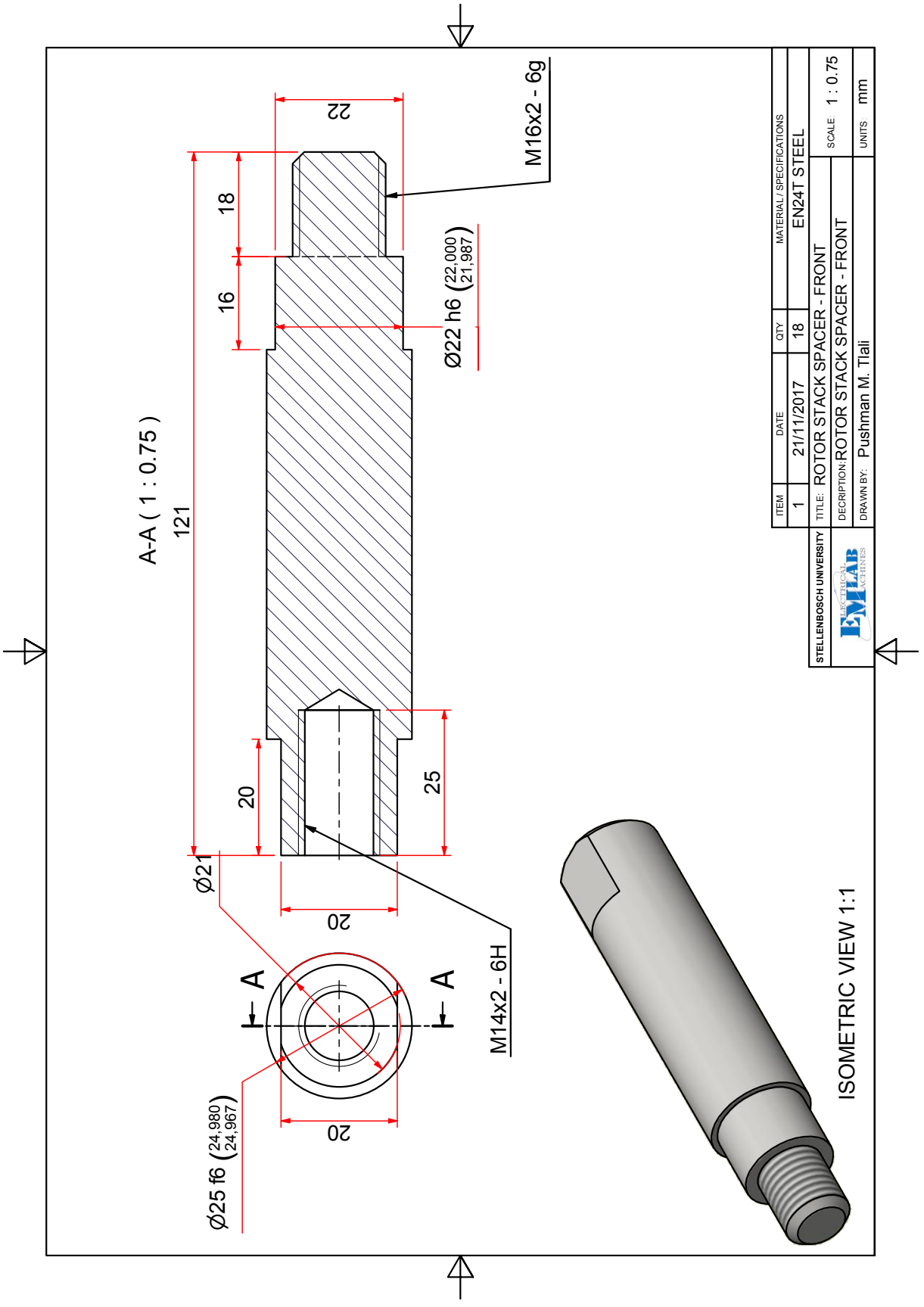

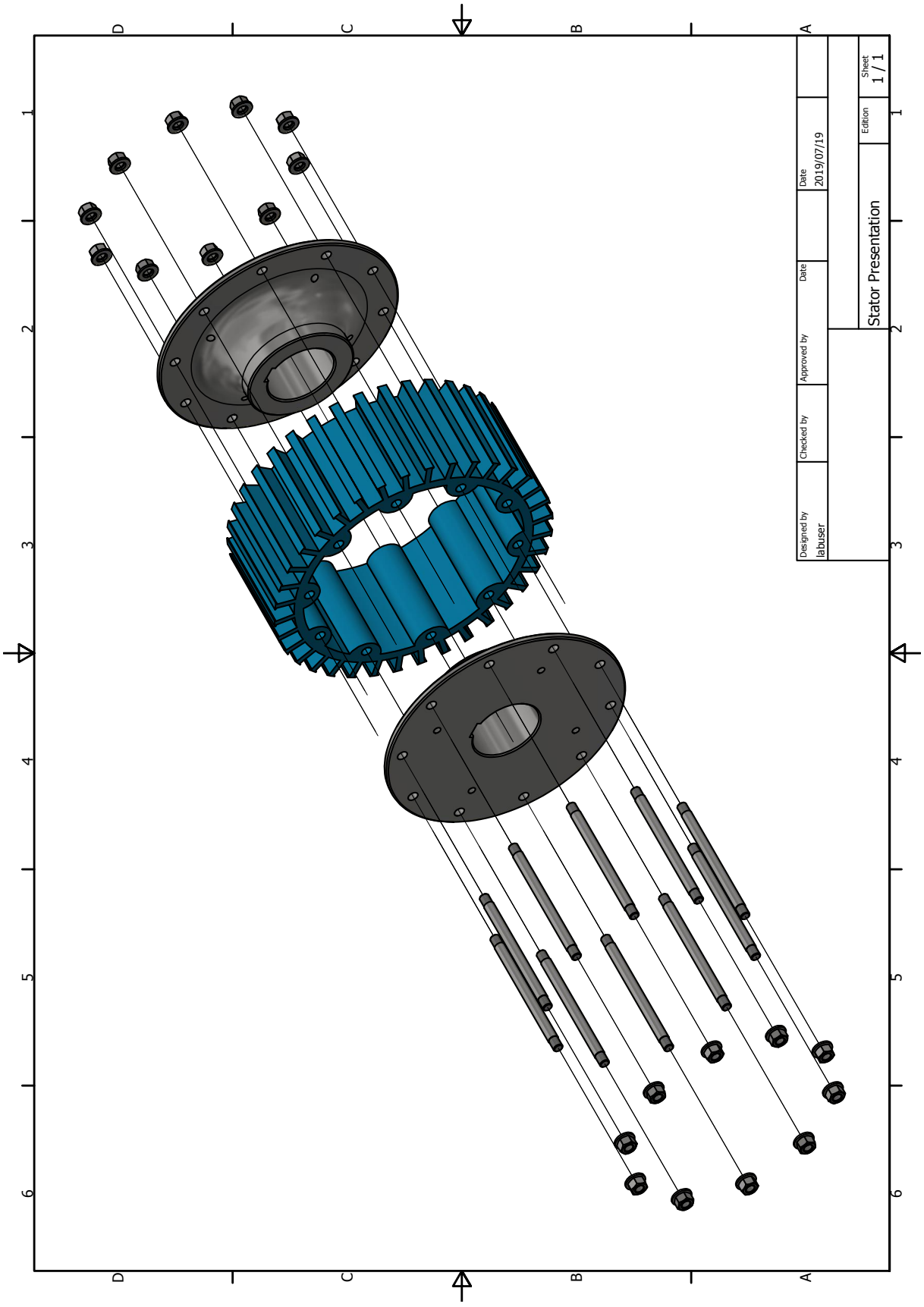

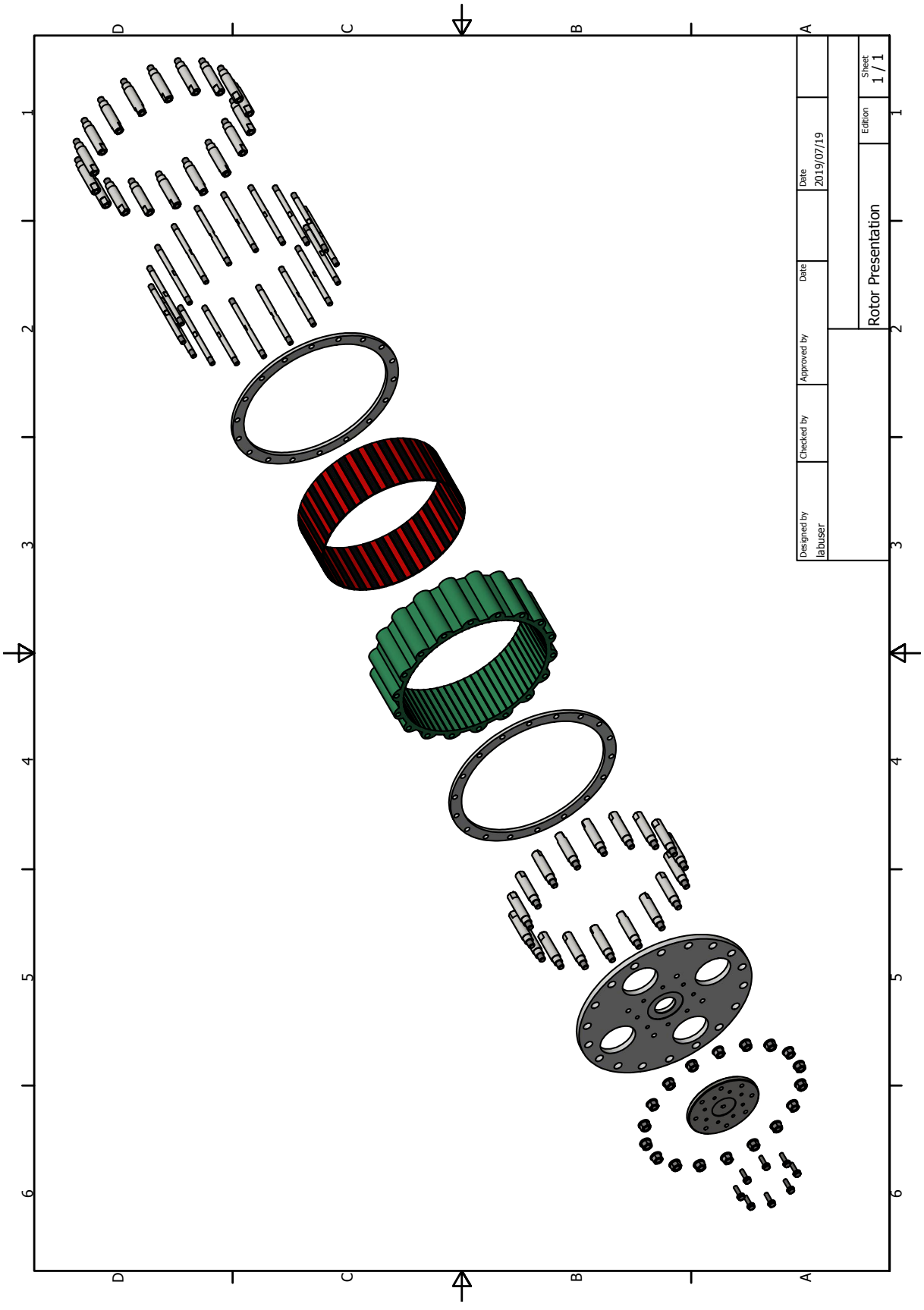

Bibliography

[1] RNS21: Renewables 2016 global status report. In: *Renewable Energy Policy Network for the 21 century*, pp. 1–32. 2016.

[2] RNS21: Renewables 2018 global status report. In: *Renewable Energy Policy Network for the 21 century*, pp. 1–325. 2018.

[3] IRENA, I.R.E.A.: Renewables 2018 global status report. In: *Renewable Capacity Statistics 2018*, pp. 1–60. 2018.

[4] Energy-Information-Administration, U.S.: International energy outlook 2016: With projections to 2040. pp. 1–290. May 2016.

[5] Wang, R.-J. and Gerber, S.: Magnetically geared wind generator technologies: Opportunities and challenges. *Applied Energy*, vol. 136, pp. 817 – 826, 2014. ISSN 0306-2619.

[6] Atallah, K. and Howe, D.: A novel high-performance magnetic gear. *IEEE Transactions on Magnetics*, vol. 37, no. 4, pp. 2844–2846, July 2001. ISSN 0018-9464.

[7] Atallah, K., Calverley, S.D. and Howe, D.: Design, analysis and realisation of a high-performance magnetic gear. *IEE Proceedings - Electric Power Applications*, vol. 151, no. 2, pp. 135–143, March 2004. ISSN 1350-2352.

[8] Gerber, S. and Wang, R.-J.: Design of a magnetically geared PM machine. In: *Power Engineering, Energy and Electrical Drives (POWERENG), 2013 Fourth International Conference on*, pp. 852–857. May 2013. ISSN 2155-5516.

[9] Jian, L., Chau, K.T. and Jiang, J.Z.: An integrated magnetic-geared permanent-magnet in-wheel motor drive for electric vehicles. In: *2008 IEEE Vehicle Power and Propulsion Conference*, pp. 1–6. Sep 2008. ISSN 1938-8756.

[10] Atallah, K., Rens, J., Mezani, S. and Howe, D.: A novel pseudo direct-drive brushless permanent magnet machine. *Magnetics, IEEE Transactions on*, vol. 44, no. 11, pp. 4349–4352, 2008. ISSN 0018-9464.

[11] Wang, Y., Ho, S.L., Fu, W.N. and Shen, J.X.: A novel brushless doubly fed generator for wind power generation. *IEEE Transactions on Magnetics*, vol. 48, no. 11, pp. 4172–4175, Nov 2012. ISSN 0018-9464.

[12] Rauch, S.E. and Johnson, L.J.: Design principles of flux-switch alternators [includes discussion]. *Transactions of the American Institute of Electrical Engineers. Part III: Power Apparatus and Systems*, vol. 74, no. 3, pp. 1261–1268, Jan 1955. ISSN 0097-2460.

[13] Pang, Y., Zhu, Z.Q., Howe, D., Iwasaki, S., Deodhar, R. and Pride, A.: Comparative study of flux-switching and interior permanent magnet machines. In: *2007 International Conference on Electrical Machines and Systems (ICEMS)*, pp. 757–762. Oct 2007.

[14] Zhang, J., Cheng, M., Chen, Z. and Hua, W.: Comparison of stator-mounted permanent-magnet machines based on a general power equation. *IEEE Transactions on Energy Conversion*, vol. 24, no. 4, pp. 826–834, Dec 2009. ISSN 0885-8969.

[15] Su, P., Hua, W., Wu, Z., Chen, Z., Zhang, G. and Cheng, M.: Comprehensive comparison of rotor-permanent magnet and stator-permanent magnet flux-switching machines. *IEEE Transactions on Industrial Electronics*, pp. 1–1, 2018. ISSN 0278-0046.

[16] Fan, Y., Chau, K.T. and Cheng, M.: A new three-phase doubly salient permanent magnet machine for wind power generation. *IEEE Transactions on Industry Applications*, vol. 42, no. 1, pp. 53–60, Jan 2006. ISSN 0093-9994.

[17] Dobzhanskyi, O., Gouws, R. and Amiri, E.: Analysis of PM transverse-flux outer rotor machines with different configuration. *IEEE Transactions on Industry Applications*, vol. 53, no. 5, pp. 4260–4268, Sep 2017. ISSN 0093-9994.

[18] Dobzhanskyi, O., Gouws, R. and Amiri, E.: Comparison analysis of AC PM transverse-flux machines of different designs in terms of power density and cost. In: *2017 IEEE 58th International Scientific Conference on Power and Electrical Engineering of Riga Technical University (RTUCON)*, pp. 1–6. Oct 2017.

[19] Chubb, L.W.: Vernier motor. 1 1933. US Patent 1894979 A.

[20] Dicke, .H.: Vernier motor. January 5 1937. US Patent 2,066,965.
Available at: http://www.google.com/patents/US2066965

[21] Li, D., Qu, R., Xu, W., Li, J. and Lipo, T.: Design procedure of dual-stator, spoke-array vernier permanent magnet machines. *Industry Applications, IEEE Transactions on*, vol. PP, no. 99, pp. 1–1, 2015. ISSN 0093-9994.

[22] Niu, S., Ho, S.L., Fu, W.N. and Wang, L.L.: Quantitative comparison of novel vernier permanent magnet machines. *IEEE Transactions on Magnetics*, vol. 46, no. 6, pp. 2032–2035, June 2010. ISSN 0018-9464.

[23] Li, J., Chau, K., Jiang, J., Liu, C. and Li, W.: A new efficient permanent-magnet vernier machine for wind power generation. *Magnetics, IEEE Transactions on*, vol. 46, no. 6, pp. 1475–1478, June 2010. ISSN 0018-9464.

[24] Abdel-Khalik, A.S., Ahmed, S. and Massoud, A.: A new permanent-magnet vernier machine using a single layer winding layout for electric vehicles. In: *2014 IEEE 23rd International Symposium on Industrial Electronics (ISIE)*, pp. 703–708. June 2014. ISSN 2163-5145.

[25] Chung, S., Kim, J., Woo, B., Hong, D., Lee, J. and Koo, D.: A novel design of modular three-phase permanent magnet vernier machine with consequent pole rotor. *IEEE Transactions on Magnetics*, vol. 47, no. 10, pp. 4215–4218, Oct 2011. ISSN 0018-9464.

[26] Zhao, F., Lipo, T.A. and Kwon, B.: A novel dual-stator axial-flux spoke-type permanent magnet vernier machine for direct-drive applications. *IEEE Transactions on Magnetics*, vol. 50, no. 11, pp. 1–4, Nov 2014. ISSN 0018-9464.

[27] Liu, C., Zhong, J. and Chau, K.T.: A novel flux-controllable vernier permanent-magnet machine. *IEEE Transactions on Magnetics*, vol. 47, no. 10, pp. 4238–4241, Oct 2011. ISSN 0018-9464.

[28] Wang, L., Shen, J., Wang, Y. and Wang, K.: A novel magnetic-geared outer-rotor permanent-magnet brushless motor. In: *Power Electronics, Machines and Drives, 2008. PEMD 2008. 4th IET Conference on*, pp. 33–36. April 2008. ISSN 0537-9989.

[29] Fu, W. and Ho, S.: A quantitative comparative analysis of a novel flux-modulated permanent-magnet motor for low-speed drive. *Magnetics, IEEE Transactions on*, vol. 46, no. 1, pp. 127–134, Jan 2010. ISSN 0018-9464.

[30] Li, D., Qu, R., Li, J., Xiao, L., Wu, L. and Xu, W.: Analysis of torque capability and quality in vernier permanent-magnet machines. *IEEE Transactions on Industry Applications*, vol. 52, no. 1, pp. 125–135, Jan 2016. ISSN 0093-9994.

[31] Hosoya, R. and Shimomura, S.: Apply to in-wheel machine of permanent magnet vernier machine using NdFeB bonded magnet-fundamental study. In: *8th International Conference on Power Electronics-ECCE Asia*, pp. 2208–2215. May 2011. ISSN 2150-6086.

[32] Li, X., Chau, K.T. and Cheng, M.: Comparative analysis and experimental verification of an effective permanent-magnet vernier machine. *IEEE Transactions on Magnetics*, vol. 51, no. 7, pp. 1–9, July 2015. ISSN 0018-9464.

[33] Li, D., Qu, R. and Zhu, Z.: Comparison of halbach and dual-side vernier permanent magnet machines. *Magnetics, IEEE Transactions on*, vol. 50, no. 2, pp. 801–804, Feb 2014. ISSN 0018-9464.

[34] Liu, C., Lee, C.H. and Chen, M.: Comparison of outer-rotor permanent magnet machines for in-wheel drives. In: *Industrial Electronics (ISIE), 2013 IEEE International Symposium on*, pp. 1–6. May 2013. ISSN 2163-5137.

[35] Li, J. and Chau, K.T.: Design and analysis of a HTS vernier PM machine. *IEEE Transactions on Applied Superconductivity*, vol. 20, no. 3, pp. 1055–1059, June 2010. ISSN 1051-8223.

[36] Ho, S., Niu, S. and Fu, W.: Design and analysis of a new dual-stator permanent-magnet machine for direct-drive applications. In: *ANSYS User Conference 2011, China.*

[37] Liu, G., Yang, J., Zhao, W., Ji, J., Chen, Q. and Gong, W.: Design and analysis of a new fault-tolerant permanent-magnet vernier machine for electric vehicles. *IEEE Transactions on Magnetics*, vol. 48, no. 11, pp. 4176–4179, Nov 2012. ISSN 0018-9464.

[38] Chung, S.-U., Chun, Y.-D., Woo, B.-C., Hong, D.-K. and Lee, J.-Y.: Design considerations and validation of permanent magnet vernier machine with consequent pole rotor for low speed servo applications. *Journal of Electrical Engineering and Technology*, vol. 8, 09 2013.

[39] Li, D., Qu, R., Li, J. and Xu, W.: Design of consequent pole, toroidal winding, outer rotor vernier permanent magnet machines. In: *2014 IEEE Energy Conversion Congress and Exposition (ECCE)*, pp. 2342–2349. Sep 2014. ISSN 2329-3721.

[40] Kazuhiro, S., Hosoya, R. and Shimomura, S.: Design of NdFeB bond magnets for in-wheel permanent magnet vernier machine. In: *2012 15th International Conference on Electrical Machines and Systems (ICEMS)*, pp. 1–6. Oct 2012.

[41] Fan, Y., Han, X., Xue, Z. and Jiang, H.: Design, analysis and control of a permanent magnet in-wheel motor based on magnetic-gear for electric vehicles. In: *2011 International Conference on Electrical Machines and Systems*, pp. 1–6. Aug 2011.

[42] Wang, L., Shen, J., Luk, P.-K., Fei, W., Wang, C. and Hao, H.: Development of a magnetic-geared permanent-magnet brushless motor. *Magnetics, IEEE Transactions on*, vol. 45, no. 10, pp. 4578–4581, Oct 2009. ISSN 0018-9464.

[43] Li, D., Qu, R. and Lipo, T.A.: High-power-factor vernier permanent-magnet machines. *IEEE Transactions on Industry Applications*, vol. 50, no. 6, pp. 3664–3674, Nov 2014. ISSN 0093-9994.

[44] Wu, L., Qu, R., Li, D. and Gao, Y.: Influence of pole ratio and winding pole numbers on performance and optimal design parameters of surface permanent-magnet vernier machines. *IEEE Transactions on Industry Applications*, vol. 51, no. 5, pp. 3707–3715, Sept 2015. ISSN 0093-9994.

[45] Liu, C., Chau, K.T. and Zhang, Z.: Novel design of double-stator single-rotor magnetic-geared machines. *Magnetics, IEEE Transactions on*, vol. 48, no. 11, pp. 4180–4183, Nov 2012. ISSN 0018-9464.

[46] Toba, A. and Lipo, T.: Novel dual-excitation permanent magnet vernier machine. In: *Industry Applications Conference, 1999. Thirty-Fourth IAS Annual Meeting. Conference Record of the 1999 IEEE*, vol. 4, pp. 2539–2544 vol.4. 1999. ISSN 0197-2618.

[47] Yang, H., Lin, H., Zhu, Z.Q., Fang, S. and Huang, Y.: Novel flux-regulatable dual-magnet vernier memory machines for electric vehicle propulsion. *IEEE Transactions on Applied Superconductivity*, vol. 24, no. 5, pp. 1–5, Oct 2014. ISSN 1051-8223.

[48] Li, J. and Chau, K.: Performance and cost comparison of permanent-magnet vernier machines. *Applied Superconductivity, IEEE Transactions on*, vol. 22, no. 3, pp. 5202304–5202304, June 2012. ISSN 1051-8223.

[49] Liu, C., Chau, K., Zhong, J., Li, W. and Li, F.: Quantitative comparison of double-stator permanent magnet vernier machines with and without HTS bulks. *Applied Superconductivity, IEEE Transactions on*, vol. 22, no. 3, pp. 5202405–5202405, June 2012. ISSN 1051-8223.

[50] Cheng, M. and Sun, L.: Torque density improvement of permanent-magnet vernier machines for hybrid electric vehicle. In: *Transportation Electrification Asia-Pacific (ITEC Asia-Pacific), 2014 IEEE Conference and Expo*, pp. 1–5. Aug 2014.

[51] Zhao, X., Niu, S. and Fu, W.: Torque component quantification and design guideline for dual permanent magnet vernier machine. *IEEE Transactions on Magnetics*, vol. 55, no. 6, pp. 1–5, June 2019. ISSN 0018-9464.

[52] Li, H., Liu, Y. and Zhu, Z.Q.: Comparative study of air-gap field modulation in flux reversal and vernier permanent magnet machines. *IEEE Transactions on Magnetics*, vol. 54, no. 11, pp. 1–6, Nov 2018. ISSN 0018-9464.

[53] Liu, W. and Lipo, T.A.: Analysis of consequent pole spoke type vernier permanent magnet machine with alternating flux barrier design. *IEEE Transactions on Industry Applications*, vol. 54, no. 6, pp. 5918–5929, Nov 2018. ISSN 0093-9994.

[54] Wang, Q., Niu, S. and Ching, T.W.: A new double-winding vernier permanent magnet wind power generator for hybrid AC/DC microgrid application. *IEEE Transactions on Magnetics*, vol. 54, no. 11, pp. 1–5, Nov 2018. ISSN 0018-9464.

[55] Xu, L., Zhao, W., Liu, G. and Song, C.: Design optimization of a spoke-type permanent-magnet vernier machine for torque density and power factor improvement. *IEEE Transactions on Vehicular Technology*, vol. 68, no. 4, pp. 3446–3456, April 2019. ISSN 0018-9545.

[56] Li, D., Zou, T., Qu, R. and Jiang, D.: Analysis of fractional-slot concentrated winding PM vernier machines with regular open-slot stators. *IEEE Transactions on Industry Applications*, vol. 54, no. 2, pp. 1320–1330, March 2018. ISSN 0093-9994.

[57] Xie, K., Li, D., Qu, R., Ren, X., Shah, M.R. and Pan, Y.: A new perspective on the PM vernier machine mechanism. *IEEE Transactions on Industry Applications*, vol. 55, no. 2, pp. 1420–1429, March 2019. ISSN 0093-9994.

[58] Zou, T., Li, D., Chen, C., Qu, R. and Jiang, D.: A multiple working harmonic PM vernier machine with enhanced flux-modulation effect. *IEEE Transactions on Magnetics*, vol. 54, no. 11, pp. 1–5, Nov 2018. ISSN 0018-9464.

[59] Kwon, H., Ro, J. and Jung, H.: Influence of a rotor eddy current on performance of a vernier permanent-magnet machine. In: *2018 21st International Conference on Electrical Machines and Systems (ICEMS)*, pp. 2822–2825. Oct 2018.

[60] Adnani, K., Shafiei, S., Millimonfared, J. and moghani, J.S.: Modified unipolar hybrid permanent magnet vernier machine using halbach array configuration. In: *2019 10th International Power Electronics, Drive Systems and Technologies Conference (PEDSTC)*, pp. 40–43. Feb 2019.

[61] Thyroff, D., Hittinger, C. and Hahn, I.: Comparison of the power factor of SMPM and SM vernier outer runner machines for traction applications. In: *2018 IEEE International Magnetics Conference (INTERMAG)*, pp. 1–4. April 2018. ISSN 2150-4601.

[62] Gerber, S. and Wang, R.-J.: Design and evaluation of a PM vernier machine. In: *Energy Conversion Congress and Exposition (ECCE), 2015 IEEE*, pp. 5188–5194. Sept 2015.

[63] Vanderplaats Resarch & Development, Inc: Theory manual. 2013, June.
Available at: http://www.vrand.com/visualDOC.html

[64] Deb, K., Pratap, A., Agarwal, S. and Meyarivan, T.: A fast and elitist multiobjective genetic algorithm: NSGA-II. *IEEE Transactions on Evolutionary Computation*, vol. 6, no. 2, pp. 182–197, April 2002. ISSN 1089-778X.

[65] Golchha, A. and Qureshi, M.S.G.: Non-dominated sorting genetic algorithm-II: A succinct survey. In: *International Journal of Computer Science and Information Technologies (IJCSIT)*, vol. 6, pp. 252–255. 2015.

[66] Potgieter, J.H.J. and Kamper, M.J.: Double PM-Rotor, toothed, toroidal-winding wind generator: A comparison with conventional winding direct-drive PM wind generators over a wide power range. *IEEE Transactions on Industry Applications*, vol. 52, no. 4, pp. 2881–2891, July 2016. ISSN 0093-9994.

[67] Ban, D., Zarko, D., Madercic, M., Zagreb, K.-K., Croatia, Z., Culig, M. and , P.: Generator technology for wind turbines, trends in application and production in croatia invited paper. 05 2019.

[68] Grauers, A.: *Design of Direct Driven Permanent Magnet Generators for Wind Turbines*. Ph.D. thesis, School of Electrical and Computer Engineering, CHALMERS UNIVERSITY OF TECHNOLOGY, 01 1996.

[69] D. Strous, T., Shipurkar, U., Polinder, H. and Ferreira, J.: Comparing the brushless DFIM to other generator systems for wind turbine drive-trains. *Journal of Physics: Conference Series*, vol. 753, 05 2019.

[70] Li, H., Chen, Z. and Polinder, H.: Optimization of multibrid permanent-magnet wind generator systems. *IEEE Transactions on Energy Conversion*, vol. 24, no. 1, pp. 82–92, March 2009. ISSN 0885-8969.

[71] Polinder, H., van der Pijl, F.F.A., de Vilder, G.. and Tavner, P.J.: Comparison of direct-drive and geared generator concepts for wind turbines. *IEEE Transactions on Energy Conversion*, vol. 21, no. 3, pp. 725–733, Sep 2006. ISSN 0885-8969.

[72] Yang, X., Patterson, D. and Hudgins, J.: Permanent magnet generator design and control for large wind turbines. In: *2012 IEEE Power Electronics and Machines in Wind Applications*, pp. 1–5. July 2012.

[73] Wen-Chang Tsai: Robust design of a 5MW permanent magnet synchronous generator using taguchi method. In: *2012 7th International Conference on Computing and Convergence Technology (ICCCT)*, pp. 1328–1334. Dec 2012.

[74] Li, H., Chen, Z. and Polinder, H.: Research report on numerical evaluation of various variable speed wind generator systems, deliverable no.: D 1b2.b.3. Tech. Rep., 2006.

[75] Aydin, E.: *Determination of best drive train technology for future onshore wind turbines as a function of the output power*. Master's thesis, The Department of Electrical Engineering of the Eindhoven University of Technology, 2013.

[76] Cao, W., Xie, Y. and Tan, Z.: *Wind Turbine Generator Technologies*. IntechOpen, 2012.

[77] ABB: Generators for wind turbines.

[78] Polinder, H., Van der Pijl, F., de Vilder, G.-J. and Tavner, P.: Comparison of direct-drive and geared generator concepts for wind turbines. In: *Electric Machines and Drives, 2005 IEEE International Conference on*, pp. 543–550. 2005.

[79] Bang, D., Polinder, H., Shrestha, G. and Ferreira, J.: Review of generator systems for direct-drive wind turbines. In: *European Wind Energy Conference & Exhibition, Brussels, Belgium, 31 March - 3 April 2008*.

[80] Goudarzi, N. and Zhu, W.D.: A review on the development of wind turbine generators across the world. *International Journal of Dynamics and Control*, vol. 1, no. 2, pp. 192–202, 2013. ISSN 2195-2698.

[81] Kadam, D. and Kushare, B.: Overview of different wind generator systems and their comparisons. *Int. J. Eng. Sci. Adv. Technol.[IJESAT]*, vol. 2, no. 4, pp. 1076–1081, 2012.

[82] Kimura, M., Ide, K., Nishihama, K., Futami, M., Ichinose, M., Fujigaki, T., Iizuka, M., Imaie, K., Yagi, Y. and Tamura, J.: A study of generator system selection for large wind turbine generator system. *IEEJ Transactions on Industry Applications*, vol. 126, no. 3, pp. 255–260, 2006.

[83] Li, H. and Chen, Z.: Overview of different wind generator systems and their comparisons. *Renewable Power Generation, IET*, vol. 2, no. 2, pp. 123–138, June 2008. ISSN 1752-1416.

[84] Yaramasu, V., Wu, B., Sen, P.C., Kouro, S. and Narimani, M.: High-power wind energy conversion systems: State-of-the-art and emerging technologies. *Proceedings of the IEEE*, vol. 103, no. 5, pp. 740–788, May 2015. ISSN 0018-9219.

[85] Johnson, M., Gardner, M.C., Toliyat, H.A., Englebretson, S., Ouyang, W. and Tschida, C.: Design, construction, and analysis of a large-scale inner stator radial flux magnetically geared generator for wave energy conversion. *IEEE Transactions on Industry Applications*, vol. 54, no. 4, pp. 3305–3314, July 2018. ISSN 0093-9994.

[86] Perez, J.M.P., Marquez, F.P.G., Tobias, A. and Papaelias, M.: Wind turbine reliability analysis. *Renewable and Sustainable Energy Reviews*, vol. 23, pp. 463 – 472, 2013. ISSN 1364-0321.

[87] Ukonsaari, J. and Bennstedt, N.: Wind turbine gearboxes: Maintenance effect on present and future gearboxes for wind turbines, report 2016:279. Tech. Rep., 2016.

[88] Errichello, R. and Muller, J.: Design requirements for wind turbine gearboxes. *NASA STI/Recon Technical Report N*, 09 1994.

[89] McMillan, D. and Ault, G.W.: Techno-economic comparison of operational aspects for direct drive and gearbox-driven wind turbines. *Energy Conversion, IEEE Transactions on*, vol. 25, no. 1, pp. 191–198, March 2010. ISSN 0885-8969.

[90] Atallah, K., Calverley, S., Clark, R., Rens, J. and Howe, D.: A new PM machine topology for low-speed, high-torque drives. In: *Electrical Machines, 2008. ICEM 2008. 18th International Conference on*, pp. 1–4. Sept 2008.

[91] Bao, G.Q. and Mao, K.F.: A wind energy conversion system with field modulated magnetic gear. In: *Power and Energy Engineering Conference (APPEEC), 2011 Asia-Pacific*, pp. 1–4. March 2011. ISSN 2157-4839.

[92] Jian, L., Chau, K. and Jiang, J.: A magnetic-geared outer-rotor permanent-magnet brushless machine for wind power generation. *Industry Applications, IEEE Transactions on*, vol. 45, no. 3, pp. 954–962, May 2009. ISSN 0093-9994.

[93] Atallah, K., Wang, J. and Howe, D.: A novel high-performance magnetic gear. *Journal of Applied Physics*, vol. 97, no. 10, pp. 1–3, May 2005. ISSN 0018-9464.

[94] Gerber, S. and Wang, R.: Evaluation of a prototype magnetic gear. In: *2013 IEEE International Conference on Industrial Technology (ICIT)*, pp. 319–324. Feb 2013.

[95] Zhu, D., Yang, F., Du, Y., Xiao, F. and Ling, Z.: An axial-field flux-modulated magnetic gear. *IEEE Transactions on Applied Superconductivity*, vol. 26, no. 4, pp. 1–5, June 2016. ISSN 1051-8223.

[96] Gardner, M.C., Johnson, M. and Toliyat, H.A.: Comparison of surface permanent magnet axial and radial flux coaxial magnetic gears. *IEEE Transactions on Energy Conversion*, vol. 33, no. 4, pp. 2250–2259, Dec 2018. ISSN 0885-8969.

[97] Filippini, M. and Alotto, P.: Coaxial magnetic gear design and optimization. *IEEE Transactions on Industrial Electronics*, vol. 64, no. 12, pp. 9934–9942, Dec 2017. ISSN 0278-0046.

[98] Chau, K., Zhang, D., Jiang, J., Liu, C. and Zhang, Y.: Design of a magnetic-geared outer-rotor permanent-magnet brushless motor for electric vehicles. *Magnetics, IEEE Transactions on*, vol. 43, no. 6, pp. 2504–2506, June 2007. ISSN 0018-9464.

[99] Qu, R., Li, D. and Wang, J.: Relationship between magnetic gears and vernier machines. In: *Electrical Machines and Systems (ICEMS), 2011 International Conference on*, pp. 1–6. Aug 2011.

[100] Venturini, M. and Leonardi, F.: High torque, low speed joint actuator based on PM brushless motor and magnetic gearing. In: *Industry Applications Society Annual Meeting, 1993., Conference Record of the 1993 IEEE*, pp. 37–42 vol.1. Oct 1993.

[101] Razzell, A. and Cullen, J.: Compact electrical machine. 2004. US Patent 6794781B2.

[102] Rasmussen, P.O., Mortensen, H.H., Matzen, T.N., Jahns, T.M. and Toliyat, H.A.: Motor integrated permanent magnet gear with a wide torque-speed range. In: *2009 IEEE Energy Conversion Congress and Exposition*, pp. 1510–1518. Sep 2009. ISSN 2329-3721.

[103] Rasmussen, P.O., Frandsen, T.V., Jensen, K.K. and Jessen, K.: Experimental evaluation of a motor-integrated permanent-magnet gear. *IEEE Transactions on Industry Applications*, vol. 49, no. 2, pp. 850–859, March 2013. ISSN 0093-9994.

[104] Mezani, S., Hamiti, T., Belguerras, L., Lubin, T., Rashed, M. and Gerada, C.: Magnetically geared induction machines. *IEEE Transactions on Magnetics*, vol. 51, no. 11, pp. 1–4, Nov 2015. ISSN 0018-9464.

[105] Bidouche, B., Lubin, T. and Mezani, S.: Design and analysis of a magnetically geared induction machine. In: *2018 XIII International Conference on Electrical Machines (ICEM)*, pp. 629–634. Sep 2018. ISSN 2381-4802.

[106] Ho, S.L., Niu, S. and Fu, W.N.: Transient analysis of a magnetic gear integrated brushless permanent magnet machine using circuit-field-motion coupled time-stepping finite element method. *IEEE Transactions on Magnetics*, vol. 46, no. 6, pp. 2074–2077, June 2010. ISSN 0018-9464.

[107] Powell, D.J., Calverley, S.D., de Wildt, F. and Daffey, K.: Design and analysis of a pseudo direct-drive propulsion motor. In: *5th IET International Conference on Power Electronics, Machines and Drives (PEMD 2010)*, pp. 1–2. April 2010.

[108] Evans, D.J. and Zhu, Z.Q.: Optimal torque matching of a magnetic gear within a permanent magnet machine. In: *2011 IEEE International Electric Machines Drives Conference (IEMDC)*, pp. 995–1000. May 2011.

[109] Tlali, P., Gerber, S. and Wang, R.-J.: Optimal design of an outer-stator magnetically geared permanent magnet machine. *Magnetics, IEEE Transactions on*, vol. 52, no. 2, pp. 1–10, Feb 2016. ISSN 0018-9464.

[110] Chen, Y., Fu, W. and Weng, X.: A concept of general flux-modulated electric machines based on a unified theory and its application to developing a novel doubly-fed dual-stator motor. *IEEE Transactions on Industrial Electronics*, vol. 64, no. 12, pp. 9914–9923, Dec 2017. ISSN 0278-0046.

[111] Niu, S., Liu, Y., Ho, S.L. and Fu, W.N.: Development of a novel brushless power split transmission system for wind power generation application. *IEEE Transactions on Magnetics*, vol. 50, no. 11, pp. 1–4, Nov 2014. ISSN 0018-9464.

[112] Gerber, S. and Wang, R.: Torque capability comparison of two magnetically geared PM machine topologies. In: *2013 IEEE International Conference on Industrial Technology (ICIT)*, pp. 1915–1920. Feb 2013.

[113] Wang, R., Bronn, L., Gerber, S. and Tlali, P.M.: Design and evaluation of a disc-type magnetically geared PM wind generator. In: *4th International Conference on Power Engineering, Energy and Electrical Drives*, pp. 1259–1264. May 2013. ISSN 2155-5532.

[114] Gerber, S. and Wang, R.: Analysis of the end-effects in magnetic gears and magnetically geared machines. In: *2014 International Conference on Electrical Machines (ICEM)*, pp. 396–402. Sep 2014.

[115] Shao, L., Hua, W., Zhu, Z.Q., Zhu, X., Cheng, M. and Wu, Z.: A novel flux-switching permanent magnet machine with overlapping windings. *IEEE Transactions on Energy Conversion*, vol. 32, no. 1, pp. 172–183, March 2017. ISSN 0885-8969.

[116] Du, Y., Xiao, F., Hua, W., Zhu, X., Cheng, M., Quan, L. and Chau, K.T.: Comparison of flux-switching PM motors with different winding configurations using magnetic gearing principle. *IEEE Transactions on Magnetics*, vol. 52, no. 5, pp. 1–8, May 2016. ISSN 0018-9464.

[117] Saou, R., Zaim, M.E. and Alitouche, K.: Optimal designs and comparison of the doubly salient permanent magnet machine and flux-reversal machine in low-speed applications. *Electric Power Components and Systems*, vol. 36, no. 9, pp. 914–931, 2008.

[118] Lee, C.H.: Vernier motor and its design. *IEEE Transactions on Power Apparatus and Systems*, vol. 82, no. 66, pp. 343–349, June 1963. ISSN 0018-9510.

[119] Rhodes, D.: Assessment of vernier motor design using generalised machine concepts. *Power Apparatus and Systems, IEEE Transactions on*, vol. 96, no. 4, pp. 1346–1352, July 1977. ISSN 0018-9510.

[120] Ishizaki, A., Tanaka, T., Takasaki, K. and Nishikata, S.: Theory and optimum design of PM vernier motor. In: *Electrical Machines and Drives, 1995. Seventh International Conference on (Conf. Publ. No. 412)*, pp. 208–212. Sep 1995.

[121] Espanet, C., Tekin, M., Bernard, R., Miraoui, A. and Kauffmann, J..: A new structure of an high torque in-wheel motor. In: *Sixth International Conference on Electrical Machines and Systems, 2003. ICEMS 2003.*, vol. 1, pp. 158–162. Nov 2003.

[122] Renedo Anglada, J. and Sharkh, S.M.: Analytical calculation of the torque produced by transverse flux machines. *IET Electric Power Applications*, vol. 11, no. 7, pp. 1298–1305, 2017. ISSN 1751-8660.

[123] Xu, W., Zhu, J., Zhang, Y. and Hu, J.: Cogging torque reduction for radially laminated flux-switching permanent magnet machine with 12/14 poles. In: *IECON 2011 - 37th Annual Conference of the IEEE Industrial Electronics Society*, pp. 3590–3595. Nov 2011. ISSN 1553-572X.

[124] Hao, L., Lin, M., Xu, D., Li, N. and Zhang, W.: Cogging torque reduction of axial-field flux-switching permanent magnet machine by rotor tooth notching. *IEEE Transactions on Magnetics*, vol. 51, no. 11, pp. 1–4, Nov 2015. ISSN 0018-9464.

[125] Dobzhanskyi, O., Gouws, R. and Amiri, E.: On the role of magnetic shunts for increasing performance of transverse flux machines. *IEEE Transactions on Magnetics*, vol. 53, no. 2, pp. 1–8, Feb 2017. ISSN 0018-9464.

[126] Dobzhanskyi, O., Gouws, R. and Amiri, E.: Comparison analysis of PM transverse flux outer rotor machines with and without magnetic shunts. In: *2016 IEEE Energy Conversion Congress and Exposition (ECCE)*, pp. 1–8. Sep 2016.

[127] Fan, Y., Huang, J., Han, X., Fu, X. and Wei, H.: Design, analysis and sensorless control of a new self-decelerating permanent-magnet motor. In: *IECON 2012 - 38th Annual Conference on IEEE Industrial Electronics Society*, pp. 4104–4109. Oct 2012. ISSN 1553-572X.

[128] Fan, Y., Zhang, L., Huang, J. and Han, X.: Design, analysis, and sensorless control of a self-decelerating permanent-magnet in-wheel motor. *IEEE Transactions on Industrial Electronics*, vol. 61, no. 10, pp. 5788–5797, Oct 2014. ISSN 0278-0046.

[129] Fan, Y., Jiang, H., Cheng, M. and Wang, Y.: An improved magnetic-geared permanent magnet in-wheel motor for electric vehicles. In: *Vehicle Power and Propulsion Conference (VPPC), 2010 IEEE*, pp. 1–5. Sept 2010.

[130] Jang, D.K. and Chang, J.H.: Design of a vernier machine with PM on both sides of rotor and stator. *Magnetics, IEEE Transactions on*, vol. 50, no. 2, pp. 877–880, Feb 2014. ISSN 0018-9464.

[131] Li, J. and Chau, K.T.: A novel HTS PM vernier motor for direct-drive propulsion. *IEEE Transactions on Applied Superconductivity*, vol. 21, no. 3, pp. 1175–1179, June 2011. ISSN 1051-8223.

[132] Sun, L. and Cheng, M.: Improvement of pole-splitting permanent-magnet vernier machine with permanent magnets on both stator and rotor sides. In: *Electrical Machines and Systems (ICEMS), 2014 17th International Conference on*, pp. 1556–1561. Oct 2014.

[133] Ishikawa, R., Sato, K., Shimomura, S. and Nishimura, R.: Design of in-wheel permanent magnet vernier machine to reduce the armature current density. In: *Electrical Machines and Systems (ICEMS), 2013 International Conference on*, pp. 459–464. Oct 2013.

[134] Zhao, W., Sun, X. and Ji, J.: Electromagnetic performance analysis of novel vernier permanent-magnet motor with improved torque capability. In: *2015 IEEE Magnetics Conference (INTERMAG)*, pp. 1–1. May 2015. ISSN 2150-4598.

[135] Xu, L., Liu, G., Zhao, W., Ji, J. and Fan, X.: High-performance fault tolerant halbach permanent magnet vernier machines for safety-critical applications. *IEEE Transactions on Magnetics*, vol. 52, no. 7, pp. 1–4, July 2016. ISSN 0018-9464.

[136] Zhao, F., Lipo, T.A. and Kwon, B.-I.: Dual-stator interior permanent magnet vernier machine having torque density and power factor improvement. *Electric Power Components and Systems*, vol. 42, no. 15, pp. 1717–1726, 2014.

[137] Jian, L., Xu, G., Gong, Y., Song, J., Liang, J. and Chang, M.: Electromagnetic design and analysis of a novel magnetic gear integrated wind power generator using time-stepping finite element method. *Progress In Electromagnetics Research*, vol. 113, pp. 351–367, 2011.

[138] Jian, L., Gong, W., Xu, G., Liang, J. and Zhao, W.: Integrated magnetic-geared machine with sandwiched armature stator for low-speed large-torque applications. *Magnetics, IEEE Transactions on*, vol. 48, no. 11, pp. 4184–4187, Nov 2012. ISSN 0018-9464.

[139] Wang, L., Shen, J. and Jin, M.: Design of a multi-power-terminals permanent magnet machine with magnetic field modulation. In: *Electrical Machines and Systems (ICEMS), 2011 International Conference on*, pp. 1–6. Aug 2011.

[140] Gao, Y., Qu, R., Li, J., Zhu, Z. and Li, D.: HTS vernier machine for direct-drive wind power generation. *Applied Superconductivity, IEEE Transactions on*, vol. 24, no. 5, pp. 1–5, Oct 2014. ISSN 1051-8223.

[141] Ho, S., Niu, S. and Fu, W.: Design and comparison of vernier permanent magnet machines. *Magnetics, IEEE Transactions on*, vol. 47, no. 10, pp. 3280–3283, Oct 2011. ISSN 0018-9464.

[142] Gieras, J. and Wing, M.: *Permanent Magnet Motor Technology: Design and Applications, Second Edition,*. Electrical and Computer Engineering. Taylor & Francis, 2002. ISBN 9780824743949.

[143] Zhu, Z.Q., Howe, D. and Chan, C.C.: Improved analytical model for predicting the magnetic field distribution in brushless permanent-magnet machines. *IEEE Transactions on Magnetics*, vol. 38, no. 1, pp. 229–238, Jan 2002. ISSN 0018-9464.

[144] Heller, B. and Hamata, V.: *Harmonic field effects in induction machines*. Elsevier Scientific Pub. Co. ; distribution for the U.S.A. and Canada, Elsevier/North-Holland Amsterdam ; New York : New York, 1977. ISBN 044499856.

[145] Zhu, Z.Q. and Howe, D.: Instantaneous magnetic field distribution in brushless permanent magnet DC motors. III. effect of stator slotting. *IEEE Transactions on Magnetics*, vol. 29, no. 1, pp. 143–151, Jan 1993. ISSN 0018-9464.

[146] Kim, B. and Lipo, T.A.: Operation and design principles of a PM vernier motor. *IEEE Transactions on Industry Applications*, vol. 50, no. 6, pp. 3656–3663, Nov 2014. ISSN 0093-9994.

[147] Pyrhonen, J., Jokinen, T. and Hrabovcova, V.: *Design of Rotating Electrical Machines*. Wiley, 2009. ISBN 9780470740088.

[148] Liwschitz-Garik, M.: *Electric machinery*. Van Nostrand, New York, N.Y., 1946.

[149] Skaar, S.E., Krøvel, Ø. and Nilssen, R.: Distribution, coil-span and winding factors for PM machines with concentrated windings. In: *Electrical Machines (ICEM), 2006 XVII International Conference on*. September 2006.

[150] Wang, K., Zhu, Z.Q. and Ombach, G.: Synthesis of high performance fractional-slot permanent-magnet machines with coil-pitch of two slot-pitches. *IEEE Transactions on Energy Conversion*, vol. 29, no. 3, pp. 758–770, Sep 2014. ISSN 0885-8969.

[151] Fitzgerald, A.E., Kingsley, C. and Umans, S.: *Electric Machinery*. McGraw-Hill series in electrical and computer engineering, 6th edn. McGraw-Hill, Boston, Mass, 2003. ISBN 0073660094.

[152] Potgieter, J.H.J. and Kamper, M.J.: Calculation methods and effects of end-winding inductance and permanent-magnet end flux on performance prediction of nonoverlap winding permanent-magnet machines. *IEEE Transactions on Industry Applications*, vol. 50, no. 4, pp. 2458–2466, July 2014. ISSN 0093-9994.

[153] Honsinger, V.B.: Theory of end-winding leakage reactance. *Transactions of the American Institute of Electrical Engineers. Part III: Power Apparatus and Systems*, vol. 78, no. 3, pp. 417–424, April 1959. ISSN 0097-2460.

[154] Krings, A., Nategh, S., Stening, A., Grop, H., Wallmark, O. and Soulard, J.: Measurement and modeling of iron losses in electrical machines. In: *Proceedings of the 5th International Conference Magnetism and Metallurgy WMM'12*, pp. 101–119. Gent University, 2012.

[155] Li, J., Abdallah, T. and Sullivan, C.R.: Improved calculation of core loss with nonsinusoidal waveforms. In: *Conference Record of the 2001 IEEE Industry Applications Conference. 36th IAS Annual Meeting (Cat. No.01CH37248)*, vol. 4, pp. 2203–2210. Sept 2001. ISSN 0197-2618.

[156] Mentor-Graphics: Magnet 2D/3D electromagnetic field simulation software. Available at: http://www.mentor.com/products/mechanical/magnet/magnet/

[157] Gerber, S. and Wang, R.: Evaluation of movement facilitating techniques for finite element analysis of magnetically geared electrical machines. *IEEE Transactions on Magnetics*, vol. 51, no. 2, pp. 1–6, Feb 2015. ISSN 0018-9464.

[158] Edwards, J.D.: An introduction to magnet for static 2D modeling. May 2014. Available at: http://www.mentor.com/products/mechanical/magnet/magnet/

[159] McFee, S., Webb, J.P. and Lowther, D.A.: A tunable volume integration formulation for force calculation in finite-element based computational magnetostatics. *IEEE Transactions on Magnetics*, vol. 24, no. 1, pp. 439–442, Jan 1988. ISSN 0018-9464.

[160] Libert, F. and Soulard, J.: Investigation on pole-slot combinations for permanent-magnet machines with concentrated windings. In: *Electrical Machines (ICEM), International Conference on*, p. 530. Sept 2004.

[161] Potgieter, J.H.J. and Kamper, M.J.: Design optimization of directly grid-connected PM machines for wind energy applications. *IEEE Transactions on Industry Applications*, vol. 51, no. 4, pp. 2949–2958, July 2015. ISSN 0093-9994.

[162] Frank, N.W. and Toliyat, H.A.: Gearing ratios of a magnetic gear for wind turbines. In: *2009 IEEE International Electric Machines and Drives Conference*, pp. 1224–1230. May 2009.

[163] Ede, J.D., Atallah, K., Jewell, G.W., Wang, J.B. and Howe, D.: Effect of axial segmentation of permanent magnets on rotor loss of modular brushless machines. In: *Conference Record of the 2004 IEEE Industry Applications Conference, 2004. 39th IAS Annual Meeting.*, vol. 3, pp. 1703–1708 vol.3. Oct 2004. ISSN 0197-2618.

[164] Nair, S., Wang, J., Sun, T., Chen, L., Chin, R., Beniakar, M., Svechkarenko, D. and Manolas, I.: Experimental validation of 3D magnet eddy current loss prediction in surface mounted permanent magnet machines. *IEEE Transactions on Industry Applications*, May 2017.

[165] Gerber, S. and Wang, R.: Cogging torque definitions for magnetic gears and magnetically geared electrical machines. *IEEE Transactions on Magnetics*, vol. 54, no. 4, pp. 1–9, April 2018. ISSN 0018-9464.

[166] Gerber, S. and Wang, R.: Statistical analysis of cogging torque considering various manufacturing imperfections. In: *2016 XXII International Conference on Electrical Machines (ICEM)*, pp. 2066–2072. Sep 2016.

[167] Gasparin, L., Cernigoj, A., Markic, S. and Fiser, R.: Additional cogging torque components in permanent-magnet motors due to manufacturing imperfections. *IEEE Transactions on Magnetics*, vol. 45, no. 3, pp. 1210–1213, March 2009. ISSN 0018-9464.

[168] Mthombeni, T.L. and Pillay, P.: Physical basis for the variation of lamination core loss coefficients as a function of frequency and flux density. In: *IECON 2006 - 32nd Annual Conference on IEEE Industrial Electronics*, pp. 1381–1387. Nov 2006. ISSN 1553-572X.

[169] Ionel, D.M., Popescu, M., Dellinger, S.J., Miller, T.J.E., Heideman, R.J. and McGilp, M.I.: On the variation with flux and frequency of the core loss coefficients in electrical machines. *IEEE Transactions on Industry Applications*, vol. 42, no. 3, pp. 658–667, May 2006. ISSN 0093-9994.

[170] Ionel, D.M., Popescu, M., Dellinger, S.J., Miller, T.J.E., McGilp, M.I. and Heideman, R.J.: Factors affecting the accurate prediction of iron losses in electrical machines. In: *IEEE International Conference on Electric Machines and Drives, 2005.*, pp. 1625–1632. May 2005.

[171] Johnson, M., Gardner, M.C. and Toliyat, H.A.: Design comparison of NdFeB and ferrite radial flux surface permanent magnet coaxial magnetic gears. *IEEE Transactions on Industry Applications*, vol. 54, no. 2, pp. 1254–1263, March 2018. ISSN 0093-9994.